UNVEILING THE ARCHITECTURE OF THE FORNAX GALAXY CLUSTER WITH ITS DIFFERENT STELLAR SYSTEMS

Yasna Ordenes Briceño

Santiago and Heidelberg
2018

Dissertation in Astronomy
submitted to the
Combined Faculties of the Natural Sciences and Mathematics
of the Ruperto-Carola-University of Heidelberg, Germany
and
Faculty of Physics of the Pontifical Catholic University of Chile
for the degree of
Doctor of Natural Science

Put forward by

Yasna Ordenes Briceño
born in Coquimbo, Chile.

Oral examination: 25 October 2018

UNVEILING THE ARCHITECTURE OF THE FORNAX GALAXY CLUSTER WITH ITS DIFFERENT STELLAR SYSTEMS

Yasna Ordenes Briceño

Referees:
Prof. Dr. Thomas Puzia
Prof. Dr. Eva Grebel

A mi pareja, amigo, partner de la vida, Ariel Tirado.
A mi familia Ordenes-Briceño, Hugo, Jacqueline, Ochin y Yordan.
A mis abuelos, Rosa y Juan. A los que ya partieron, Periquito y Julita.

ABSTRACT

A crucial question in astronomy is how galaxies assemble their mass over cosmic time. In this thesis, we focus on the Fornax Galaxy Cluster as a laboratory to study galaxy evolution processes, as it is the second closest galaxy cluster which allows a detailed view of its cluster members. It hosts a variety of stellar systems from giant galaxies to dwarf galaxies and more compact and dense ones such as globular clusters and ultra-compact dwarf galaxies which we call compact stellar systems (CSSs). We use data from the *Next Generation Fornax Survey* (NGFS) with optical imaging obtained with the Dark Energy Camera (DECam) mounted at Blanco/CTIO and near-infrared data obtained with VIRCam at VISTA/ESO. This data provides deep and homogeneous photometry in $u'g'i'JK_s$ spatially covering the Fornax cluster out to half its virial radius. We investigate the properties of nucleated dwarf galaxies and compact stellar systems in the Fornax core region ($r < 0.25r_{vir}$). Furthermore, we study the dwarf galaxy population with $M_B > -16$ in the outer region of Fornax at radii of $0.25 < r/r_{vir} < 0.5$. The main results of this thesis are as follows: (1) We have discovered 271 previously undetected dwarf galaxies in the outer Fornax cluster region, increasing the the total Fornax dwarf galaxy population from NGFS and other catalogs to a total number of 643 dwarfs with 181 being nucleated. (2) The study of 61 nuclear star clusters in dwarf galaxies showed that the nuclei have a bimodal mass distribution and that the scaling relation between nuclei mass and host galaxy mass holds for dwarf galaxies but at a less steep slope compared to brighter galaxies. The mass ratio $\mathcal{M}_{\rm nuc}/\mathcal{M}_{\rm gal}$ shows a clear anti-correlation with $\mathcal{M}_{\rm gal}$ for the lowest masses, reaching up to 10%. (3) A total of 1666 CSS candidates have been studied in the core region of Fornax, being the most clean photometriccally selected sample using support vector machine techniques. Age, metallicity and mass were estimated for each CSS. A division of the properties in subgroups showed that the metal poor and old CSSs are sparsely distributed, intermediate metallicity and young CSSs are preferentially located along the East-West direction of Fornax centered in NGC 1399 and the most metal rich CSSs are concentrated in the vecinity of NGC 1399 and around the brightest galaxies. These different distributions for the metallicity and age subgroups allow us to constrain the mass assembly history of the Fornax Cluster. (4) Besides the Fornax cluster, we also discover five very diverse dwarf galaxies in another region of the sky, i.e. Hickson Compact Group 90 (HCG 90). Two of these dwarfs are a dwarf galaxy pair and one is a nucleated dwarf galaxy. According to their luminosity and structural parameters, they are similar to the dwarf galaxies we found in Fornax.

ZUSAMMENFASSUNG

Eine entscheidende Frage in der Astronomie ist wie Galaxien ihre Masse im Laufe der Entwicklung des Universums zusammenzustellen. In dieser Arbeit konzentrieren wir uns auf den Fornax-Galaxienhaufen, ein ideales Labor um Galaxienentwicklungsprozesse zu untersuchen. Da Fornax der am zweitnächsten gelegene Galaxienhaufen ist, ist eine detaillierte Untersuchung seiner Galaxienpopulation möglich. Er beherbergt eine Vielzahl von Sternsystemen, von massereichen Galaxien bis zu Zwerggalaxien und kompakteren und dichteren Sternsystemen wie Kugelsternhaufenhaufen und ultrakompakten Zwerggalaxien. Wir benutzen Daten vom *Next Generation Fornax Survey* (NGFS), bestehend aus Aufnahmen mit der Dark Energy Camera (DECam) des 4-Meter Cerro Tololo Blanco Teleskops im Optischen und Daten des ESO/VISTA Teleskops mit VIRCAM im Nahen Infrarot. Diese Daten liefern homogene und tiefe Photometrie im gesamten Survey und decken einen großen Wellenlängenbereich ab ($u'g'i'JK_s$). Wir untersuchen die Eigenschaften von Zwerggalaxien mit Nukleus und kompakte Sternsysteme im Zentralbereich des Fornax-Haufens ($r < 0.25 r_{vir}$). Außerdem untersuchen wir die Zwerggalaxienpopulation ($M_B > -16$) in den äußeren Bereichen $0.25 < r/r_{vir} < 0.5$ des Fornax-Haufens. Die wichtigste Ergebnisse dieser Arbeit sind wie folgt: (1) Wir haben 271 zuvor nichtdetektierte Zwerggalaxien in den äußeren Bereichen des Fornax-Haufens katalogisiert, resultierend in insgesamt 643 Zwerggalaxien, wobei 181 davon einen Nukleus aufweisen. (2) Die Untersuchung von 61 nuclear star clusters in Zwerggalaxien zeigen eine bimodale Massenverteilung. Wir finden dass die Skalenrelationen zwischen Nukleus Masse und der entsprechenden Host-Galaxie für Zerggalaxien gelten, jedoch mit geringerer Steigung und dass das Massenverhältnis $\mathcal{M}_{nuc}/\mathcal{M}_{gal}$ eine klare Anti-Korrelation mit $\mathcal{M}_{gal}$ für die niedrigsten Massen bis 10% aufweist. (3) 1666 Kandidaten für kompakte Sternsysteme wurden im Zentralbereich des Fornax-Haufens untersucht. Dies stellt das beste photometrisch selektierte Sample mit Hilfe von vector machine techniques dar. Alter, Metallizität und Masse wurden für jedes kompakte Sternsystem bestimmt. Eine Unterteilung der Eigenschaften in Untergruppen zeigte dass die metallarmen und alten kompakten Sternsysteme diffus verteilt sind, Objekte mit mittlerer Metallizität und jungem Alter jedoch vorzugsweise entlang der Ost-West-Richtung von Fornax zentriert um NGC 1399 anzutreffen sind und das die metallreichsten kompakten Sternsysteme in der Nähe von NGC 1399 und den hellsten Galaxien konzentriert sind. Diese unterschiedlichen Verteilungen für die Alters- und Metallizitätsunterteilungen geben einen Hinweis über die Entwicklungsgeschichte des Fornax-Haufens. (4) Neben dem Fornax Galaxienhaufen präsentieren wir fünf sehr unterschiedliche Zwerggalaxien in einem anderen Bereich des Himmels, in der Hickson Compact-Group 90 (HCG 90). Zwei der Zwerge sind ein Zwerggalaxienpaar und eine ist eine Zwerggalaxie mit Nukleus. Entsprechend ihrer Leuchtkraft und strukturellen Parametern sind diese mit den Zwerggalaxien in Fornax vergleichbar.

PUBLICATIONS

Part of the work shown in my thesis have appeared previously in the following publications:

The Next Generation Fornax Survey (NGFS): IV. Mass and Age Bimodality of Nuclear Clusters in the Fornax Core Region. Authors: Yasna Ordenes-Briceño, Thomas Puzia, Paul Eigenthaler et al. 2018, ApJ, 860, 4.

The Next Generation Fornax Survey (NGFS): III. Revealing the Spatial Substructure of the Dwarf Galaxy Population inside half of Fornax's Virial Radius. Authors: Yasna Ordenes-Briceño, Paul Eigenthaler, Matthew Taylor, Thomas Puzia et al. 2018, ApJ, 859, 52.

The Next Generation Fornax Survey (NGFS): II. The Central Dwarf Galaxy Population. Authors: Paul Eigenthaler, Matthew Taylor, Thomas Puzia, Yasna Ordenes-Briceño et al. 2018, ApJ, 855,142.

Faint Dwarf Galaxies in Hickson Compact Group 90. Authors: Yasna Ordenes-Briceño, Matthew Taylor, Thomas Puzia et al. 2016, MNRAS, 463, 1284.

The passioned, enthusiastic, curious and self motivated people,
science and the world need more of us.
A lxs apasionadxs, entusiastxs, curiosxs y auto motivadxs,
la ciencia y el mundo necesitan más como nosotrxs.
— Yasna Ordenes-Briceño

ACKNOWLEDGMENTS

This is the end of a stage, of a lot of growth both as a person and intellectually. The hours of study and research have been totally worth it. I have enjoyed this cycle a lot and with mixed feelings now I must close it.

During my time as a PhD student I have met many beautiful people, in addition to the beautiful people who were already in my life, who have contributed in one way or another to reach this point where I am today. I thank my supervisor Thomas Puzia, who has been always there, thanks for all the support, trust and learning given. To my supervisor Eva Grebel, always attentive and willing to help, her scientific comments have been very valuable. It has been a pleasure to have both of you as supervisors and guides of my PhD thesis. To the research groups of the IA in Santiago and ARI in Heidelberg, the meetings and scientific discussions were very fruitful to improve or obtain new ideas for the science that one is doing and also learn to communicate it, specially to Roberto, Paul E., Karla, Matt, Faezeh, Zdenek and Michael. To the administrators of each institute for their willingness to support us as students, especially Mariela, Carmen Gloria and Cynthia. To the IA's cleaning staff, Sonia and Maria, for the conversations and good vibes.

How not to thank my couple, Ariel Tirado, for all the support given in this process and always enhancing our skills and looking together for new challenges as a couple and as individuals. To my family Ordenes-Briceño, my mom Jacqueline, my dad Hugo and my brothers Ochin and Yordan, they are always there in everything, supporting me in every madness/challenge that I undertake, thanks. I have a large family supporting me on the maternal (Briceño-Gomez) and paternal (Ordenes-Campos) side, always I have felt your unconditional support, a special thanks to my grandparents Rosa, Juan and Julia, Sergio. To my friends who are scattered in various places of Chile and the world, I can only mention some here, Cristi, Paito, Paul L., Mary, Karla, Cris. To my adoptive grandmothers, Rosita and Maria Ines from the nursing home I visit.

To all the women in science who have overcome thousands of barriers to be where they are today, in a science that has been preferentially for men. Things are changing now, in some places more quickly than in others. The path that the new generations faces is much more kind than a few years ago, however we are still far to reach equity. Women in science who managed to surpass social barriers and followed their passion, my admiration to you.

From the age of 13 that I was dreaming about studying the Universe, with that wonderful sky that can be seen from the region of Coquimbo and here I am with my goal of being Astrophysicist fulfilled. A lot remains to be done, to explore, to find or be found by new challenges and to continue growing as a person and as scientist. To conclude I want to emphasize my immense gratitude to every person who have been part of this path.

"Me estremecieron mujeres que la historia escribió entre laureles
y otras desconocidas gigantes, que no hay libro que las aguante.
— Mujeres, Silvio Rodriguez

AGRADECIMIENTOS

Esta es la finalización de una etapa, de mucho crecimiento tanto como persona como intelectualmente. Las horas de estudio y de investigación han valido totalmente la pena. He disfrutado mucho de este ciclo y con sentimientos encontrados ahora debo cerrarlo.

Durante mi etapa de estudiante de doctorado he conocido muchas personas lindas, además de las personas lindas que ya estaban en mi vida, que han aportado de una u otra forma para llegar a este punto en el que estoy hoy. Agradezco a mi supervisor Thomas Puzia, que ha estado ahi siempre, gracias por todo el apoyo, confianza y el aprendizaje entregado. A mi supervisora Eva Grebel, siempre atenta y dispuesta a ayudar, sus comentarios cientificos han sido muy valiosos. Ha sido un placer tenerlos a los dos de supervisores y guias de mi tesis de doctorado. A los grupos de investigación del IA en Santiago y ARI en Heidelberg, las reuniones y discusiones científicas fueron muy fructiferas para mejorar u obtener nuevas ideas para la ciencia que uno esta haciendo y también aprender a comunicarlas, especialmente a Roberto, Paul E., Karla, Matt, Faezeh, Zdenek and Michael. A los administrativos de cada instituto por su disposición a ayudarnos a nosotros como estudiantes, en especial a Mariela, Carmen Gloria y Cynthia. Al personal del aseo del IA, Sonia y Maria, por las conversaciones y buenas vibras.

Como no agradecer a mi pareja, Ariel Tirado, por todo el apoyo entregado en este proceso y siempre potenciando nuestras habilidades y buscando nuevos desafíos como pareja y como individuos. A mi familia Ordenes-Briceño, mi mamá Jacqueline, mi papá Hugo y mis hermanos Ochin y Yordan, siempre estan ahi en todas, apoyandome en cada locura/desafio que me propongo, muchas gracias. Tengo una gran familia respaldandome por parte materna (Briceño-Gomez) y paterno (Ordenes-Campos), siempre he sentido su apoyo incondicional, un agradecimiento especial a mis abuelos Rosa, Juan y Julita, Periquito. A mis amigos que estan esparcidos por varios lugares de Chile y del mundo, solo podre mencionar a algunos, Cristi, Paito, Paul L., Mary, Karla, Cris. A mis abuelas adoptivas, Rosita y Maria Ines del hogar de adultos mayores que visito.

A todas las mujeres en ciencia que han superado miles de barreras para estar donde estan hoy, en una ciencia que ha sido preferencialmente para hombres. Las cosas estan cambiando ahora, en algunos lugares más rápido que en otros, por eso el camino que enfrentamos las nuevas generaciones es mucho más amable que hace unos años atrás, pero aún falta bastante para llegar a la equidad. A las mujeres en ciencia que lograron sobrepasar las barreras sociales y seguir su pasión, mi admiración a ustedes.

Desde los 13 años que soñaba con estudiar el Universo, con ese maravilloso cielo que se puede ver desde la región de Coquimbo y aqui estoy con mi meta de ser Astrofísica cumplida. Aún queda mucho por hacer, explorar, encontrar o ser encontrado por nuevos desafios y seguir creciendo como persona y como científica. Solo recalcar mi gratitud inmensa a cada una de las personas que han sido parte de este lindo camino.

CONTENTS

LIST OF FIGURES

LIST OF TABLES

1

INTRODUCTION

1.1 CLUSTER AND GROUP OF GALAXIES

Stellar systems complete in themselves was the basis of our definition of galaxies given by Edwin Hubble in 1926, it was also the starting point for these *nebulae* to be recognized as extragalactic stellar systems (Hubble, 1926). By naked-eye only five of this "nebulae" are visible, our own Milky way (a part of it), Andromeda (M31), M33, the Large Magellanic Cloud (LMC) and the Small Magellanic Cloud (SMC). In the Southern skies by looking to the Milky Way we could see how it is a galaxy from inside, a nebula with conglomeration of stars, dust and gas. With the help of telescopes, astronomers could investigate further out their properties and soon realize that our closest neighbors where just a tiny fraction of the vast population of galaxies in the universe and with an inmense zoo of morphologies. A first attempt to classify them into type of galaxies according to their appearance was Hubble in his work *Extragalactic Nebulae* (Hubble, 1926). He divided the 400 nebulae in his catalogue from photographic plates into three main divisions, ellipticals, spirals and irregular galaxies. In his work *"The realm of the nebulae"* (Hubble, 1936), he describes the sequence of nebular types (now known as the Hubble tunning fork) and an intermediate stage nebulae was added between type E7 and Sa/Sab, it was designated as S0 or lenticular galaxy. At that time, it was believed that ellipticals evolve to become spiral nebulae, thus lenticular galaxies were a very important stage in all theories of nebular evolution, as consequence the name "early-type" galaxies was assigned to ellipticals and "late-type" galaxies to spirals. This evolutionary path is no longer valid, but nowadays we still use the term of early-type to refer to elliptical and/or lenticular galaxies (ETGs) and late-type to refer to spirals and/or irregular galaxies (LTGs).

The current zoo of galaxy morphologies continue growing with the progress in technology and more sophisticated instruments. However, as a general picture for giant galaxies the one described by Hubble (1936) was quite complete. The real picture for galaxies of each family is much more complex in terms of surface brightness, kinematics, bulge-to-disk ratio, bar, gas fraction, among others. The detailed explanation is beyond the scope of this introduction, but a good review of the different properties between morphological type of galaxies can be found for instance in the book *Extragalaxtic Astronomy and Cosmology* (Schneider, 2015, chapter 3) and *Galaxies in the Universe* (Sparke, & Gallagher, 2007).

Galaxies are not uniformly distributed in space, but prefer to gather together in group and cluster of galaxies, forming overdense regions in the Universe. Group and cluster of galaxies differ mainly in the number of bright galaxies they contain. A group of galaxies is normally defined as 4 to 5 massive galaxies (e.g. Hickson, 1982), our most nearby example is the group we are, the Local Group (LG). With an extension of $\sim$1 Mpc, the LG has two massive spirals, the Milky Way and Andromeda, besides the spiral M33 and the two irregular galaxies LMC and SMC, in adittion of more than 100 dwarf galaxies (McConnachie, 2012). A cluster of galaxies can contain hundreds to thousand of galaxy members. The first catalog of galaxy clusters was done by Abell (1958), where he detected 1682 clusters in the Northern sky using the Palomar Observatory facilities. The identification was done tracing overdensities of galaxies with the following criteria: galaxy members are no more than two magnitudes fainter than the third brightest member and do not have a projected distance from the center larger than the Abell radius $r_{Abell} = 3h_{50}^{-1}$ Mpc. The Southern counterpart catalog was published in the work by Abell et al. (1989), with a total number of 4076 clusters, which includes the galaxy clusters identified in the previous study in the Northern hemisphere. Abell catalog divides the cluster into six richness class, depending on the member numbers, richness 0 means N< 50, thus they were not considered in the final cluster catolog. A richness class 5 means that the cluster contains more than 300 luminous galaxies.

Galaxy clusters are the most massive gravitationally bound systems in the universe with total masses in the range 10^{14} to $10^{15}M_{\odot}$. Observing a galaxy cluster in different wavelength show that the optical apperance is only a small fraction of the total mass of a galaxy cluster. X-ray observations show that the most massive visible component of clusters is the hot gas ($T \sim 3 \times 10^{7}$ K) coming from the *intracluster medium* (ICM), hot gas in between the galaxies. A massive cluster defined in the optical with the Abell richness class, in X-ray would be an extended X-ray emission from the hot gas as a result of a deep gravitational potential. The velocity dispersion of galaxy clusters correlates with the reachness of clusters, for instance Becker et al. (2007) measured the mean velocity dispersion for 13823 clusters selected with SDSS in a redshift range $0.1 < z < 0.3$ and found that σ_v increases from 202 ± 10 km/s for small groups and can be more than 854 ± 102 km/s for large clusters.

1.1.1 *Morphological classification of galaxy clusters*

The morphological classification of clusters is based in the distribution of galaxies inside the cluster. There are different classification in the literature, but they coincide in three main types: regular, intermediate and irregulars distributions. For instance, Zwicky et al. (1961) classified regular clusters as compact and irregular as open and with or without strong central concentrations. Meanwhile, a classification by Rood, & Sastry (1971) indicates six subtypes, from irregular to regular, from a complete irregular distribution (I), to a more centrally distribution of galaxies, with two bright galaxies in the center (B) or a cD galaxy dominating the cluster center (cD). A cD galaxy is more massive than a regular elliptical galaxy, the most striking characteristic it is a low surface brighteness extended stellar halo (Morgan, & Lesh, 1965; Matthews et al., 1964), they are located at the kinematical center of their cluster (Quintana, & Lawrie, 1982) and on high density peaks, 2-3 times greater than peaks without a cD galaxy (Beers, & Geller, 1983). It is beleived that this massive ellipticals are the consequence of the evolutionary process of dense environments (Dressler, 1984).

1.1.2 *Morphology-density relation*

With the study of 55 nearby galaxy clusters, Dressler (1980) showed that the increasing number of elliptical and S0 population is tightly related with the dependence of galaxy morphology and the environment density, the so called morphology-density relation. As consequence of this relation, low density fields are dominated by spirals and high density fields by ellipticals and S0 galaxies. According to the work of Postman, & Geller (1984), this relation holds for galaxy groups which have a galaxy density larger than $\simeq 5\,\mathrm{Mpc}^{-3}$. For density below than this limit the morpholgy fraction seems to be independent of the environment.

Large survey of galaxies with spectroscopic redshifts like 2dF Galaxy Redshift Survey (2dFGRS, Colless et al., 2001) and the Sloan Digital Sky Survey (SDSS, York et al., 2000) have found an agreement with early works on this relation. For instance, Domínguez et al. (2002) using the 2dF Galaxy group catalog in the redshift range $0.02 < z < 0.05$ found that the morphology-density relation is clearly seen up to galaxy groups with virial masses of $M_{virial} \geqslant 10^{13.5} M_{\odot}$. Goto et al. (2003) using SDSS galaxies in the redshift range of $0.01 < z < 0.054$ confirmed that ETGs increase and LTGs decrease toward increasing local galaxy density, and that in the outer region of clusters, the morphology-density relation becomes less noticeable, thus physical mechanism to change the galaxy morphology acts in denser environments, i.e. in the inner regions of clusters.

1.1.3 *Color-magnitude relation*

The color of galaxies in clusters have a small spread, with a tight color-magnitude relation (Baum, 1959; de Vaucouleurs, 1961). Visvanathan, & Sandage (1977) confirmed the color-magnitude relation (CMR) using galaxies from nine nearby galaxy clusters, they showed that the relation is strongly wavelength dependent with a maximum near $\lambda 3500$, a tight relation is seen in the $u - V$ vs V diagram, with brighter galaxies having redder colors. They further noticed the universality of this relation, the color-magnitude relation for all their sample have slope and scatter for their CMR is roughly constant. They can be made to coincide to form a common composite correlation and it can be used to find relative distances. Extensively studies have been done in the literature to check the validity of the color-magnitude relation both, in low and high redshift galaxy clusters (Sandage, & Visvanathan, 1978; Bower et al., 1992; Stanford et al., 1998; Ellis et al., 1997; Kodama & Arimoto, 1997; Blakeslee et al., 2003; Mei et al., 2006, 2009), where an insignificant small spread and similar slope is found for clusters from different epochs.

The remarkable agreement in the CMR of galaxy clusters and its little evolution with redshift indicates that the ETGs in clusters have formed at earlier times of the Universe, and have evolve passively since then into the old stellar population we observe in the local examples.

1.1.4 *Star formation rate - local projected density relation*

The difference in colors between spirals in clusters and spirals in the field detected in the Virgo cluster by Holmberg (1958), was the first hint that the star formation rate in a cluster environment is reduced or suppressed. On the other hand, the HI content is much lower than in field galaxies with this HI-deficiency preferentially occur in high-density regions (Davies, & Lewis, 1973; Kennicutt, 1983; Giovanelli, & Haynes, 1983; Chincarini et al., 1983). The absence of emission lines in galaxies of clusters compared to the field was identified long ago (Osterbrock, 1960; Gisler, 1978; Dressler et al., 1985). Balogh et al. (1997, 1998) measured the equivalent width of [OII] $\lambda 3727$ emission line for cluster and field galaxies at $0.2 < z < 0.55$ and found that the emission lines in cluster galaxies at all distances from the cluster center ($< 2R_{200}$) are less common than in field galaxies.

Large statistical samples of galaxies with $SFR_{H_{\alpha}}$ measurements at $0.05 < z < 0.1$ from 2dFGRS (Lewis et al., 2002) and SDSS (Gómez et al., 2003) were used to study the relation between SFR and environment. They found agreement with the work of Balogh et al.. SFR increases towards the cluster outskirts. The correlation found between star formation rate and local projected density is independent of cluster velocity dispersion and disappears at projected density approximately to the mean density at the cluster virial radius. They conclude that this relation is not restricted to cluster cores, but are effective in all groups where the density exceeds this local density value.

These observational evidence point to a transformation process, that a star-forming field galaxy experience when infalling into a high density environment, like a galaxy cluster, where its star formation is reduced until is totally quenched (gas resevoir depleted) and finally become one more of the passively evolving member of the cluster.

1.1.5 *Butcher-Oemler effect*

An important evidence was obtained by Butcher, & Oemler (1978, 1984) about the evolution of galaxy clusters, when they analyzed a cluster sample at low and at high redshift ($z < 0.4$) and found that the fraction of blue galaxies (spirals) increases with redshift (Butcher-Oemler effect). Although the above study was based only in photometric results, spectroscopically confirmation was made by several studies (e.g. Dressler, & Gunn, 1982, 1992).

The study by Ellingson et al. (2001) of 16 rich X-ray luminous galaxy clusters with $0.17 < z < 0.55$ found evolution in the fractional population where in the core of clusters a similar population is found either at low or at high redshift, however, more star-forming galaxies are found at high redshift clusters in a radii outside of the core region. De Propris et al. (2004) used the 2dFGRS sample of 60 clusters at z < 0.11 with spectroscopically confirmed members and compared to the field galaxy population at the same redshift and found blue galaxy fraction in all clusters, with some of them with fraction larger than 40%, and did not find correlation between the galaxy cluster properties such as richness, substructure and concentration. Using Spitzer/MIPS 24μm and near-infrared for 30 massive galaxy clusters at $0.02 < z < 0.40$, Haines et al. (2009) detect an increment of $\sim 3\%$ in the fraction of blue galaxies at $z = 0.02$ and $\sim 10\%$ at $z = 0.30$.

The Butcher-Oemler effect bring a perspective of clusters as active sites for galaxy evolution and the environmental effect that their member suffers dramatically transform their morphologies and star formation histories over cosmic time.

1.1.6 *Color distribution of galaxies in different environments*

Color-magnitude diagrams are useful tools to infer the mass assembly and star formation histories of galaxies. As was explained in Section 1.1.3 the color of galaxies in a cluster environment have a small spread, this tight correlation for the galaxies in cluster environment is called the red sequence. However, when comparing with the field population or losely groups a blue population of galaxies appears. With the increment of large surveys mapping the sky (e.g. 2dFGRS and SDSS) astronomers have been able to study the galaxy population to higher redshift in all environments, it was soon realized that the red sequence is only one side of the broader phenomenon of galaxy color.

Strateva et al. (2001) studied the optical colors of more than 100 thousands of galaxies with SDSS data and found that the distribution of galaxies in the color-color diagram was strongly bimodal, using a morpholgy separation subsamples they showed that the two peaks corresponds to early and late-type galaxies, driven by their different stellar populations. Later studies have confirmed the galaxy color bimodality (e.g. Baldry et al., 2004; Balogh et al., 2004, and references therein), the galaxies belonging to the red peak are the red sequence seen in high density environments, the ones in the bluer peak are refered as the blue cloud, and the population in between are called the green valley (Martin et al., 2007; Wyder et al., 2007). The simplest interpretation for these features are attributed to the idea of an evolutionay sequence from the blue cloud towards the red sequence, with transformation process in between (green-valley galaxies) causing to quench star formation and get a passively evolving stellar population. Although, it has also been argued that the green valley galaxies may only be the overlap of two broad red and blue distributions (Taylor et al., 2015) or passive galaxies where the star formation has been rejuvenated (e.g. Thilker et al., 2010; Mapelli et al., 2015).

1.1.7 *Quenching mechanisms*

As we have seen in the above sections, galaxies are affected by their environment over cosmic time causing changes in their morphology and star formation the latter might be either by the removal and/or expulsion of the existing gas reservoir, or by preventing the accretion of new material.

The mechanism at play can be divided in three main categories: (i) secular evolution of the galaxy mainly from Active Glactic Nuclei (AGN) and Supernovae (SNe) feedback (ii) galaxy-intracluster medium interaction (iii) tidal interaction and galaxy mergers. AGN feedback from SMBH is an efficient mechanism to heat the halo gas and impede the cooling, this works more efficiently when the AGN is in the radio mode (e.g. Springel et al., 2005). The relation found between SMBH mass and its host mass (Magorrian et al., 1998) and galaxy velocity dispersion (Ferrarese, & Merritt, 2000) confirm the tight link of the SMBH with the evolution of its host galaxy . SNe explosions are energetic enough to remove a large fraction of gas for low mass galaxies up to $\sim 10^8\,M_\odot$ (Dekel, & Silk, 1986). Low mass galaxies (LTG regular and dwarf galaxies) due to their shallow gravitational potential and/or less bound gas are more prone to be affected by the hot intracluster medium that resides in dense environments which exerts pressure that removes the galaxy's gas, this effect is called ram-pressure stripping (Gunn, & Gott, 1972; Lin, & Faber, 1983). They are also affected by "galaxy harassment", due to tidal induced mass loss by close encounters with more massive galaxies and/or the tidal field of the cluster itself (Moore et al., 1998), this lead to gas fuelling to the central region of galaxies, resulting in star formation than can cause the gas to be exhausted and thus the SF quenched. Galaxy mergers are expected to be relevant in transforming galaxies, simulations have predicted that unequal mass spirals can form a lenticular galaxy (Bekki , 1998) and major merger produce giant ellipticals (Toomre, & Toomre, 1972; Naab, & Burkert, 2003). The high relative speeds of galaxies in the core of clusters make difficult the mergers, only close encounters, but in the cluster outskirts mergers are more likely to take place (Mihos et al., 2004).

1.1.8 *The Fornax Galaxy Cluster*

The Fornax cluster is the nearest high-density region in the Southern hemisphere ($m-M = 31.51$ mag or $D_L = 20.0$ Mpc, Blakeslee et al., 2009). Early studies about the galaxies in Fornax were done by (Hodge, 1959; Hodge et al., 1965; Welch et al., 1975; Hodge, 1978). Jones, & Jones (1980) analazyed photometry for 40 galaxies in the Fornax region complete to $B = 16$ mag and spectra to confirm membership for 25 of them, they found mean radial velocity as $v = 1395$ km/s and projected velocity dispersion of $\sigma = 361$ km/s. A complete catalog in the area was made by Ferguson (1989) with 2678 galaxies in 40 degree square by visual inspection of photometric plates taken with a 2.5m telescope at Las Campanas Observatories. Of the complete catalog 340 galaxies are selected as likely Fornax members down to absolute magnitude $M_B \simeq -20$mag, but complete up to complete $M_B \simeq -18$mag. Although the Fornax cluster is not classified as a rich cluster in the Abell catalog, its is predominant in the Southern hemisphere by its nearness, regular morphology and compactness. The galaxy distribution is centrally dominated by the cD galaxy, NGC 1399, which has an extensive stellar envelope (Schombert, 1986) and has a radio jet structure (Paolillo et al., 2002). Its bright galaxies are mostly ellipticals (e.g. NGC 1404, NGC 1382, NGC 1379), lenticulars (e.g. NGC 1381, NGC 1380) and some late type galaxies (e.g. NGC 1365, NGC 1350, NGC 1436). The S0 galaxy, NGC 1316 also called Fornax A, it is a radio source with an active nucleus and two radio lobes (Wade, 1963; Schweizer, 1980; Kim, & Fabbiano, 2003). In comparison with the Northern counterpart Virgo cluster (D=16 Mpc, (Mei et al., 2007; Blakeslee et al., 2009)), Fornax is more compact and with higher central density, around seven times less galaxies than Virgo and 2.5 times denser in the core than Virgo (Ferguson, & Sandage, 1988).

A dynamical analysis done by Drinkwater et al. (2001) for 108 member of the Fornax cluster in the magnitudes range $-16 > M_B > -13.5$ with a mean velocity for the total sample of $< v >= 1493 \pm 36\,\mathrm{km/s}$ and a velocity dispersion of $\sigma = 374 \pm 26\,\mathrm{km/s}$. They found that Fornax cluster is composed by two substructures (see Fig. 1), the main Fornax cluster centered on NGC 1399 and a subcluster 3 degree Southwest which includes NGC 1316, with the subcluster bound to Fornax and infalling towards the cluster, still has an intense star formation. They measure some parameters of Fornax at a radius of 1.4 Mpc, such the total mass $(7 \pm 2) \times 10^{13}\,M_\odot$, luminosity $2 \times 10^{11}\,L_\odot$ and a mass-light-to ratio of $300 \pm 100\,M_\odot/L_\odot$.

A $^{12}\mathrm{CO}(1-0)$ and HI survey for 21 Fornax galaxies (Horellou et al., 1995) showed that lenticular galaxies near the core of Fornax have HI deficiency, the CO emission from Fornax is weak in general with 11 detection of 21 and less than 10% of the gas is in molecular state, on average. Two spirals in their survey (NGC 1350 and NGC 1425) are poor HI-rich spirals with weak H_{alpha} emission.

X-ray observations of Fornax (see Fig. 1) with the Chandra Fornax Survey (Scharf et al., 2005) with a coverage of 1 degree centered in the cD galaxy shows highly asymmetric morphology in the soft-band $(0.3 - 1.5\,\mathrm{keV})$ of the intracluster gas. NGC 1399 seems to be offset compared to the intracluster core emission. NGC 1404 show an extended Xray gas emission distorted towards NGC 1399. The temperature map of the intracluster gas in the Fornax mosaic show that the majority of the gas does not exceed $T < 1.6\,\mathrm{keV}$ and shows a plume for NGC1404 of cooler material to the SouthEast. Another galaxy showing signs of interaction with the intracluster gas is NGC 1387 with a significant X-ray halo. The majority of X-ray active galaxies in Fornax are distributed between the Fornax core and the infalling structure identified by Drinkwater et al. (2001), away from the bulk of the intracluster gas.

1.1.9 *Hickson Compact Group 90*

Hickson compact groups (HCGs) are defined as small groups of four or more massive galaxies located in relative isolation (Hickson, 1997). Given that they rival the cores of galaxy clusters as the most dense galaxy environments in the nearby universe (e.g. Rubin et al., 1991; Ponman et al., 1996; Proctor et al., 2004),

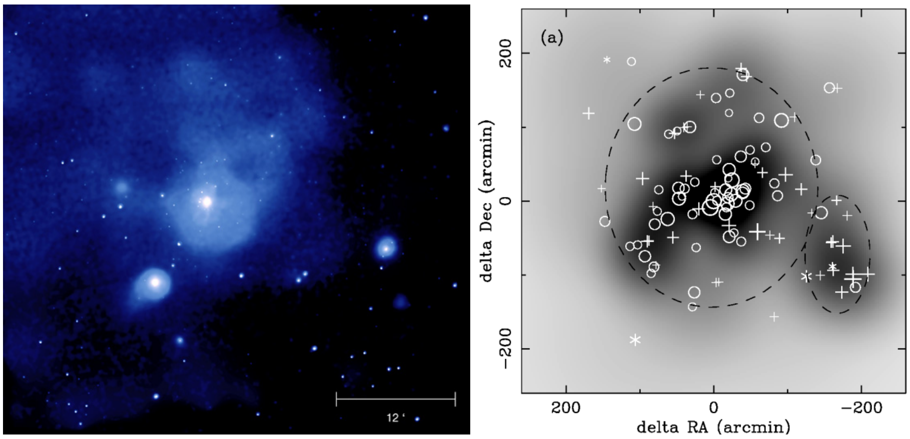

Figure 1: Left panel: soft-band $(0.3-1.5\,\mathrm{keV})$ X-ray image of the Fornax mosaic (Scharf et al., 2005), from left to right the brightest galaxies are NGC 1404, NGC 1399 (cD), NGC 1387. Right panel: number density distribution of Fornax galaxies on the sky (gray scale) with positions of cluster members shown in circles for ETGs and plus signs/asterisks (late-type galaxies). The dashed ellipses are the 2σ limits of the two subclusters in Fornax, the main cluster and the Southwest subcluster (Drinkwater et al., 2001).

and with typical velocity dispersion of $\sigma \simeq 200\,\mathrm{km\,s^{-1}}$ (Hickson et al., 1992), HCGs are expected to be the ideal environment for galaxy mergers and tidal interactions (e.g. Mamon, 1992). Such events can also generate kinematically decoupled structures with active star formation, so-called tidal dwarf galaxies (TDGs), which have masses similar to dwarf galaxies resembling the metallicities of their hosts and lacking dark matter (e.g. Kroupa et al., 2010; Gallagher et al., 2010). HCGs may also host UDGs and constitute analogues to sites of dwarf galaxy pre-processing before their infall onto larger clusters.

At a distance of 33.1 Mpc ($m-M = 32.6\,\mathrm{mag}$, see Blakeslee et al., 2001), HCG 90 is one of the most nearby compact galaxy groups accessible from the Southern Hemisphere. The 19 known members have a group radial velocity of $v_r \simeq 2\,600\,\mathrm{km\,s^{-1}}$, and a velocity dispersion of $\sigma \simeq 193\,\mathrm{km\,s^{-1}}$, typical of HCGs (Zabludoff & Mulchaey, 1998). The core is dominated by three bright galaxies (NGC 7173/HCG 90b, NGC 7176/HCG 90c, NGC 7174/ HCG 90d), with a fourth giant galaxy (NGC 7172/HCG 90a) located to the north of the core (see Fig. 42), which is a Seyfert 2 galaxy and a bright X-ray source. Despite the relative proximity, there have been no detailed studies on its LSB dwarf galaxy population, as most attention has been paid to the group's bright and/or ultra-compact dwarf (UCD) (de Carvalho et al., 1994; Ribeiro et al., 1994; Da Rocha et al., 2011), and giant galaxies. This avenue of study is ripe for investigation, as other HCGs have been shown to host faint dwarfs (Campos et al., 2004; Carrasco et al., 2006; Krusch et al., 2006; Konstantopoulos et al., 2013), which are to be expected from theoretical considerations, despite the dynamically more hostile environments in these systems (Zandivarez et al., 2014).

HCG 90 is at an interesting stage of evolution. Several indications of interactions between its galaxies are evidenced by morphological disturbances, a diffuse X-ray halo, and intra-group light (Mendes de Oliveira & Hickson, 1994; Zabludoff & Mulchaey, 1998; White et al., 2003; Desjardins et al., 2013). It is proposed that current interactions between the core galaxies, strongly between HCG 90b/d and weakly between HCG 90c/d, have given rise to diffuse intra-group light that contributes ~45 percent to the total light (White et al., 2003). Additionally, a warm gas envelope is shared by HCG 90b and d, while tidal bridges have been found between HCG 90b, c, and d (Plana et al., 1998; Mendes de Oliveira & Hickson, 1994). All this makes HCG 90 an intriguing laboratory to investigate interactions between giant and dwarf galaxies, and their star cluster satellites.

This thesis is mainly focused in a galaxy cluster environment, in particular the Fornax galaxy cluster. There is one special chapter dedicated to a galaxy group environment, the HCG 90, with the aim to compare the different environments, but only focused in the dwarf galaxy population comparison. In the following sections of the introduction, the different stellar systems contained in a galaxy cluster are review with emphasis in the dwarf galaxy population, nuclear star clusters and compact stellar systems.

1.2 DWARF GALAXY POPULATION

In the annual review by (Hodge, 1971), he used the definition for dwarf galaxies as *galaxies of small intrinsic size, small absolute luminosity and low surface brightness*. At that time only few members of the Local Group were identified as member of the LG, e.g. Ursae Minor and Draco (Wilson, 1955), Sculptor (Shapley, 1938), Fornax (Shapley, 1939), LeoI and LeoII (Harrington, & Wilson, 1950), NGC 205 (Messier, 1798) and NGC 185 (Herschel, 1789) and outside the Local Group dwarf galaxies also started to be detected (e.g. Hodge et al., 1965; Sandage & Binggeli, 1984; Karachentseva et al., 1985; Impey et al., 1988). Further progress with photometric plates in the dwarf population was not possible due to instrumental limitations. The implement of charge couple device detectors in astronomy change the course for the low surface brightness science and an exponential growth in the number of dwarf galaxies have been and will continue being detected.

Dwarf galaxies are the most numerous type of galaxies in the universe, and according to the hierarchical assembly scenario are the essential ingredients for the build up of massive galaxies.

The Local Group dwarf population is now about 10 times larger in number than half century ago, with more than 100 nearby dwarfs, an overview of the properties of our closest dwarf population can be found in the reviews by Tolstoy et al. (2009); McConnachie (2012) and some of the new LG dwarf members in Laevens et al. (2015); Koposov et al. (2015); Bechtol et al. (2015).

The rise of large detector arrays in present-day observatories have helped to survey large areas of the sky in different environments throughout the local Universe (e.g., Chiboucas et al., 2013; Merritt et al., 2014; van Dokkum et al., 2015; Muñoz et al., 2015; Ordenes-Briceño et al., 2016; Müller et al., 2017; Venhola et al., 2017; Wittmann et al., 2017; Eigenthaler et al., 2018).

1.2.1 *Morphological types*

The overwhelming number of dwarf galaxy population have made possible to understand in much more detail the stellar population, surface brighteness, gas fraction, mass-to-light ratio, among other properties. The general agreement to consider a galaxy as a dwarf is when its absolute magnitue is $M_V > -18$ mag (Grebel et al., 2003). Dwarfs can be grouped in two main groups according to their properties: Early-type dwarfs, which tend to be gas poor, quiscent, preferentially found in high dense environments and late-type dwarfs with a higher gas fraction and with star formation, regularly found in low dense environments. For the early-type dwarfs, we have the dwarf ellipticals (e.g. Ferguson, & Binggeli, 1994), dwarf spheroidals (e.g. Grebel et al., 2003), ultra-faint galaxies (e.g. Belokurov et al., 2006) and ultra-diffuse galaxies (van Dokkum et al., 2015; Mihos et al., 2015). For the late-type dwarfs (e.g. Schombert et al., 1995; Matthews, & Gallagher, 1997), we have the dwarf spirals, dwarf lenticulars, dwarf irregulars and blue compact dwarf galaxies. As this thesis is about a cluster environment, further details will be given only for the early-type dwarfs, further information about the different morpologycal type and the late-type dwarfs can be found in Grebel (2001), the book *Galaxies in the Universe* (Sparke, & Gallagher, 2007, ,chapter 4).

The main differences between the different early-type dwarfs are in surface brightness, luminosity and size. Dwarf ellipticals are bright and have a higher central stellar density, for instance in the LG only are found near Andromeda galaxy (McConnachie, 2012). Dwarf Spheroidals are more diffuse, with lower surface brightness and less concentration in the galaxy center compared to dwarf ellipticals. Smaller in size and much fainter than dSph are the ultra-faint dwarfs, they have luminositues comparable with those of globular clusters. On the other hand, the ultra-diffuse galaxies have similar low surface brightness than dSph but much more extended in size and less luminous. van Dokkum et al. (2015) considered a galaxy as an ultra-diffuse galaxy when the effective radii was $r_{\mathrm{eff}} \geqslant 1.5\,\mathrm{kpc}$.

1.2.2 *Surface Brightness Profiles*

The surface brightness profiles of galaxies are well parameterized by a (Sérsic , 1963) model with the form:

$$I(r) = I_e \exp\left\{-b_n[(r/r_e)^{1/n} - 1]\right\} \tag{1}$$

With r_e as the effective radius, I_e as the intensity at r_e, n as the shape or Sersic index which definess the curvature of the model. b_n is a constant chosen to be consistent with r_e to enclose half of the galaxy luminosity (Caon et al., 1993). Capaccioli et al. (1989) estimated an empirical value for the constant b_n to be $\simeq 2n - 0.327$.

de Vaucouleurs (1948) studied the light distribution of early-type galaxies, including the bulge of disc galaxies and found a power law $\propto r^{1/4}$, thus later with the generalized Sersic model this would be $n = 4$. For disk galaxies an exponential profile with $n = 1$ is a good approximation for their light profile.

The work by Ferrarese et al. (2006) using exquisite data from the Advance Camera Survey on the Hubble space telescope for Virgo Early-type galaxies showed that their light profiles are generally well described by a Sérsic model with index n depending on the luminosity, increasing steadily for brighter ETGs.

Bright galaxies have complex light profiles, usually with more than one component. For instance, spiral galaxies have a disc, bulge and halo as symmetric components and the asymmetric component are their spirals arms, which are harder to model (e.g. Kormendy, 1977, 1979; Peletier, & Balcells, 1996; Kormendy et al., 2009). Therefore, when trying to fit a galaxy with complex light profile, there are residuals left for the components that are not symmetric and easy to fit. These residuals are very helpful to identify hidden components and/or signature of interaction or mergers (e.g. Ferrarese et al., 2006; Kormendy et al., 2009).

The profile for dwarf galaxies is normally well fit by a single Sersic model for magnitudes fainter than $M_V \simeq -16$ mag, after that the light profiles gets more complex, requiring the fit of more profiles. For instance, in the Virgo cluster, more than 50% of the bright early-type dwarfs were found to show underlying disk features (Lisker et al., 2006a).

1.2.3 *Stellar population*

A galaxy has composite stellar population in terms of age and metallicity with stars of different spectral types and luminosities, the distribution of ages and metallicities of a galaxy can tell us about its star formation history.

The nearby dwarfs in the LG can be resolved into individual stars. Several studies have investigated the chemical composition of LG dwarfs using their red giants (e.g. Geisler et al., 2005; Koch et al., 2008,?; Kirby et al., 2017). Red giant stars (see Sect.1.4.1.1) are sensitive to metallicity, in a color magnitude diagram we see it when the range in color for red giants is wide that implies a larger spread in metallicity of the stellar system.

The use of the information from CMDs in combination with spectroscopic metallicity for individual red giant branch stars is a tool to constrain the star formation and chemical evolution histories of composite stellar populations. The technique is known as synthetic CMD method and is based on comparing the observed CMD with a theoretical one that is created via Monte Carlo simulation, extracting the parameters for stars from stellar evolutionary tracks (or isochrones) with different star formation laws, IMFs, binary fractions, age-metallicity relation, among other parameters (see the review by Tolstoy et al., 2009). The resulting synthetic CMD have to reproduce all the main features of the observational one (e.g. shape of the CMD, luminosity, color distribution, etc). An example of the SFH that can be obtained with this method is shown in Fig. 2 for three LG dwarfs: LGS 3, LeoA and Cetus (Tolstoy et al., 2009).

For extragalactic studies, galaxy colors are widely used as proxy mainly for the metallicity but also for age of the galaxy stellar population. The color of galaxies in a cluster environment have a small spread, the so called red sequence of galaxies (see Section 1.1.3 and 1.1.6). The studies in the literature until some years ago were done in the bright galaxy regime due to different problems: (i) low stastic in the dwarf regime, only the brightest dwarfs were in the sample. (ii) a lack of a large dwarf sample with color information and with lower surface brightness. Recent studies have shown that the red sequence for bright galaxies in a cluster is naturally extended towards the dwarf regime, getting broader in color and with a flatter distribution towards fainter magnitudes compared to the bright regime (Roediger et al., 2017; Eigenthaler et al., 2018). No color bimodality is seen neither in the Virgo or Fornax cluster as expected, suggesting that their galaxy members have been long enough in their potential to have truncated star formation. Spectroscopic studies of dwarf galaxies using Lick absorption line indices revealed intermediate to old ages, subsolar metallicities and around solar α-element abundances (e.g. Geha et al., 2003; Michielsen et al., 2008; Paudel et al., 2010; Chilingarian, 2009; Koleva et al., 2009). For bright dEs, stellar population gradients were found for a large fraction of dEs, some dEs have a radially steep decreasement in metallicity, but some show no gradients. The stellar age seems to remain constant or slightly increasing outwards.

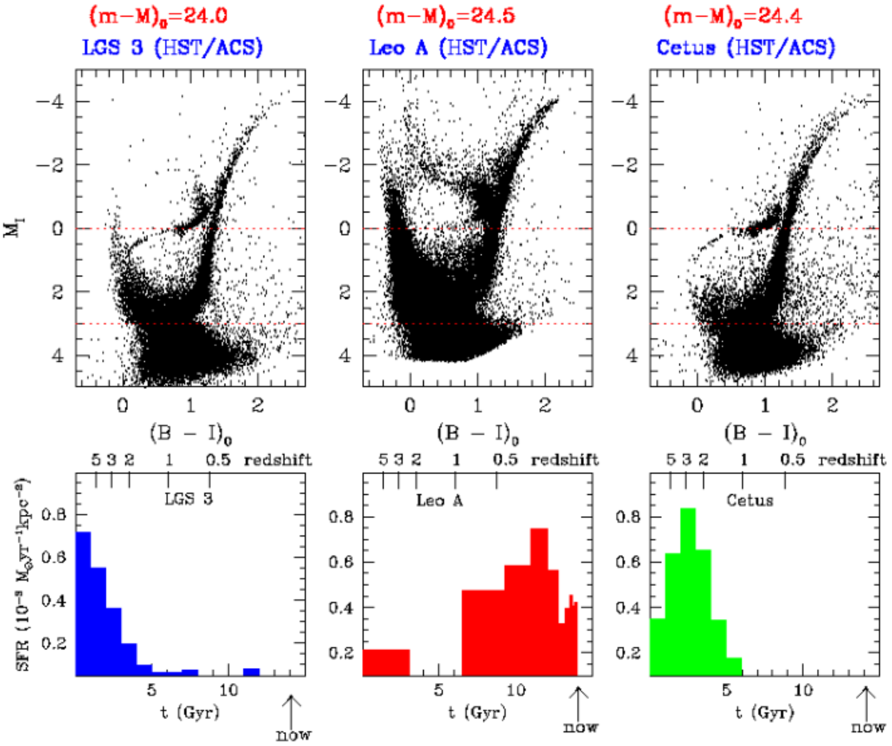

Figure 2: HST/ACS CMDs and SFHs for three LG dwarf galaxies: LGS 3, Leo A and Cetus (Tolstoy et al., 2009).

1.2.4 *Scaling relations*

The fundamental plane (FP) for ellipticals is a tight correlation between three parameters: effective radius, central velocity dispersion and effective surface brighteness (Djorgovski, & Davis, 1987; Faber et al., 1987, and references therein). The FP link the structural and dynamical properties with their stellar content. The Kormendy relation is a projected FP into the r_{eff},I_e (Kormendy, 1977) and the Faber-Jackson relation when the FP is preojected into σ, L (Faber, & Jackson, 1976). The existence of the FP and its small scatter (e.g. Jorgensen et al., 1996) points to a uniform formation proccess for the massive ellipticals, with tight age and metallicity constraints for their stellar population. For more details see the review by Renzini (2006). The extension of the FP towards the low mass galaxies was first studied by Kormendy (1985) finding a discontinuity between the parameter correlation for ellipticas and those of dwarf galaxies. Interesting results of this study are: (*i*) the seven dwarfs from the Local Group and the three in the Virgo Cluster have a radius vs luminosity relation but not as the bright ellipticals. (*ii*)The dwarf ellipticals in his sample have larger core radius when increasing luminosity. (*iii*) the dwarf spheroidals also have smaller velocity dispersions than comparable ellipticals. (*iv*) Fainter spheroidals have lower central surface brightnesses. *v* dSph, dwarf spirals and irregular galaxies have identical range in the parameter correlations. *vi* bulges and ellipticals, dwarf spheroidals, and globular clusters are three remarkably different kinds of stellar systems.(Binggeli, & Cameron, 1991) studied the correlation properties of ETGs in Virgo cluster, they found that in the radius range between $0.1-1$ kpc, the relation with luminosity shows two well distinct classes, clasyfing them into the "classical" types (E,S0) and the "dwarf" types (dE,dS0). The dichotomy seen in the FP parameter between elliptical and dwarf galaxies is understood as a proof of the the different formation processes for both systems. The common idea is that ellipticals formed from the continuous merger events and dSph formed via environmental and secular processes from a late-type dwarf with star formation into dSph with little or non SF processes (e.g. Kormendy et al., 2009).

A recent study done by Eigenthaler et al. (2018) analyzed the color and structural parameters for 258 dwarf galaxies in the core region of the Fornax galaxy cluster, covering stellar masses in the range of $\log(\mathcal{M}/M_{\odot}) \simeq 5.5 - 9.5$, the majority of them with effective surface brightness of $\sim\ 1 - 10\,M_{\odot}/pc^{-2}$ but the massive dwarfs reach $\sim\ 100\,M_{\odot}/pc^{-2}$. The scaling relations in size-mass-surface density plane for Fornax dwarfs with lower stellar masses than $\log(\mathcal{M}/M_{\odot}) < 8$ starts to deviates towards lower effective surface mass density ($\sum_{eff,\eta_*}$) In the size-luminosity plane (see Fig.3), this is seen as the faint dwarfs to be positevely inclined with respect to the lines of equal $\sum_{eff,\eta_*}$. In their scaling relations they overplot other family systems, among them the Local Group dwarfs that were catalogued in McConnachie (2012), some of them being the ultra-faint dwarf galaxies. Their scaling relations appear to line up seamlessly with the Fornax dwarf sample occupying the lower stellar masses and lower surface mass densities. On the extended objects regime of the size-luminosity diagram, there is the well known sequence for bright ETGs, beside that there is another sequence that emerges for the UDG type. A few UDGs were found in the core region of Fornax, but overplotting the UDG parameters from the literature, it is seen a clear sequence for them, as a natural extension of the more extended low surface brightness dwarf galaxies (dSph).

1.3 NUCLEAR STAR CLUSTERS

Nuclear star clusters are very dense stellar systems with sizes similar to globular cluster (GCs, $\sim 3 - 10\,\text{pc}$) (Böker et al., 2004; Côté et al., 2006; Turner et al., 2012; den Brok et al., 2014; Georgiev & Böker, 2014; Puzia et al., 2014) but with a broader range of masses $10^5 - 10^8\,M_{\odot}$ (e.g., Walcher et al., 2006; Georgiev et al., 2016; Spengler et al., 2017). Nuclei are a common characteristic in galaxies, from dwarfs to giants. The nucleation fraction can reach around 70-80% and is independent of the galaxy morphology (Böker et al., 2004; Côté et al., 2006; Georgiev et al., 2009; Turner et al., 2012; den Brok et al., 2014; Georgiev & Böker, 2014; Muñoz et al., 2015; Eigenthaler et al., 2018). As NSCs are common in all galaxy types, this suggests that their formation is instrinsically linked to galaxy evolution.

The nuclear star cluster in the Milky Way has been studied extensively (Launhardt et al., 2002; Schödel et al., 2009; Chatzopoulos et al., 2015, e.g.). The study by Schödel et al. (2014) used mid-IR data to overcome the interstellar extinction toward the galactic center and found that the NSC is centered on Sgr A* has a half light radius of $r_h = 4.2 \pm 0.4\,\text{pc}$ and stellar mass of $M = 2.5 \pm 0.4\ \times 10^7\,M_{\odot}$ with axis ratio $q = 0.71 \pm 0.02$ and flattened along the Galactic plane.

The nucleation fraction decreases with luminosity (e.g., Muñoz et al., 2015), going from as high as $\sim 90\%$ for galaxies brighter than $M_i \leqslant -16\,\text{mag}$ to 0% for $M_i \leqslant -10\,\text{mag}$. This may be related to instrument sensitivity limits, beyond which it becomes harder to detect the lowest surface brightness spheroids and, thus, to associate a nucleus with a low-surface-brightness galaxy spheroid. Towards the bright galaxy regime, it has been noticed that nuclei are no longer detected for galaxies with $M_B < -19.5\,\text{mag}$. This might be related to the fact that the central parsecs of bright galaxies can have complex surface brightness

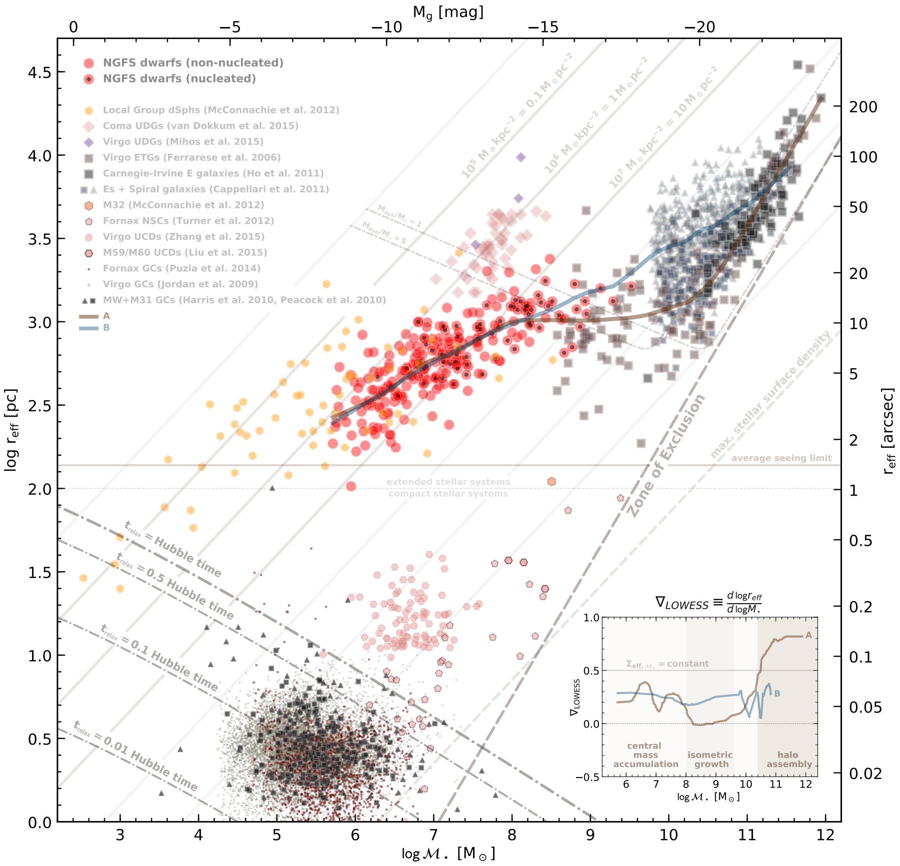

Figure 3: Effective radius versus stellar mass relation for NGFS galaxies (red symbols) and various other stellar systems (Eigenthaler et al., 2018).

profiles, which makes it difficult to separate the galaxy light from the nucleus light, if at all present (e.g. Côté et al., 2006; Turner et al., 2012).

1.3.1 *Stellar population*

The stellar population properties of nuclei are complex, revealing multiple stellar populations rather than being old and metal-poor objects. Using spectra, Rossa et al. (2006) found in a sample of 40 late-type galaxies (LTGs) that the luminosity weighted ages of half of the nuclei is younger than 1 Gyr, within a range from 10 Myr to very old ages $\geqslant 10$ Gyr (see also Walcher et al., 2006). For 26 early-type galaxies (ETGs) in the Virgo cluster, Paudel et al. (2011) found spectroscopic evidence that the age distribution of nuclei is dominated by young ages. In terms of metallicity, their work revealed a broad metallicity distribution of the nuclei, from -1.22 dex to $+0.18$ dex, which was wider compared to the host galaxy metallicity range. When analyzing age and metallicity distributions in radial profiles using bins along the major axis of the dwarf galaxies, Paudel et al. found that the inner bins are dominated by young ages and broader metallicity distributions than outer regions.

In the Virgo cluster about 15% of the Virgo early-type dwarfs brighter than $M_B = -15.5$ mag reveal blue centers, which were spectroscopically shown to correspond to recent star formation (Lisker et al., 2006b). A more recent study by Spengler et al. (2017) observed in the same cluster that, on average, the nuclei and host galaxies have similar metallicities with a mean metallicity of 0.07 ± 0.3 dex, but if they exclude the galaxies that deviate from the mass-metallicity relation then nuclei are on average 0.20 dex more metal-rich than their host galaxies.

The observational evidence of young ages in stellar nuclei hints towards a picture where star-formation episodes seems to be frequent and repetitive. However, the underlying old stellar population for individual nucleus (> 1 Gyr) is hard to detect in spectroscopy data, as the young stellar population is the one that dominate the spectrum. Therefore, an accurate age determination for the most recent and the oldest star formation episodes is still needed.

1.3.2 *Coexistence with Massive Black Holes*

At the bottom of the potential well of a galaxy where the nuclear star clusters are located also are found massive black holes (MBH). In our own galaxy, there is strong evidence for the existence of a MBH coming from stellar dynamics, the MBH mass is $4 \times 10^6\,M_\odot$ and it is located at the heart of the Milky Way's NSC (e.g. Genzel et al., 2010).

The presence of MBHs in other galaxies has been probed over the years, and it is believed that it is an ubiquitous component for massive galaxies ($> 10^{10}\,M_\odot$) (see the review Kormendy & Ho, 2013). In some galaxies the nuclear star cluster coexist with the MBH (e.g. Seth et al., 2008; Graham, & Spitler, 2009; Neumayer & Walcher, 2012; Nguyen et al., 2018). For some galaxies, it is confirmed the presence of a stellar nuclei but no apparent MBH (Gebhardt et al., 2001; Valluri et al., 2005), while some massive ellipticals with an enhance core have MBHs but lack of NSCs (Côté et al., 2006). Nevertheless, for low mass galaxies the presence of central BHs is not well constrained (e.g. Miller et al., 2015), but we know that most of them host a nucleus (e.g. Turner et al., 2012; Georgiev & Böker, 2014; Spengler et al., 2017). As the low mass galaxies dominate the number density in the Universe, the look for BHs in low-mass galaxies is important to constrain galaxy evolution models. Recently, Nguyen et al. (2018) presented a study of the NSCs and MBHs of three low-mass early-type galaxies in the field: M 32, NGC 5102, and NGC 5206. They measured their dynamical masses for the BHs and NSCs using stellar kinematics, photometry and Jeans Anisotropic Models.

These studies confirm the view that BHs and NSC coexist in the inner parsecs of galaxies. The absence of NSC in the high mass galaxy regime and the abscence of BHs in the low mass regime are intriguing. Probably as we have seen with the study of Nguyen et al. (2018), BHs will continue to be detected in dwarf galaxies, the question is whether there is a limit in mass to have a BH-NSC coexistence in dwarf galaxies. At the high mass regime, the lack of detection of NSCs can be related with the complex inner parsecs for massive and with high dense cores galaxies and/or that the MBH in the center dissolve the NSC due to an increment in its sphere of influence to radii similar to those of the nuclear cluster (e.g. Bekki, & Graham, 2010; Antonini , 2013).

1.3.3 *Scaling relations*

Nuclear cluster studies have revealed several correlations between nuclei and their host galaxy, such as the nucleus to galaxy luminosity relation (Carollo et al., 1998; Lotz et al., 2001; Graham, & Guzmán, 2003; Böker et al., 2004; Côté et al., 2006), their velocity dispersion and galaxy mass[1] and sérsic index (e.g.

---

[1] For late-type galaxies, this would be the bulge mass.

Ferrarese et al., 2006; Rossa et al., 2006; Graham, & Driver, 2007), and the size-luminosity relation (Böker et al., 2004; Côté et al., 2006; Turner et al., 2012; Georgiev & Böker, 2014; den Brok et al., 2014; Spengler et al., 2017). These correlations indicate a connection between the nucleus and the formation of its parent galaxy.

The general trend in the luminosity relation are that the brighter the galaxy the brighter its nucleus or the larger is the nucleus. Although, for LTGs the slope of the relations is less steep, indicating that for a fixed mass (or luminosity) the stellar nucleus seems to have a lower mass and size than the nucleus of ETGs (Georgiev & Böker, 2014).

The ratio between the nuclei over galaxy luminosity has been studied in dense environments like Fornax and Virgo clusters and found a large scatter in the luminosity range $M_B > -15\,\mathrm{mag}$ with a mean value $\langle \eta_L \rangle = 0.41\%$ in Fornax (Turner et al., 2012) and $\langle \eta_L \rangle = 0.3\%$ for Virgo (Côté et al., 2006).

1.3.4 *Formation scenarios*

The two proposed formation scenarios for nuclei are globular cluster infall due to dynamical friction (Tremaine et al., 1975) and in situ star formation (van den Bergh, 1986). The latter needs a mechanism to funnel gas into the galaxy center. Some studies suggest mechanism to carry the gas inwards to be galaxy mergers between two disk galaxies (Mihos & Hernquist, 1994), supernova feedback outflows that become stalled because the intergalactic medium (IGM) pressure prevents the gas from escaping the dwarf galaxy (Babul & Rees , 1992), and gas disks embedded in an old stellar spheroid (Bekki , 2007).

Observational studies for ETGs have argued that the predominant mechanism for nucleus formation in more massive galaxies are dissipative processes, sinking gas to the central galaxy regions with star formation occurring *in situ*, while for low-mass galaxies nucleus formation occurs via GC infall due to short dynamical timescales (e.g. Lotz et al., 2004; Côté et al., 2006; Turner et al., 2012). In this context, we note that in the Virgo cluster, more than 50% of the bright early-type dwarfs were found to show underlying disk features, with the disk fraction decreasing to only a few % for such dwarfs fainter than $M_B = -15.5\,\mathrm{mag}$ (Lisker et al., 2006a), corresponding to $\log(\mathcal{M}_\star/M_\odot) \simeq 8.6$ (see Fig. 7 in Eigenthaler et al., 2018). Moreover, about 15% of the Virgo early-type dwarfs brighter than $M_B = -15.5\,\mathrm{mag}$ reveal blue centers, which were spectroscopically shown to correspond to recent star formation (Lisker et al., 2006b). In a more recent work, Spengler et al. (2017) have compared their multi-band photometry of nuclei with scaling relation predictions from Bekki (2007) and Antonini et al. (2015) and inferred that there is no single preferred formation scenario for nuclei, suggesting a mix of processes instead (see also Da Rocha et al., 2011).

Secular processes such as stellar winds, supernova (SN) and black-hole (BH) feedback can affect the nucleus formation and evolution. For instance, by helping with gas supply to the nuclear regions through stellar winds from newly formed stars (radiation drag, Kawakatu & Umemura, 2002) or slowing down the nucleus growth due to SN-driven winds contributing to the mass loss in dwarf galaxies and likely changing the dynamical friction timescales for orbiting star clusters to sink to the center (Lotz et al., 2001), or dynamically heating the nuclear cluster due to a massive central BH (Antonini et al., 2015).

1.4 COMPACT STELLAR SYSTEMS

The agglomerations of stars in a small radii were observed for the first time several centuries ago, the first documented observations were done by Halley (1677), Kirch (1681), Lacaille (1752), Messier (1764). However, it was not until 1786 when William Herschel published his catalog of Nebulae and cluster of stars (Herschel, 1786) that the name of globular clusters was used to define this high stellar dense objects.

With the development of new technology to observe the skies for obtaining higher resolution images, it was possible to study the vecinity of galaxies beyond the Milky Way with much more details. This led to astronomers to find other compact stellar systems with properties between galaxies and GCs. For example, M 32, an Andromeda's satellite, it was considered an outlier in the common description for dwarf galaxies in the LG (Faber, 1973; Sandage, & Tammann, 1981; Wirth, & Gallagher, 1984; Nieto, & Prugniel, 1987) because its properties are more consistent to being the extension towards the low luminosity regime of the giant elliptical family, with its high-surface brightness, with centrally concentration of stars, thus it was clasified and named as a compact elliptical (cE). Another type of object also was identified in the end of the last century, they were called ultra-compact dwarf galaxies (UCDs, Hilker et al., 1999; Drinkwater et al., 2000). Hilker et al. (1999) described them as "very compact and have surface brightnesses comparable to globular clusters, however their luminosities are in the range of dwarf elliptical nuclei".

In the existence of more compact stellar systems (CSSs) than only the classic GCs, we use then the term of CSSs to refer to dense and compact stellar objects such as globular clusters, ultra compact dwarf galaxies and compact ellipticals. However, this introduction will be focused mainly in globular cluster properties (higher number density for CSSs). Nevertheless, information for UCDs and cEs will be also given.

1.4.1 *Globular clusters*

Globular clusters (GCs) are ideal tracers of the assembly of galaxies across comic time. Their high density and compact sizes allow them to survive the evolution of their parent galaxies, besides their ubiquous presence in all morphological type of galaxies.

The known Milky Way globular clusters are more than 150 (Harris, 1996, , his updated version of 2010)[2], but there might be more hidden by the Galactic disk and bulge. New surveys to discover the "hidden" globular clusters are now using NIR images to see through the dust (e.g. VVV survey Saito et al., 2012). Our closest massive neighbour, Andromeda contain more than 350 globular cluster (Barmby et al., 2000; Galleti et al., 2006, and references therein for new M31 GCs). Outside the LG, the largest GC population is the one for M 87, the brightest galaxy cluster in the Virgo cluster with ~8000 high probability GCs and a total of ~14000 GC candidates (Harris, 2009).

1.4.1.1 *Stellar population*

The proximity of Milky Way GCs made them the subject for tons of studies to understand their stellar population of these intriguing objects. As Galactic GCs are resolved into individual stars, the different spectral-type (surface temperature) stars their masses, ages and metallicities can be analyzed. A typical GC

---

[2] http://physwww.mcmaster.ca/ harris/mwgc.dat

can contain 10^4 to 10^7 stars. The study of the stellar content in GCs is done using the Hertzsprung-Russell (HR) diagram, with the spectral type or surface temperature as a function of luminosity. The GAIA space mission is currently mapping our Galaxy surveying more than a thousand million stars, the HR diagram of GAIA *data release 2* is shown in Fig.4 to illustrate how deep is GAIA reaching into the lower mass MS stars of our vecinity. Color-magnitude diagram is the observational counterpart of the HR diagram with the aparent magnitude used instead of luminosity, thus there is not need to know the distance for each star. The color-magnitude of a GC normally holds stars from the main-sequence (MS, hydrogen-core burning), red giant branch (RGB, hydrogen-shell burning), red clump or horizontal branch (HB, helium-core burning), Asymptotic Giant Branch (AGB, helium-shell burning) and blue stragglers. Blue stragglers are main sequence stars, more luminous and hotter than the main sequence turn off (MSTO). They are believed to be the outproduct of the GC evolution in its central region. The MSTO is point of inflexion in the HR-diagram, where stars leave the MS due to hydrogen is exhausted in the core.

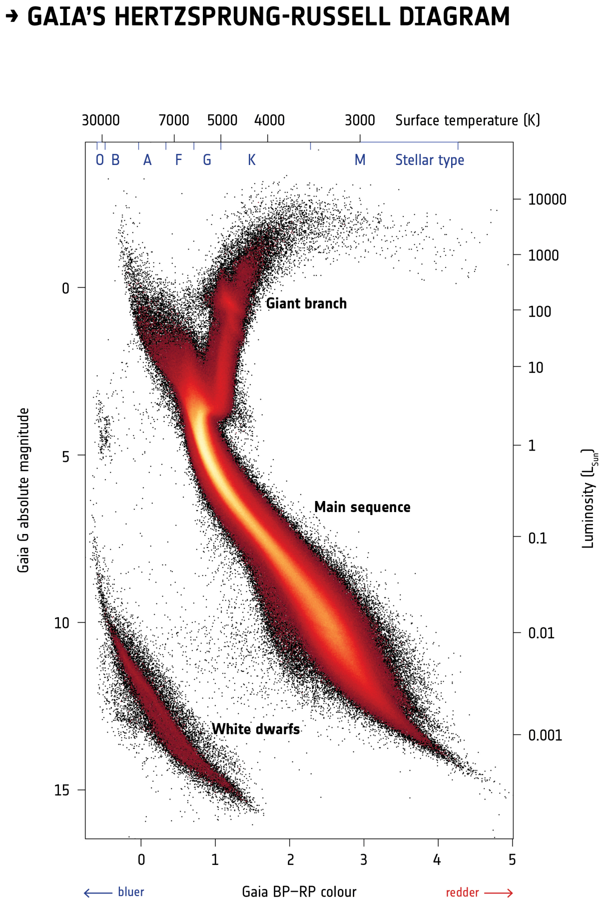

Figure 4: Hertzsprung-Russell diagram for all stars in the GAIA DR2 (Gaia Collaboration et al., 2018).

The HR diagram shows the evolution of stars in their different life stages. The color (or surface temperature) and the magnitude of a star depends on the mass and chemical composition. The initial mass is crucial for the evolutionary path a star will follow. In a GC, their stars are born with a range of masses, their distribution function is described by the initial mass function (IMF) with a power law (α). First studied by Salpeter (1955) for masses in the range of 0.1 to $100\,M_\odot$ with $\alpha = 2.35$. Later, Kroupa (2001) studying the IMF of young star clusters in the galaxy introduced a two-power law IMF as a function of stellar mass. The power law remains as for Salpeter for $M > 0.5 M_\odot$, for $0.08 < \mathcal{M}/M_\odot < 0.5$ is $\alpha = 1.3$ and for $M < 0.08 M_\odot$ is $\alpha = 0.3$.

To obtain absolute ages of GCs one method is to use the separation in magnitudes between the MSTO and the horizontal branch at the same color, the more evolved the system the larger the magnitude difference, once the distance is fixed the age can be derived from the absolute magnitude MSTO (Vandenberg et al., 1990). For instance, Carretta et al. (2000) review the method using distances obtained from Hipparcos catalog and estimated a median age for 9 GCs of $11.5 \pm 2.6\,$Gyr. Using isochrone fitting method in the CMDs to obtain ages, the ACS survey for Galactic GCs program, obtained high quality photometry for 65 GCs covering main-sequence stars up to $\sim 0.2\,M_\odot$, about 7 mags below the MSTO, they determined ages in the range of 12 to 14 Gyr for most of the Galactic GCs (Sarajedini et al., 2007; Dotter et al., 2010). Therefore, the general agreement of different measurements is that the Galactic GCs are old stellar systems, older than 10 Gyrs. Ages for GCs outside the MW are more difficult to constrain, with the current instrumentation for the closest galaxies can only detect stars in the brightest region of the CMD,i.e RGB, AGB and HB stars, which are more sensitive to metallicity than age. For unresolved GCs, integrated light spectroscopy is normally used to measure ages and metallicities for the extragalactic GCs, using Balmer lines that are sensitive to age. Studies using this method have confirmed old ages for most of them (e.g Cohen et al., 1998; Puzia et al., 2005)

The chemical composition view of GCs has changed in the last 10 years. Once thought that GCs have a single age and metallicity also known as simple stellar populations, but that picture is not valid anymore, as observations for individual GCs have revealed significant star-to-star chemical abundance variations. Observational studies have found multiple branches for MS and RGB and extended HBs in the CMDs of many Galactic GCs (e.g. Piotto et al., 2007, 2012; Milone et al., 2012). Spectroscopic studies demonstrated that most clusters have signifcant variations in C, N, O, Na, and Al (e.g. Carretta et al., 2009; Pancino et al., 2010). This abundance variations in GCs are intepreted as the presence of multiple stellar populations, where the second generation is believed to have formed from the processed/enriched material of the first generation of stars and enriched in N, Na and sometimes Al and depleted in C, O and sometimes Mg. Furthermore, each GC has its own specific multiple population pattern (e.g. Carretta et al., 2009). The exact nature for the nucleosynthesis sources is still a matter of debate, e.g. the mass budget problem, all the suggested stellar sources of enriched material can only produce about 1-10% of the second generation of stars (see (see Bastian, & Lardo, 2017, for a recent review in this topic).

1.4.1.2 *Structural parameters*

The study of the spatial distribution of stars within GCs has been used to derive empirical density law to describe the structure of clusters. King (1962) estimated a radial density profile that is represented by three parameters: the core and tidal radius and the richness factor. The core radius is defined as the radius at which the central surface brightness drop to half and measures the internal energy of the system. The tidal radius is defined as the radius at which the stars are not longer bound to the GC and measures the external tidal field. The richness factor is related to the central surfce brightness and measures the total number of stars in the GC. An early systematic study was performed by Peterson, & King (1975) to determine the structural parameters of 101 GCs, their estimated parameters are: densities of $\sim 10^2 - 10^4\,M_\odot pc^{-3}$, velocity dispersions of $\sim 2 - 10\,km/s$ and escape velocities of $\sim 10 - 40\,km/s$. Later, using spectroscopy data Pryor et al. (1993) for 56 Galactic GCs they estimated dynamical masses of $\sim 10^4 - 10^6\,M_\odot$, global mass-to-light ratios $M/L \sim 2$, densities of $\sim 10^2 - 10^6\,M_\odot pc^{-3}$ and velocity dispersions of $\sim 3 - 15\,km/s$. Beside the core and tidal radius to describe the spatial structure, the radius at which half of the cluster luminosity is emitted, called the half-light radius or effective radius, r_{eff}.

The sizes of globular clusters are expressed in terms of the effective radius, r_{eff}. Large statistics are needed to see the trend of size with other parameters. (van den Bergh et al., 1991) determined r_{eff} for 98 Galactic GCs by fitting a kron profile (Kron, & Mayall, 1960) to the photometric measurements and found a mean value of $< r_{eff} >\sim 5\,pc$ and identify a correlation between GC diameter and Galactocentric distance. Kundu, & Whitmore (2001) used the HST with its Wide Field and Planetary Camera 2 (WFPC2) to measure the sizes for several hundreds of GCs in 28 ellipticals fitting a King profile (King, 1962) to obtain $< r_{eff} >\sim 2.4 \pm 0.4\,pc$. Jordán et al. (2005) estimated the sizes of ~5000 GCs in the Virgo cluster with a higher resolution camera, the ACS on HST as part of the ACS Virgo cluster survey (ACSVCS). The mean value size for Virgo GCs is $< r_{eff} >\sim 2.7 \pm 0.4\,pc$, in this study they confirmed the trend of increasing GC radius with galactocentric distance, and also found that the average value of r_{eff} decreases when going towards redder galaxy hosts. Another interesting result was found when separating in red and in blue GCs, with the red GCs being ~17% smaller than the blue ones.

There is general agreement that the mass-to-light ratios for GCs are low, $M/L \sim 2$. One interesting study with M/L higher than usual is the one done by Taylor et al. (2015), who analyzed the star cluster system of NGC5128 (Centaurus A) a giant elliptical, and found mass-to-light ratios $M/L \sim 30$ for some globular clusters.

1.4.1.3 *Specific frequency*

The richness of the GC population of a galaxy, i.e. the total number of GCs that contains was used back in the eighties by Harris, & van den Bergh (1981) to introduce a parameter related to the formation efficiency that a galaxy has to form GCs. It is called specific frequency S_N and is defined as the number of GCs (N_{GC}) per unit galaxy luminosity normalized by a galaxy with an absolute magnitude of $M_V = -15$.

$$S_N = N_{GC}\, 10^{0.4(M_V+15)} \tag{2}$$

M_V is the absolute magnitude of the galaxy in study that is measured in the same area as for the total number of GCs. A systematic study of S_N for different ETGs and LTGs galaxies was done by Harris et al. (1991). His sample of ETGs (dEs, So, Es and cD galaxies) have $< S_N >\sim 5$ and the LTGs (I, Sc, Sb, Sa) have $< S_N >\sim 1$, thus ETGS being more efficient to form GCs resulting in a larger population of GCs compared to LTGs. The current range of S_N values for different morphological types are: $S_N \sim 0.5 - 1$ for spirals (Goudfrooij et al., 2003; Rhode, & Zepf, 2004), $S_N \sim 2 - 6$ for So galaxies and regular ellipticals (Kundu, & Whitmore, 2001; Peng et al., 2008), $S_N \sim 4 - 15$ for giant ellipticals (Harris et al., 1991; Peng et al., 2008; Jordán et al., 2004; Georgiev et al., 2010),

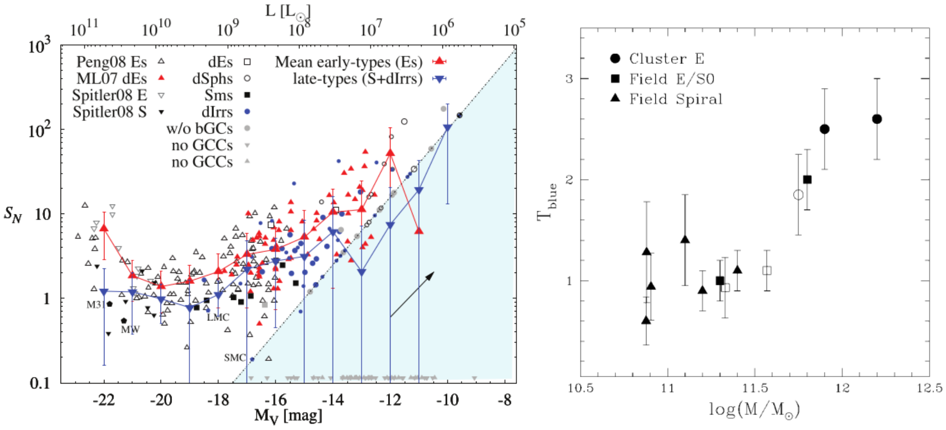

Figure 5: Left panel: Specific frequency S_N versus absolute galaxy magnitude M_V for different galaxy masses, morphologies and environments (Georgiev et al., 2010). Right panel: Mass-normalized numbers of blue GCs for 13 giant galaxies vs. galaxy stellar mass in log-space (Rhode et al., 2005).

$S_N \sim 0-100$ for dwarf galaxies (Harris et al., 1991; Peng et al., 2008; Georgiev et al., 2010). The S_N values for ellipticals and dwarfs are similar but they show a different trend with luminosity, with dwarfs having an anti-correlation between S_N and M_V opposite than for ellipticals, this trend holds for low and high density environments (e.g. Peng et al., 2008; Georgiev et al., 2010) (see left panel of Fig. 5). There is no correlation between S_N and host galaxy luminosities.

However, the stellar populations in elliptical and spiral galaxies are not the same, they have different mass-to-light ratios, for that reason Zepf, & Ashman (1993) defined a parameter T as the number of globular clusters per stellar galaxy mass ($M_g al$) normalized by a galaxy with stellar mass of $10^9 M_\odot$.

$$T = \frac{N_{GC}}{M_{gal}/10^9 M_\odot} \tag{3}$$

Zepf, & Ashman (1993) found mean T values for elliptical and spiral galaxies of $< T >\sim 5.3$ and $< T >\sim 2.2$, respectively. This result implied that per unit stellar mass, elliptical galaxies have more than twice N_{GC}. Rhode et al. (2005) also estimated T values using the blue GC population for 6 spirals and 7 ETGs. They found an overall trend of increasing T with increasing galaxy mass. For the six spiral galaxies, the weighted mean value is $< T >\sim 1.2$, and for the massive Virgo Cluster elliptical galaxies T is twice the value of the spiral galaxies (see right panel of Fig. 5).

1.4.1.4 *Color distributions*

The color of globular cluster are accessible when doing photometry in two or more filtes. The analysis of globular cluster color distribution has been for long time used to study the star formation history of the parent galaxy, because its shape have shown features of multimodality. As the color of GCs depends mainly in the age and metallicity of their underlying stellar population, the presence of modes in the color distribution hints to different star formation episodes and/or mechanisms. Early works have already shown that the mean color dispersion of the GC population in elliptical galaxies is higher compared to the ones found for M 31 and the Milky Way (e.g. Couture et al., 1991). With the advent of HST/WFPC2 more accurate color distributions were measured for more GCs in many more galaxies, confirmed the multimodes, where for a high fraction of ETGs the color distribution was at least bimodal (Gebhardt, & Kissler-Patig, 1999; Larsen et al., 2001; Kundu, & Whitmore, 2001). One problem with the interpretation for the modes in color distribution was the degeneracy of broad band colors with respect to age and metallicity, also known as the age-metallicity degeneracy (Worthey, 1994). Using the information for ages from the local population of GCs in our Galaxy and some extragalactic-GCs studies with spectroscopy, there is enough evidence to assume old ages for GCs in general (Cohen et al., 1998; Puzia et al., 2005; Dotter et al., 2010). Therefore, it is beleived that the main driver for the multimodes in color distribution is metallicity (e.g. Brodie, & Strader, 2006). Spectroscopic studies for the Milky Way GCs have revealed two distinct population in metallicity (Zinn, 1985; Armandroff, & Zinn, 1988; Minniti, 1995; Côté, 1999) the "Halo" GCs with low metallicity and non-rotating population and the "bulge" GCs with high metallicity content and rotating population. Peng et al. (2006) using ACSVCS data studied the GC color distribution for 100 ETGs in the Virgo cluster with galaxy absolute magnitudes in the range $-22 < M_B < -15$. They found that the metal-poor GC is present in almost all their galaxy sample, however the metal-rich GCs increases with luminosity (see Fig. 6). They also found that the colors for red and blue GCs correlate with the parent galaxy luminosity and color, a steeper slope seen for red GCs.

The use of optical and NIR photometry is an efficient method to at least break partially the age-metallicity degeneracy, where the sensitivity in metallicity is increased compared to color distributions only with optical colors. Pioners in the method are studied done by Kissler-Patig et al. (2002); Puzia et al. (2002); Hempel et al. (2003) which also found that the dispersion in colour is mainly driven by metallicity and the difference seen for mean colour of GCs in spirals and elliptical galaxies is mainly due to a higher GC mean metallicity content in ellipticals compared to spirals.

1.4.1.5 *Luminosity function*

The GC luminosity function (GCLF) is the number of GCs per magnitude interval. (Hanes, 1977) studied the GCLF for 20 galaxies in the Virgo cluster and compared them with those of the LG. This comparison made him realize of the universal shape of the GCLF, well fitted with a Gaussian distribution.

$$\Phi(M) = A \exp\left(\frac{-(M - M^0)^2}{2\sigma^2_{GCLF}}\right) \tag{4}$$

Crucial parameters that shape the GCLF are: M^0 as the absolute magnitude of the peak, also called turnover magnitude and σ_{LF} as the dispersion of the GCLF. The parameter A is a normalization factor, which represent the richness of a GC population. The study of the GCLF for galaxies in different enviroments done byHarris et al. (1991) showed that the GCLF for galaxies are similar but not exactly the same. He found a dependence in luminosity, the mean values for the entire sample are $< M^0_V >= -7.1$ and $\sigma_{LF,V} = 1.2$ and for the bright galaxies are $< M^0_V >= -7.3$ and $\sigma_{LF,V} = 1.4$. Although, there was evidence that the GCLF varies with luminosity, its parameters are very homgeneous for the bright ellipticals, thus this led astronomers to use the turnover magnitude as a

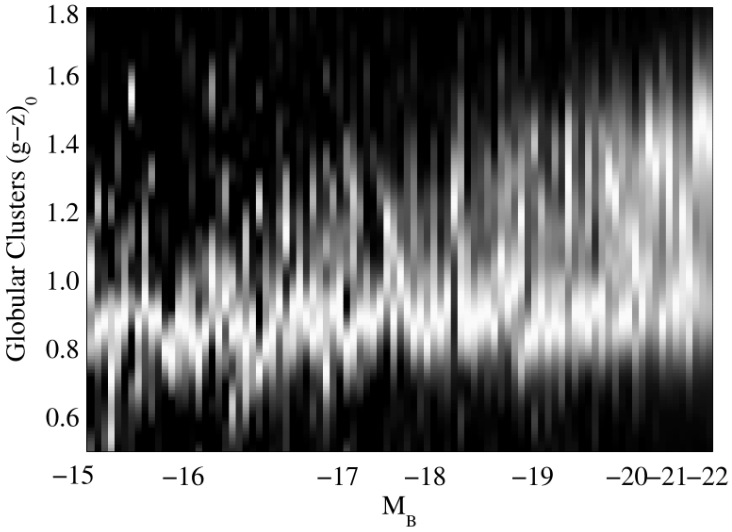

Figure 6: Color distributions for the GC population of 100 ETGs in Virgo cluster ordered by host galaxy absolute luminosity M_B. Each column is a kernel density estimation for the GC color distribution of one galaxy. Peak densities are shown in white. From left to right are shown galaxies with increasing luminosity. The blue GC is common for most of galaxies, but the color and relative fractions of red GCs depend strongly on galaxy luminosity (Peng et al., 2006).

method to determine distances for faraway ellipticals (e.g. Ferrarese, & Merritt, 2000; Harris et al., 2001; Kundu, & Whitmore, 2001).

The separation in blue and red GCs and the measurement of their GCLF performed by Larsen et al. (2001) showed that the turnover for the blue GCs was brighter than for the red one and that the bright side of the GCLF has similar shape (power law) as for the luminosity function for young stellar clusters (Zhang, & Fall, 1999; Zepf et al., 1999). Jordán et al. (2007), using the ACSVCS, derived the GCLF for 89 galaxies and derived their parameters as luminosity distribution but also as a mass distribution, assuming $M/L = 2$. The GCLF turnover converted to stellar mass of $M^0 = 2.2 \pm 0.4 \times 10^5 M_\odot$. Later, Villegas et al. (2010) measured the GCLF for 132 ETGs in Virgo and Fornax clusters, they confirmed their previous results of the tight correlation between σ_GCLF and the absolute magnitude of the host galaxy.

1.4.1.6 *Formation scenarios*

Globular cluster, their formation and evolution is still an open question. Due to the exciting information about them that has appeared in the last decade both, at low and high redshift, new interesting has acquired to understand their formation mechanisms. Their ages (oldest ~12.5 Gyr) made them a relic of times around the reionisation period. The GC formation was believed to be an special phenomenon of the early universe. For instance, Peebles, & Dicke (1968) noticed that typical GC's masses are comparable to the Jeans mass shortly after recombination and Fall, & Rees (1985) suggested that GC formation occurred in collapsing proto galaxies as a result of thermal instabilities. Therefore, in these scenarios old GCs would be different than younger GCs formed at later epochs. However, massive young stars clusters were discovered in the local universe (e.g. Holtzman et al., 1992; Whitmore et al., 2010) showing similar properties in mass, size, density and stellar populations to those of old GCs. The new scenario proposed is the formation of GCs in normal star formation processes (Kruijssen, 2015), there is still caveats in reproducing some of the observables, but work is ongoing to understand processes such the formation and destruction of GCs, initial cluster mass using the information from young massive clusters (e.g. Li et al., 2017; Renaud et al., 2017; Pfeffer et al., 2018). Observational evidence supporting this scenario come from high-redshift studies that have been able to resolve proto-GCs using gravitational lensing, their sizes range $\sim 20-40\,\mathrm{pc}$ at redshifts of $z=2-6$ (e.g. Vanzella et al., 2017; Johnson et al., 2017), with properties similar to local young massive clusters in terms of size, mass and relation to the SFR of their host galaxies. Further confirmation would need information about their stellar population properties, but the current instrumentation does not allow to get such information yet. For more details about the current understanding of GC formation see the review by Forbes et al. (2018).

1.4.2 *Ultra compact dwarf galaxies*

Ultra compact dwarf galaxies are found mostly in dense environments, such as Fornax, Virgo, Coma, Centaurus galaxy clusters and in groups of galaxies such the Hickson compact group (Jones et al., 2006; Mieske et al., 2009; Madrid et al., 2010; Da Rocha et al., 2011; Misgeld & Hilker, 2011; Liu et al., 2015), but some are also found in the field (Taylor et al., 2010; Norris, & Kannappan, 2011; Norris et al., 2014). Their typical parameters are absolute magnitudes of $-13.5 < MV < -11mag$, or in stellar mass $2\times10^{6} < \mathcal{M}/M_{\odot} < 10^{8}$, half-light radii in the range $r_{\mathrm{eff}} = 10-100\,\mathrm{pc}$ (Misgeld et al., 2008; Da Rocha et al., 2011). UCDs follow a size-luminosity relation, i.e. more luminous objects have larger half-light radii. The colors of UCDs cover the ranges of the observed colours for normal GCs (Evstigneeva et al., 2008; Hilker, 2009; Misgeld & Hilker, 2011). Mass-to-light ratios for UCDs are very similar to GCs, with typical values of $M/L = 2-5$ (Hilker et al., 1999; Drinkwater et al., 2003; Haşegan et al., 2005; Mieske et al., 2008; Dabringhausen et al., 2008; Taylor et al., 2010; Frank et al., 2011).

The main channels proposed for their formation can be summarized in three: (i) UCDs are the merger product of massive young cluster (Fellhauer, & Kroupa, 2002) (ii) They are remnant of stripped nuclei of dwarf galaxies (Bekki et al., 2003; Ideta, & Makino, 2004; Pfeffer & Baumgardt, 2013). (iii) They formed insitu with the majority of the GCs and represent the bright tail of the globular cluster luminosity function (Mieske et al., 2004; Gregg et al., 2009; Mieske et al., 2012). The GC luminosity function extended to the bright regime indicates that most UCDs might be simply the GCs more massive than for example those found around the Milky Way and are only found in galaxies with rich GC populations (e.g. Fellhauer, & Kroupa, 2002, 2005; Hilker, 2006; Norris, & Kannappan, 2011; Mieske et al., 2012; Liu et al., 2015). According to observational evidence for 5 UCDs in the field/groups environment and UCD data from the literature, Norris, & Kannappan (2011) found that the UCD formation channels in a given galaxy depends on its environment and interaction history, suggesting that some of them are just the brightest GCs population and the others are stripped nuclei. One example for a massive stellar object is $W3$ found in the elliptical NGC 7252 (Maraston et al., 2004). Its dynamical mass is $(8\pm2)\times10^{7}\,M_{\odot}$ and an age consistent with $\sim 300-500\,\mathrm{Myr}$, this mass is much higher than the range of masses of typical GCs. An extended star formation history was found for NGC 4546-UCD1, its SFH extends several Gyrs (Norris et al., 2015). Another observational evidence for some UCDs to be stripped nuclei came with the findings of high central velocity dispersions, that dynamical models of the data suggest that the high central velocity dispersion peak is due to the presence of a SMBH with masses of the order few times $10^6\,M_\odot$ Seth et al. (2014); Ahn et al. (2017), such SMBH is expected to be found in galaxies.

1.4.3 *Compact Ellipticals*

The prototype for cE is M32, the nearby satellite of Andromeda. Its magnitude $M_V \simeq -17$ and effective radius of its bulge of $\sim 100\,\mathrm{pc}$ (Graham, 2002) place it in the size-luminosity relation for dwarf galaxies, but its central surface brightness (four times of a dwarf elliptical) makes it a compact and dense stellar object.

Later observations in other environments have further detected more of these cEs (e.g. Mieske et al., 2005; Chilingarian et al., 2007; Chilingarian, 2009; Price et al., 2009; Smith Castelli et al., 2012; Huxor et al., 2013; Paudel et al., 2014; Norris et al., 2014; Chilingarian, & Zolotukhin, 2015). Their cEs properties are galaxies with high stellar densities similar to the centers of giant ellipticals but have masses that are two orders of magnitude smaller $M \sim 10^9 M_\odot$.The formation scenarios are mainly three: (i) tidal stripping of a larger elliptical or the bulge of a disk galaxy (King, 1962; Faber, 1973; Nieto, & Prugniel, 1987; Bekki et al., 2001). (ii) the low mass tail of the true elliptical galaxy population (Wirth, & Gallagher, 1984). (iii) dwarf to dwarf mergers (Paudel et al., 2014). The study done by Graham (2002) showed that the surface brightness profile for M 32 is best fit by a compact Sersic for the bulge and a second component with low surface brightness and fit with an exponential disk profile. Their result points towards M 32 being the compact bulge of a stripped spiral rather than a elliptical galaxy. Guérou et al. (2015) presented they study of compact, low mass ETGs with integral field unit spectroscopy data (IFU) in the Virgo clusters and found the cEs sample are located in high-density regions, often close to a massive galaxy. have experienced long-lived interactions with their environment, including ram-pressure stripping and gravitational tidal forces, that may be responsible for their compact nature. The discovery of isolated cEs (Huxor et al., 2013; Paudel et al., 2014) challenged the idea of the tidal stripping scenario, for that reason (Paudel et al., 2014) proposed the dwarf-dwarf merger to form the isolated population of cEs. Kormendy et al. (2009) reviewing the structure of ellipticals and spheroidals, suggested that M 32 is just the faintest example for the family of ellipticals as seen by the absolute magnitude vs central surface brightness diagram.

1.5 HIERACHICAL ASSEMBLY SCENARIO

The modern understanding of structure formation states that every galaxy forms within dark matter halos Peebles (1982); Blumenthal et al. (1984). The standard model of cosmology is based on the cosmological principle, the Universe is homogeneous and isotropic. This assumption is very good to describe the Universe at large scale when averaging over scales of $R \sim 200h^{-1}\,\mathrm{Mpc}$. However, on small scales the Universe is inhomogeneous. There is evidence for this coming from the galaxy distribution projected on the sky (3D galaxy distribution) determined by redshift surveys (e.g. 2dFGRS, Colless et al., 2001), and the presence of cluster of galaxies, superclusters of galaxies and voids. Voids are nearly spherical regions which abscence of bright galaxies. Beside this evidence, the small anisotropies detected in the cosmic microwave background of $\Delta T/T \sim 10^{-5}$ indicates that the Universe contained small inhomogeneities at redshift $z \sim 1100$. This is the epoch where radiation interacted with matter for the last time, these photons traveled freely through the universe and now we observe them as a relic radiation called the Cosmic Microwave Background (CMB Penzias, & Wilson, 1965).

It is believed that fluctuations in the matter distribution were created right after the big bang and their growth were caused by gravitational instabilities that evolve with time (due to their self-gravity) to form the large structures in the Universe we see today. Initially the density distribution of baryons was much smoother than that of dark matter. When the interaction of baryons and photons ceased to exist (recombination epoch), was when baryons could fall into the potential well of dark matter and start to follow their distribution. However, when the gas became dense enough, physical mechanisms that dark matter are not suceptible with, start to play a role such as cooling and dissipational heating, thus changing their distributions (White, & Rees, 1978).

In a LCDM Universe, dark matter halos are the places where matter collapse converting potential energy into kinetic energy, virializing the halo. According to the power spectrum of density fluctuations the lower mass halos form first, and more massive halos can form later by successive halo mergers. One dark matter halo is composed of multiple distinct density peaks, called subhalos. Star formation occurs in halo only when the gas can cool efficiently. Star formation inside halos proceeds either by insitu or exitu processes to form the variety of stellar systems we see today.

Evidence for the existence of cold dark matter comes from the rotational velocity of galaxies at large radii which show a flattening behaviour from the center reaching a plateau, which indicates the presence of a galactic halo composed of non-luminous matter. The mass of galaxy clusters measured by dynamical mass, X-ray or gravitational lens also has shown that clusters contain much more mass than is visible, with ~20% coming from the stars in galaxies and the intracluster medium and the remaining ~ 80% consists in dark matter. Further evidence is obtained from the small anisotropies observed in the CMB, from which cosmological parameters of the Universe are determined. The Universe today is dominated by dark energy ($\omega_\Lambda = 0.685 \pm 0.007$) and cold dark matter ($\omega_m = 0.315 \pm 0.007$), with the baryon density contributing only $\omega_b = 0.0493$ (or $\omega_b h^2 = 0.0224 \pm 0.0001$) (Planck Collaboration et al., 2018).

The first stars, galaxies and quasar formed in the Universe start to reionize it at some time around $z \sim 10$. Large spectroscopic data sample of galaxies from the present epoch to high redshift ($z \sim 8$) has made possible to measure the emission history of all stars in galaxies with UV, optical, and IR wavelength to understand the cosmic history of star formation. The star-formation rate density peaked around $z \sim 2$, and declined exponentially at later times, where at $z = 1.3$ already half of the stellar mass observed today was formed (Madau, & Dickinson, 2014).

Cosmological simulations in the ΛCDM framework still faces problems to reproduce all the observables at small scales, the main problems are: (i) missing satellites - ΛCDM simulations produce more low mass subhalos than are actually observed (Moore et al., 1999; Klypin et al., 1999). (ii) cusp-core problem - the central profiles of galaxies are less steep and less dense than ΛCDM predicts for halos (Flores, & Primack, 1994; Moore, 1994). (iii) too big too fail problem - most of the massive subhaloes in dissipationless ΛCDM simulations are too dense to host any of the bright satellites of a galaxy like the Milky Way (Boylan-Kolchin et al., 2011). For more details about structure formation we refer the reader to the book *"Extragalactic Astronomy and Cosmology"*Schneider (2015) and for a review of the issues to be solved by ΛCDM simulations to Bullock, & Boylan-Kolchin (2017). The solutions come mainly from a better treatment of the baryonic physics in the simulations where feedback has an essential role to model the shape of galaxies (e.g. Fattahi et al., 2018).

2

SCIENCE DATA AND ITS PROCESSING: THE NEXT GENERATION FORNAX SURVEY

2.1 OBSERVATIONS

The *Next Generation Fornax Survey* (NGFS) is an ongoing deep multi-wavelength survey that covers the entire Fornax galaxy cluster out to its virial radius (1.5 Mpc) in optical and near-infrared (NIR).For the optical photometry, NGFS uses the Cerro Tololo Inter-American Observatory (CTIO) 4-meter Blanco telescope in combination with the *Dark Energy Camera* (DECam Flaugher et al., 2015). This wide-field camera has 62 CCDs (currently, only 60 chips are working), each of them with 2048×4096 pixels, a total field of view (FoV) of 2.2 degree and spatial resolution of $0.263''/\mathrm{pixel}$. For the NIR photometry, NGFS uses the European Southern Observatory (ESO) 4.1-meter *Visible and Infrared Survey Telescope for Astronomy* (VISTA) telescope with its intrument *VISTA InfraRed CAMera* (VIRCam) (Sutherland et al., 2015). VIRCam contains 16 chips of 2048×2048 pixels with 1.65 degree diameter FoV and pixel resolution of $0.34''/\mathrm{pixel}$. For all observations we use a Fermat spiral dithering strategy aiming at measuring, modeling and subtracting the surface brightness variations due to telluric emission across the field of view (FOV) of each camera. Figure 7 illustrates the Fornax cluster region that is aimed to be covered by the NGFS with DECam (gray-tiles) to reach out to its virial radius ($r_{\mathrm{vir}} \simeq 1.4\,\mathrm{Mpc}$; Drinkwater et al., 2001), the survey is centered on the dominant NGC 1399 galaxy. The current coverage is shown with a darker-gray color, composed of nine tiles, for which seven of them are homogeneously mapped, covering the cluster out to $\sim 50\%$ of its virial radius $\simeq 700\,\mathrm{kpc}$. NGFS observations are designed to detect point-sources at $S/N = 5$ down to $u' = 26.5$, $g' = 26.1$, $i' = 25.3$, $J = 24.0$ and $K_s = 23.3$ AB mag, which corresponds to the GC luminosity function (GCLF) turnover at $M_V \simeq -7.4$ mag (e.g., Rejkuba , 2012).

2.2 IMAGE PROCESSING

The initial image processing is carried out by the CTIO Community Pipeline (CP; Valdes et al., 2014), focusing mainly on instrumental signature removal, e.g., bias subtraction, flat-fielding, cross-talk correction. The NIR VIRCAM observations were processed from scratch starting with the raw data. In order to obtain a high quality science image, we developed a pipeline to process DECam and VIRCam data. As the data from DECam was acquire first, its pipeline was first constructed by one of the former NGFS postdoc Dr. Roberto Muñoz, who put together a wrapped-up software pipeline to manage Terabites data, that was the case for the Fornax cluster DECam observations. Starting with this setup for DECam, in the work of this thesis the pipeline was updated to improve some issues found with the photometric calibration. For the case of VIRCam data, in this thesis work we use the bones structure of DECam pipeline to develop a new one, that takes care of the special issues in the image processes of NIR data, e.g. background subtraction. NIR observation are more difficult to process than optical ones due to the variable background from stronger atmospheric absorption (water vapor and carbon dioxide in the atmosphere) and telluric emission throughout the 1 to 2.5 micron wavelength region. The back-

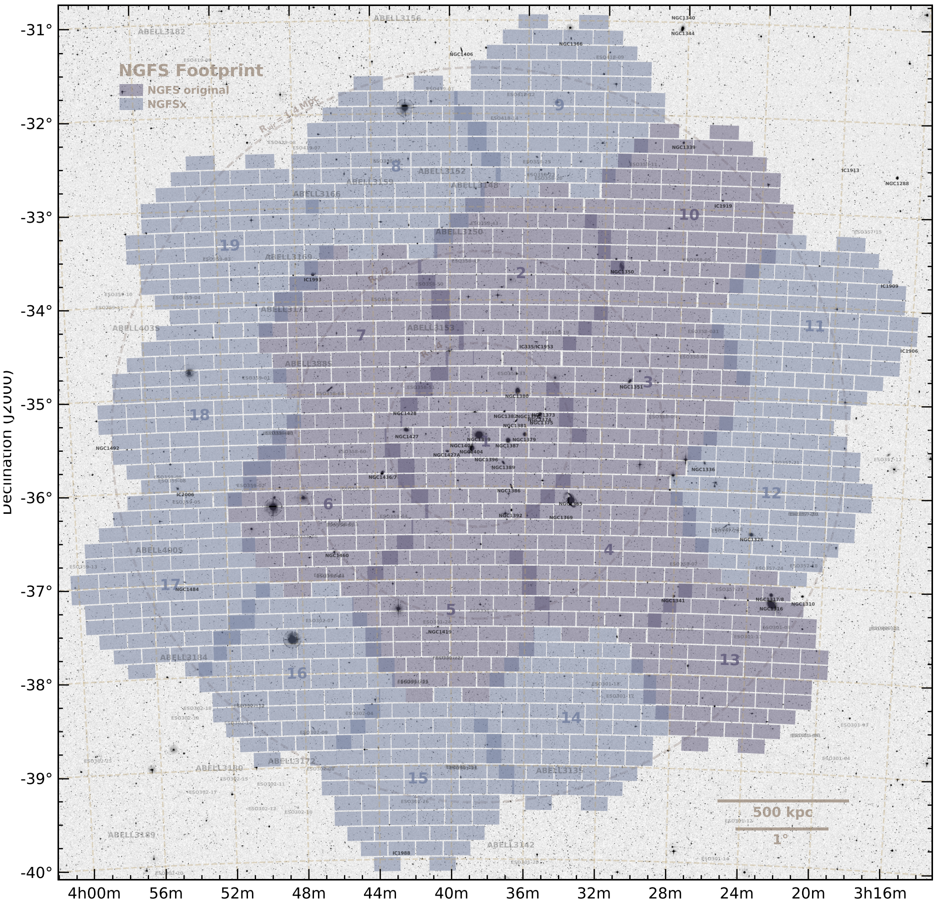

Figure 7: NGFS Survey footprint of the optical coverage in the Fornax cluster. The large dashed circle indicates its virial radius ($r_{vir} \sim 1.4$ Mpc; Drinkwater et al., 2001). The smaller dashed circles show $r_{vir}/2$ and $r_{vir}/4$ radii. Galaxies from the NGC/IC and ESO catalog (Lauberts & Valentijn, 1989) are labeled, as well as Abell galaxy clusters with 50 or more member galaxies

ground in K_s-band can reach thousands of ADU/s, depending strongly on the temperature and humidity of the observation night. We model the sky of individual images to obtain the sky variations using a surface fit or spline[1] fit with a given grid size to perform the interpolation.

The external software to perform the astrometry and photometry calibration is SCAMP (v2.2.6, Bertin , 2006) and Source Extractor (SE, v2.19.5, Bertin & Arnouts, 1996). For the astrometric calibration for both data set, we use the reference stars from the 2MASS Point Source Catalog (Skrutskie et al., 2006) or the SDSS stripe 82 standard star frames.

To ensure accurate photometric calibration, we cross-verified it with the globular cluster catalog from Kim et al. (2013) in the Fornax area, which was compiled using U, B, V and I-band photometry taken with MOSAIC-II camera on CTIO/Blanco. We use the empirical transformation equations from Jordi et al. (2006) for the comparison, finding good agreement within the uncertainties. Finally, we proceed to the final image stacking performed with the software SWARP (v2.19.5 Bertin et al., 2002) and the source detection with SE. Figure

---

[1] spline is a piecewise polynomial

8 shows the composite RGB image using $u'g'i'$ for the central region of Fornax cluster, NGC 1399 located at the center of the tile.

The average seeing on the DECam stacked images is $2.06 \pm 0.09''$, $1.38 \pm 0.06''$, and $1.23 \pm 0.02''$ in the u', g', and i' filter, respectively. The pixel scale of our final DECam image stacks is 0.263″ which corresponds to 25.5 pc at the distance of the Fornax cluster. The average seeing on the VIRCam stacked J and K_s images is $0.87 \pm 0.03''$ and $0.89 \pm 0.05''$, respectively. With a spatial resolution of $0.34''/\text{pix} = 33$ pc at the distance of Fornax.

2.3 PHOTOMETRY

Object detection and photometry in the science image stack, for each of the five filters, are performed with SE using a point spread function (PSF) model created with PSF Extractor (PSFEx, v3.16.1 Bertin, 2011), which takes into account spatial PSF variation across the detectors. We correct the photometry for foreground Galactic extinction, which we take from Schlafly & Finkbeiner (2011). Reddening values for the different filters are calculated assuming the Fitzpatrick (1999) reddening law with $R_V = 3.1$. The mean Galactic extinction in the direction of Fornax considering the extinction towards its brightest members inside $0.25R_{vir}$ is $A_V = 0.035$ mag. The derived magnitudes in optical passbands are all in the AB system and the NIR magnitudes were transformed from the Vega to the AB system using $K_s(m_{AB} - m_{Vega}) = 1.85$ mag and $J(m_{AB} - m_{Vega}) = 0.91$ mag (Blanton & Roweis , 2007). The $u'g'i'JK_s$ PSF photometry catalogs are crossmatched with each other to create a master catalog of objects with homogeneous information in all five filters. In this work, we do not require a completeness analysis as we aim for a full SED catalog with five filters, thus, our depth is defined by the limits of u' and K_s bands, which are the shallowest in the current NGFS observations. The faintest objects in each filter have magnitudes of $u' = 25.52$, $g' = 24.07$, $i' = 23.28$, $J = 22.92$, $K_s = 23.35$ AB mag.

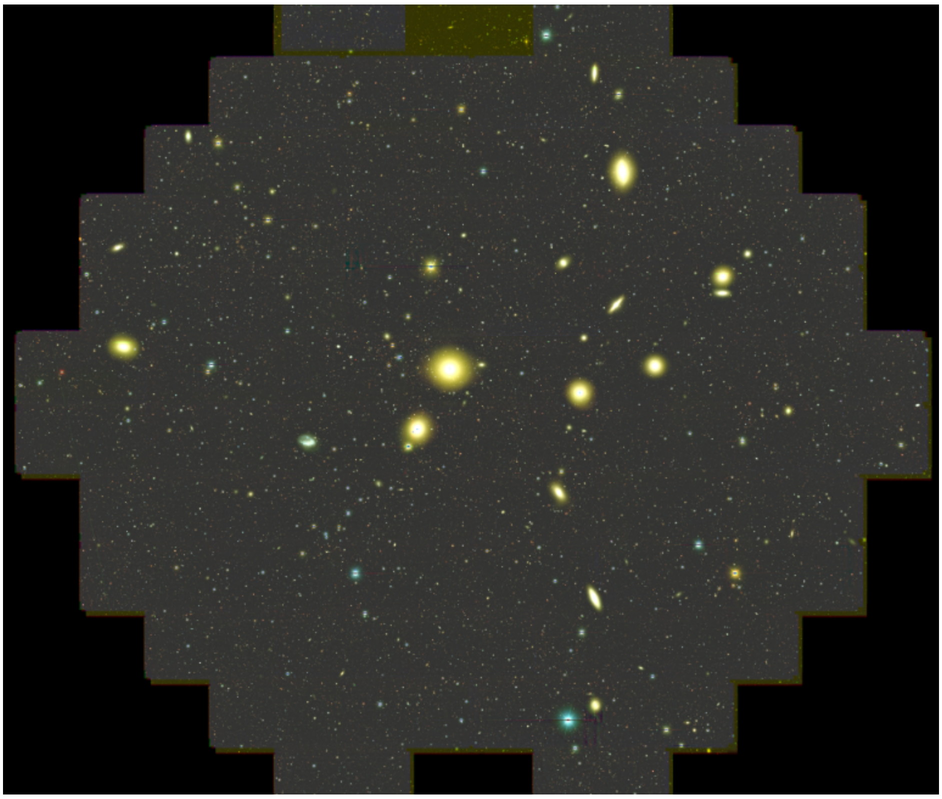

Figure 8: Illustration of the $u'g'i'$ color composite image for the inner 3 deg^2 of the NGFS survey footprint, centered on the brightest Fornax galaxy NGC 1399, located close to the center of the field.

3

DWARF GALAXY POPULATION INSIDE HALF THE VIRIAL RADIUS OF FORNAX

3.1 CONTEXT

Large populations of low-mass dwarf galaxies are ideal for studying the dependence of galaxy formation and evolution processes in the transition zones between field and cluster environments, especially in rich galaxy clusters. Statistically significant samples allow us to study their clustering properties on large scales and potentially probe the dark matter (DM) fine-structure within the cluster halo. This distribution in return serves as an ideal laboratory for comparisons with predictions from structure formation models.

In previous contributions (Muñoz et al., 2015; Eigenthaler et al., 2018), we presented the NGFS results focusing on the inner $\sim 3\,\deg^2$ ($\leqslant r_{\mathrm{vir}}/4$) region of the Fornax cluster. We presented optical colors and structural parameters for 258 dwarf galaxy candidates, reaching out to a projected distance of $\sim 350\,\mathrm{kpc}$ from NGC 1399, with the spatial distribution of which suggesting a rich and sub-structured dwarf galaxy population extending well beyond these limits.

In this work we expand upon these initial results by using the surrounding DECam pointings (NGFS tiles 2-7; see Fig. 7). In the following, we refer to the surrounding NGFS tiles (2-7) as the outer footprint. The goal of this paper is to update the known population of Fornax dwarf galaxies out to $\leqslant r_{\mathrm{vir}}/2$, where one might expect to witness the transition from the central galaxy population to those residing in the cluster outskirts.

3.2 ANALYSIS

3.2.1 *Detection of LSB dwarf galaxy candidates*

RGB full-color image stacks, constructed from the individual $u'g'i'$ frames are used to detect the LSB dwarf galaxy candidates. This color information help to distinguish between background objects and the dwarfs, mainly due to their difference in color, sizes and morphology characteristics, such as nucleated or non-nucleated and a flatter surface brightness profiles than their brighter counterparts. The by-eye dwarf detection strategy used for the central tile (Eigenthaler et al., 2018) is again utilized, where several members of the NGFS team (KAM, KXR, MAT, PE, THP, YOB) independently compiled dwarf candidate lists for tiles 2-7. Cross-matching lists and setting a minimum threshold of three independent detections yields a new robust list of dwarf galaxy candidates projected within $r_{\mathrm{vir}}/2$ of NGC 1399. By far, galaxy color is the most useful characteristic to identify dwarfs. Figure 9 shows some examples of dwarfs in the RGB image and a single-filter image for comparison, the dwarfs clearly stand out in the RGB image with a distinctive color compared to obvious background galaxies of similar angular size. While all frames are fully reduced, we defer a full color and stellar population analysis to a future work and limit the scope of the present work to a monochromatic i'-band presentation of magnitudes, structural parameters and spatial distribution characteristics.

We identify 271 new dwarf galaxy candidates, of which 39 are nucleated. Together with the 121 previously found NGFS dwarfs from the central tile (Muñoz et al., 2015; Eigenthaler et al., 2018), there is a total of 392 new dwarfs, out of which 56 are nucleated, that were discovered in the NGFS data.

We complement our final catalog with the known dwarf galaxy population in Fornax, using the likely members in the Fornax Cluster Catalog (FCC, Ferguson, 1989). In the outer NGFS footprint ($0.25 < R/R_{vir} \leqslant 0.5$), we find a total of 114 FCC galaxies (29.6%) and in the so-far searched NGFS survey area a total of 251 literature galaxies (39%; Ferguson, 1989; Mieske et al., 2007). Taking into account the dwarfs from existing catalogs and the new NGFS dwarfs, the total Fornax dwarf galaxy population reported in this work consists of 643 dwarfs, of which 462 are non-nucleated and 181 are nucleated.

3.2.2 *Structural parameters of the dwarf candidates*

The surface brightness profiles for the dwarfs are studied with GALFIT (v3.0.5 Peng et al., 2002) using a Sérsic profile (Sérsic , 1963; Caon et al., 1993). Our procedure has been described in detail in Muñoz et al. (2015) and Eigenthaler et al. (2018). It is an iterative process where the light profile is approximated with a one-component fit to the 2D galaxy surface brightness distribution. We run GALFIT on cutout images of $105'' \times 105''$ in size ($\simeq 10.2$ kpc × 10.2 kpc) using object masks created from SE segmentation maps and PSF models created with PSFEx (Bertin, 2011). For nucleated dwarfs, we iterate the method described above several times and improve the object mask in each iteration step until the nucleus is completely masked (see Eigenthaler et al., 2018; Ordenes-Briceño et al., 2018b, for more details). The final fitting profile considers only the spheroid light component of the dwarf galaxy, leaving a residual image (original – spheroid model) with the nuclear cluster in the galaxy center. The analysis of the nuclear star clusters is presented in chapter 4 (Ordenes-Briceño et al., 2018b). In the following we focus on the structural parameters of the spheroid sample. The dwarf candidates from the outer footprint have absolute i'-band magnitudes in the range $-18.80 \leqslant M_{i'} \leqslant -8.78$ with photometric errors <0.1 mag, effective radii between $1.8''$ to $22.8''$ ($r_{\mathrm{eff},i'} = 0.18$–$2.22$ kpc at the Fornax cluster distance of $D_L = 20.0$ Mpc), a mean Sérsic index of $\langle n \rangle_i = 0.81$, and an average axis ratio of $\langle b/a \rangle_{i'} = 0.69$.

3.3 RESULTS

Comparing the central and outer region in terms of mean structural parameters and nucleation fraction, we see some interesting differences mostly in the mean magnitudes and effective radii. Non-nucleated dwarfs in the central region are brighter and larger with $\langle M_{i'} \rangle = -11.99 \pm 0.12$ mag and $\langle r_{\mathrm{eff},i'} \rangle = 0.61 \pm 0.03$ kpc, relative to non-nucleated dwarfs in the outer region which have $\langle M_{i'} \rangle = -11.65 \pm 0.10$ mag and $\langle r_{\mathrm{eff},i'} \rangle = 0.55 \pm 0.02$ kpc. Nucleated dwarfs in the central region have significantly fainter average luminosities but are similar in average size compared to their nucleated counterparts in the outer footprint, $\langle M_{i'} \rangle = -12.43 \pm 0.21$ mag, $\langle r_{\mathrm{eff},i'} \rangle = 0.91 \pm 0.04$ kpc (central) and $\langle M_{i'} \rangle = -13.87 \pm 0.2$ mag and $\langle r_{\mathrm{eff},i'} \rangle = 0.95 \pm 0.04$ kpc (outer). These differences are more pronounced when comparing the nucleated and non-nucleated dwarf population, i.e. the non-nucleated dwarf population is fainter than nucleated dwarfs by $\Delta \langle M_{i'} \rangle = 0.44$ mag in the central region and $\Delta \langle M_{i'} \rangle = 2.25$ mag in the outer region. In addition, the non-nucleated dwarf population is, on average, smaller than the nucleated dwarf population by $\Delta \langle r_{\mathrm{eff},i'} \rangle = 0.3$ kpc and $\Delta \langle r_{\mathrm{eff},i'} \rangle = 0.4$ kpc, in the central and outer region, respectively.

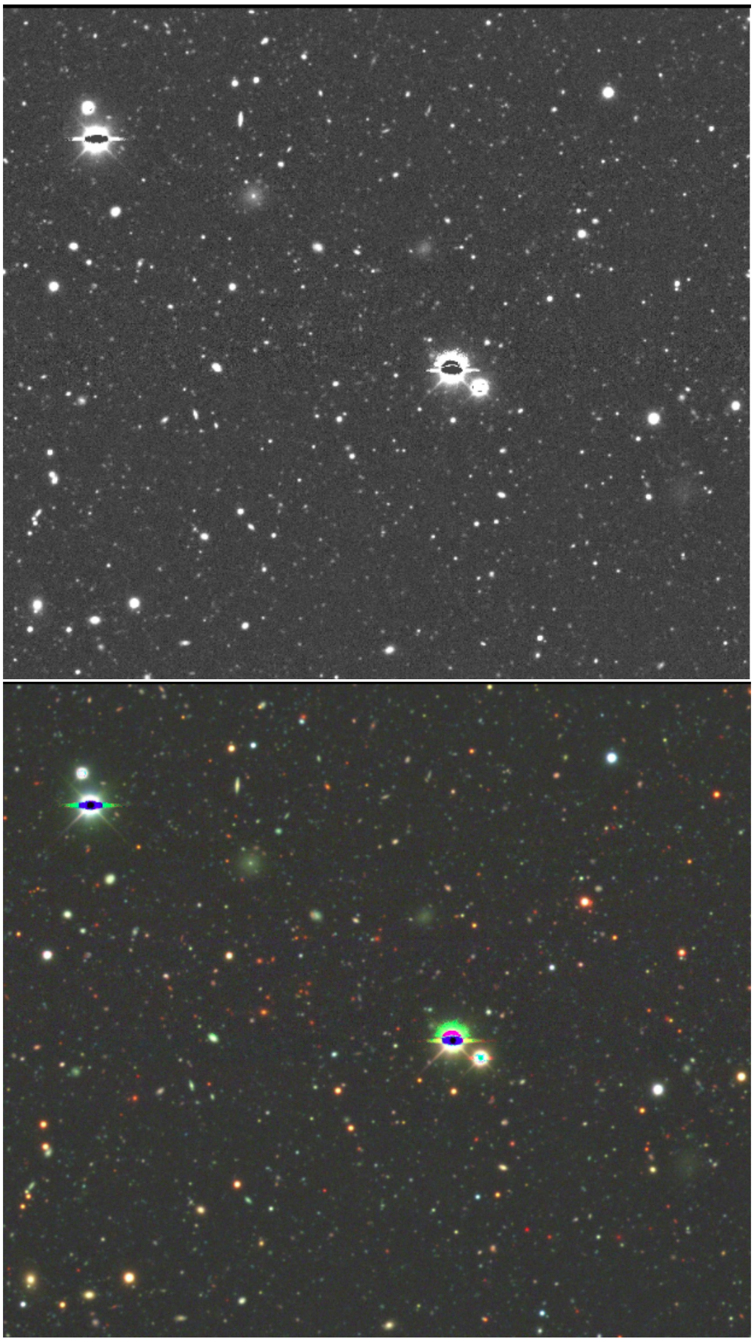

Figure 9: *Top panel*: Random field of our NGFS central pointing as seen through the g-band filter. *Bottom panel*: RGB image stack using the combined depth of the u+g+i-band observations. Note the clear distinction in color and shape of the three, low surface brightness Fornax dwarf galaxy candidates (one nucleated, two non-nucleated) in comparison with background galaxies.

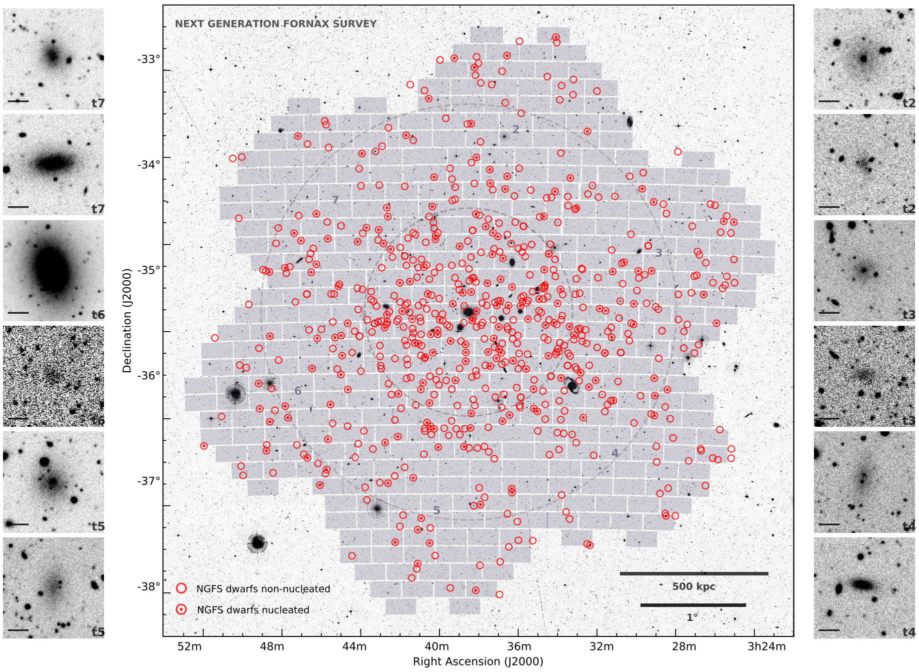

Figure 10: Illustration of the spatial distribution of Fornax dwarf galaxy candidates in a greyscale underlying image from DSS. The footprint of the NGFS survey (inside $\simeq r_{\rm vir}/2$), which is indicated by the grey shaded DECam tiles with tile 1 for the central region and tiles 2-7 for the outer region (see also NGFS footprint in Fig. 1 Eigenthaler et al., 2018), labeled with their respective numbers (middle panel). The position of non-nucleated dwarfs are shown by red open circles while the nucleated dwarfs are marked by red circles with a central dot. Left and right panels show examples of the newly detected dwarfs in the different NGFS footprint tiles (2-7). Each stamp image contains the NGFS tile number (bottom right) which contains the corresponding dwarfs galaxy as well as the scale bar (solid line) showing $10.3'' \mathrel{\hat{=}} 1$ kpc at the bottom left of each panel. Gray-dashed circles show NGC 1399-centric distances of $r_{vir}/4$ ($\simeq$ 350 kpc) and $r_{vir}/2$ ($\simeq$ 700 kpc).

Non-nucleated dwarfs have similar mean sizes and luminosities independent of local environmental density, i.e. central vs. outer region. However, central nucleated dwarfs are on average about 1.4 magnitudes fainter than nucleated dwarfs in the outer regions. In the central regions nucleated and non-nucleated have similar magnitudes but different mean sizes. However, in the outer region, nucleated dwarfs are on average brighter and larger than the non-nucleated dwarfs. Table 5 lists the IDs, coordinates, and structural parameters for the dwarf candidates at cluster-centric radii $r_{\rm NGC1399} > r_{\rm vir}/4$, complementing the sample from Eigenthaler et al. (2018) for the inner region ($r_{\rm NGC1399} < r_{\rm vir}/4$).

3.3.1 *Size-Luminosity Relation*

Scaling relations are useful tools to gain insight into the link of the formation processes between different astronomical objects. We illustrate in Figure 11 the size-luminosity relation in terms of the effective radius and absolute i'-band magnitude for the entire NGFS dwarf sample. A total of 452 non-nucleated and 178 nucleated dwarfs are shown. Thirteen dwarfs do not have structural parameter information due to very low surface brightness and/or complicated contamination in their nearby environment (e.g. bright star spikes, detector blemishes, crowded field). To map a large luminosity range, we overplot different galaxy samples, including Local Group dwarfs (McConnachie, 2012), ultra-diffuse galaxies from the Coma and Virgo clusters (van Dokkum et al., 2015; Mihos et al., 2015), and giant ellipticals from Fornax, Virgo and the Carnegie-Irvine catalog (Ferrarese et al., 2006; Ho et al., 2011). The NGFS dwarf sample by itself covers a range in absolute magnitude of $-18.80 \leqslant M_{i'} \leqslant -8.78$ mag and effective radii $r_{\mathrm{eff},i'} = 0.11 - 2.72$ kpc, comprising an effective surface brightness from $\langle \mu_{i'} \rangle_e = 20 - 28$ mag arcsec^{-2}. The sequence of giant ellipticals stretching from the upper-to-center-right of the diagram is connected to that of the NGFS dwarfs and dSphs (center to lower-left) by an intermediate bridge of galaxies. The bridge spans the $-20 < M_{i'} < -15$ mag, $0.6 \leqslant r_{\mathrm{eff},i'}/\mathrm{kpc} \leqslant 2$ parameter space and blends the brightest NGFS dwarfs with the faint regime of ETGs. We note here that the dwarfs in this group consist primarily of nucleated candidates such that 44/63 of these dwarfs show clear nuclei.

Ultra-diffuse galaxies (UDGs) seem to follow their own sequence, roughly along constant effective surface brightness, avoiding the bridge between dwarf and giant galaxies. Although UDGs seem to have similar magnitudes to the brightest dwarf galaxies they are much more extended. UDGs have been detected in multiple environments (e.g. Mihos et al., 2015; Koda et al., 2015; Muñoz et al., 2015; van Dokkum et al., 2015; Janssens et al., 2017; Lee et al., 2017; Venhola et al., 2017). They show signatures of massive dark-matter halos (e.g. Beasley et al., 2016; van Dokkum et al., 2016) and their population size scales with the mass of the central halo (van der Burg et al., 2016, 2017; Janssens et al., 2017). Together with predictions from theoretical studies this suggests that UDGs are a consequence of rapidly spinning, massive halos ($\geqslant 10^{10}\,M_{\odot}$) that recently fell into denser environments (e.g. Rong et al., 2017; Amorisco, 2018). In our NGFS footprint, six UDG candidates are found in the central region, and one in the outer region. Their magnitudes and effective radii are in the range $-15.62 \leqslant M_{i'} \leqslant -13.85$ mag and $r_{\mathrm{eff},i'} = 1.79 - 2.72$ kpc, respectively. Of the seven candidates, two harbor a nuclear star cluster. Their properties make them very similar to UDGs found in other galaxy cluster environments, such as Coma and Virgo (van Dokkum et al., 2015; Mihos et al., 2015). A curious Local Group counterpart is the currently disrupting Sagittarius dwarf galaxy ($M_V = -13.5$ mag and $r_{\mathrm{eff}} = 2.6$ kpc, McConnachie, 2012) with its nucleus and the central star cluster M54 (Bellazzini et al., 2008; Mucciarelli et al., 2017).

Figure 11 shows that the nucleation fraction of the NGFS dwarf sample decreases strongly with luminosity. The overall nucleation fraction is 28% for the entire luminosity range of the NGFS dwarfs. Nonetheless, the nucleation fraction reaches ~90% at bright magnitudes, i.e. $M_{i'} \leqslant -17$ mag, and drops to zero at the faintest galaxy luminosities, i.e. $M_{i'} \geqslant -9.56$ mag. This limit marks the currently faintest nucleated galaxy in the NGFS dwarf galaxy sample (see also Muñoz et al., 2015; Ordenes-Briceño et al., 2018b).

3.3.2 *Spatial Distribution*

Figure 12 shows the spatial distribution of the dwarf galaxy candidates in the NGFS survey region, with dashed black circles indicating NGC 1399-centric radii of $r_{\mathrm{vir}}/4$ and $r_{\mathrm{vir}}/2$ that correspond to ~350 and 700 kpc at the distance of Fornax. The dwarfs and giant galaxies are distributed throughout the field with

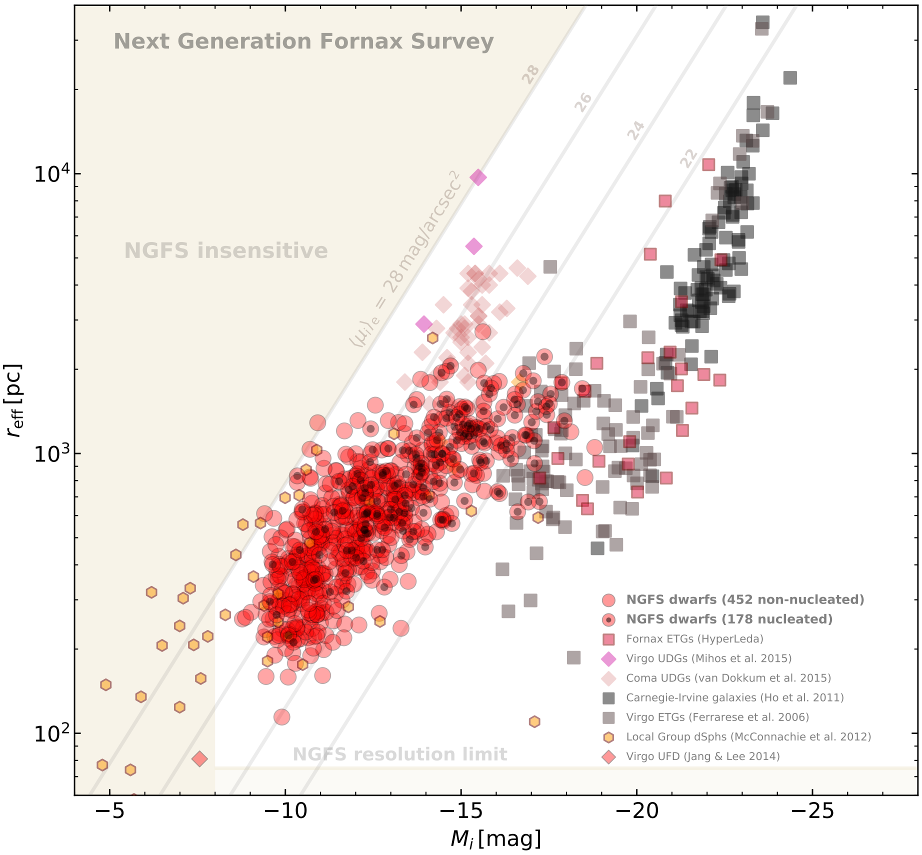

Figure 11: Size-luminosity relation for dwarf and giant galaxies in Fornax and the nearby universe (see the legend at the bottom right). Galaxy size is given by the effective radius and the luminosity represented as the absolute i′-band magnitude. The NGFS dwarf population are shown in red circles with black dots indicating the nucleated galaxies. The data for bright Fornax ETGs were taken from the HyperLeda database (`http://leda.univ-lyon1.fr`), where the effective radii were computed, in order of preference, from Caon et al. (1994), de Vaucouleurs et al. (1991), and Lauberts & Valentijn (1989). Lines of constant average effective surface brightness are indicated for $\langle\mu_{i'}\rangle_e = 28, 26, 24, 22\,\text{mag arcsec}^{-2}$. An approximate surface brightness limit of our NGFS data is illustrated by the shaded region toward the top left. The spatial resolution limit (0.8″in the i′ filter, corresponding to ~78 pc) is indicated by light shaded region in the bottom part of the diagram, below this limit objects appear as unresolved point sources in our NGFS data at the distance of Fornax ($m-M=31.51$ mag or $D_L=20.0$ Mpc, Blakeslee et al., 2009).

the projected dwarf galaxy surface number density profile, $\Sigma_N(\alpha, \delta)$, shown by the color shading, computed along a 15×15 bins grid—corresponding to physical bin sizes of 152×146 kpc^2—and show the resulting 2D histogram smoothed with Lanczos interpolation. We also estimate $\Sigma_N(\alpha, \delta)$by a non-parametric kernel density estimate using a Gaussian kernel of 0.25 deg bandwidth and show resulting curves of iso-density contours by grey-scaled thin solid lines. We point out that variations in surface brightness limits due to bright galaxy haloes do not affect the results since the typical size of a galaxy halo is negligible compared to the area studied here and the structures found therein.

Both $\Sigma_N(\alpha, \delta)$estimates show a general concentration of dwarfs in the core regions of Fornax within $r \leqslant 350$ kpc. NGC 1399 itself can be seen to occupy an apparent saddle-point between two main dwarf galaxy over-densities towards the East and West (see Figs. 10 and 12, and also Muñoz et al., 2015). The projected distribution of dwarfs in the Western over-density generally follows that of the giant galaxies, which may suggest a physical association. While the current data cannot confirm such a connection, we note the contrast with the ~ 200 kpc-scale over-density to the East. This group shows a more regular morphology, and lies in between to the projected positions of only two bright galaxies, complicating the notion of physical origins with nearby giant hosts. Weaker density contrasts are found for a third "orphan" group of dwarf candidates located near $(\alpha, \delta) \approx (03^h33^m, -35.75^o)$.

3.4 DISCUSSION

The top two panels of Figure 13 show the $\Sigma_N(\alpha, \delta)$profile calculated with respect to NGC 1399. To guard against potential biases introduced in choosing arbitrary binsizes, we resample the dwarf galaxies using both a constant and an adaptive binning strategy. For the former, we choose constant bins between 5′and 25′, in steps of 1′. At each step we calculate $\Sigma_N(\alpha, \delta)$in each of the corresponding annuli and show the aggregated data as dots. We have done this procedure for non-nucleated and nucleated dwarfs, and the entire dwarf sample. Similarly, the middle panel of Figure 13 shows the data based on adaptive bin sizes with the three samples described above. Here, bins are chosen such that each of them contains exactly N dwarf candidates with $5 \leqslant N \leqslant 25$. The constant binning produces a much smoother variation in $\Sigma_N(\alpha, \delta)$, while the adaptive binning shows a sensitivity to local dwarf over-densities resulting in artificially small annuli and corresponding spikes in the $\Sigma_N(\alpha, \delta)$profile. We approximate the dwarf $\Sigma_N(\alpha, \delta)$profiles by a power-law model, following other radially dependent projected densities (e.g. $\Sigma_N(\alpha, \delta) \propto \exp(A R^{\alpha})$; Einasto, 1965; Sérsic , 1963) by Markov-Chain Monte Carlo (MCMC) sampling. We use MCMC with a normal prior to sample the posterior probability of (A, α) 10^5 times, which allows sufficient burn-in to skip over stochastic or unreliable results from early iterations so that each chain converges to consistent, well-defined peaks in the marginalizeds parameter estimate distributions. The resulting $\Sigma_N(r)$ estimates are shown in the two top panels of Figure 13 as solid curves. The text displays the means of the posterior probability density functions for α alongside the corresponding 95% confidence limits. The projected radial surface number density for the non-nucleated dwarfs has a flat distribution up to ~ 350 kpc and slowly declines beyond that radial distance. On the other hand, nucleated dwarfs have a steeper $\Sigma_N(r)$ distribution than non-nucleated dwarfs, being more concentrated in the inner regions near the cD galaxy NGC 1399 and decreasing rapidly outwards. This is similar to the results of Lisker et al. (2007) who found based on SDSS photometry ($M_B \lesssim -13$ mag) that the bright nucleated dwarf galaxy

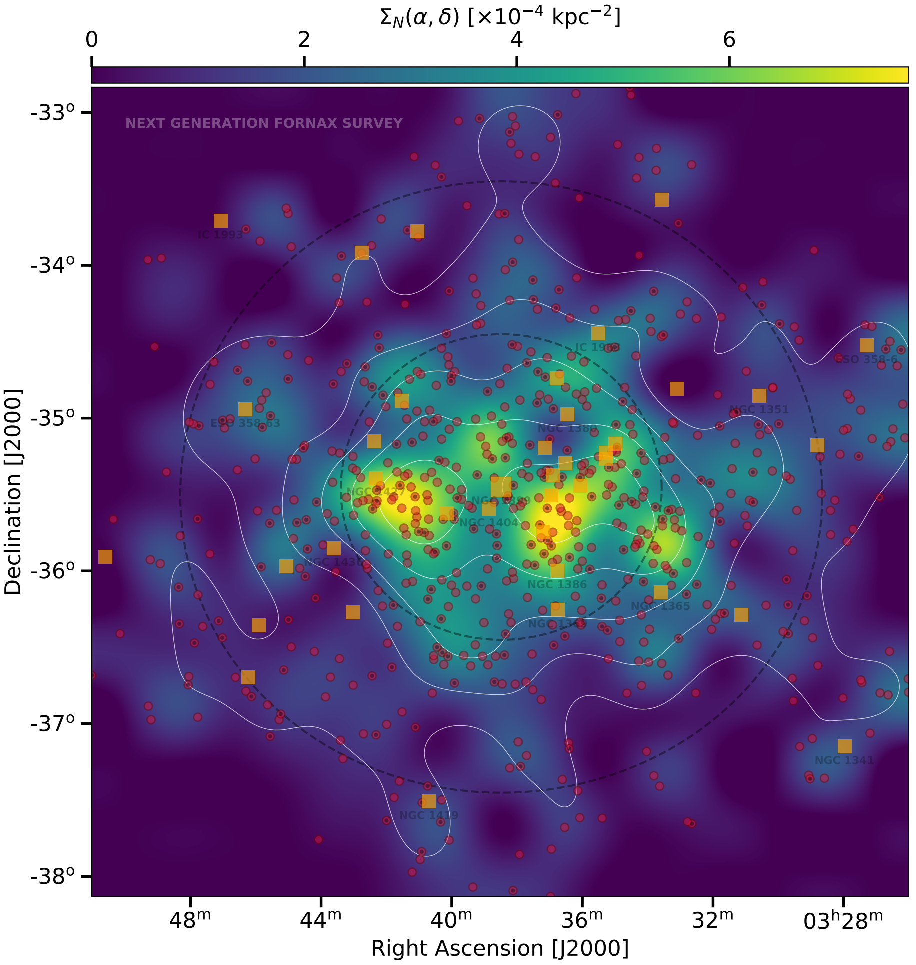

Figure 12: The distribution of dwarf galaxies (fainter than $M_{i'} \approx -19$ mag) in the Fornax galaxy cluster within about half of its virial radius ($\sim r_{\text{vir}}/2$) shown as a surface number density distribution (see colorbar scale). Overplotted are the NGFS dwarf candidates (red dots) and bright Fornax galaxies ($M_{i'} \lesssim -19$ mag, orange squares) with NGC 1399 shown by the large square. Black dashed circles show NGC 1399-centric distances of $r_{\text{vir}}/4$ ($\simeq$ 350 kpc) and $r_{\text{vir}}/2$ ($\simeq$ 700 kpc), while solid contours represent 2D Gaussian KDEs with a 0.25 degree kernel width.

population in the Virgo galaxy cluster is more centrally concentrated than the non-nucleated dwarf population.

The bottom panel of Figure 13 shows the results of a two-point angular correlation function ($\hat{w}(\theta)$; Landy & Szalay, 1993) analysis of the dwarf galaxy candidates, using the same three samples (non-nucleated, nucleated, and all dwarfs). The two-point angular correlation function quantifies the excess probability of finding galaxy pairs at a given angular separation over a random distribution without a restriction to Gaussianity (e.g. Connolly et al., 2002; Sato et al., 2009), and is typically used to constrain cosmological parameters and structure formation models (e.g. Bernardeau et al., 2002; Cooray & Sheth, 2002; Tegmark et al., 2002, 2004; Dolney et al., 2006). Noting the steepening of the $\Sigma_N(\alpha,\delta)$ profile at ~350 kpc and the $\Sigma_N(r)$ distribution, we split the total sample into those dwarf galaxies inside and outside of this radius and estimate $\hat{w}(\theta)$ for each sub-population. The solid lines along with $\pm 1\sigma$ bounds show the results for the three samples, in addition to all-outer and all-inner dwarfs, with correlation lengths θ binned in steps of $10'$ for the total, non-nucleated and nucleated sample, and $5'$for the two sub-samples. Estimating $\hat{w}(\theta)$ using different bin sizes reveals mild deviations but with the overall behaviors unchanged.

Given that the likelihood of finding two points separated by an angular distance θ compared to a purely uniform distribution is encapsulated by $\hat{w}(\theta)$, we find particularly strong evidence for dwarf clustering on sub-100 kpc scales for the overall and outer dwarf population. In particular, the outer dwarf galaxies appear more likely to be clustering on scales approaching ~ 50 kpc with a notable decrease on scales $\geqslant 100$ kpc. Overall, the apparent smaller clustering scale appears superimposed on the ~ 350 kpc-scale over-density shown in Figure 12. This larger clustering scale is reflected by the almost flat $\Sigma_N(\alpha,\delta)$ profile within ~ 350 kpc, outside of which a general steepening of the profile is seen, modulo local, projected dwarf clustering and sub-groups. Conversely, the dwarf population inside of $r \approx 350$ kpc does not appear to show as strong evidence for clustering at any scale, but we note that the limited spatial region will tend to mute $\hat{w}(\theta)$. In any case, we check against an underlying uniform distribution of dwarf galaxies by creating a large artificial set of 3D dwarf galaxy coordinates, uniformly distributed within a 1 Mpc radius sphere centered on NGC 1399. We limit this population to those lying within the coordinate limits of our observed sample, and extract the 2D projected distances from NGC 1399. Two-sample Kolmogorov-Smirnov tests comparing the simulated NGC 1399-centric projected separations and position angles to the new dwarfs rule out a flat surface density distribution of dwarf galaxies within the NGFS field of view at a very high confidence level (i.e. $p = 0.004$ for separations and $p \ll 0.001$ for galaxy position angles).

Figure 14 shows an alternate view of the spatial distribution. Here we show the projected number density as a function of azimuthal angle (Φ; degrees East of North) and radial distance from NGC 1399. Symbols are as in Figure 12 with dashed lines indicating $r_{\rm vir}/2$ and $r_{\rm vir}/4$, which corresponds to 350 and 700 kpc from NGC 1399. We apply $(\Delta\Phi = 36°, \Delta r_{\rm NGC1399})$ binning and smooth the 2D histogram with Lanczos interpolation, which serves to highlight dwarf groupings aligning along "lines-of-sight" to NGC 1399, which do not appear as obvious as in the projected (α, δ) space (see Fig. 12). Nevertheless, similar $\leqslant 100$ kpc-scale overdensities are apparent at all radii, further supporting the non-uniformity of the Fornax dwarf galaxy population, in particular the E-W bimodality shown near $r_{\rm NGC\,1399} = r_{\rm vir}/4 \approx 350$ kpc. Spectroscopic observations are required to assess the phase-space coherence of the found dwarf galaxy overdensities.

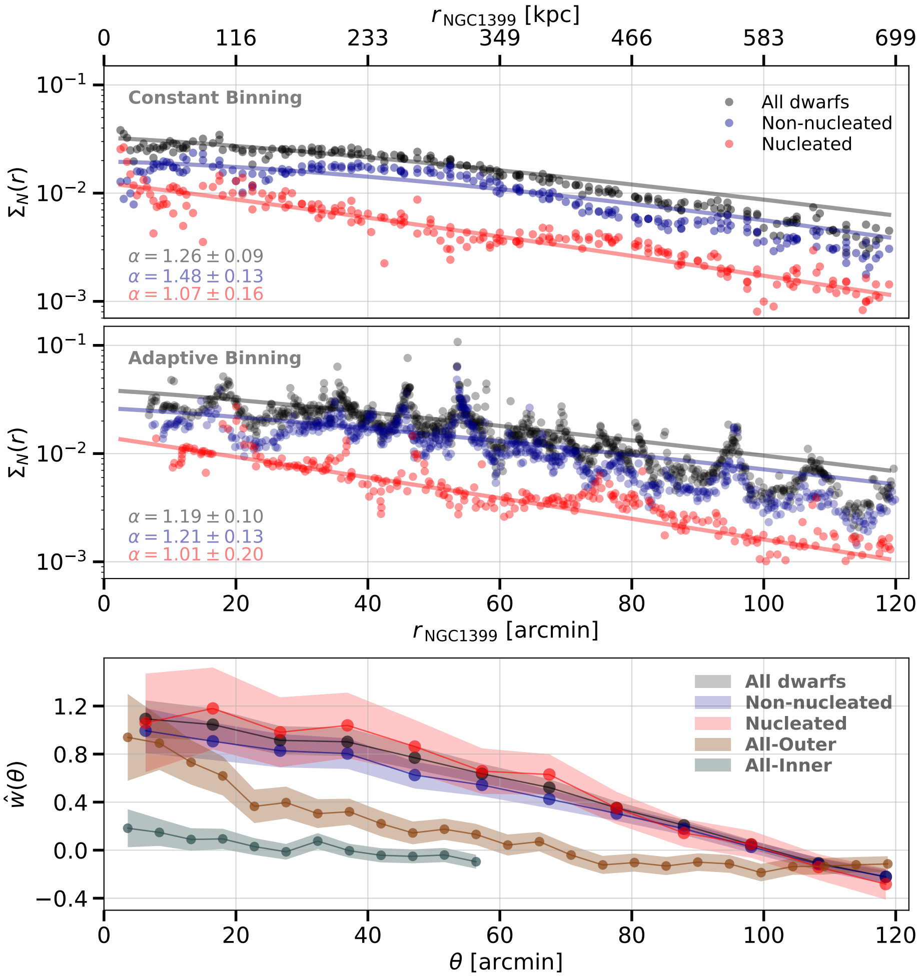

Figure 13: The two upper panels show radial surface number density distributions of dwarfs using constant (top) and adaptive (middle) binning strategies (see text). An Einasto profile (Einasto & Haud, 1989) is fit to each of these distributions, with the exponential slope and bootstrapped uncertainties indicated. Only the homogeneously sampled region within 700 kpc ($r_{\mathrm{vir}}/2$) of NGC 1399 is considered. *Bottom panel*: The two-point angular correlation functions and associated bootstrapped uncertainties are shown for the total (blue), and outer/inner samples (brown/grey; split at $r = 350$ kpc).

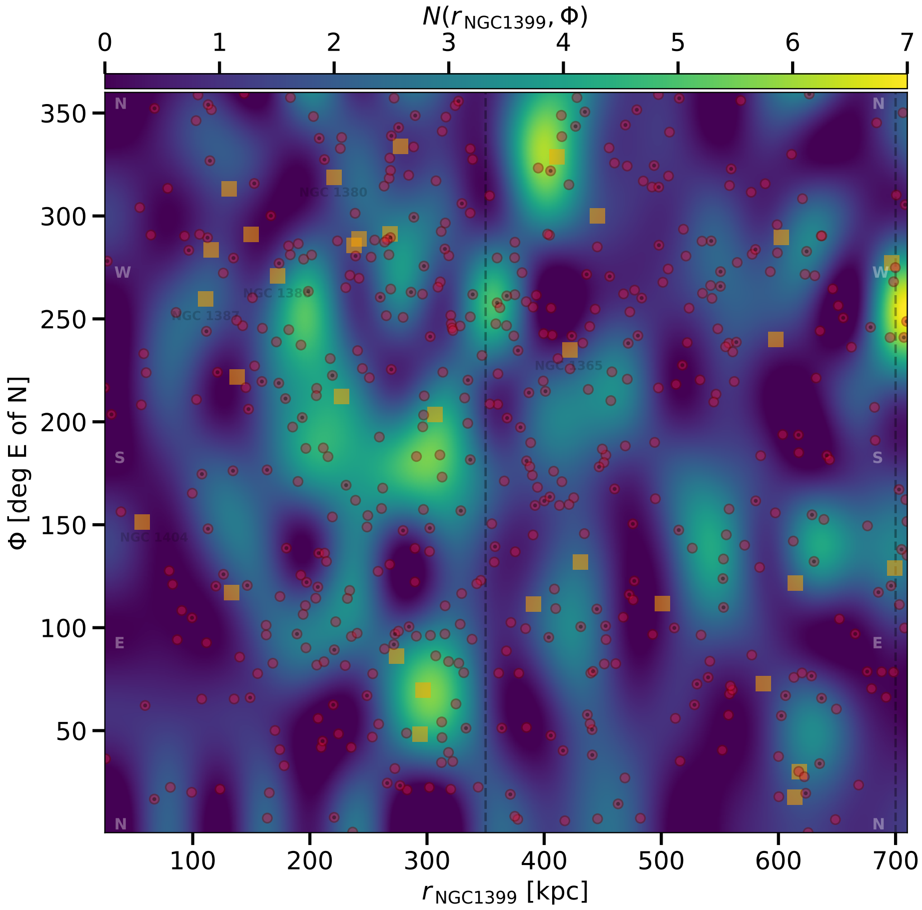

Figure 14: 2D density distribution showing dwarf clustering in the $\Phi - r_{\mathrm{NGC1399}}$ space, smoothed using Lanczos interpolation. Red circles are dwarf galaxies while orange squares show the locations of bright Fornax galaxies. Dashed vertical lines indicate the NGC 1399-centric radii of $r_{\mathrm{vir}}/4$ ($\simeq$350 kpc) and $r_{\mathrm{vir}}/2$ ($\simeq$700 kpc).

Taken together, the evidence of clustering at $\leqslant$ 100 kpc scales within the central cluster-centric radius of ~ 1 Mpc of Fornax broadly concurs with the growing observational evidence for the common occurrence, and importance, of dwarf galaxy pairs and groups in low-mass galaxy evolution and transformation in the Local Universe (e.g. Martínez-Delgado et al., 2012; Annibali et al., 2016; Ordenes-Briceño et al., 2016; Stierwalt et al., 2017). Theoretical considerations predict that close associations between dwarf galaxies should be common in that as many as 50% of $10^6\,M_{\odot}$-scale dwarf galaxies might be expected to have companions within ~50 kpc (Wetzel et al., 2015; Wheeler et al., 2015). Given the isolated natures of many of the recently discovered dwarf pairs/groups, combined with the locations of other purported dwarf groups ranging out to ~ 100 kpc from giant galaxy hosts, the current findings may indicate that at least some of these groups are truly interacting in the halos of Fornax giant galaxy members, or that they may have origins in the primordial universe and are falling into the Fornax cluster environment for the first time.

3.5 SUMMARY

In this work we have reported the discovery of 271 previously undetected dwarf galaxies in the outer Fornax cluster regions at radii $r_{\mathrm{vir}}/4 < r < r_{\mathrm{vir}}/2$ using deep composite u', g' and i' image. From the 271 dwarf candidates we find 39 to be nucleated. Together with our previous study of the central Fornax region, the new dwarfs detected with NGFS data are 392, of which 56 are nucleated. The total Fornax dwarf galaxy population from NGFS and other catalogs rises, therefore, to a total of 643 with 181 being nucleated, yielding an overall nucleation fraction of 28%.

The absolute i'-band magnitudes for the outer NGFS dwarfs are in the range $-18.80 \leqslant M_{i'} \leqslant -8.78$ with effective radii $r_{\mathrm{eff},i'} = 0.18 - 2.22\,\mathrm{kpc}$ and an average Sersic index $\langle n \rangle_{i'} = 0.81$. Non-nucleated dwarfs are found to be fainter and smaller by $\Delta\langle M_{i'}\rangle = 2.25\,\mathrm{mag}$ and $\Delta\langle r_{\mathrm{eff},i'}\rangle = 0.4\,\mathrm{kpc}$ than the nucleated dwarfs. We demonstrate a significant clustering of dwarf galaxies on scales $\lesssim 100\,\mathrm{kpc}$, and projected surface number density profile estimates, $\Sigma_N(r)$, show a concentration of dwarfs in the Fornax core region within $r \leqslant 350\,\mathrm{kpc}$. $\Sigma_N(r)$ has a flat distribution up to $\sim 350\,\mathrm{kpc}$, beyond which it declines for the non-nucleated dwarfs. The nucleated dwarfs have a steeper $\Sigma_N(r)$ distribution, being more concentrated towards NGC 1399 and decreasing rapidly outwards.

This is the first time the transition from cluster to field environment has been established for the very faint dwarf galaxy population with robust sample statistics.

4

NUCLEAR STAR CLUSTERS IN THE FORNAX CORE REGION

4.1 CONTEXT

Dwarf galaxies dominate the galaxy number density in dense environments. Whether they contain a compact stellar nucleus at their centers, or not, is an important distinction among the dwarf galaxy population. Nuclei are a common characteristic in galaxies, from dwarfs to giants. Considerable observational efforts were recently undertaken to map the nearby galaxy cluster regions in Virgo and Fornax, with deep, homogeneous, wide-field surveys reaching low surface-brightness dwarf galaxies ($\langle \mu_{e,i} \rangle \simeq 29$ mag arcsec^{-2}, see e.g. Ferrarese et al., 2012; Mihos et al., 2005, 2017; Muñoz et al., 2015; Eigenthaler et al., 2018).

In dense galaxy cluster environments, nucleated galaxies have been studied up to now in galaxies brighter than $M_i \simeq -15$ mag in Fornax and Virgo (Turner et al., 2012; Côté et al., 2006) using the Advance Camera Survey (ACS) in the Hubble Space Telescope (HST), with a sample of 31 and 45 nuclei, respectively.

In this work we explore, for the first time, the faint nucleated dwarf galaxy luminosity regime in terms of their photometric properties and scaling relations.

4.2 ANALYSIS

4.2.1 *Sample selection*

The nucleated dwarf galaxy sample of this work originates in the NGFS sample studied by Eigenthaler et al. (2018) which consists of 258 dwarf galaxies in the inner 25% of the virial radius of the Fornax cluster ($R_{\rm vir}/4 \simeq 350$ kpc; Drinkwater et al., 2001), centered on the cD galaxy NGC 1399 (see Fig. 15). Of this total dwarf galaxy population, we consider 75 (29%) to be nucleated based on the following selection criteria: *(i)* the central object is located at the photometric centre of the spheroid or slightly offset ($\leqslant 3''$), *(ii)* the nuclear cluster is detected in at least two filters, and *(iii)* the central object appears as a point source. From the 75 nucleated dwarfs, we could further analyze 61 nuclei. For six galaxies the surface brightness profile fits of their spheroid light did not converge to robust solutions, due to contamination by nearby objects or/and too low surface brightness values. For eight of them that have good spheroid profile fits, we encountered unstable solutions in the very inner regions, mainly due to saturation of nearby sources, too-low S/N, and/or stacking artifacts in the area. Since we are primarily interested in robust panchromatic photometry, we, therefore, exclude these objects from the subsequent analysis. Two nucleated dwarf galaxies in our sample overlap with the ACS Fornax Cluster Survey sample (Côté et al., 2006), FCC202 and FCC136, which are shown in Figure 15 as red ellipses with green edges.

Even with sub-arcsecond seeing, the spatial resolution of DECam (1 pix = 25.5 pc) and VISTA (1 pix = 33 pc) all nuclei at the Fornax distance are unresolved point sources. Nucleus detections in the central NGFS dataset for each filter reach these magnitudes: $u' \simeq 25.2$ mag, $g' \simeq 26.2$ mag, $i' \simeq 25$ mag, $J \simeq 21.9$ mag, and $K_s \simeq 23.1$ mag. The faintest nucleated dwarf galaxy detected in the Fornax central region has an absolute magnitude of $M_i \simeq -10.8$ mag.

Figure 16 shows the gallery of g'-band images of our nucleated dwarf galaxy sample, ordered by decreasing luminosity of their spheroid component from top left to bottom right. It is worth noting that the spheroid axis ratios and position angles of the dwarf galaxies are mostly consistent with rounded systems ($\epsilon < 0.55$; see Eigenthaler et al., 2018). Although the ellipticity distributions of the spheroid light components[1] of nucleated and non-nucleated dwarfs cover a similar range, Eigenthaler et al. showed that the nucleated dwarfs are systematically round than their nucleus-devoid counterparts by $\Delta\epsilon \approx 0.1$. In addition, the spheroids of nucleated dwarfs have on average larger half-light radii ($\Delta r_{\mathrm{eff}} \approx 0.2 - 0.3$ kpc) than non-nucleated dwarfs.

We also observe that towards lower galaxy luminosities, the nucleus luminosity becomes more prominent compared to the luminosity of the galaxy spheroid, something that contrasts with the relation found for bright galaxies (Turner et al., 2012). Our main goal in this article is, therefore, to characterize the faint population of nuclear star clusters in the dwarf galaxies in the central Fornax region in terms of the information provided by their luminosities and colors using the broad SED coverage of our NGFS filter set.

4.2.2 *Spatial distribution*

Figure 15 shows how our nucleated dwarf sample improves the sample size in terms of spatial coverage and luminosity range compared to previous studies in the same region, in particular those based on the ACSFCS observations which included nine nucleated dwarf galaxies. The spatial distribution of the nucleated dwarfs in the central Fornax region follows the spatial distribution of the non-nucleated dwarf galaxy population, with a slight anisotropy in the east-west direction where the dwarf galaxy surface density appears to be mildly elevated compared to the north-south direction and with individual density peaks that follow the distribution of the giant galaxies (see Muñoz et al., 2015). Our earlier studies indicated that there may be a higher clustering of dwarf galaxies on length scales below ~ 100 kpc. In galactocentric distance from NGC 1399, the non-nucleated sample show a flat distribution out to ~ 350 kpc, meanwhile the nucleated dwarfs have a peak in surface number density at a cluster-centric radius of ~ 200 kpc and declining outwards. Thus, data from the full NGFS survey footprint is required to understand the overall nucleated vs. non-nucleated galaxy distribution in the Fornax galaxy cluster. Some intriguing results on this topic from the sample presented in this work will be addressed in the discussion section below.

4.2.3 *Nucleation fraction*

The nucleation fraction (f_{nuc}) according to the previous work of Turner et al. (2012) for the Fornax region is 72% with galaxy luminosities of their sample reaching as low as $M_B \simeq -16$ mag, thus, only covering the bright galaxy regime. The NGFS nucleated dwarf galaxy sample extends this limit to $M_{g'} \simeq -10.5$ mag. In Muñoz et al. (2015), we have found that f_{nuc} depends strongly on the galaxy luminosity. In Figure 17 we use the NGFS dwarf galaxy sample to estimate cumulative and differential f_{nuc} as a function of galaxy luminosity in a window of 20 galaxies and smooth it using a Locally Weighted Scatterplot Smoothing (LOWESS) fit (e.g., Cleveland, 1981) to inspect the general trend. The

---

[1] This considers only the spheroid light component of the dwarf galaxy, excluding the nuclear star cluster.

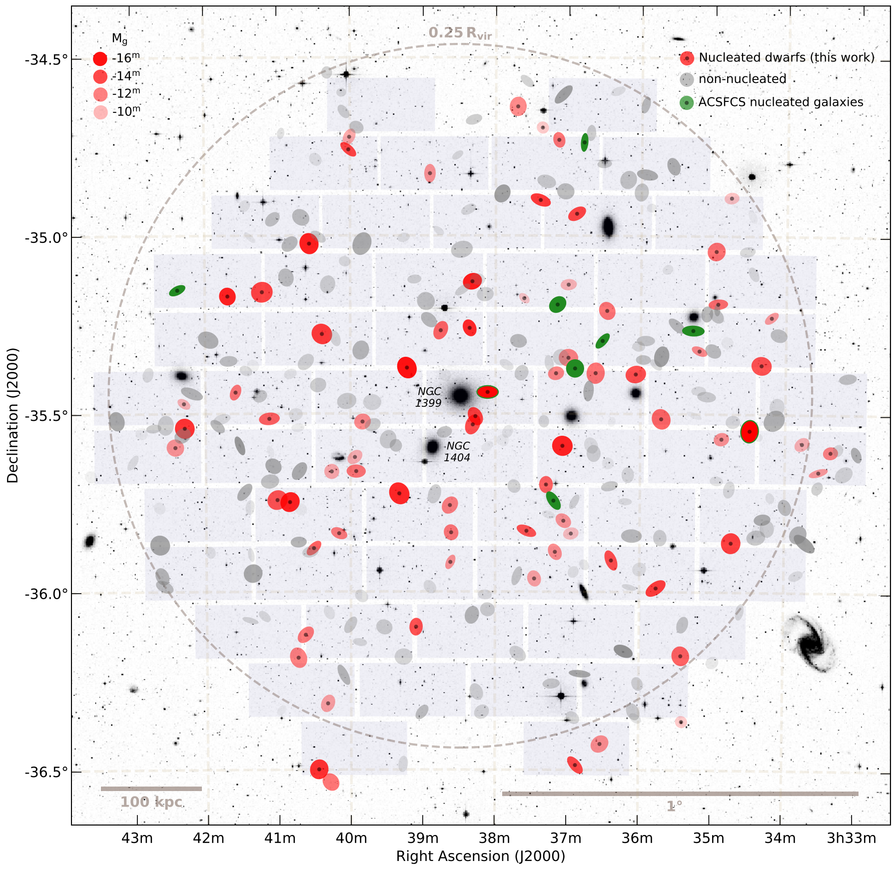

Figure 15: Central region of the Fornax galaxy cluster of the inner ~ 25% of the virial radius ($R_{vir}/4$, see dashed circle), showing the spatial distribution of nucleated dwarfs (red symbols), non-nucleated dwarfs (grey symbols), and the nucleated galaxies studied by the ACSFCS (green symbols; see Côté et al., 2006). The field is centered on the giant elliptical cD galaxy NGC 1399, which is located at the center of the field. The symbol transparency parameterizes the galaxy luminosity as indicated in the top left corner, i.e. more transparent symbols indicate fainter galaxies, while the ellipticity and position angle of the symbol represent the same parameters of the corresponding galaxy spheroid. Two red ellipses with green edges mark the two dE,N galaxies (FCC 202 and FCC 136) that are included in both the ACSFCS sample and this work.

blue and the orange lines show the differential and cumulative f_{nuc} distributions, i.e. $\Delta f_{\text{nuc}}/\Delta g'$ and $f_{\text{nuc}}(< g')$ respectively. For the bright NGFS dwarf galaxies ($M_{g'} \leqslant -16$ mag) f_{nuc} reaches $\geqslant 90\%$. On the other hand, fainter galaxies show systematically lower f_{nuc} values, reaching zero at absolute magnitudes $M_{g'} \simeq -10$ mag. Although finding nucleated dwarfs towards fainter magnitudes depends on both the point-source detection limit (see values in Sect. 4.2.1) and the surface brightness limit of our NGFS data ($\langle \mu_{i'} \rangle_e \approx 28$ mag arcsec^{-2}, see Muñoz et al., 2015; Eigenthaler et al., 2018), it is unclear whether ultra-low surface brightness spheroids are nucleated or not, as there may be detected nuclei in our NGFS point-source catalogues for which our photometry failed to detect the surrounding ultra-low surface brightness spheroid. However, given the rel-

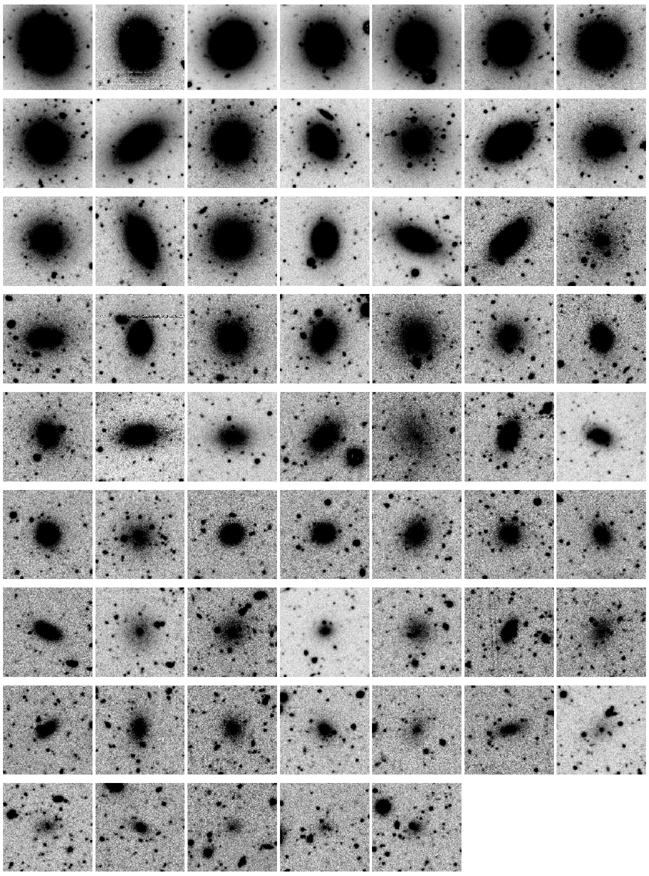

Figure 16: Postage stamp g'-band images for the 61 nucleated dwarfs, sorted by the g'-band luminosity of their spheroid component, which is well approximated by a Sérsic profile (see Eigenthaler et al., 2018). Each image has $200{\times}200\,\mathrm{pix}^2$, corresponding to $5.1{\times}5.1\,\mathrm{kpc}^2$ at the Fornax distance.

atively faint point-source detection limit, we have a strong indication that for the sample of detected low surface brightness dwarf galaxy spheroids in Fornax, the nucleation stops at a well-defined galaxy luminosity ($M_{g'} \simeq -10\,\mathrm{mag}$), corresponding to a galaxy stellar mass of $\log \mathcal{M}_\star \approx 6.4$ (Eigenthaler et al., 2018).

4.2.4 *Morphological decomposition of nucleus and spheroid*

Nuclei studies are affected by the host galaxy luminosity, and, therefore, it is necessary to subtract the galaxy spheroid light in order to study their intrinsic properties. To accomplish this, we have developed an iterative approach to surface brightness profile fitting of dwarf galaxies using GALFIT (v3.0.5; Peng et al., 2002) and Sérsic models in the $u'g'i'$ bands (for more details, see Eigenthaler et al., 2018) and in the JK_s bands. The process to fit the light of a nucleated dwarf requires more iterations to achieve the best residual image, where the nucleus and spheroid are clearly separated. The procedure to fit dwarf galaxies is as follows: *i)* a cutout image centered in the dwarf galaxy is created with size of $105''{\times}105''$(10.2 kpc ×10.2 kpc); *ii)* a mask image is created to cover all the sources around the dwarf, thus, creating a "dwarf-only" image; *iii)* GALFIT is run over the cutout image using a PSF model (created with PSFEX) and the mask. If the nucleus is present, a compact stellar object is left at or near the

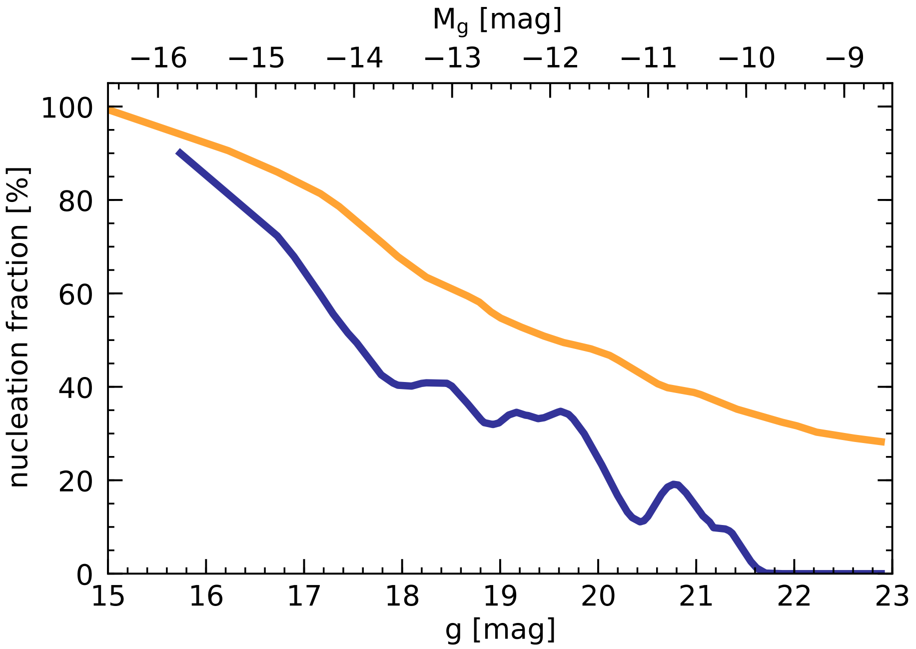

Figure 17: Nucleation fraction (f_{nuc}) of Fornax dwarfs as a function of g'-band galaxy luminosity. The orange line shows the cumulative distribution ($f_{nuc}[< g']$), while the blue curve illustrates the differential relation ($\Delta f_{nuc}/\Delta g'$).

dwarf galaxy center; *iv)* the residual image is used to construct a new mask with the nucleus included; *v)* the steps from *ii)* to *iv)* are repeated at least three times to obtain the best nucleus-spheroid decomposition, leaving a residual image including the nucleus only. Examples of the galaxy fitting process for two dwarf galaxies with different spheroid surface brightness levels and ellipticities are shown in Figure 18. The dwarf galaxy images in the $u'g'i'$ filters are shown in the top-row panels, while the bottom-row panels show the corresponding residual images after the subtraction of the spheroid component. The nucleus of each dwarf is clearly visible in the center of each residual image. In several cases, other compact objects are found near the nucleus, which could be potential satellite globular clusters. The analysis of the nucleus neighborhood and its constituent stellar populations will be presented in a forthcoming paper (Ordenes-Briceño et al., *in prep.*).

4.2.5 *Photometry*

After the spheroid-nucleus fitting procedure we run SE with the corresponding PSF model and generate a catalog with the PSF photometry in all filters for each nucleus. From the 61 dwarf galaxies (see Fig. 16), 60 nuclei remain with reliable i'-band, 59 with g'-band, 28 with u'- and K_s-band photometry, 43 have good J-band. The reasons for this inhomogeneity are partially or non-overlapping DECam and VISTA field of views, bad S/N and/or stacking in that area due to small overlap of the individual images, saturated or simply too faint nuclei. Photometry in $u'g'i'JK_s$ is available for 28 nuclei. Table 6 shows the coordinates, photometry, and stellar masses for the 61 nuclei. The photometry is corrected for foreground Galactic extinction with values taken from the latest Schlafly & Finkbeiner (2011) recalibration of the Schlegel et al. (1998) dust reddening maps. Reddening values for the different filters are calculated assuming the Fitzpatrick (1999) reddening law with $R_V = 3.1$. The average foreground extinction towards the central region of Fornax measured according to the brightest galaxies, i.e. $A_u = 0.056$, $A_g = 0.043$, $A_i = 0.022$, $A_J = 0.009$, $A_{K_s} = 0.004$.

4.3 RESULTS

4.3.1 *Color-magnitude and color-color diagrams*

Figure 19 illustrates the color-magnitude diagrams (CMDs) in the filter combinations $(u'-i')_0$, $(u'-g')_0$ and $(g'-i')$ vs. g'_0. The nuclei of this work are shown as red circles and their host galaxy spheroid components as orange squares. For comparison, we plot also radial-velocity confirmed compact stellar systems (CSSs, i.e. GCs and UCDs) near the cD galaxy, NGC 1399 from the clean compilation catalog in Wittmann et al. (2016) as blue symbols.

The nuclei occupy the bluest parts of the CSS distribution in all three colors with mean values $\langle (u'-i')_{0,\mathrm{nuc}} \rangle = 1.71 \pm 0.03$, $\langle (u'-g')_{0,\mathrm{nuc}} \rangle = 1.02 \pm 0.03$, $\langle (g'-i')_{0,\mathrm{nuc}} \rangle = 0.73 \pm 0.03$ compared to CSSs that cover a significantly broader range of colors with mean values $\langle (u'-i')_{0,\mathrm{CSSs}} \rangle = 2.15 \pm 0.02$, $\langle (u'-g')_{0,\mathrm{CSSs}} \rangle = 1.28 \pm 0.01$, $\langle (g'-i')_{0,\mathrm{CSSs}} \rangle = 0.87 \pm 0.01$. The broader distribution for CSSs and their extension to redder colors is mainly due to their larger spread in metal content reaching super-solar values (e.g. Kissler-Patig et al., 1998). On the other hand, both samples have similar luminosity distributions. One of the key findings here is that the NGFS nuclei show a flat color-magnitude relation (CMR). Whether this is due to no significant changes in the stellar population content as a function of stellar mass will be discussed below. We point out that this is opposite to other results from studies focused on nuclei in the brighter nucleated dwarf galaxy regime, where a CMR for nuclei was found in the magnitude range $-16 \geqslant M_B \geqslant -18$ mag, while for nucleated galaxies brighter than $M_B \simeq -18$ mag the relation becomes flatter again (Côté et al., 2006; Turner et al., 2012; Spengler et al., 2017).

In comparison to the nuclei, the spheroid components of their host galaxies show a shallow but measurable CMR with the spheroid colors becoming redder for brighter systems. Table 1 summarizes the numerical properties of the weighted linear least-square fits to the CMR of nuclei and spheroids in various filter combinations. The CMR of the red-sequence galaxies (including dwarfs) in Virgo and Fornax was recently shown to become flatter going from brightest galaxies towards the faint dwarf luminosity regime (Roediger et al., 2017; Eigenthaler et al., 2018). The CMR is usually interpreted as a mass-metallicity relation (MZR) due to deeper potential wells retaining more metals produced by stars during the secular evolution of the galaxy compared to their less massive counterparts (e.g. Kodama & Arimoto, 1997; Tremonti et al., 2004; Kewley & Ellison, 2008; Torrey et al., 2017, and references therein). In relation to the flat CMR of the nuclei we find at the overlap luminosity of $M_{g'} \simeq -11.0$ mag an offset of $\delta(u'-i')_0 \approx 0.2$ and $\delta(u'-g')_0 \approx 0.31$, but a relatively small offset in the optical color of $\delta(g'-i')_0 \approx 0.13$. These color offsets have implications for the differences in stellar population contents between nuclei and the surrounding galaxy spheroids and provide constraints for the formation mechanisms of galaxy nuclei and the build-up of galaxies and CSSs in galaxy clusters. We will come back to this point in the discussion section.

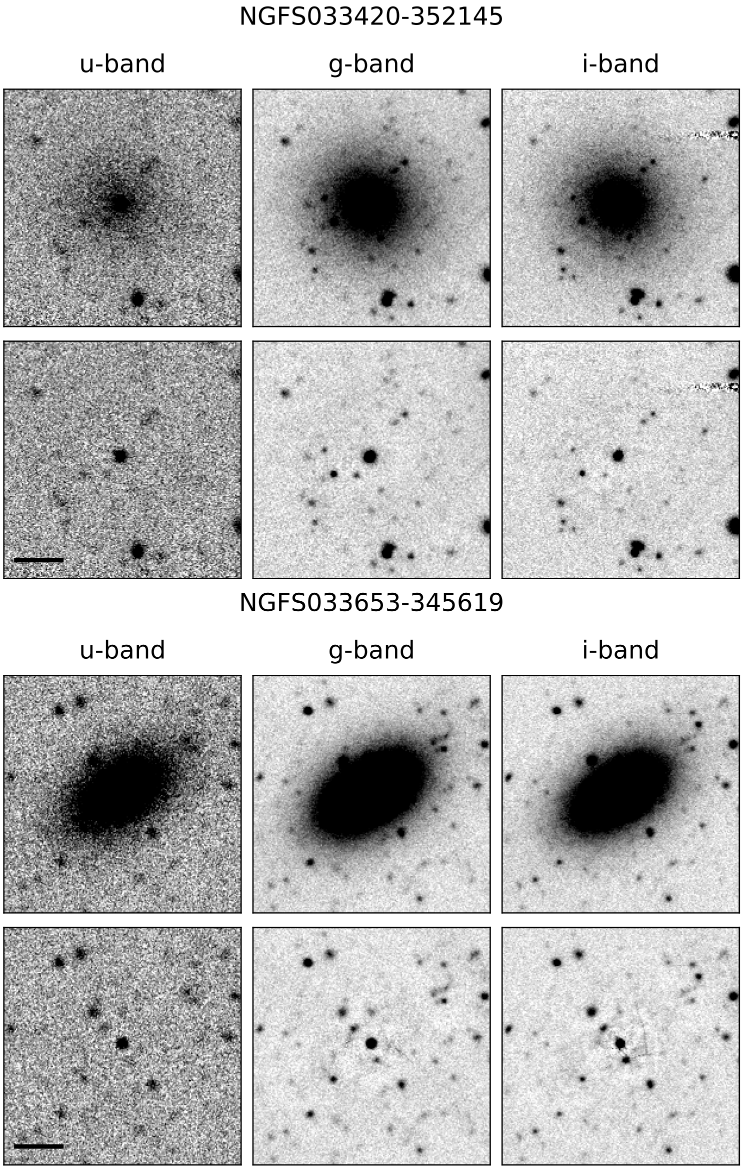

Figure 18: Ilustration of the galaxy fitting for two dwarf galaxies in the three optical bands, u′g′i′ from left to right, respectively. The top rows show the original image and the bottom rows show the best residual images (GALAXY – MODEL), where the nuclear star cluster is deliberately left in the center, and is visible in all filters. A scale bar (solid line) is shown at the bottom left image corresponding to $10.3'' \hat{=} 1$ kpc.

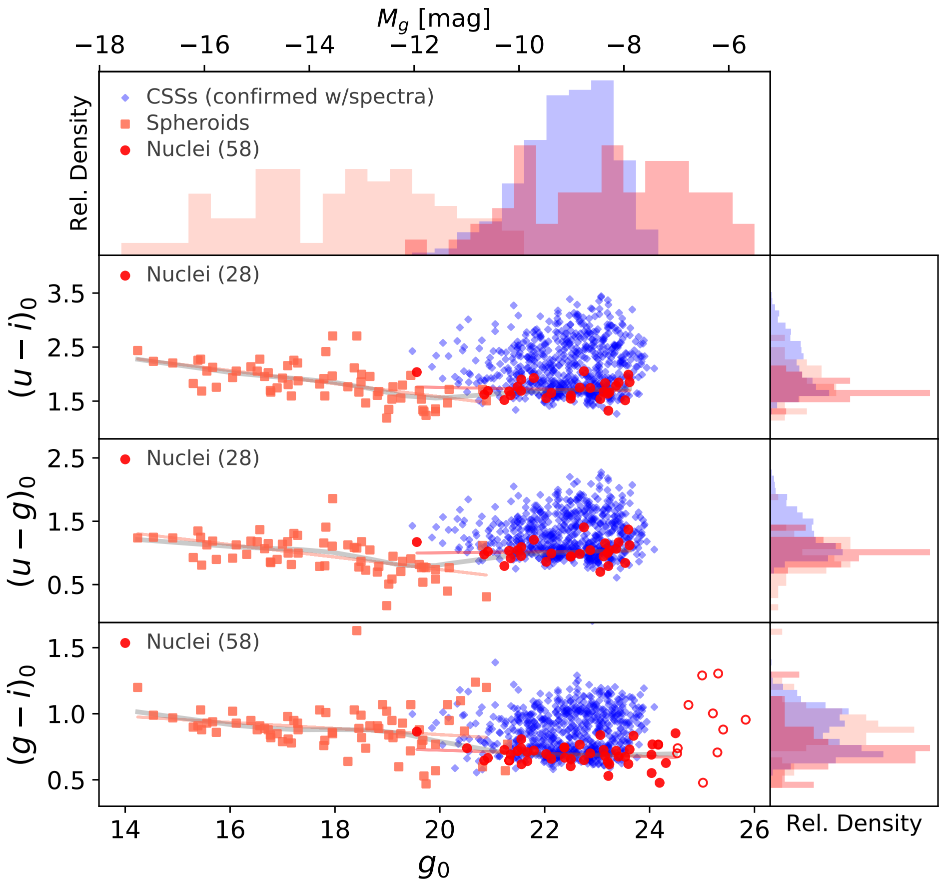

Figure 19: Color-magnitude diagrams for the NGFS sample nuclei shown as red circles. Blue diamonds are CSSs that were confirmed by radial velocities, taken from Wittmann et al. (2016), and orange squares mark the spheroid colors and luminosities of the host dwarf galaxies in which the nuclei of our sample were found. Linear relations show the weighted least-square fits to the nuclei and spheroid color-magnitude relations (see text for details), while the grey curve is a LOWESS fit to the combined nuclei+spheroid sample.

Table 1: Nucleus and spheroid color-magnitude relations

Linear wLSQ fits	r	p	σ
$(u'-i')_{\rm nuc} = -0.017\,g' + 2.094$	−0.103	0.602	0.032
$(u'-i')_{\rm sph} = -0.121\,g' + 4.008$	−0.582	$8.511 \cdot 10^{-7}$	0.022
$(u'-g')_{\rm nuc} = +0.008\,g' + 0.848$	+0.050	0.800	0.030
$(u'-g')_{\rm sph} = -0.098\,g' + 2.704$	−0.560	$2.744 \cdot 10^{-6}$	0.019
$(g'-i')_{\rm nuc} = -0.012\,g' + 0.969$	−0.175	0.267	0.011
$(g'-i')_{\rm sph} = -0.023\,g' + 1.303$	−0.229	0.076	0.013

The left column shows the weighted least-square fits for nuclei and spheroids in various filter combinations (see Fig. 19), the second column gives the correlation coefficient (r) and the next the p-value for the hypothesis that the CMR has zero slope, while the last column is the standard error of the gradient. The relations for the spheroids are valid in the range $-18 \leqslant g' \leqslant -10.5$, while the corresponding relations for the nuclei are valid in the range $-11 \leqslant g' \leqslant -7.5$ mag.

Figure 20 shows two color-color diagrams, i.e., $(u'-g')_0$ vs. $(g'-i')_0$ or $u'g'i'$ (top panel) and $(u'-i')_0$ vs $(i'-K_s)_0$ or $u'i'K_s$ (bottom panel), where gray dots represent all the detected NGFS sources for which PSF-based photometry could be obtained in the central region of Fornax (Fig. 15). These color-color diagrams, in particular the $u'i'K_s$ plane with its broad SED coverage, are powerful tools to distinguish among different object types, such as foreground stars, background galaxies and CSSs (Muñoz et al., 2014). The upper-left cloud of objects in both diagrams shows the location of red-shifted background galaxies, while in the lower parts of the $u'g'i'$ diagram, a tight sequence holds for individual foreground stars and star clusters, but in the $u'i'K_s$ diagram even these objects are separated into two sequences. Here the central sequence marks the star cluster sequence, as it is shown by the confirmed CSSs (blue symbols) from the very central parts of the Fornax cluster. Our nuclei sample (red filled circles) is located in the same color-color region and confined to the bluest parts of the star cluster sequence, as was already seen in the color-magnitude diagrams (see Fig. 19). The analysis of the complete star-cluster photometry catalog in the central Fornax region with the new GCs and UCDs candidates will be reported in a future work. In the subsequent analysis we focus on the dwarf galaxy nuclei.

4.3.2 *Stellar mass estimates*

Stellar masses for our NGFS nuclei are estimated using a χ^2 minimization approach to fit stellar population synthesis models to the photometric information from the NGFS filters $g'i'JK_s$, $g'i'J'$, or $g'i'$, according to the photometry available for each nucleus. We exclude the u'-band photometry due to its sensitivity to very young stellar populations with low mass fractions and/or potential AGN emission components, if any. The mass errors are estimated with Monte-Carlo simulations by drawing one thousand random values from a normal probability distribution function with a mean corresponding to the observed magnitude and a standard deviation equal to the magnitude error, and propagating these values through the following calculations. SSP models from Bruzual & Charlot (2003, hereafter BC03) with the 2016 update[2], MILES atlas (Sánchez-Blázquez et al., 2006), and an initial mass function (IMF) from Kroupa (2001) are used to estimate luminosity weighted stellar masses. We consider metallicities in the range $0.0001 \leqslant Z/Z_\odot \leqslant 0.5$ and ages older than 1 Gyr to avoid the stochasticity typically found at younger ages (e.g. Cerviño et al., 2002; Cerviño & Luridiana, 2004; Fouesneau & Lançon , 2010). The stellar mass distribution of our nuclei covers the range $\log(\mathcal{M}_\star/M_\odot) = 4.8-7.3$ with uncertainties ranging from ~8% to 43% and a mean uncertainty of $\sim 19\%$, propagated from the photometric errors. We point out that there are systematic uncertainties of the mass estimates related to the choice of population synthesis models and the set of filters used to compute the mass-to-light conversion (see Powalka et al., 2016a, 2017; Zhang et al., 2017), which for our sample we estimate to be at most ~ 0.2 dex.

The stellar mass distribution for the NGFS nuclei is illustrated in Figure 21, together with the distribution of the confirmed CSSs in the Fornax region, for which we estimate their masses with the same procedure applied to our nuclei, as well as the nucleated NGFS dwarf spheroids [3], for which we use the mass measurements estimated in Eigenthaler et al. (2018), which are based on the parametrizations of the mass-to-light ratios as a function of various colors

---

[2] http://www.bruzual.org/~gbruzual/bc03/Updated_version_2016/

[3] Note that we consider the spheroid mass alone, i.e. the nucleated spheroid mass does not include the nucleus.

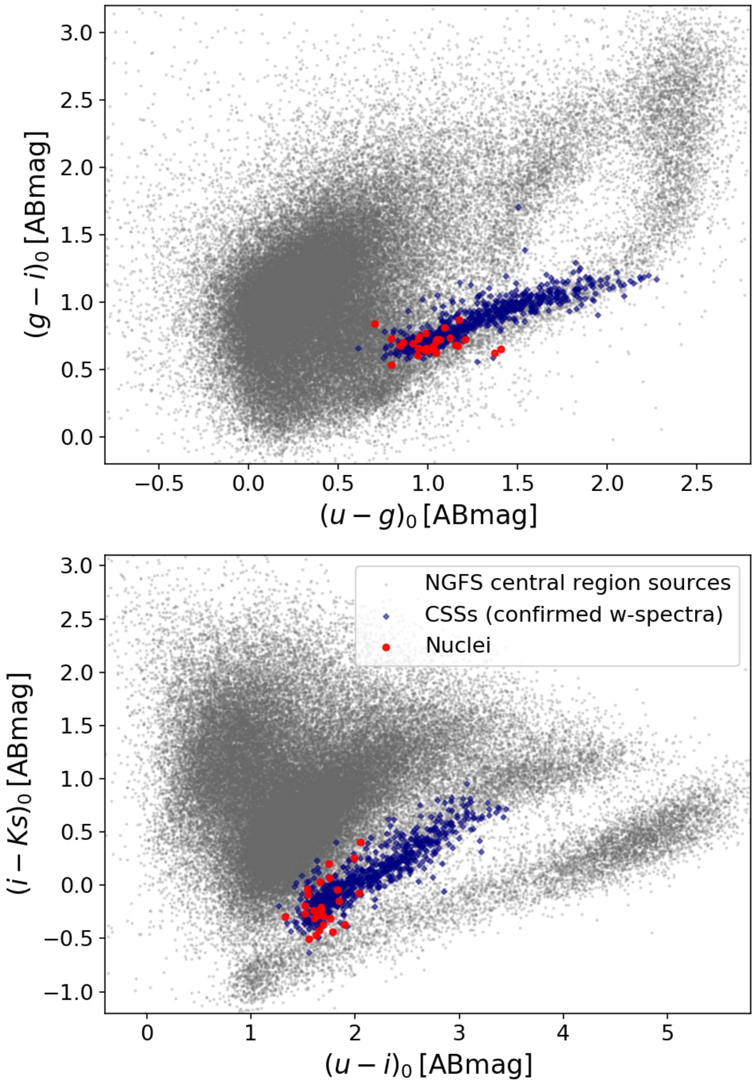

Figure 20: Color-color diagrams, $(u'-g')_0$ vs. $(g'-i')_0$ (top panel) and $(u'-i')_0$ vs. $(i'-K_s)_0$ (bottom panel), showing as gray dots all the NGFS central sources in the $R < R_{vir}/4$ with PSF photometry. The red filled circles represent the nuclei of this work and the blue diamonds show the confirmed CSSs in the surroundings of the cD galaxy NGC 1399. Compact stellar systems such as GCs, UCDs and nuclei lie in a very narrow region in color-color space, which makes the $u'g'i'$ and $u'i'K_s$ diagrams very powerful tools to select CSSs candidates.

given in Bell et al. (2003). We point out that our sample dwarf spheroids do not show any signs of star formation activity and, hence, their optical colors serve as good indicators for their stellar masses (see Zhang et al., 2017, for the numerical accuracy of these conversions). An Epanechnikov-kernel probability density estimate (KDE) is overplotted for each distribution together with its 1-σ uncertainties.

We observe that the mass distributions for the three populations are quite different morphologically and cover different mass ranges. At the low-mass end, this is due to differences in the respective selection functions. The NGFS nuclei sample reaches lower masses than the CSS sample, because the spectroscopic

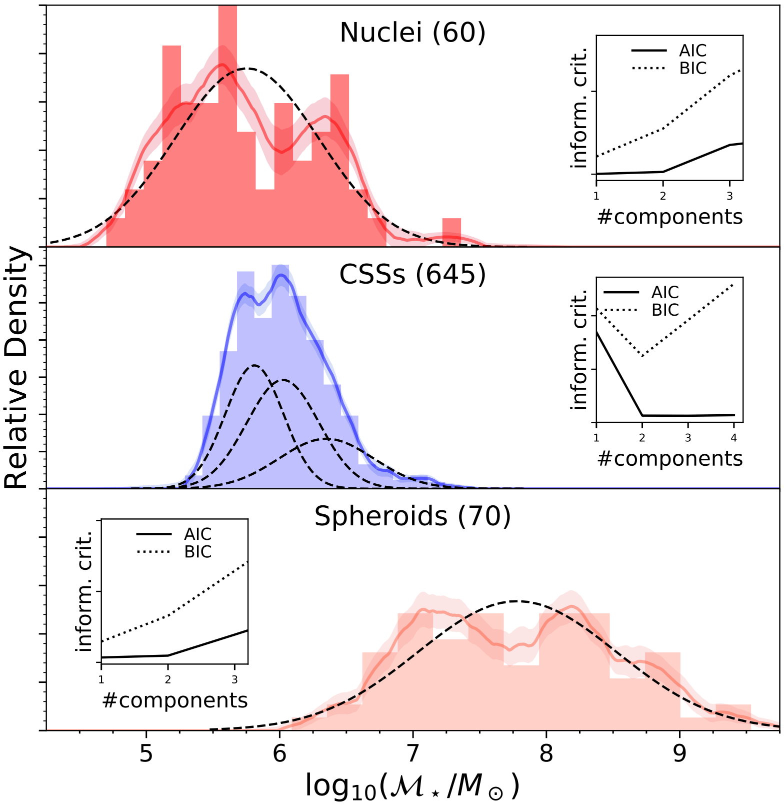

Figure 21: Mass distribution for the NGFS nuclei (top panel), the radial-velocity confirmed CSSs in Fornax (middle panel), and the dwarf spheroids (bottom panel). The probability density distribution for each sample is overplotted using an Epanechnikov-kernel density estimate together with the 1-σ uncertainty ranges. The size of each sample is given in parentheses in the corresponding panel. The inset figures show the Aikake and Schwarz's (Bayesian) information criteria (AIC and BIC, see Ivezić et al., 2014), which define the most likely number of Gaussian components for each distribution; here we use the AIC. The corresponding Gaussians are indicated by the dashed curves.

selection function for the radial-velocity confirmation of CSSs in Fornax has a brighter cut-off (Wittmann et al., 2016) than the NGFS point-source detection limit (see Sect. 4.2.1). The mass distribution of dwarf spheroids is limited at the lower-mass end by the surface brightness detection limit of these systems (see Eigenthaler et al., 2018). The nuclei population spans more than two orders of magnitude in stellar mass and shows a bimodal distribution, for which the peaks are located at $\log(\mathcal{M}_\star/M_\odot) \simeq 5.38$ and ~ 6.25, the latter value is consistent with ultra-compact dwarf (UCD) masses (e.g., Misgeld & Hilker, 2011). Although the AIC marginally prefers one over two components, the Epanechnikov density distribution favors two components. We find that the CSS distribution is formally trimodal[4] with its peaks located at $\log(\mathcal{M}_\star/M_\odot) \simeq 5.81, 6.02$ and

---

[4] We point out that the AIC has a minimum at three components, but the AIC for two components is numerically very close to the formal minimum. In addition, the BIC gives two as the most likely number of components, which indicates that bimodality or trimodality are equally likely representations of the CSS mass distribution.

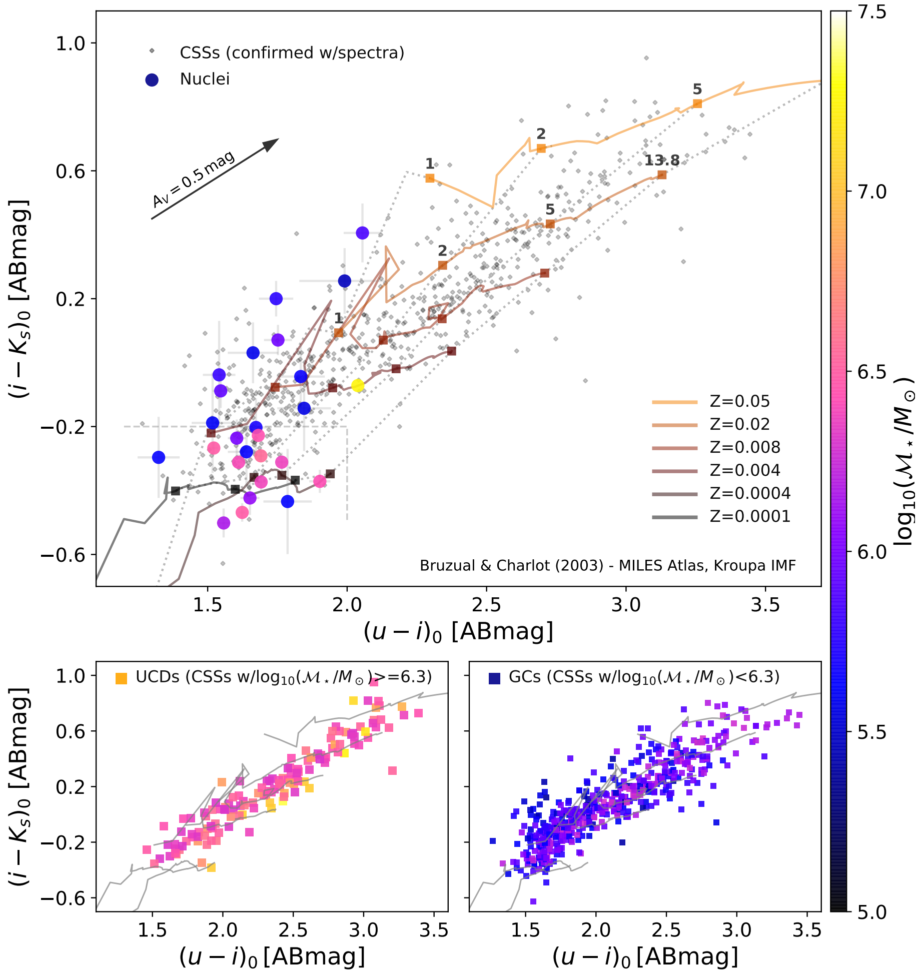

Figure 22: *Top panel:*$(u'-i)_0$ vs. $(i'-K_s)_0$ color-color diagram with SSP models from BC03 using the MILES stellar library and a Kroupa IMF. Iso-metallicity tracks are shown as solid lines, ranging from $Z = 0.0001$ to 0.05 (see legend). Squares mark ages of 1, 2, 5, and 13.8 Gyr on each iso-metallicity track (see labels on the $Z = 0.05$ and $Z_\odot$ track). These points are connected by dotted iso-age lines. Nuclei are color coded using their stellar masses as indicated by the colorbar. The arrow in the top-left corner shows a reddening vector of $A_V = 0.5$ mag. *Bottom panels:* The left and the right panels indicate the color-color relations of UCDs and GCs, respectively. Their stellar masses are color-coded on the same scale as for the top panel. GC stellar masses range from $10^{5.4}$ to $10^{6.3}$ $M_\odot$. UCD stellar masses range from $10^{6.3}$ to $10^{7.5}$ $M_\odot$.

~ 6.35, with the last component extending towards higher masses, reminiscent of UCDs as well. We will not discuss this interesting feature of the Fornax globular cluster mass function in this work, as it requires an in-depth analysis of the sample selection function, but keep our focus on the dwarf galaxy spheroids and nuclei. The dwarf spheroid mass distribution occupies a broad range of more than three magnitudes with a mild, but statistically non-significant bimodality ($\log[\mathcal{M}_\star/M_\odot] \simeq 7.25$ and ~ 8.25), with its single-Gaussian peak at $\log(\mathcal{M}_\star/M_\odot) \simeq 7.8$. To our knowledge this is the first time such hints for multi-modalities in the nucleated spheroid mass and the nucleus mass distribution have been detected. Together they may give us hints at the importance of different formation mechanisms of stellar nuclei.

4.3.3 *Stellar population properties*

Color information in combination with population synthesis model predictions can be used to understand the stellar population properties of the nuclei, such as age, metallicity, and correlations with their mass. The $u'i'K_s$ diagram helps minimize the age-metallicity degeneracy that affects broadband filters. Figure 22 illustrates the $u'i'K_s$ diagram with over-plotted SSP models from BC03, showing iso-metallicity tracks for the range $0.0001 < Z < 0.05$ with equivalent ages of $1, 2, 5$, and $13.8\,\mathrm{Gyr}$. Filled circles stand for NGFS nuclei color-coded by their stellar masses. As in the previous figures, radial-velocity confirmed CSSs are shown for comparison purposes. We observe that the NGFS nuclei occupy approximately the bluer half of the CSSs $u'i'K_s$ spread, which is consistent with sub-solar metallicities ($Z < Z_\odot$) and/or a young stellar age component. This is in line with the measurements of Paudel et al. (2011), who find from spectroscopy of relatively bright Virgo dwarf galaxies ($-18.5 \geqslant M_{r,\mathrm{gal}} \geqslant -15.5$) that their nuclei ($-13.3 \geqslant M_{r,\mathrm{nuc}} \geqslant -10.2$) cover a large range of metallicities from slightly super-solar ($+0.18\,\mathrm{dex}$) to significantly sub-solar ($-1.22\,\mathrm{dex}$) values. However, it is still challenging to disentangle ages and metallicities for stellar systems older than a few Gyr at any metallicity based on photometry alone. The inversion of broadband color information into stellar population parameters is notoriously difficult (Hansson et al., 2012; Powalka et al., 2016a, 2017) and is facing limitations in light of potentially as yet to be understood systematics related to the galaxy cluster environment (Powalka et al., 2016b). Given the previous considerations, we refrain from assigning numerical age and metallicity values to the nuclei, but analyze them in groups.

4.3.3.1 *Bimodality in nucleus stellar population properties*

Although there is no clear mass-color relation, the mass bimodality of our NGFS nuclei is seen as mainly two groups in the $u'i'K_s$ plane, hereafter referred to as groups $\mathcal{A}$ and $\mathcal{B}$, and indicates a bimodality in their stellar population parameters. The nuclei in group $\mathcal{A}$ have stellar masses $\geqslant 10^6\,M_\odot$ and lie in the bluest color-color region of the $u'i'K_s$ plane with $(u'-i')_0 < 2.0\,\mathrm{mag}$ and $(i'-K_s)_0 < -0.2\,\mathrm{mag}$. Nuclei in group $\mathcal{B}$ cover a more extended $u'i'K_s$ color space with redder average colors, i.e., $(i'-K_s)_0 \geqslant -0.2\,\mathrm{mag}$, and comprise objects with stellar masses $\leqslant 10^6\,M_\odot$[5]. The mean masses for the groups are close to the masses of the two peaks in the nuclei stellar mass distribution, but it is worth noticing that from the total sample, 26 nuclei have high-quality $u'i'Ks$ photometry to robustly estimate their color-color distribution. This is mainly the reason for the slightly different peaks between the bimodal mass distribution and the mean masses of the two groups considered here. In any case, it is clear that according to the nucleus mass distribution from Figure 21, there is a bimodality of nuclei which is also reflected in the $u'i'K_s$ diagram and that bimodality correlates with stellar population parameters specific for two nuclei sub-groups.

Assuming SSP-like stellar populations, we observe that our NGFS nuclei in group $\mathcal{A}$ host very metal-poor stellar populations ($Z < 0.0004 = 0.02\,Z_\odot$)

---

[5] One exception in group $\mathcal{A}$ is the massive nucleus in the center of dwarf NGFS034050-354454 with a stellar mass of $\log(\mathcal{M}_\star/M_\odot) \simeq 7.26$ and colors consistent with $Z \simeq 0.004$ and ~3 Gyr (yellow symbol in Fig. 22)

with luminosity-weighted ages older than $\sim 2\,\text{Gyr}$. In contrast, the nuclei in group $\mathcal{B}$ show colors equivalent to metallicities in the range $0.004 < Z < 0.02$ $(0.2 < Z/Z_\odot < 1)$, and ages younger than $\sim 2\,\text{Gyr}$. The reddening vector in Figure 22 illustrates how an intrinsic reddening of $A_V = 0.5\,\text{mag}$, equivalent to $E_{B-V} = 0.16$ for a Milky Way reddening curve, would affect the $u'i'K_s$ color-color space. The reddening direction points towards increasing metallicity values, but does not affect the age significantly – if anything, it pushes the colors towards older equivalent ages. Alternatively, chemical abundance ratios different from the ones assumed in the solar-scaled BC03 models may bias the age and metallicity estimates. Evidence that this is indeed the case comes from the study of Paudel et al. (2010) who found super-solar $[\alpha/\text{Fe}]$ ratios in nuclei of Virgo dwarfs. In their photometric study of compact stellar systems in the Virgo cluster, Powalka et al. (2016b) found intriguing offsets in multi-color relations pointing towards younger ages of some Virgo GCs. Although test showed the influence of increased $[\alpha/\text{Fe}]$ on colors, the team found that typical α-element enhancements of Local Group GCs were producing too small color offsets to match the observations at old ages. We, therefore, tentatively conclude that the younger ages of the nuclei in group $\mathcal{B}$ are not primarily due to intrinsic reddening and $[\alpha/\text{Fe}]$ variations, but likely due to genuinely younger and more metal-rich stellar populations, which lie in terms of stellar mass in the low-mass mode of the nucleus stellar-mass bimodality. Overall, these results point to different formation histories and perhaps different mechanisms of nucleus formation between the two groups. We will come back to this in the discussion section.

4.3.3.2 *Comparison of nuclei with confirmed UCDs*

The nuclei masses are shown in color-code in the $u'i'K_s$ color-color diagram in Figure 22 (top panel) and are compared to the corresponding stellar mass distribution of radial-velocity confirmed CSSs in Fornax (bottom panels). From this CSS sample, UCDs are selected with a stellar-mass cut so that $\log \mathcal{M}_\star/M_\odot(\text{UCD}) \geqslant 6.3$ (e.g. Taylor et al., 2010; Mieske et al., 2013), avoiding any restriction in color (i.e. metallicity), while GCs are selected with $\log \mathcal{M}_\star/M_\odot(\text{GC}) < 6.3$ from the same parent CSS sample. The final UCD sample exhibits stellar masses within the range $\log(\mathcal{M}_\star/M_\odot) = 6.3-7.4$, whereas the GCs cover the mass range $\log(\mathcal{M}_\star/M_\odot) = 5.4-6.3$, which is limited at the low-mass end by the spectroscopic selection function of the CSS sample (Wittmann et al., 2016). The majority of our NGFS nuclei are less massive than $\log(\mathcal{M}_\star/M_\odot) \simeq 6.8$ with the exception of three objects with a stellar mass of $\log(\mathcal{M}_\star/M_\odot) \simeq 7.2-7.3$ (see Fig. 21), only one of which has a $u'i'K_s$ color and is plotted in Figure 22.

Comparing the stellar masses and stellar population parameters of nuclei with those of UCDs reveals that the members of the low-mass mode of our sample nuclei cannot be the progenitors of Fornax UCDs. These dwarf nuclei have simply too low masses to be considered a parental population. However, nuclei that are members of the high-mass mode could potentially be considered progenitors of metal-poor Fornax UCDs. Considering that the initial mass of UCD progenitors may be even higher than their current mass and given their likely mass evolution, as suggested in some UCD formation scenarios that involve stripping (e.g. Zinnecker et al., 1988; Bassino et al., 1994; Bekki et al., 2003; Goerdt et al., 2008; Pfeffer & Baumgardt, 2013), even this evolutionary connection may be questionable given the similar present-day masses of high-mass dwarf nuclei and metal-poor UCDs. This may not be the case for the most massive dwarf nucleus in our sample, NGFS034050-354454n, which qualifies as a potential intermediate-metallicity Fornax UCD seed, even after 90% of its present-day mass is lost. In any case, our data suggest that the progenitors of the massive, metal-rich UCDs in Fornax have long been destroyed and have no present-day counterparts in dwarf galaxy nuclei. This is consistent with previous spectroscopic studies (Evstigneeva et al., 2007; Francis et al., 2012).

4.3.3.3 *Comparison of nuclei with confirmed GCs*

The picture is different when we compare the properties of nuclei and GCs. Essentially all of our nuclei can be considered potential future GCs, once the spheroid envelopes surrounding them are stripped during their dynamical evolution within the Fornax cluster (Goerdt et al., 2008; Bekki et al., 2003; Smith et al., 2013, 2015). Such potential nuclei remnants may become future members of the Fornax GC system. The younger stellar ages of the low-mass mode nuclei indicate extended star formation histories and, therefore, prolonged chemical enrichment processes that may lead to signficant abundance spreads, especially in Fe-peak elements. Such future GCs could be clearly identified with the next-generation of 30m class telescopes via their spreads in stellar iron abundances, something that has been measured in numerous Milky Way star clusters (e.g., Willman & Strader, 2012). Alternatively, high-spatial resolution imaging allows one to identify remnant nuclei candidates in the half-light radius vs. luminosity parameter space, which has been done for the Local Group star clusters (Ma et al., 2006). Furthermore, the characteristic age-metallicity relation found for a subset of Galactic GCs (VandenBerg et al., 2013; Leaman et al., 2013) is consistent with our observation of decreasing stellar ages in more metal-rich nuclei. This suggests that at least the Galactic GC sub-population with a significant age-metallicity relation could have in part their origins in the cores of nucleated dwarf galaxies (see also Marín-Franch et al., 2009; Forbes & Bridges, 2010; Dotter et al., 2011; de Boer et al., 2015).

4.3.4 *Differences between nuclei and galaxy spheroids*

The color difference in various filter combinations between the nucleus and its host galaxy spheroid is shown in Figure 23 as a function of nucleus luminosity ($g_{0,\mathrm{nuc}}$) and galaxy spheroid luminosity ($g_{0,\mathrm{sph}}$). The nucleus-to-galaxy mass ratio is encoded by the symbol color and has a range from $0.1\% - 10\%$. The color differences are more correlated with the spheroid light than with the nucleus luminosity, which implies that the mechanisms that lead to the color offsets must be acting more on galaxy scales rather than nucleus scales. One can think of processes that are correlated with the total dwarf galaxy mass which, for instance, lead to more massive galaxies holding on more efficiently and longer to their gas supply than their small-mass counterparts; this is especially true in the galaxy cluster environment.

We find relations for the color differences $\Delta(u'-i')_0$ and $\Delta(u'-g')_0$ vs. $g_{0,\mathrm{nuc}}$ and $g_{0,\mathrm{sph}}$. These near-UV+optical colors map a broader SED range which is more sensitive to changes in stellar population parameters, while a shallower trend in $\Delta(g'-i')_0$ is consistent with the narrower SED coverage. This is mainly due to the enhanced sensitivity of the u-band to the Balmer break flux compared to the redder filters. Bright nuclei ($M_{g,\mathrm{nuc}} \lesssim -10$), on average, $\Delta(u'-i')_0 = -0.35$, $\Delta(u'-g')_0 = -0.15$, and $\Delta(g'-i')_0 = -0.2$ mag bluer than their host galaxy, indicative of younger and/or more metal-poor stellar populations (see Fig. 22). According to the BC03 models, these color differences correspond consistently to an age difference of $\Delta t/t \simeq -0.8$ at old absolute ages (~ 13 Gyr) and low metallicities $Z = 0.0001 - 0.004$ ([Fe/H] $\simeq -2.3$ to

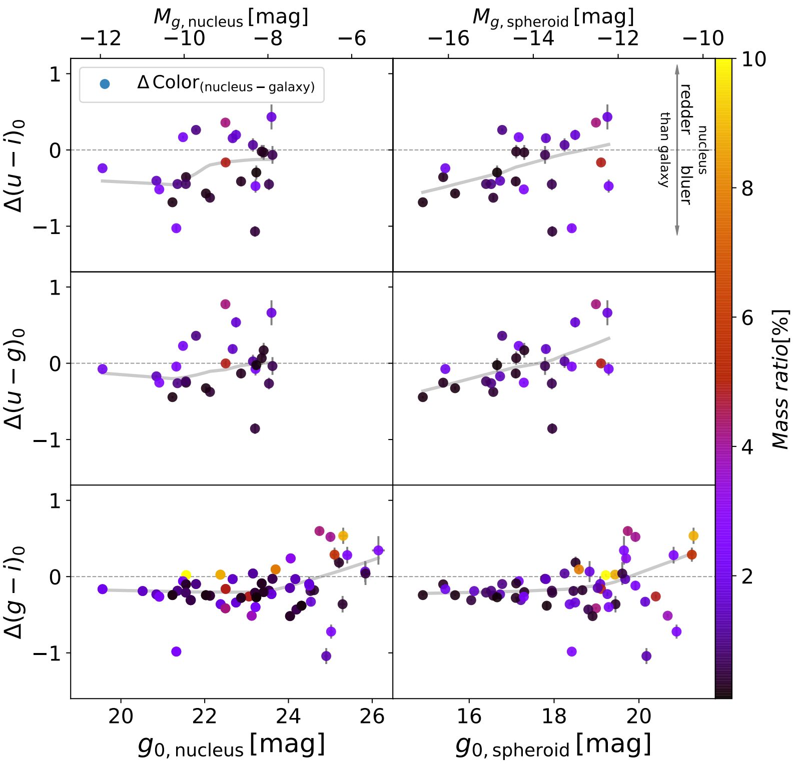

Figure 23: Color differences between the nucleus and its host dwarf galaxy spheroid in $\Delta(u'-i')_0$, $\Delta(u'-g')_0$, and $\Delta(g'-i')_0$ (top to bottom panels) vs. $g_{0,\mathrm{nucleus}}$ (right panels) and vs. $g_{0,\mathrm{spheroid}}$ (left panels). Color code of the symbols shows the corresponding nucleus-to-galaxy mass ratio encoded by the vertical colorbar. The gray curves represent LOWESS fits to the data. The arrows in the top panel show the directions in which the nucleus becomes redder or bluer than its host galaxy. Note that photometric errors are for most data points smaller than the symbol size.

-1.6 dex), and an age difference of $\Delta t/t \simeq -0.5$ at young absolute ages (~ 2 Gyr) and solar metallicities. It can also be attributed to a metallicity difference of $\Delta[\mathrm{Fe/H}] \approx -1$ dex at old absolute ages (~ 13 Gyr) and intermediate-to-low metallicities ($[\mathrm{Fe/H}] \simeq -0.5$ to -1.6 dex) and to $\Delta[\mathrm{Fe/H}] \approx -0.3$ dex at solar metallicities, respectively. These metallicity differences change at young absolute ages (~ 2 Gyr) to $\Delta[\mathrm{Fe/H}] \approx -1.3$ dex at intermediate to low metallicities and $\Delta[\mathrm{Fe/H}] \approx -0.6$ dex at solar metallicities, respectively. Similar color differences have been reported in previous studies (see Lotz et al., 2004; Côté et al., 2006; Turner et al., 2012). However, owing the depth of the present data, we find that there is a transition point around $g_{0,\mathrm{nuc}} \approx 24$ mag ($M_{g,\mathrm{nuc}} \approx -7.5$) or $g_{0,\mathrm{sph}} \approx 19$ mag ($M_{g,\mathrm{sph}} \approx -12.5$), where the average $(g'-i')_0$ offset becomes insignificant at the expense of an increasing galaxy-to-nucleus color variance. This feature is noticeable in $(u'-i')_0$ and $(u'-g')_0$ colors already at brighter nucleus luminosities around $g_{0,\mathrm{nuc}} \approx 22$ mag ($M_{g,\mathrm{nuc}} \approx -9.5$) or $g_{0,\mathrm{sph}} \approx 17.5$ mag ($M_{g,\mathrm{sph}} \approx -14$).

Another important feature is the steep relation seen in the $\Delta(u'-i')_0$ and $\Delta(u'-g')_0$ colors vs. $g_{0,\mathrm{sph}}$: here we observe that low nucleus-to-galaxy mass ratios ($< 2\%$) only occur up to a magnitude $g_{0,\mathrm{sph}} \approx 17.5$ mag ($M_{g,\mathrm{sph}} \approx -14$) where we find almost exclusively blue nuclei, while for fainter dwarfs we have a mixture of nucleus-galaxy color differences and nucleus-to-galaxy mass ratios. We note that all the trends described here are not due to photometric uncertainties, but stellar population properties that vary substantially from nucleus to nucleus.

These results paint the following picture: as a dwarf nucleus begins to grow, starting with a low nucleus-to-galaxy mass ratio, its stellar population content is dominated by more metal-poor and/or younger stars than the typical star in its host spheroid. Nuclei with higher nucleus-to-galaxy mass ratios must have either reached higher metal enrichment at similar ages or were formed earlier with enough time for their stellar populations to evolve and redden sufficiently. A distinction between these two scenarios could easily be made using spectroscopically determined [α/Fe] ratios, which are indicators of star formation timescales (e.g., Matteucci & Greggio, 1986), allowing us to discern between prolonged star formation histories vs. short and early star-formation bursts (e.g., Tsujimoto et al., 1995; Matteucci & Recchi, 2001), which may be driven by the environment (e.g., Thomas et al., 2005; Puzia et al., 2005).

4.4 DISCUSSION

4.4.1 *Formation mechanisms*

The astrophysical mechanisms responsible for the differences in stellar population content of the galaxy spheroid and the nucleus are numerous, but can be categorized to be mainly due to two processes: *i)* the inflow of gas into the nuclear regions which triggers star formation processes (e.g., van den Bergh, 1986; Antonini et al., 2015), and *ii)* the accretion of GCs into the galaxy central regions via dynamical friction (e.g., Tremaine et al., 1975; Lotz et al., 2001). However, the relatively shallow dwarf galaxy potentials can be easily affected by environmental and secular processes. Secular processes such as stellar winds, supernova (SN) and black-hole (BH) feedback can affect the nucleus formation and evolution, for instance, by helping with gas supply to the nuclear regions through stellar winds from newly formed stars (radiation drag, Kawakatu & Umemura, 2002) or slowing down the nucleus growth due to SN-driven winds contributing to the mass loss in dwarf galaxies and likely changing the dynamical friction timescales for orbiting star clusters to sink to the center (Lotz et al., 2001), or dynamically heating the nuclear cluster due to a massive central BH (Antonini et al., 2015). Whether the gas comes from disk instabilities, galaxy mergers (with some gas content) or primordial gas, the dynamical timescales for the gas to sink down to the nuclear reservoir depend on the size of the galaxy, being longer with increasing galaxy size and, thus, mass (Eigenthaler et al., 2018). Therefore, in more massive galaxies the inflowing material would have more time to fragment and undergo star-formation, leaving smoother and relatively steeper stellar population gradients imprinted in the spheroid component. Consequently, the spheroids of low-mass dwarfs would have smaller and more stochastic population gradients due to gas and/or GCs having shorter sink-in timescales, leading to a more stochastic color difference between nucleus and host galaxy than for more massive dwarfs. This is exactly what we observe in Figure 23 for $M_{g,\mathrm{sph}} \leqslant -14$ and $M_{g,\mathrm{nuc}} \leqslant -9.5$ mag.

4.4.2 *Scaling relations*

One of the physical scaling relations that nuclei follow is the nucleus-to-galaxy mass relation (see Fig. 24) which has been shown to hold for bright ETGs (e.g., Spengler et al., 2017). To test whether such a relation applies to our dwarf galaxy sample we use the masses derived for the nuclei in this work (Sect. 4.3.2) and their spheroid masses from Eigenthaler et al. (2018). In order to compare our sample with nucleated galaxies at higher masses and those located in different environments, we make use of literature data. For the bright nucleated galaxies in the Fornax cluster sample from ACSFCS (Turner et al., 2012), the corresponding nucleus masses are estimated with the same method described in Section 4.3.2 using their g, z photometry. For their host galaxies the B, V magnitudes were obtained from HyperLEDA and together with the relations from Bell et al. (2003) we estimate the masses in a self-consistent procedure as for the NGFS dwarf galaxies (Eigenthaler et al., 2018). For the Virgo cluster, we use the masses estimated in the Virgo Redux work (Spengler et al., 2017) for nuclei and hosts. In addition, we include the results of recent studies by Nguyen et al. (2017, 2018) for field ETGs to estimate the dynamical mass for their central BH and their nuclear star cluster. In Nguyen et al. (2017), the central SMBH dynamical mass for NGC 404 was estimated to be $1.5 \times 10^5 M_\odot$. In Nguyen et al. (2018) four field ETGs were studied. Three of them were found to contain BHs with masses of $2.5 \times 10^6 M_\odot$ (M32), $8.8 \times 10^5 M_\odot$ (NGC 5102) and $4.7 \times 10^5 M_\odot$ (NGC 5206). The catalog of nucleated late-type galaxies (LTGs) comes from Georgiev et al. (2016) with 228 moderately inclined spiral galaxies with morphological type code $T \geqslant 3$ or later than Sb at distances < 40 Mpc. Nuclei from Local Volume (LV) dwarf irregular (dIrr) and early-type dwarf galaxies come from Georgiev et al. (2009). For the Milky Way and Andromeda nuclear star clusters we use $\mathcal{M}_{\rm MW,NSC} = (2.5 \pm 0.4) \times 10^7 M_\odot$ from Schödel et al. (2014) and $\mathcal{M}_{\rm M31,NSC} = (3.5 \pm 0.8) \times 10^7 M_\odot$ from Kormendy & Ho (2013).

The relation between nucleus and host galaxy stellar mass is shown in Figure 24 (top panel), where we see a clear mass correlation between nuclei and their host galaxies across the entire galaxy mass range ($6 \leqslant \log[\mathcal{M}_*/M_\odot] \leqslant 11$). For ETGs, this relation is shallower for lower-mass galaxies compared to the massive galaxy regime with a break in slope around $\log(\mathcal{M}_*/M_\odot) \simeq 9.7$. The relation for dwarf galaxies scales as $\eta_n \propto \mathcal{M}_{\rm gal}^{-0.5}$, while for massive ellipticals it follows a much steeper relation, $\eta_n \propto \mathcal{M}_{\rm gal}^{4}$. The discussion of the astrophysical reasons for these two regimes go far beyond the scope of this paper.

Compared to ETGs, there is a higher dispersion and a less inclined slope for the LTG relation, which is more noticeable in the massive galaxy range, as was already pointed out by Georgiev et al. (2016). This indicates that the nuclei in LTGs are on average less massive at a fixed host galaxy mass than nuclei in ETGs. The weighted linear and polynomial least-square fits are shown in Table 2. Based on considerations that the mechanisms, that are responsible for the build-up of the central massive objects are similar for nuclei and massive BHs, previous studies have discussed their possible evolutionary connection (e.g., Ferrarese et al., 2006; Neumayer & Walcher, 2012). For the purpose of comparison, we illustrate the black-hole-galaxy mass relation from McConnell & Ma (2013) with its 1σ and 3σ uncertainty limits. This relation was obtained from fitting the compilation of 35 ETGs with dynamical measurements of the bulge stellar mass, with mass range of $10^9 - 10^{12} M_\odot$. Their sample is well populated for bulges more massive than $2 \times 10^{10} M_\odot$ (see their Figure 3). Assuming that we can extrapolate to lower bulge masses, we see in Figure 24 that the scaling relation for BHs and their ETG hosts is similar to the relation between nuclei and their host galaxy mass down to $10^9 M_\odot$. For galaxies with lower masses the nucleus-to-galaxy mass relation becomes flatter.

The mass ratio between nucleus and its host galaxy ($\eta_n = \mathcal{M}_{\rm nuc}/\mathcal{M}_{\rm gal}$) as a function of galaxy mass is shown at the bottom panel of Figure 24. We find a

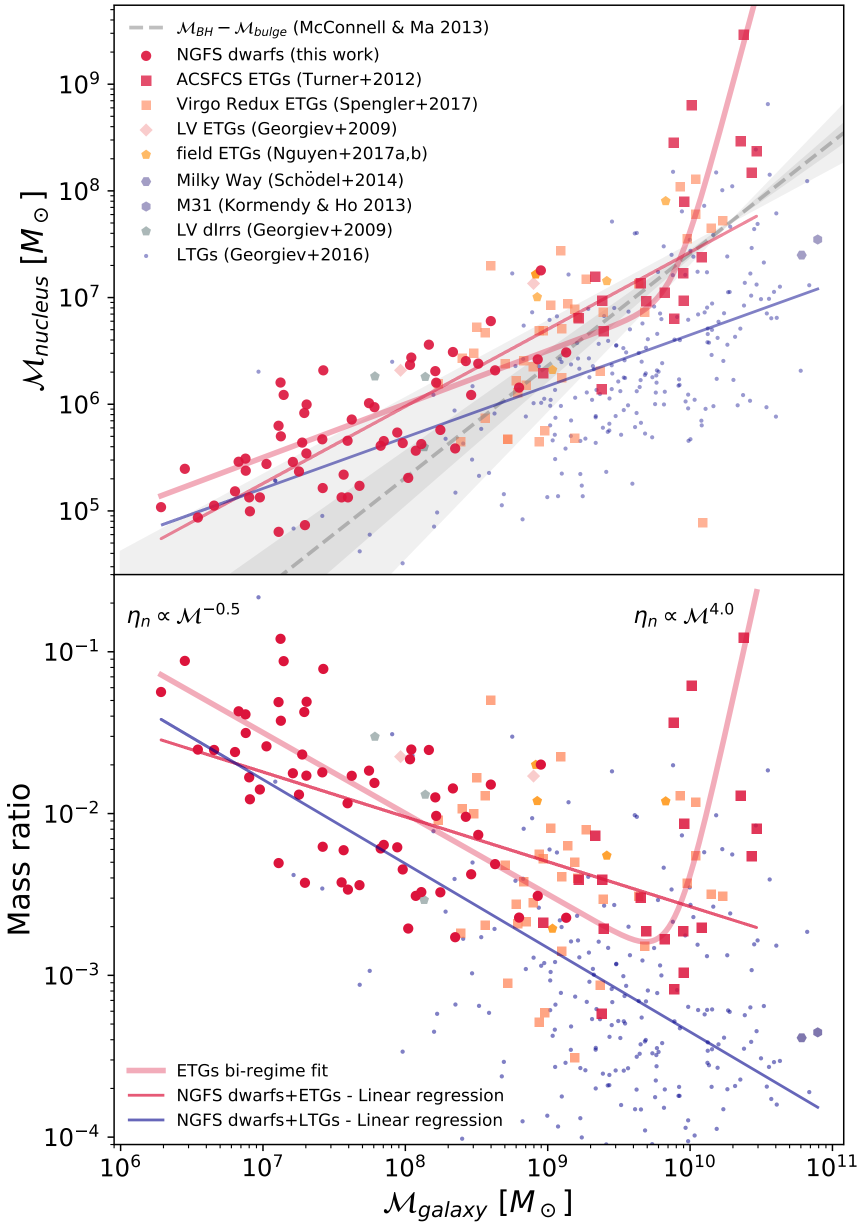

Figure 24: *Top panel:* Nucleus vs. host galaxy stellar mass for different subsets of nucleated NGFS galaxies and other galaxies from the literature. The SMBH mass vs. galaxy mass relation from McConnell & Ma (2013) is shown with 1σ and 3σ limits as dashed-line and shaded regions, respectively. *Bottom panel:* Nucleus-to-galaxy mass ratio ($\eta_n = \mathcal{M}_{nuc}/\mathcal{M}_{gal}$) vs. galaxy mass. We approximate the ETG data with a bi-regime fit for which the slopes of the low-mass and high-mass galaxy masses are labeled.

clear anti-correlation of η_n vs. $\mathcal{M}_{gal}$ over the entire galaxy mass range, i.e. the lower the galaxy mass the more significant becomes the nucleus. In the massive galaxy regime ($\mathcal{M}_{gal} > 10^9\,M_\odot$) we note a large scatter in the relation, which is the main reason why previous studies assumed a constant equivalent luminosity ratio $\eta_{n,L} = \mathcal{L}_{nuc}/\mathcal{L}_{gal}$ for their samples, like for instance, the ACS Virgo nucleated galaxies with $\langle\eta_{n,L}\rangle = 0.30\% \pm 0.04\%$ (Côté et al., 2006),

$\langle\eta_{n,L}\rangle = 0.41\% \pm 0.04\%$ for the ACS Fornax nucleated galaxies (Turner et al., 2012) and $\langle\eta_{n,L}\rangle = 0.1\%$ for LTGs (Georgiev et al., 2016). However, in the faint dwarf galaxy regime ($\mathcal{M}_{\rm gal} \leqslant 10^9\,M_\odot$) there appears a clear and strong trend, reaching to $\eta_n \simeq 10\%$ for a dwarf galaxy with a stellar mass of $10^7 M_\odot$. The four low-mass ETGs studied by Nguyen et al. (2017, 2018) have η_n values up to 1.7%, which are in agreement with the general trend. The extension of the η_n vs. $\mathcal{M}_{\rm gal}$ anti-correlation towards the faint dwarf galaxy population appears to be similar for ETGs and LTGs. This, in turn, suggests that nuclei at the smallest masses are subject to localized processes that work on parsec scales within the galaxy core regions independent of galaxy type.

[ht!]

Table 2: Scaling relations

Fit	Parameters	Fornax	NGFS dwarfs + ETGs	NGFS dwarfs + LTGs
		$\mathcal{M}_{\mathrm{nucleus}}$ vs. $\mathcal{M}_{\mathrm{galaxy}}$		
Linear regression	a	0.766 ± 0.048	0.723 ± 0.046	0.480 ± 0.033
$y = ax + b$	b	-0.096 ± 0.396	0.197 ± 0.392	1.850 ± 0.305
Polynomial-fit degree=3	a	0.068 ± 0.038	0.055 ± 0.038	0.031 ± 0.025
$y = ax^3 + bx^2 + cx + d$	b	-1.573 ± 0.946	-1.273 ± 0.976	-0.703 ± 0.654
	c	12.418 ± 7.881	10.245 ± 8.214	5.646 ± 5.685
	d	-28.085 ± 21.677	-22.923 ± 22.821	-10.212 ± 16.313
		$\eta_n = \mathcal{M}_{\mathrm{nucleus}}/\mathcal{M}_{\mathrm{galaxy}}$ vs. $\mathcal{M}_{\mathrm{galaxy}}$		
Linear regression	a	-0.234 ± 0.048	-0.277 ± 0.046	-0.520 ± 0.033
$y = ax + b$	b	-0.096 ± 0.396	0.198 ± 0.392	1.850 ± 0.305
Polynomial-fit degree=3	a	0.069 ± 0.038	0.055 ± 0.038	0.031 ± 0.025
$y = ax^3 + bx^2 + cx + d$	b	-1.573 ± 0.946	-1.273 ± 0.976	-0.703 ± 0.654
	c	11.418 ± 7.881	9.245 ± 8.214	4.646 ± 5.685
	d	-28.087 ± 21.677	-22.924 ± 22.821	-10.212 ± 16.313

For the nucleus vs. galaxy mass relation ($\mathcal{M}_{\mathrm{nucleus}}$ vs. $\mathcal{M}_{\mathrm{galaxy}}$) we set $y \equiv \log(\mathcal{M}_{\mathrm{nucleus}})$ and $x \equiv \log(\mathcal{M}_{\mathrm{galaxy}})$.
For the mass ratio (η_n) relation as a function of galaxy mass (η_n vs. $\mathcal{M}_{\mathrm{galaxy}}$) we define $y \equiv \log(\eta_n)$ and $x \equiv \log(\mathcal{M}_{\mathrm{galaxy}})$.

4.4.3 *Comparison with theoretical predictions*

The two proposed formation scenarios for nuclei are globular cluster infall due to dynamical friction (Tremaine et al., 1975) and in situ star formation (van den Bergh, 1986). The latter needs a mechanism to funnel gas into the galaxy center. Some studies suggest mechanism to carry the gas inwards to be galaxy mergers between two disk galaxies (Mihos & Hernquist, 1994), supernova feedback outflows that become stalled because the intergalactic medium (IGM) pressure prevents the gas from escaping the dwarf galaxy (Babul & Rees , 1992), and gas disks embedded in an old stellar spheroid (Bekki , 2007). We proceed to compare the nucleus sample available for the Fornax cluster (NGFS and ACSFCS nuclei) with scaling relation predictions for different formation scenarios in a similar approach as in Spengler et al. (2017). Figure 25 illustrates the comparison of empirical results with theoretical predictions.

4.4.3.1 *Bekki model predictions*

Pure dissipative models such as the one put forward by Bekki (2007), which takes into account feedback from SNe and super-massive BHs, depend mainly on the spheroid mass ($0.025 < \mathcal{M}_{\rm sph}/10^9 M_\odot < 5.0$), the initial gas mass fraction ($0.02 \leqslant f_{\rm gas} \leqslant 0.5$), the spheroid surface brightness (SB), and the chosen IMF (bottom or top-heavy). Some of the more relevant nucleus properties in the numerical results of this model are that η_n can reach up to 5%, more massive spheroids have more metal-rich nuclei and less massive spheroids can hold a young nucleus due to longer timescales of nucleus formation. Compared to the Fornax nucleated galaxy sample, the Bekki model (gray-dashed curves in Fig. 25) reproduces the η_n values for galaxies with masses of $\mathcal{M}_{\rm gal} \lesssim 10^8\,M_\odot$, but predicts too massive nuclei in more massive galaxies relative to the observations. The predicted trend in the η_n-galaxy mass relation is too steep for massive nucleated galaxies in contrast to the empirical results. Although the observed mass ratios reach up to 10%, they do so only at the lowest ($\sim 10^7\,M_\odot$) and highest sampled masses ($\geqslant 10^{10} M_\odot$), while the model reaches those values at smaller masses. For masses of the order of $10^{9.5}\,M_\odot$, the mass ratio η_n for our sample is about one order of magnitude smaller than the predicted values. Clearly the theoretical ingredients of the Bekki (2007) model ought to be adjusted to better reproduce the observed hockey-stick trend of the $\eta_n - \mathcal{M}_{\rm gal}$ relation, where stronger suppression within the model framework of the nucleus mass accumulation process at intermediate masses (10^8–$10^{10}\,M_\odot$) seems necessary. In light of the relatively high fraction of disk components in intermediate-mass dwarfs (see Lisker et al., 2006a), this may be accomplished by either an enhanced disk/spheroid growth mode and/or suppression of the nuclear mass accumulation mechanism, e.g. via advective angular momentum transport, bar instabilities, and/or the presence of a central black hole (Curir et al., 2008, 2010; Foyle et al., 2010; Goz et al., 2015; James & Percival, 2018).

4.4.3.2 *Antonini et al. model predictions*

An hybrid approach to modeling the formation of galaxy nuclei was undertaken by Antonini et al. (2015) where two nucleus formation models are considered. The first model is the cluster-inspiral (CliN) model, which simulates star cluster mergers in the center of an isolated galaxy with a pre-existing central BH. The second is a galaxy formation (GxeV) model, which tracks the evolution of baryonic structures in dark-matter merger trees. The GxeV model includes

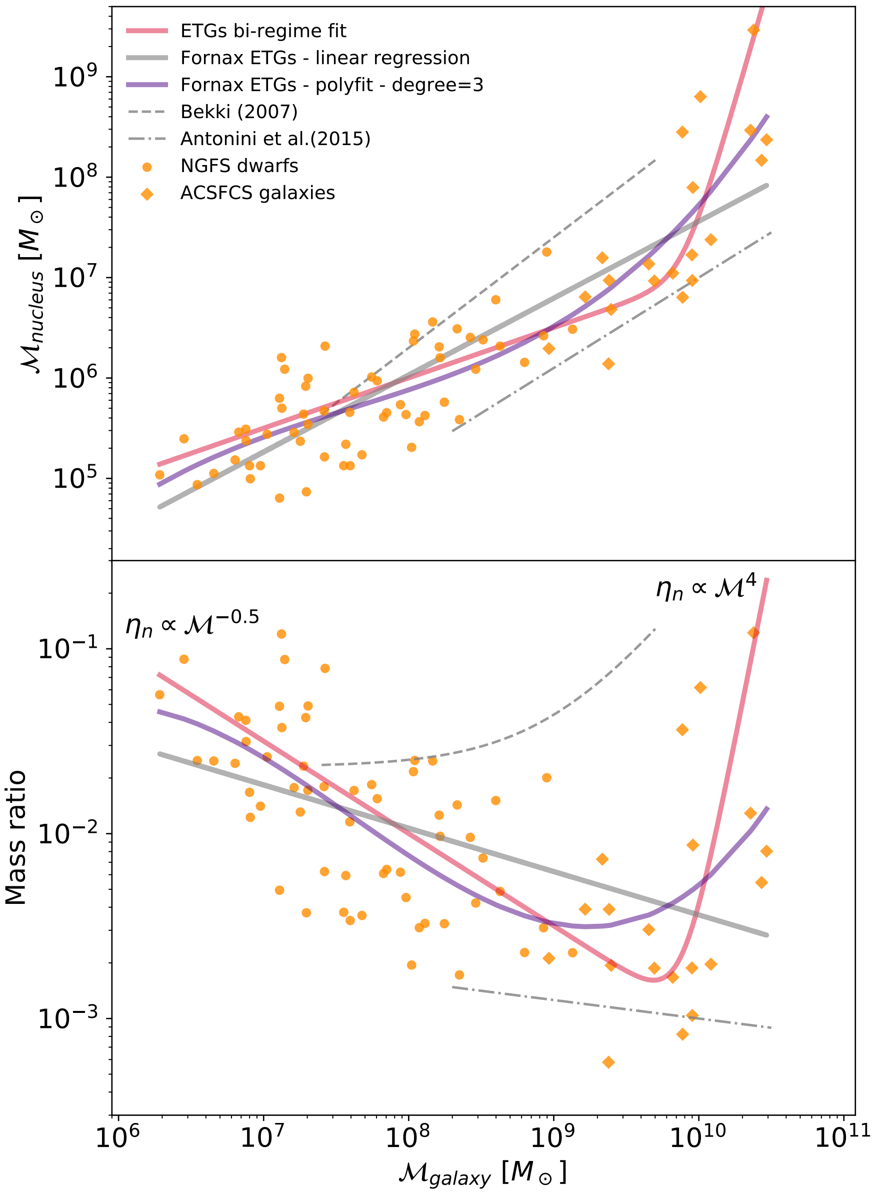

Figure 25: Scaling relations of the nucleus and galaxy masses. *Top panel*: Nucleus vs. galaxy mass relation for all nucleated galaxies in the Fornax core region (NGFS dwarfs and ACSFCS sample). *Bottom panel*: Nucleus-to-galaxy mass ratio ($\eta_n = \mathcal{M}_{nuc}/\mathcal{M}_{gal}$) as a function of galaxy mass. Solid lines show the weighted least-square fits, the numerical values of which are shown in Table 2. Both panels show model predictions for nucleus formation. See the legend and text for more details.

galaxy evolution, dissipative processes, mergers between galaxies, tidal interactions, and coexistence with super-massive BHs. This hybrid approach considers two possibilities for nucleus growth from high-redshift to the present-day by migration of star clusters and/or in situ formation. Both models, CliN and GxeV, have similar scaling relations but GxeV has a larger dispersion in the nucleus masses than CliN does. In addition, CliN cannot form nuclei more massive than

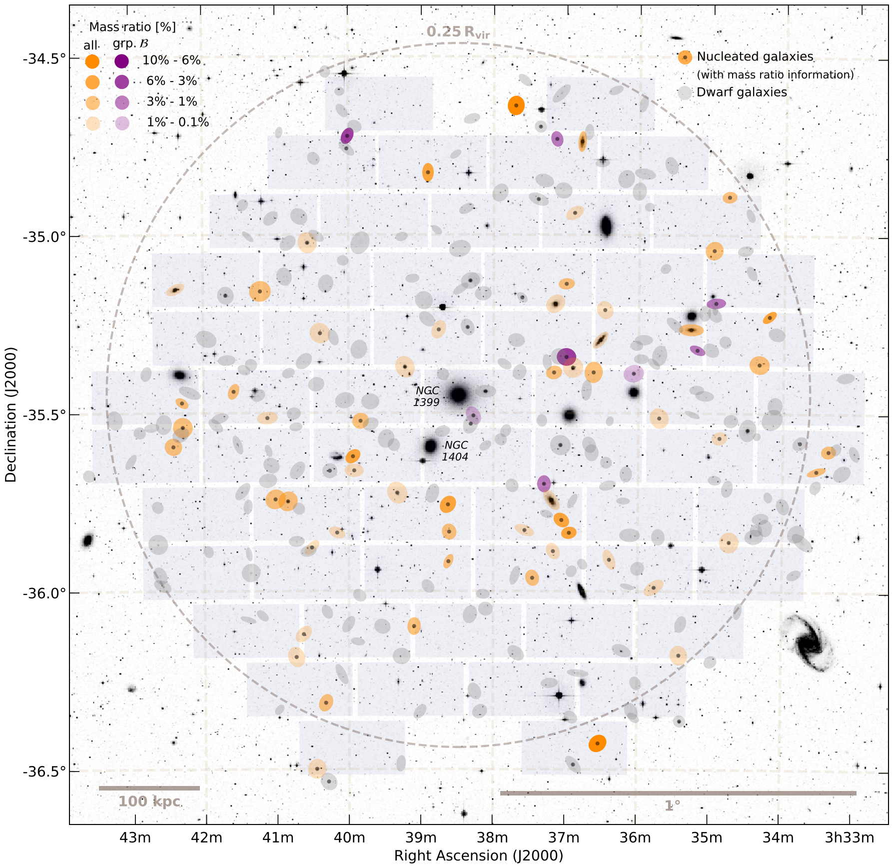

Figure 26: Illustration of the central region of the Fornax galaxy cluster showing the spatial distribution of non-nucleated (gray symbols) together with nucleated dwarfs, which are shown as orange symbols (NGFS dEN and ACSFCS) if mass ratio information is available. Otherwise, they are shown in gray scale as well. The symbol transparency parameterizes the mass ratio as $\eta_n = \mathcal{M}_{nuc}/\mathcal{M}_{gal}$ ranging from 10%-0.1% of the host galaxy mass, which is indicated in the top left corner. Group $\mathcal{B}$ nuclei (see Sect 4.3.3) which are younger and more metal-rich than group $\mathcal{A}$ are shown in purple.

a few $10^7\ M_\odot$, but GxeV can. Antonini et al. tested the case without BH heating and found that both models still are able to form massive nuclei without any constraint on velocity dispersion or galaxy mass. One interesting prediction is that nuclei can be formed with one mechanism alone, the in situ star formation. However, a shallower slope is then obtained for the nucleus-galaxy mass relation relative to the scenario when both mechanisms are at work.

When comparing the predictions (CliN and GxeV are similar in this parameter space, dash-dotted lines in Fig. 25) with Fornax nucleated galaxies, the predicted masses tend to be a factor of a few smaller than the observed ones over the mass range covered by the models ranging from $2 \times 10^8\ M_\odot$ to $3 \times 10^{10}\ M_\odot$. Antonini et al. notice the offset and argue that the underweight of model nuclei is due to the interaction of the nucleus with the central massive BH, which makes the nucleus lose stars faster, in addition to galaxy mergers, where BH binaries form and efficiently eject surrounding stars. These effects have a greater impact in more massive galaxies than in low-mass dwarfs. The overall prediction by Antonini et al. (2015) is that both mechanisms are likely active during nucleus growth and that their relative contribution depends on the star-cluster formation efficiency. These models show that for galaxies less massive than $\sim 3\times10^{11}\,M_\odot$ *in situ* star formation contributes $\sim$50% of the nucleus mass and becomes more important for more massive galaxies. This suggests that massive galaxies are more efficient in driving the gas flows to the galaxy core regions than are low-mass galaxies. This gas funneling allows for subsequent star formation to progress to more advanced stages with implications for the resulting chemical makeup of the stellar populations, which would exhibit lower [α/Fe] element ratios.

In any case, the Antonini et al. (2015) models require modification in order to reproduce the sharp upturn of the observed $\eta_n - \mathcal{M}_{gal}$ relation.

4.4.4 *Correlation of the nucleation strength with the spatial distribution in Fornax*

Figure 26 shows the spatial distribution of the galaxies in the central region of the Fornax cluster, where the nucleated galaxies from the NGFS and ACSFCS sample with mass ratio information are shown in orange symbols, while the rest of the dwarf galaxies are indicated by gray symbols. In this plot, the transparency of the symbols for the nucleated dwarfs is parameterized by the nucleus-to-galaxy mass ratio (η_n) as indicated in the legend in the top left corner. We find that dwarfs located closer to massive galaxies have mass ratios below 1%. However, we see that the dwarfs with the highest mass ratios in our sample are located on the edges of the field of view at North and South direction.

In Section 4.3.3 we introduced two nucleated dwarf groups according to their stellar population parameters derived from SSP model predictions in the $u'i'Ks$ diagram. We defined group $\mathcal{B}$ of nuclei that appear younger and more metal-rich than the nuclei of group $\mathcal{A}$, which appear, on average, older and more metal-poor. The nuclei from group $\mathcal{B}$ are marked with purple ellipses in Figure 26, which reveals a strong asymmetry in their spatial distribution, where virtually all of the younger and metal-rich nuclei are located in an overdensity westwards of the Fornax center. This suggests that dwarf galaxies in different regions of the Fornax cluster must have experienced different formation histories. We will test the significance of this overdensity once the dwarf sample from the entire NGFS footprint is available.

4.5 SUMMARY

We have characterized 61 nuclear star clusters in the Fornax cluster region ($\leqslant R_{vir}/4$). We used deep and homogeneous $u'g'i'JK_s$ photometry to obtain information on their luminosity and color distributions. In the following we summarize our main results.

- The nucleation fraction (f_{nuc}) depends strongly on the galaxy luminosity, reaching $f_{nuc} \geqslant 90\%$ for the bright NGFS dwarf galaxies ($M_{g'} \leqslant -16$ mag) and dropping to zero at absolute galaxy magnitudes fainter than $M_{g'} \simeq -10$ mag. The galaxy luminosity at which the nucleation stops corresponds to a stellar mass of $\log \mathcal{M}_* \simeq 6.4\,M_\odot$. As the NGFS data have a very faint point source detection limits ($M_{g'} \approx -5.4$ mag) this is an astrophysical effect and clearly not related to observational constraints.

- Color-magnitude diagrams using various filter combinations show that nuclei occupy the bluest parts in color space, but have a comparable luminosity coverage to the distribution of compact stellar systems (CSSs) in Fornax. The latter distribution is significantly broader, which is mainly due to the large spread in metal content. Nuclei in dwarf galaxies show a flat color-magnitude relation, which is opposite to the trend found for UCDs and the dwarf galaxy spheroids which both show a positive color-luminosity relation.

- We derive stellar masses for our nuclei with a mean uncertainty of $\sim 19\%$ and find that the nucleus stellar mass distribution covers the range of $\log(\mathcal{M}_*/M_\odot) = 4.8-7.3$. We find that the nucleus mass distribution is bimodal, with peaks located at $\log(\mathcal{M}_*/M_\odot) \simeq 5.38$ and 6.25. The second peak is consistent with UCD masses. We derive stellar masses for our CSS comparison dataset, which is limited at the low-mass end by the spectroscopic selection function.

- The combination of the $u'i'K_s$ diagram with SSP model predictions reveals a bimodality in the stellar population parameters of nuclei, which is congruent with the two groups in the mass distribution function of NGFS nuclei. We define two groups with group $\mathcal{A}$ comprising nuclei with colors $(u'-i')_0 < 2.0$ mag and $(i'-K_s)_0 < -0.2$ mag, which according to SSP models is consistent with metal-poor stellar populations ($Z < 0.02\,Z_\odot$) and ages older than 2 Gyr. The nuclei in group $\mathcal{A}$ have stellar masses $> 10^6\,M_\odot$. Group $\mathcal{B}$ contains less massive objects and covers a more extended region in the $u'i'K_s$ color space with redder average colors, an indication of a larger range in metallicity $0.2 < Z/Z_\odot < 1$ and ages younger than 2 Gyr. With the exception of one object the masses of the group $\mathcal{B}$ nuclei are all $< 10^6\,M_\odot$.

- Dividing the CSS sample confirmed by radial velocity into GCs and UCDs using a stellar mass cut at $\log(\mathcal{M}_*/M_\odot) = 6.3$ shows that the low-mass mode of our sample nuclei (group $\mathcal{B}$) cannot be progenitors of Fornax UCDs. On the other hand, the high-mass mode nuclei located in bright galaxies could be potential progenitors of metal-poor UCDs. Notwithstanding, our NGFS nuclei could all be considered as potential future GCs, once their host galaxy spheroids are stripped due to the dynamical evolution of the system inside the Fornax cluster environment.

- Color differences between the nucleus and its parent galaxy spheroid correlate more with the spheroid light than with the nucleus luminosity. Therefore, the mechanism that produces these color offsets is more likely to be acting on galaxy scales. Colors with a wide SED coverage, such as $\Delta(u'-i')_0$ and $\Delta(u'-g')_0$, are more sensitive to changes in stellar populations and show a steeper relation with spheroid luminosity than $\Delta(g'-i')_0$. Bright nuclei tend to be bluer than their host galaxy. Nonetheless, as we sample fainter galaxy luminosities, we find a transition point where the color offset becomes more stochastic and we find both bluer and redder nuclei than their host. This transition occurs at $M_{g',\mathrm{nuc}} \simeq -7.5$ or $M_{g',\mathrm{sph}} \simeq -12.5$ for $\Delta(g'-i')_0$ and $M_{g',\mathrm{nuc}} \simeq -9.5$ or $M_{g',\mathrm{sph}} \simeq -14.0$ for $\Delta(u'-i')_0$ and $\Delta(u'-g')_0$.

- Scaling relations such as the nucleus-to-galaxy mass relation ($\mathcal{M}_\mathrm{nuc}$ vs. $\mathcal{M}_\mathrm{gal}$) show a clear mass correlation between nuclei and their host galaxy over the entire mass range of our NGFS sample. This relation shows a break in the slope at $\log(\mathcal{M}_*/M_\odot) \simeq 9.7$ where we find a shallower slope for dwarf galaxies relative to their more massive counterparts. Comparing with the BH-galaxy mass relation, we find that it has a similar relation to the nuclei and their host galaxy mass down to $10^9\,M_\odot$. For galaxies with lower masses, their nucleus-galaxy mass scaling relation becomes flatter than the BH-galaxy mass relation. For the nuclei-to-galaxy mass ratio vs. galaxy mass relation ($\eta_n = \mathcal{M}_{\rm nucleus}/\mathcal{M}_{\rm galaxy}$ vs. $\mathcal{M}_{\rm galaxy}$) an interesting anti-correlation is found. The lower the galaxy mass the more prominent becomes the nucleus with a scaling $\eta_n \propto \mathcal{M}_{\rm gal}^{-0.5}$. For masses higher than the break at $\log(\mathcal{M}_*/M_\odot) \simeq 9.7$ we find a positive correlation of the form $\eta_n \propto \mathcal{M}_{\rm gal}^4$. These relatively strong trends for low-mass and high-mass galaxies reach values up to $\eta_n \simeq 10\%$ for dwarf galaxies with a stellar mass of $10^7\,M_\odot$ and massive ellipticals at $10^{11}\,M_\odot$.The low-mass anti-correlation seems to be similar for ETGs and LTGs, suggesting that it is independent of galaxy type.

- The spatial distribution of the Fornax nucleated dwarfs shows that they are preferentially distributed along the East-West direction. Knowing the location of the nucleated dwarfs with highest η_n values, we observe that they lie at the edges of the central NGFS footprint to the North and South. We also find that the nuclei that are members of group $\mathcal{B}$ that are relatively metal-rich and have ages younger than 2 Gyr lie predominantly westward of NGC 1399, suggesting a more extended star formation history of nuclei in that direction.

Our NGFS study has extended the galaxy nucleus research towards the faint galaxy luminosity regime down to $\log(\mathcal{M}_*/M_\odot) \simeq 6$, finding nucleus-galaxy scaling relations that are quite different compared to the results obtained from bright galaxies. Theoretical models still fail to explain the observed scaling relations for the low-mass regime and do not account for the apparent transition between low-mass and high-mass galaxies. However, we find that the models by Bekki (2007) and Antonini et al. (2015) appear to frame our observations, which may indicate that a combination of their prescriptions may best represent reality. Overall our NGFS nucleus sample gives crucial insights into the formation mechanism at work, showing that nuclei are likely formed via two different mechanisms, i.e., formation via dynamical friction acting on GCs sinking to the center and star formation processes in the central regions. The full NGFS footprint will provide a larger sample and help us to better understand the fascinating properties and the formation mechanisms of the nucleus population in dwarf galaxies.

5

PANCHROMATIC VIEW OF THE FORNAX COMPACT STELLAR SYSTEMS

5.1 CONTEXT

Compact stellar systems such as globular clusters and ultra-compact dwarf galaxies are ideal tracers of the assembly of galaxies across cosmic time. Their high density and compact sizes allow them to survive the evolution of their parent galaxies. The stellar population of CSSs can tell us crucial information about their metallicity, age and mass distributions to understand the environment they formed in and reside in today.

The inner region of the Fornax cluster where the cD galaxy NGC 1399 is located, has been extensively studied in the past. A wealth of compact stellar systems are found and a total of 656 of them are spectroscopically confirmed (e.g. Schuberth et al., 2010). The CSSs of other galaxies in the vicinity of NGC1399 have also been studied, for instance NGC1404 (Richtler et al., 1992), NGC 1387, NGC 1379 and NGC 1374 (Bassino et al., 2006) and 43 ETGs studied with HST/ACS Fornax cluster survey (Jordán et al., 2007). However, we still lack a coherent global picture of its CSSs from images covering a wider area, with deep, homogeneous and panchromatic photometry. This is the aim of this work, to provide the most clean photometric CSS selected sample for the Fornax core region ($r < 0.25r_{vir} \sim 350\,\mathrm{kpc}$) using the NGFS data with $u'g'i'JK_s$ photometry information to obtain their stellar population properties.

5.2 ANALYSIS

5.2.1 *Bright galaxy subtraction*

The study of compact stellar systems is affected by the radially declining light of their parent galaxies. The steep slopes of the galaxy surface brightness profiles near their cores is interpreted by source detection software as drastic changes in the background, hampering the detection of faint sources. Therefore, to detect CSSs close to the center of their host galaxies, first we need to subtract their galaxy light profiles.

We create models for galaxies[1] in the Fornax core region using the task ELLIPSE (Jedrzejewski, 1987) from the package STSDAS in IRAF (Tody, 1986), which fits elliptical isophotes to the galaxy surface brightness profiles. As galaxies are not perfectly symmetrical, the isophotes are allowed to vary in central coordinates, positional angle, ellipticity and the a4 and b4 Fourier parameters (indicators of diskyness or boxyness). For the ELLIPSE fitting, we mask all the detected point-like sources (except the galaxy to be fitted) using the SEGMENTATION MAP from a first SE pass. Once we have the isophotes from ELLIPSE, we use the BMODEL task within STSDAS/IRAF to construct the 2D surface brightness model for each galaxy. We subtract the model from the original image for the brightest galaxies in all the filters. We begin by subtracting the brightest extended galaxies, as they contribute to the background of the smaller,

---

[1] This process was done by Dr. Karla Alamo-Martinez.

less luminous ones, and progress with subtracting the galaxy light profiles of the fainter galaxies.

With the new images, i.e. without the light of the most massive galaxies, we proceed with the detection and photometry for all objects in the central core region of the Fornax galaxy cluster ($r < 0.25r_{vir} \sim 350\,\mathrm{kpc}$).

5.2.2 *Photometry*

Source detection and photometry in the galaxy-free image stack, for each of the five filters are performed with SE using a point spread function (PSF) model created with PSF Extractor (PSFEx, v3.16.1 Bertin, 2011), which takes into account spatial PSF variations across the detectors. We correct the photometry for foreground Galactic extinction (Schlafly & Finkbeiner , 2011). Reddening values for the different filters are calculated assuming the Fitzpatrick (1999) reddening law with $R_V = 3.1$. The mean Galactic extinction in the direction of Fornax is $A_V = 0.035\,\mathrm{mag}$. The derived magnitudes in optical passbands are all in the AB system and the NIR magnitudes were transformed from the Vega to the AB system using $K_s(m_{AB} - m_{Vega}) = 1.85\,\mathrm{mag}$ and $J(m_{AB} - m_{Vega}) = 0.91\,\mathrm{mag}$ (Blanton & Roweis , 2007). The $u'g'i'JK_s$ PSF photometry catalogs are crossmatched with each other to create a master catalog of objects with homogeneous information in all five filters. In this article, we do not require a completeness analysis as we aim for a full SED catalog with five filters, thus, our depth is defined by the limits of u' and K_s bands, which are the shallowest in the current NGFS observations. The faintest objects in each filter have magnitudes of $u' = 25.52$, $g' = 24.07$, $i' = 23.28$, $J = 22.92$, $K_s = 23.35$ AB mag.

Color-color relations of all objects in the master catalog with $u'g'i'JKs$ PSF photometry are shown in Figure 27 with the red dots indicating radial-velocity confirmed CSSs from Wittmann et al. (2016) that collects and homogenizes information from Schuberth et al. (2010); Dirsch et al. (2004); Bergond et al. (2007). The set of color-color diagrams in Figure 27 illustrates the diagnostic utility of the combination of near-UV and near-infrared filters to distinguish between different stellar populations and/or object types. In plots such as $(u' - g')$ vs. $(g' - K_s)$ (designated $u'g'K_s$ hereafter), as well as $u'i'K_s$ and $u'JK_s$, four main groups of objects can be recognized. These groups are background galaxies at various redshifts, passive redshifted early-type galaxies, compact stellar systems in Fornax, and foreground Milky Way stars (see also Muñoz et al., 2014). In the other color combinations, the four groups are not clearly separated (e.g. $g'i'J$). Although, the $u'g'i'$ color-color diagram shows only three clear sequences, where the CSS sequence is merged with the bluest region of the stellar sequence, this diagram still bears diagnostic power to differentiate between point sources and more extended targets. We further use the $u'g'i'$ diagram together with other similarly powerful diagrams to understand the separation between point-like and extended sources.

Figure 28 shows four color-color diagrams ($u'g'i'$, $u'i'K_s$, $u'g'K_s$ and $u'JK_s$) color coded with the SE spread-model parameter. This parameter provides information on the compactness of a source, comparing the PSF model with the profile of the object. Lower numerical values for the spread-model parameter indicate compact sources (e.g. stars and unresolved CSSs) while larger values are consistent with more extended objects (e.g. galaxies). In every subplot of Figure 28 we observe that the sequences of compact sources correspond to stars and CSSs sequence (cf. Fig. 27). A larger dispersion in spread-model values is seen for the extended sources toward the top-left of each diagram. In the galaxy region of the $u'i'K_s$ diagram we see a progressively declining size of objects to-

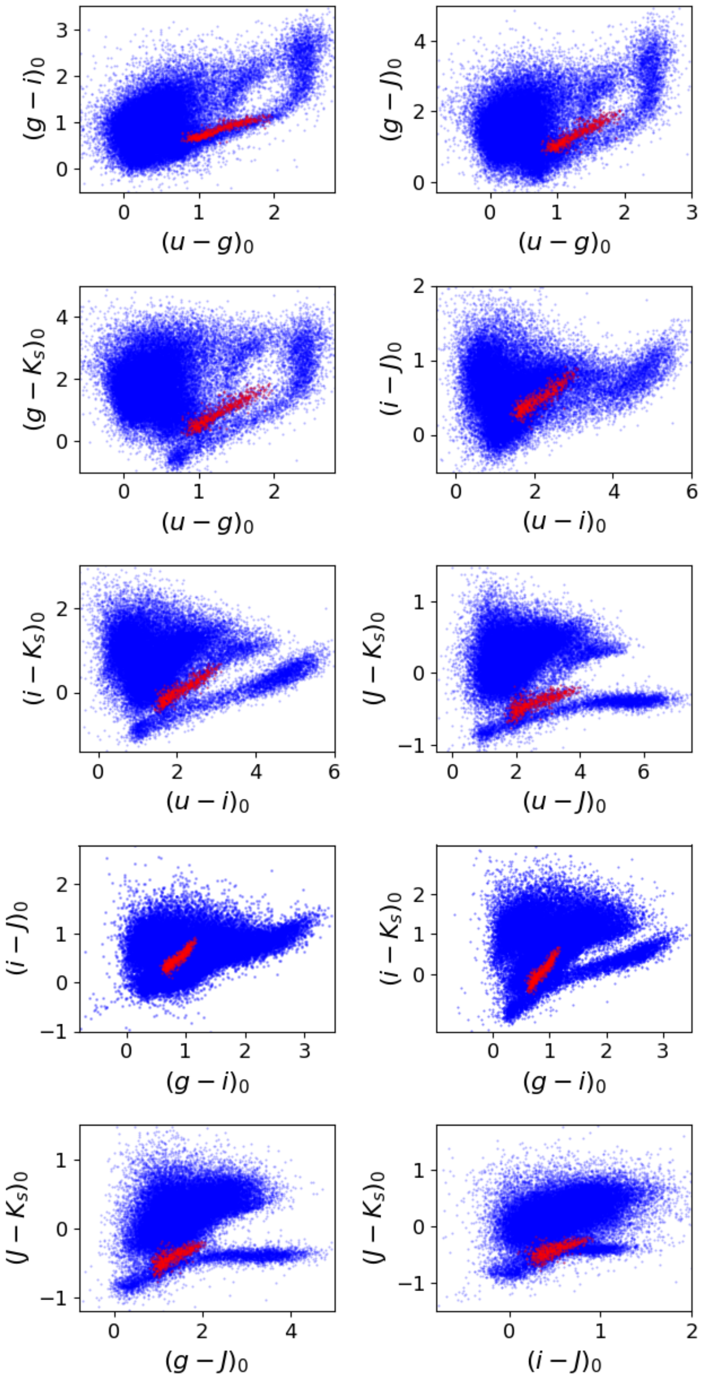

Figure 27: Color-color diagrams for all sources with panchromatic photometry in the central regions of the Fornax galaxy cluster, shown as blue dots. Red dots indicate the CSSs, which were spectroscopically confirmed to be members of the Fornax cluster by their radial velocities (Wittmann et al., 2016). Note that the different diagrams present the same source sample for which photometric information is available in all filter combinations (u′g′i′JKs).

wards redder $(i'-K_s)$ and bluer $(u'-i')$ colors, which we attribute to a redshift effect (Muñoz et al., 2014).

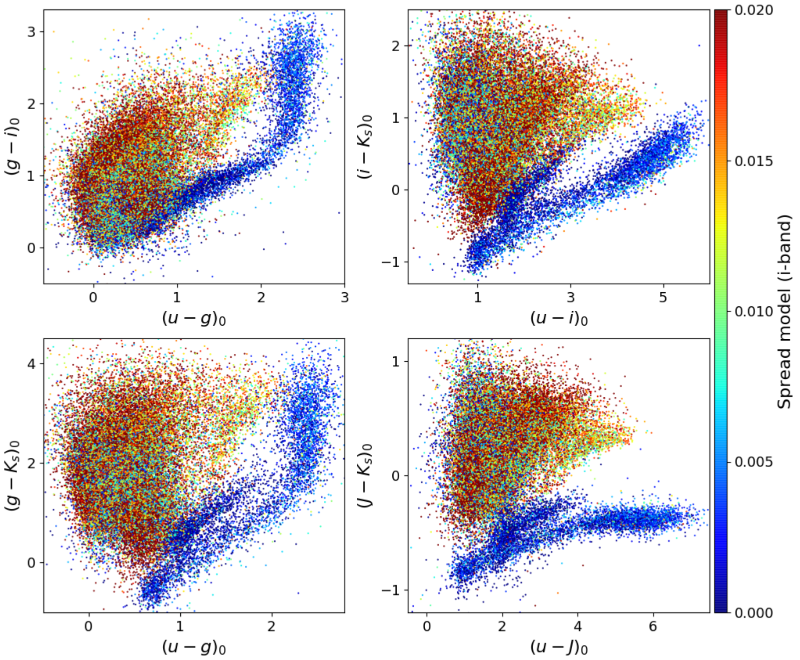

Figure 28: Color-color diagrams for the four filter combinations in which the best separation between different object types is realized with the spread-model parameter, which is parameterizing the symbol colors using the i'-band data. Blue symbols indicate point-like sources while redder symbol colors show more extended objects.

5.2.3 *Selecting Compact Stellar System with Machine-Learning Methods*

The broad SED coverage available for each object in the master catalog, together with the confirmed radial velocity CSSs, gives us an idea where our CSS candidates are located. However, a clean CSS selection sample is still hard to obtain given the overlapping distributions of stars and galaxies in the various color-color parameter spaces (see Figs. 27 and 28). To decrease the foreground and background contamination from the CSS selection, we implement a new method, which uses supervised machine-learning techniques, specifically the support vector machine (SVM[2]) for source classification. As we have four main object types according to the available photometric information, we use these four groups for the SVM code to classify, i.e. foreground stars, CSSs in Fornax, passive ellipticals and background galaxies, and thus we deal with a multi-class problem. As training sample, or support vectors, we provide the radial velocity confirmed stars (Schuberth et al., 2010) and CSSs in Fornax and a selected subsample for the two galaxy population from the $u'g'K_s$ and $u'g'i'$ color-color diagrams. The features used for the training and the catalog to be classified are 13 in total: the 9 different color combination and four parameters related to the compactness of the sources in i filter, which is the deepest band with the best seeing. These source morphology/compactness parameters are: full width half maximum (FWHM), flux radius, spread-model, and compactness factor ($C_i = m_{APER}(2\,\mathrm{pix}) - m_{APER}(8\,\mathrm{pix})$, Powalka et al., 2016b). For the decision functions we use the radial basis function (*rbf*) and the polynomial function as ker-

---

[2] An implementation of this code is available in the Python package scikit-learn (Pedregosa et al., 2012).

nels (Pedregosa et al., 2012). Linear functions do not work with our data as the classes are not linearly separable. We run the *rbf* and polynomial kernels changing their parameters as follows $C = [1, 5, 10, 15]$ (regularization parameter), $\gamma = [1, 5, 10, 100]$ and the degree $= [2, 3, 4, 5]$m, *rbf* kernel depends only in C and γ (16 runs) and the polynomial function depends in C and degree (16 runs). In total we run the SVM classification 32 times. The classification for all sources in the master catalog $u'g'i'JK_s$ is saved for each run. Each object is assigned a relative probability according to how many times out of the 32 runs the object is classified in that class. Therefore, a source classified 32 of the 32 times as CSS, has a probability of 100% of being a CSS.

In Figure 29 we show the same color-color diagrams as in Figure 28, but this time we color-code all objects classified as CSS candidates with their respective relative probability assigned during the SVM selection. Objects with red colors have 100% probability of being a CSS, blue-color symbols show objects which were found in only one of the runs to belong to the CSS class, thus, have $\sim$3% probability. Most contamination in the CSS candidate sample comes from the galaxy region and the stellar sequence, specifically from the red edges and from the bluest parts of the CSS sequence, respectively.

A total of 2516 objects are classified as CSS in at least one of the 32 runs. 607 objects (24%) are catalogued as CSSs in the SVM runs. There are 1424 CSS candidates with $\geqslant$80%, 1666 with $\geqslant$60%, 1765 with $\geqslant$50%. Hereafter, only CSS candidates with relative probability larger than 60% ($p_{CSS} \geqslant 60$) are considered for the subsequent analysis.

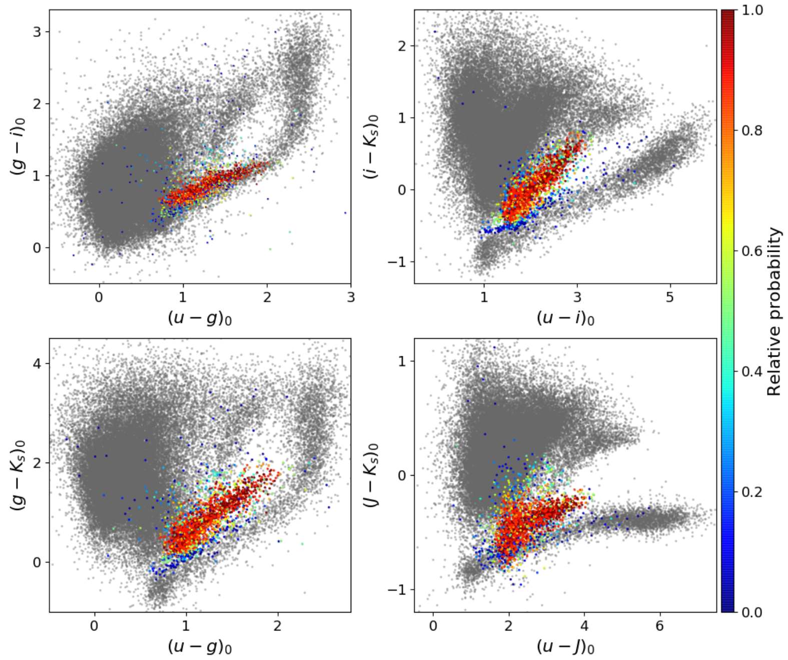

Figure 29: Same color-color diagrams as shown in Fig. 28. Gray dots show the objects from the master catalog of sources in the central region of Fornax's cluster. In color are shown the CSS candidates from the SVM technique selection, color coded is the relative probability assigned by the SVM classification. The redder the higher the probability to be a CSS.

5.3 RESULTS

5.3.1 *Color-magnitude diagrams*

Color-magnitude diagrams (CMDs) with the five filters u', g', i', J and K_s as a function of $(u' - K_s)_0$ and $(g' - i')_0$ as base colors are shown in Figure 30 for all SVM-selected CSSs candidates ($p_{CSS} \geqslant 0.6$). The horizontal lines indicate the limiting magnitude in each filter until which the entire sample is complete. CSSs are shown with a lighter color for magnitude fainter than these limits. Corresponding color distributions for $(u' - K_s)_0$ and $(g' - i')_0$ are shown in the upper panels of the figure. The step-filled histogram shows the complete sample in the limit magnitude for the u'-band and the step one all the sources. In all color-magnitude diagrams there is a greater fraction of blue CSSs compared to red ones. A clear bimodality in color is seen for g' and i' vs $(g' - i')$ diagram.

5.3.2 *Estimation of the stellar population properties for the CSS candidates.*

In the following, we take advantage of the broad SED information of our CSS candidates and among them the NIR bands that are less affected by evolved hot stars (blue horizontal branch stars and blue stragglers) that can be present in GCs older than 8 Gyr (e.g. Yi, 2003). We attempt, in this work, to estimate individual stellar population properties such as metallicity, age and mass for each CSS in our sample. We make use of the models from (Bruzual & Charlot, 2003, hereafter BC03) with the 2016 update[3], MILES atlas (Sánchez-Blázquez et al., 2006), and an initial mass function (IMF) from Kroupa (2001). We decide to use BC03, because these SSP models cover the photometric color range of our candidates. It is beyond the scope of this paper to compare results with different population synthesis models and their systematic uncertainties that contribute to the stellar population parameter estimates derived here. We point out, however, that despite the systematic uncertainties in the *absolute* stellar metallicities and ages, their *relative* measurements are very well described by the BC03 models. For a review of this issue we refer the reader to the comprehensive model comparison in Powalka et al. (2016b, 2017).

5.3.2.1 *Assessing the age-metallicity degeneracy*

Prior to deriving CSS ages and metallicities we attempt to quantify the degree of age-metallicity degeneracy in each of the color combinations shown in Figure 31. For this purpose we plot the age spread for each iso-metallicity available in BC03, i.e. $Z/Z_\odot = 0.005, 0.02, 0.2, 0.4, 1.0, 2.5$ as a function of color, spanning ages from 1 to 14 Gyr. The ideal case would be a color that does not depend on age but only on metallicity, in such case each iso-metallicity lines would be just a single point in the parameter space of Figure 31. None of these broad-band colors can break the age-metallicity degeneracy completely. We observe that those colors which are constructed with the u'-band filter have a strong degeneracy between metallicity and age (e.g. Worthey, 1994). The metallicity sensitivity of all colors decreases at the blue end, where a small color change can translate in large age and metallicity differences. Furthermore, colors which are constructed from two filters with a small central wavelength difference show, in general, a more pronounced age-metallicity degeneracy than filter combinations which involve more widely separated filter central wavelengths. This is particularly true

---

[3] http://www.bruzual.org/~gbruzual/bc03/Updated_version_2016/

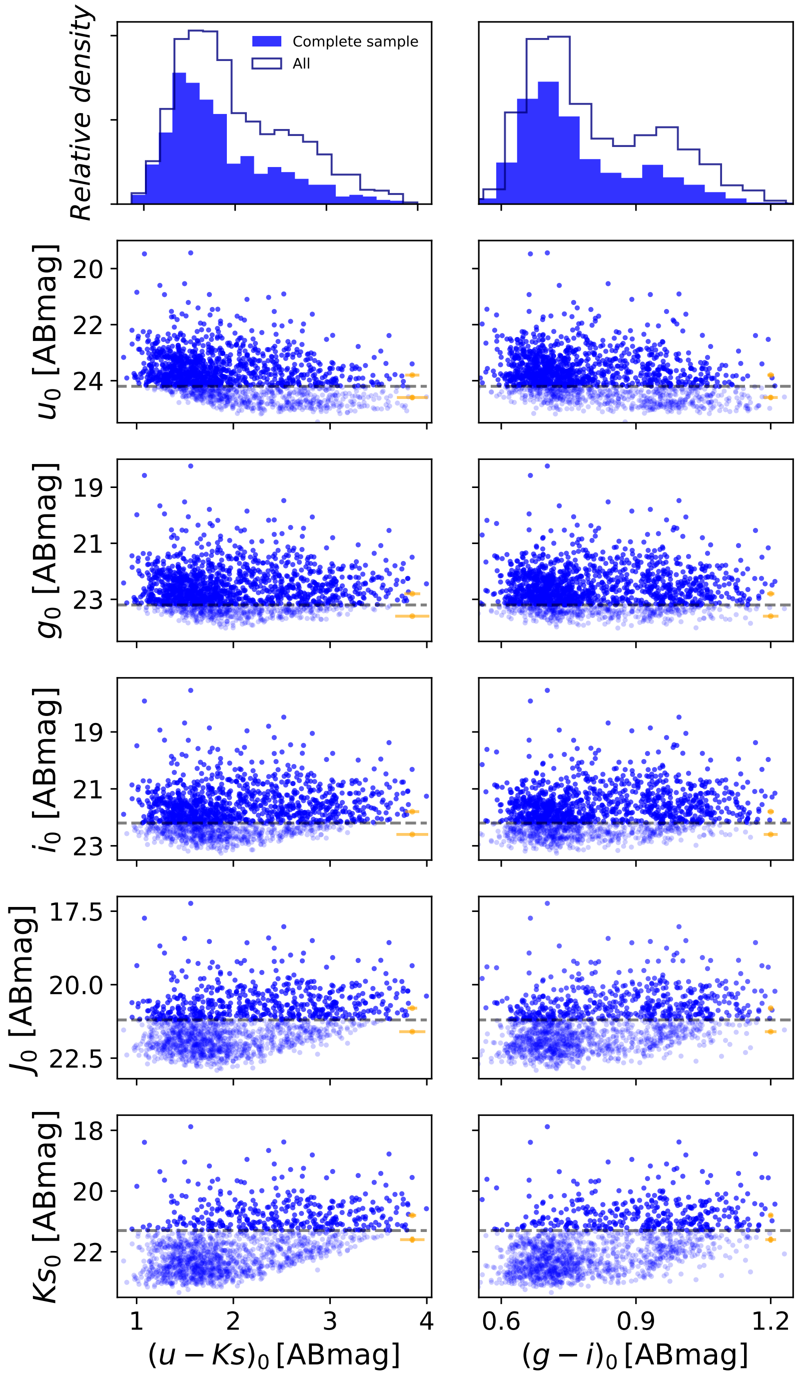

Figure 30: Color-magnitude diagrams for u', g', i', J and K_s as a function of $(u'-K_s)$ (left panels) and $(g'-i')$ (right panels). SVM-selected CSS candidates ($p_{CSS} \geqslant 0.6$) are shown in blue circles. A horizontal line in each panel shows the limiting magnitude brighter of which the color distributions of the samples are complete. Below this line, fainter objects are shown in lighter colors, and the corresponding color distributions become incomplete. In the top panels we show the color distributions for the photometrically complete sample (filled histogram) and the entire sample (open histogram). Median photometric error bars are shown at the bottom-right side of each panel.

for the widely used $(g' - i')$ color. We attempt to quantify the age-metallicity degeneracy of the colors by computing the following parameter:

$$\xi = \langle \Delta\text{color} \rangle / \langle \Delta c \rangle \tag{5}$$

where Δcolor is the full dynamical range of all colors covered by the age-metallicity grid of the models, while Δc is the color spread due to age for a specific color. These numbers are provided in Figure 31 for each color and are documented on top of each panel. The color with the formally largest ξ parameter, i.e. with the smallest age-metallicity degeneracy, is $(J - K_s)_0$, followed by $(i - J)_0$ and $(i - K_s)_0$. However, the overlap between iso-metallicity tracks in color space is still present. The color that provides the best compromise, i.e. high ξ parameter value and least overlapping between iso-metallicity tracks, is $(i' - K_s)_0$. Thus, we deem this color as a robust way to compute metallicities for CSSs.

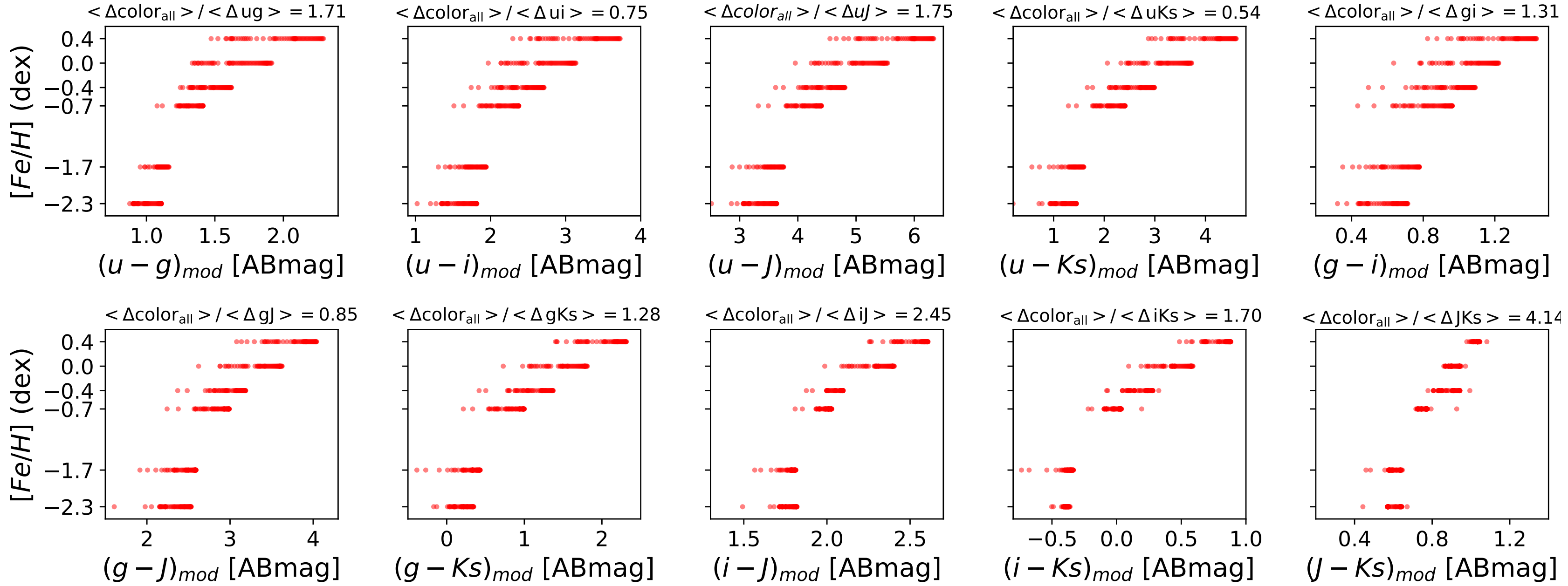

Figure 31: Model metallicity from BC03 and its dependence in color space. Each panel has six iso-metallicity tracks with ages from 1 to 14 Gyr. At the top part of each panel the ratio between mean difference for all colors and the mean difference for the specific color of that panel.

We repeat the same exercise but now in color-color space to find the best color-color diagram to compute metallicity. Figure 32 illustrates 10 color-color diagrams, with BC03 SSP models overplotted in the same range of metallicity and ages explained above. More metal-poor tracks are located in the bottom part and metal-rich tracks in the upper part of each panel. The two large panels, correspond to the $u'i'K_s$ diagram, which is frequently used to understand and distinguish between different object types (e.g. Muñoz et al., 2014; Powalka et al., 2016b; González-Lópezlira et al., 2017) and the $g'i'K_s$ diagram. According to the grid of BC03 SSP models, the $g'i'K_s$ diagram covers in a more complete way the range in ages and metallicities of our CSS candidates and shows less degeneracy in these parameters in comparison to the $u'i'K_s$ diagram. In addition, the other panels of Figure 32 illustrate the degeneracy between age and metallicity for other color-color combinations. For many of them, the model grids are ambiguous (i.e. overlapping) and do not coincide entirely with the data. Furthermore, only when having the reddest filters combined with NIR bands, the age-metallicity degeneracy is significantly reduced. Therefore, of all these color-color combination, we choose the $g'i'K_s$ diagram to obtain metallicities and ages for the CSS candidates.

5.3.2.2 *Metallicity and age determination*

Metallicity is obtained with two main interpolators from SCIPY and MATPLOTLIB in python. For the $i'-K_s$ color, we use the 1d-interpolator with the interpolation types 'slinear' (spline interpolation in first order) and 'nearest'. For the $g'i'K_s$ color-color information, we use the GRIDDATA multi-dimensional interpolator with the 'cubic' (spline interpolation in third order), 'linear' (piecewise linear interpolant) and 'nearest' method. We interpolate $i'-K_s$ or $g'i'K_s$ from the BC03 models to obtain the metallicity for our CSS candidates. Age is estimated simultaneously when using GRIDDATA together with the BC03 model information for $g'i'K_s$.

We estimate the metallicity and age uncertainties using a Monte-Carlo approach by drawing one thousand random values for each CSS passband luminosity from a normal probability distribution function with a mean corresponding to the observed magnitude and a standard deviation equal to the magnitude error, and propagating these values through the calculations explained above.

We stress that formally young ages might be either because the CSS formed relatively recently or they may host multiple stellar populations the younger of which may be dominating their emission. Spectroscopic follow-up is required to further constrain their stellar population parameters.

5.3.2.3 *Mass determination*

For the luminosity-weighted masses, we use three methods: 1) a χ^2 minimization approach, where the entire photometric information ($u'g'i'JK_s$) of the candidates is fit with the BC03 models with the same range described above for metallicity and age. 2) The second approach calculates the metallicity using GRIDATA in $g'i'K_s$ space with the 'nearest' method; with that information we can obtain the V-band luminosity assuming a M/L_V ratio at 12 Gyr to compute the masses. 3) The third method uses the result of the metallicity and age from the GRIDDATA interpolator using the 'nearest' method to obtain its V-band luminosity and M/L_V ratio for each CSS individually to determine their mass.

Beside our decision of using a particular population synthesis model (BC03), the set of filters to compute the mass-to-light conversion will also contribute to the systematic uncertainties in the mass determination (see Zhang et al., 2017),

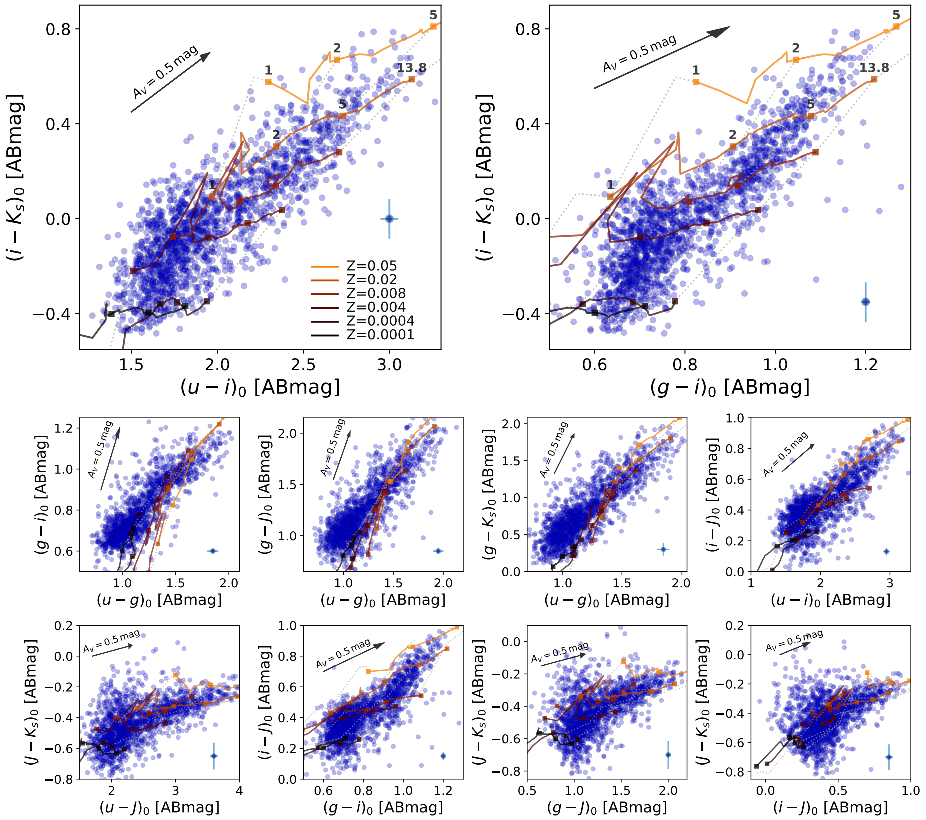

Figure 32: Color-color diagrams for 10 color-color combination with BC03 SSP models. SSP models from BC03 are overplotted with the metallicity range indicated in the legend. Ages of 1, 2, 5 and 13.8 Gyr are indicated in the iso-metallicity tracks with squares. Mean errors for each color-color diagram are shown in the bottom-right of each panel.

to which method one and two will be most vulnerable. The third method relies on the fact that the ages and metallicities computed for each CSS are close to their real values. We estimate the statistical mass uncertainties with the same Monte-Carlo method as for the age and metallicity uncertainties. Another caveat here is the assumption of simple stellar population models for CSSs. According to the studies of Galactic GCs, multiple stellar populations have been found either as features in the color-magnitude diagrams (multiple main-sequences and main-sequence turn-off magnitudes, broad color distributions and multi-modalities of red giant branch stars) and/or gradients in chemical abundance from spectroscopic studies (e.g. Piotto et al., 2007; Carretta et al., 2009). For a recent review on multiple stellar population in globular clusters we refer to Bastian, & Lardo (2017).

Figure 33 illustrates how the $g'i'K_s$ color-color plane encodes the stellar parameters metallicity, age and mass for various interpolation modes. In this figure, we can directly compare the systematics involved in the different interpolation methods used to estimate the CSS parameters, as well as observe the overall gradients in the color-color plane for each parameter. For the following analysis, we use the metallicity and age results from the GRIDDATA 'cubic' interpolation method using the $g'i'K_s$ grid, while the CSS masses are obtained using method 3) described above.

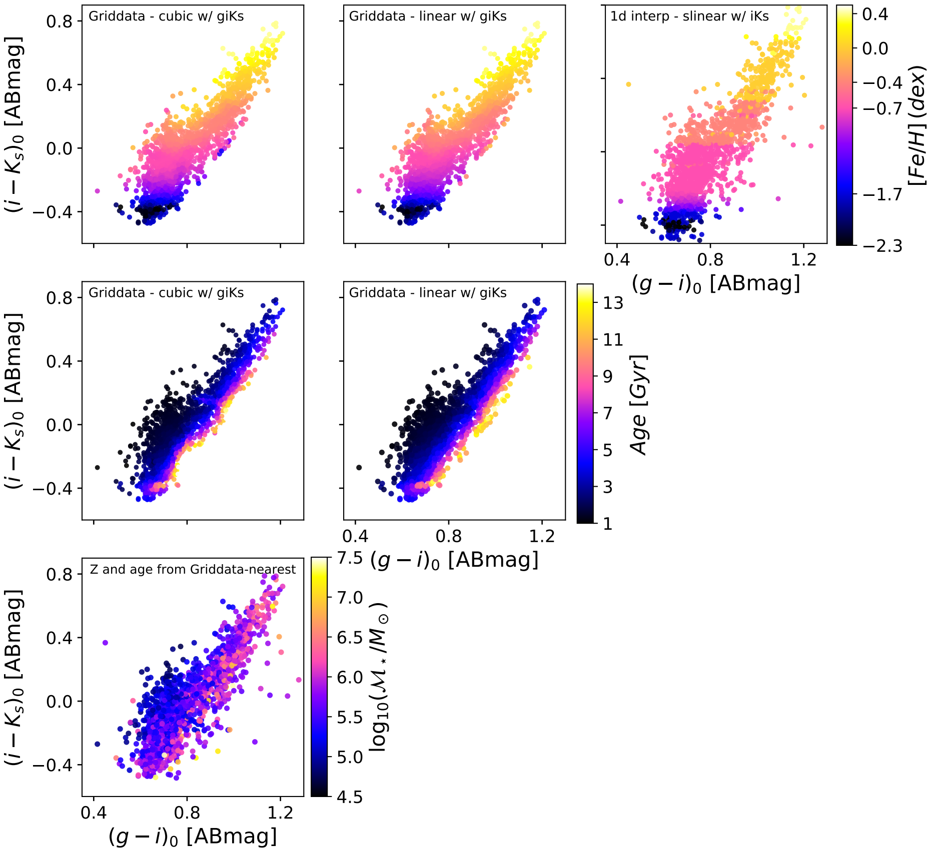

Figure 33: g′i′Ks diagram color coded with the different parameters for the CSS candidates, metallicity at the top panels, age at the middle panels and mass at the bottom panel. The method used for each panel is written in the top region.

5.3.2.4 *CSS stellar population parameter distributions*

The resulting distributions from all the methods explained above are shown in Figure 35 for all CSS stellar population parameters. Changing the interpolation method does not change the overall shape of the distributions for the case of the age and metallicity. However, the mass estimation can change significantly when using different methods, mainly due to the selection of M/L_V for individual CSSs. Method 1 and 2 estimate much more massive systems than method 3, simply because of artificially adopting a fixed mass-to-light ratio. We remind the reader that method 2 assumes an M/L_V for an age of 12 Gyr and method 3 uses the results from the GRIDDATA interpolation with the $g'i'K_s$ information. The age distribution shows that there is a significant number of younger CSSs with ages in the range of 1-4 Gyr. This results in lower M/L_V values and as a consequence leads to lower luminosity-weighted CSS masses. This causes an increase at the low-mass end of the distribution and a drop at high masses. This illustration is a reminder of the sensitivity of CSS mass estimates to their stellar population parameters.

The stellar mass distribution of our CSSs from method 3) varies in the range $\log(\mathcal{M}_\star/M_\odot) = 4.6-7.4$ with mean statistical uncertainty of 15% and a maximum mass uncertainty up to 50%. The uncertainties for age and metallicity are relatively high, because the model grid is in certain parameter space locations

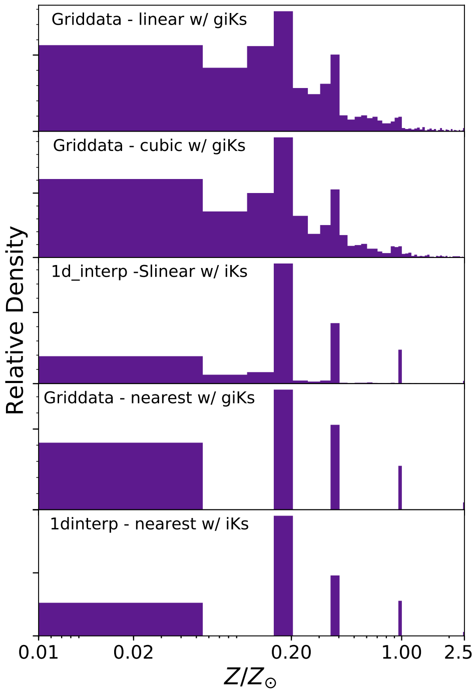

Figure 34: Metallicity distribution for the CSS candidates obtained using $i'K_s$ or $g'i'K_s$ information using BC03 models with different techniques, details are explained in the section 5.3.2.

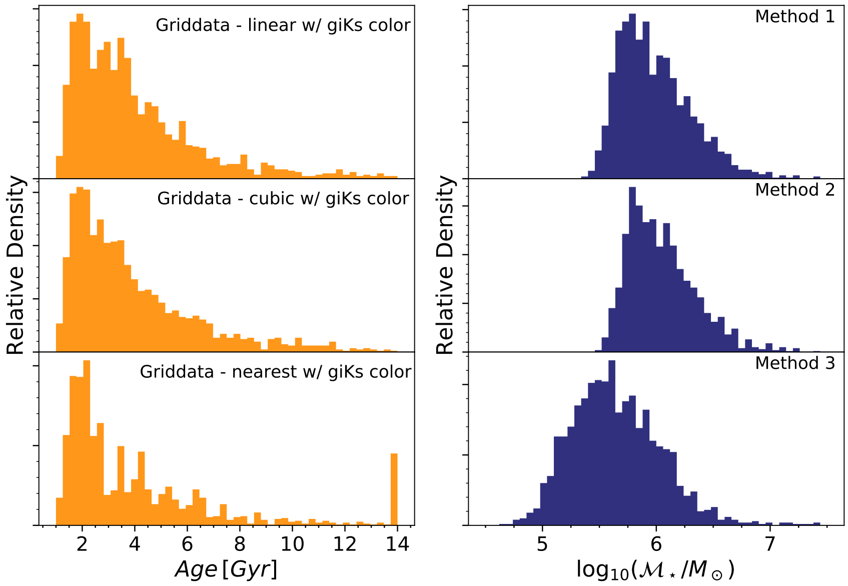

Figure 35: Age and mass distributions for the CSS candidates obtained using color information and BC03 models with different techniques, details are explained in the section 5.3.2.

quite dense in color-color space, so that a small variation in color can cause a significant change in age and/or metallicity. To avoid such systematics and analyze the broad average properties of the CSS in the Fornax core region we use only three sub-populations in age and metallicity to understand their main CSS population trends and remain least sensitive to the uncertainties in the derived photometric stellar population parameters.

5.3.3 *CSS color distribution as a function of cluster-centric distance*

Figure 36 shows the color distributions for $(u' - i')$, $(u' - K_s)$, $(g' - i')$, $(g' - K_s)$, $(i' - K_s')$ from top to bottom panels, respectively. The sample is divided into three subpopulations according to their distance with respect to the central Fornax galaxy (NGC 1399, cD galaxy). The CSSs located in the inner region of Fornax, i.e. up to one effective radius from NGC 1399 ($r_{\mathrm{eff,i}} = 5.05'$, see Iodice, et al., 2016), i.e. $r \leqslant 0.1$ deg are referred to as NGC 1399 inner CSSs. According to the study of Iodice, et al. (2016), the surface brightness profile of NGC 1399 extends out to $\sim 5{-}6r_{\mathrm{eff}}$. For this study, we call NGC 1399 outer CSSs those objects located within $1 < r_{\mathrm{eff}} \leqslant 5$ ($0.1 < r < 0.5$ deg). The third group are those CSSs residing outside $\sim 5r_{\mathrm{eff}}$ ($r > 0.5$ deg) and we refer to them as intra-cluster CSSs. We point out that the term intra-cluster CSSs merely refers to their location within Fornax with respect of the cD galaxy and does neither imply any formation mechanism nor origin.

NGC 1399 inner CSSs ($R_{\mathrm{eff}} \simeq 6$ kpc) show the classical bimodality seen in giant galaxies (e.g. Zepf, & Ashman, 1993; Puzia et al., 1999; Gebhardt, & Kissler-Patig, 1999; Larsen et al., 2001; Kundu, & Whitmore, 2001; Peng et al., 2006), which is more noticeable in the $(g'{-}i')$ color distribution. Outside the cluster centric distance of $R_{\mathrm{eff}} \simeq 0.1$ deg the number of red CSSs starts to decline, but a red CSS component is always present at all radii covered in this work out to $0.25r_{\mathrm{vir}} \simeq 350$ kpc. The ACSVCS study of Peng et al. (2006) on the color distribution of GCs in 100 ETGs in the Virgo cluster using HST/ACS data found observational evidence for bimodal or asymmetric GC color distributions. Clearly bimodal $(g{-}z)$ color distributions tend to be present only in the brightest galaxies. Another interesting result was that all the ACSVCS galaxies hold a sub-population of blue GCs, which have similar colors across the entire ACSVCS galaxy sample. Nonetheless, the fraction and color of red GCs depends strongly in the galaxy luminosity, with a decline in red GC numbers towards fainter galaxies. According to the ACSVCS results, the trend we see in Figure 36 for a declining fraction of red CSSs toward larger cluster centric distances is due to the change in host luminosity, where near the bright cD galaxy NGC 1399 a relatively large fraction of red CSSs is observed, while the CSS samples further out host a significantly smaller population of red CSS but instead are comprised of larger fractions of blue CSSs. This is indicative of the assembly history of the Fornax central galaxy, which likely grew by accretion of smaller systems onto the halo regions, thus augmenting the number of relatively blue CSSs.

5.3.4 *CSS mass distribution as a function of cluster-centric distance*

The stellar mass distribution of the CSSs in the Fornax regions is shown in Figure 37. The same three spatial sub-groups are used here, which are defined according to their radial distance to the cD galaxy NGC 1399 as in Figure 36. The probability density distribution for each sample is overplotted using an Epanechnikov-kernel density estimate together with the $1 - \sigma$ uncertainty ranges. The inset figures show the Aikake and Schwarz (Bayesian) information criteria (AIC and BIC, Ivezić et al., 2014), which define the most likely number of Gaussian components for each distribution; here we use the AIC. The corresponding Gaussians are indicated by the dashed curves.

NGC 1399 inner CSSs show an extended mass distribution with a significant component of more massive CSSs. Epanechnikov probability density and Aikake criteria favour two main components, with peaks at $\log_{10}(\mathcal{M}/M_\odot) \simeq 5.5$ and 6.0. Going outwards in radius, away from the cD galaxy, a remarkable feature is that the number of low-mass CSSs increases and the number of the most massive CSSs declines. Few massive CSSs are found in the intra-cluster CSS sub-group. NGC 1399 outer CSSs have a relatively sharp edge at the low-mass end of the distribution but a more extended tail towards the high-mass CSS regime. For the NGC 1399 outer CSSs and the intra-cluster CSSs the mass distribution is peaking near $\log_{10}(\mathcal{M}/M_\odot) \simeq 5.5$, which is similar to the lower-mass peak of the NGC 1399 inner CSS sub-sample. We remind the reader that our sample is complete for clusters with masses down to $\log_{10}(\mathcal{M}/M_\odot) = 5$, thus, the relative decrease in low-mass CSS numbers in the NGC 1399 inner CSS sub-sample is likely valid down to that mass limit, but has to be taken with caution.

5.3.5 *Age and metallicity trends*

To understand the general trends of the CSSs in the central of Fornax region, we divide the CSS ages and metallicities, estimated in Section 5.3.2, into three sub-samples. For metallicity the subsample are as follows: metal-poor CSSs with $Z/Z_\odot \leqslant 0.03$ or $[\mathrm{Fe/H}] \leqslant -1.5$ dex, intermediate metallicity CSSs with $0.03 < Z/Z_\odot \leqslant 0.5$ or $-1.5 < [\mathrm{Fe/H}] \leqslant -0.2$ dex and metal-rich CSSs with metallicities of $Z/Z_\odot > 0.5$ or $[\mathrm{Fe/H}] > -0.2$ dex. For age the three sub-sample are: young CSSs with ages $\leqslant 4$ Gyr, intermediate-age CSSs with ages between 4 and 8 Gyr and old CSSs with ages > 8 Gyr. Figure 38 shows the mass distributions for the metallicity sub-groups in the left panel and for the age sub-groups in the right panel.

We observe that the metal-poor CSSs with 144 objects has a sifnificanty narrower mass distribution compared with the intermediate metallicity or metal-rich CSS sub-groups. This narrow distribution has a peak mass at $\log_{10}(\mathcal{M}/M_\odot) \simeq 5.65$ and an extended tail towards the most massive CSSs. The most populated sub-group contains the intermediate metallicity CSSs, with 1132 members, the distribution of which shows a dominant component of low-mass CSSs with a peak around $\log_{10}(\mathcal{M}/M_\odot) \simeq 5.4$. We find no intermediate-metallicity CSS with masses larger than $\log_{10}(\mathcal{M}/M_\odot) \approx 6.5$, their distribution seems to favour at least three different components according to the Epanechnikov KDE, as well as AIC and BIC. Metal-rich CSSs seem to follow a broad Gaussian distribution with a peak at $\log_{10}(\mathcal{M}/M_\odot) \simeq 5.7$.

Following the definition of our age sub-groups, the young CSSs is the most populated subgroup with 1012 members. Their mass distribution appears bimodal according to the Epanechnikov KDE, AIC and BIC, with peaks at $\log_{10}(\mathcal{M}/M_\odot) \simeq 5.2$ and 5.7, with the dominant fraction belonging to the low-mass CSS regime and with no tail towards the more massive CSSs. The intermediate-age CSS mass distribution with 459 objects has two components with peaks at $\log_{10}(\mathcal{M}/M_\odot) \simeq 5.6$ and 6.1, significantly higher than the young CSS sub-sample. Old CSSs have a narrower distribution than the other two sub-groups, with a broad distribution centred around $\log_{10}(\mathcal{M}/M_\odot) \simeq 6$ and evidence for few CSSs with masses greater than $\log_{10}(\mathcal{M}/M_\odot) \simeq 6.5$.

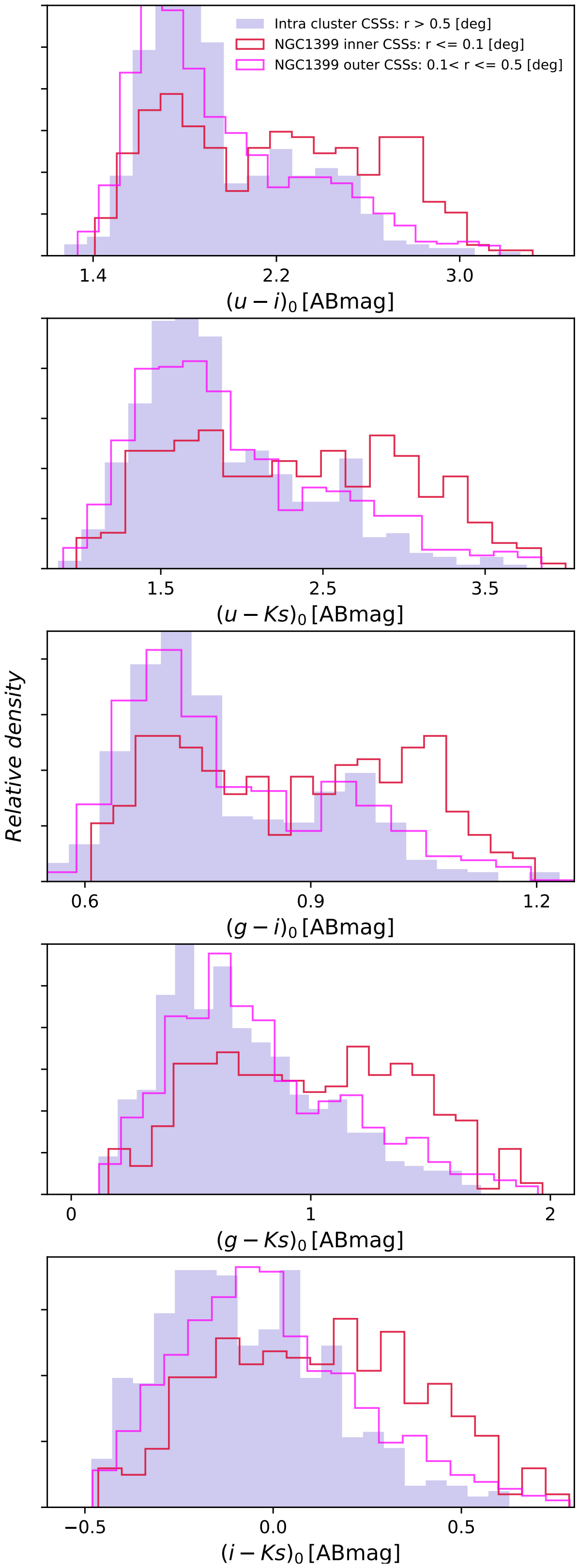

Figure 36: CSS color distributions for three different spatial sub-groups of CSSs: NGC 1399 inner CSSs located $r \leqslant 0.1$ deg (red), NGC 1399 outer CSSs within $0.1 < r \leqslant 0.5$ deg (pink), and intra-cluster CSSs at $r > 0.5$ deg (violet).

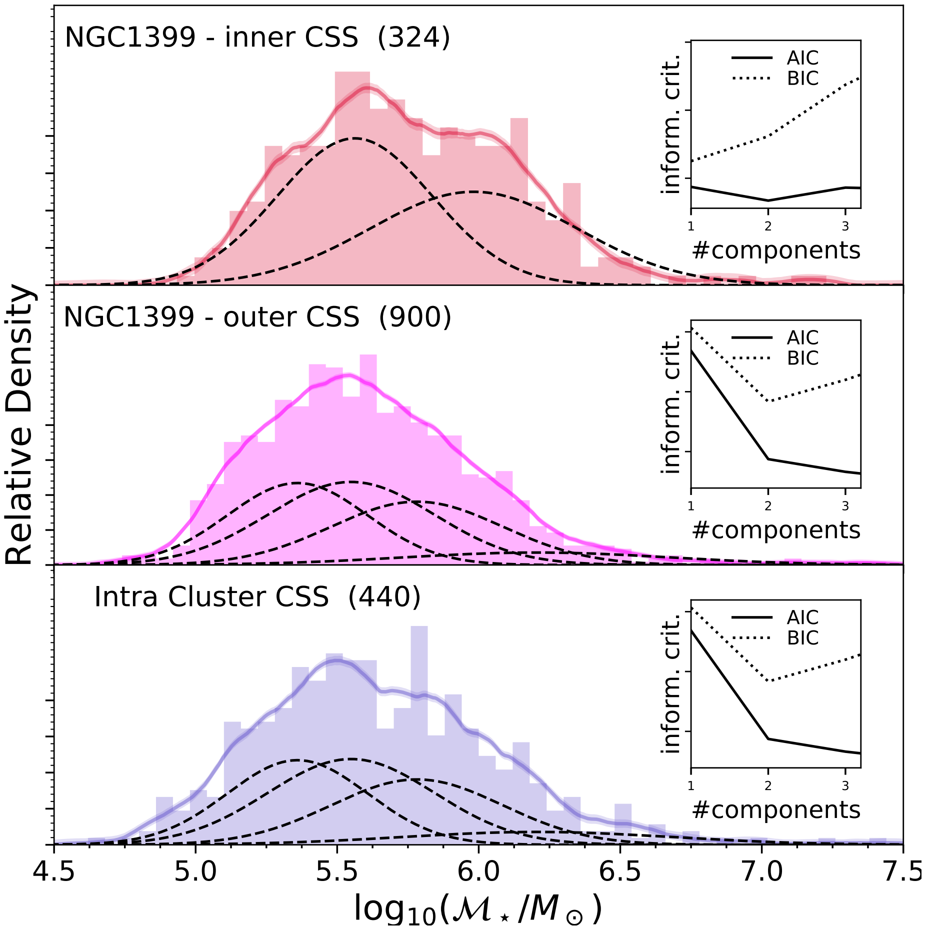

Figure 37: Mass distribution for the CSSs candidates in the central Fornax region. From top to bottom the panel illustrates: inner NGC 1399 CSSs ($r \leqslant 0.1$ deg), outer NGC 1399 CSSs ($0.1 < r \leqslant 0.5$ deg) and intra-cluster CSSs ($r > 0.5$ deg). More explanation for the subplots is given in the text. The size of each sample is given in parentheses in the corresponding panel. The Epanechnikov-kernel density estimate together with the $1-\sigma$ uncertainty ranges is indicated in each subplot. The inset figures show the Aikake and Schwarzâs (Bayesian) information criteria (AIC and BIC, Ivezić et al., 2014), which define the most likely number of Gaussian components for each distributions. We show the corresponding Gaussians with dashed curves using the AIC criteria.

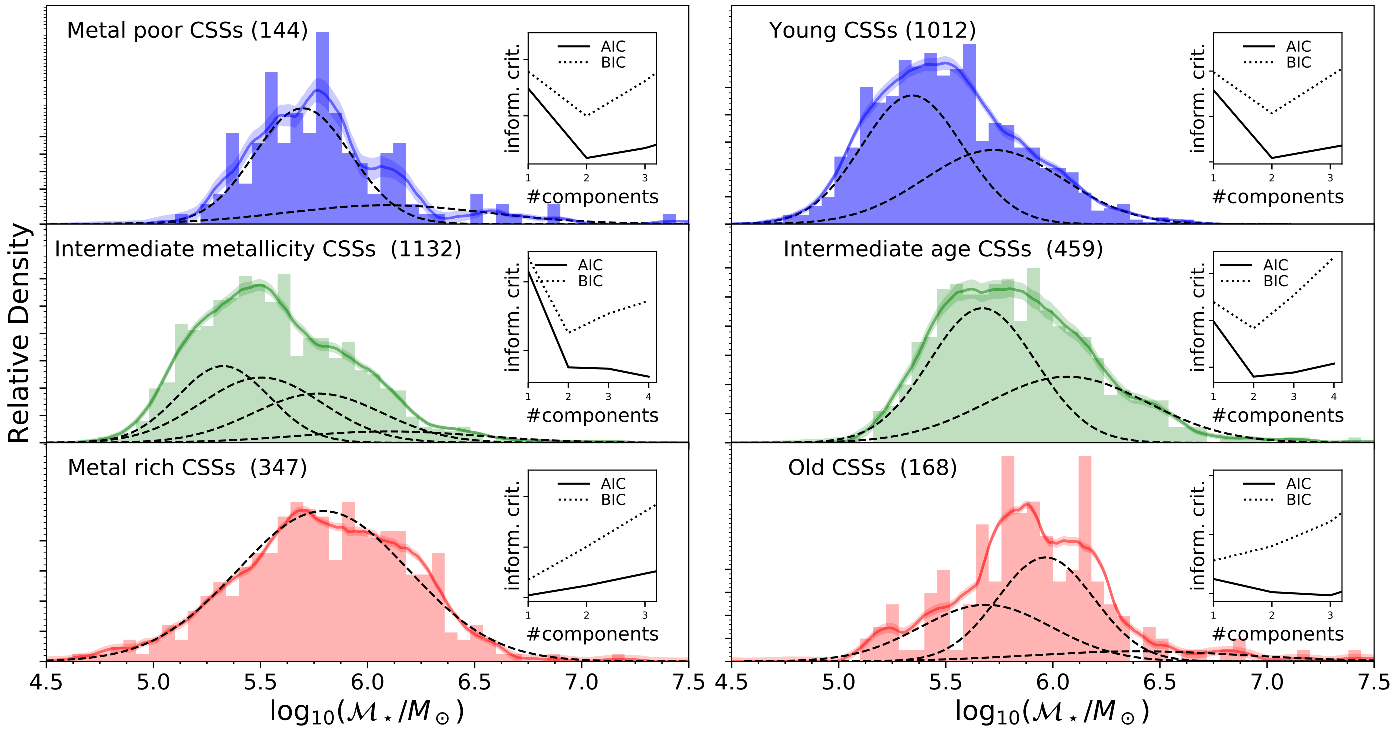

Figure 38: CSS mass distributions for three metallicity and age sub-groups. *Left panels:* the sub-groups are, from top to bottom, metal-poor CSSs with $Z/Z_\odot \leqslant 0.03$, intermediate metallicity with $0.03 < Z/Z_\odot \leqslant 0.5$ and metal-rich CSSs with metallicities of $Z/Z_\odot > 0.5$. *Right panels:* the subgroups in age are from top to bottom, young CSSs with ages $\leqslant 4$ Gyr, intermediate ages in the range $4 <$age$\leqslant 8$ Gyr and old CSSs with ages > 8 Gyr. The same probability density estimator and Bayesian analysis as in Figure 37 for the number of Gaussian components for each distribution are shown here.

5.4 DISCUSSION

CSSs are a powerful tool to decipher the formation and The spatial distribution of CSS candidates in the central region of Fornax ($r < 0.25\, r_{\rm vir} \simeq 350\,{\rm kpc}$) as a function of their stellar population properties can give us information about how this galaxy cluster has assembled and evolved over time.

5.4.1 *Spatial distributions*

The spatial distributions of the three metallicity sub-groups are shown in Figure 39. Additionally, we overplay the locations of all dwarf galaxies identified by NGFS with grey ellipses, taken from Eigenthaler et al. (2018), where the transparency indicates their magnitudes (see the top-left legend). We find that the three CSS metallicity sub-samples have entirely different spatial distributions. While the metal-poor CSSs appear to follow an intra-cluster distribution with no clustering around the Fornax galaxies, the intermediate-metallicity CSSs show a markedly asymmetric distribution along the East-West axis of the Fornax cluster, resembling a "disky" structure, with many of them clustered around NGC 1399 and other lower-luminosity galaxies located within this "disky" structure, with the exception of NGC 1380. On the other hand, most of the metal-rich CSSs appear to be clustered around the cD galaxy NGC 1399 and fewer around the other bright galaxy members of Fornax, such as NGC 1404, NGC 1387 and NGC 1380.

The spatial distribution showing the three CSS age sub-groups are shown in Figure 40. Young CSSs have an asymmetric distribution with most of them located in the East-West region of the Fornax cluster and a trend towards the West side of the cluster and the surroundings of NGC 1399. Clustering of young CSSs around galaxies is seen for many and not only around the brightest ones, but also around some galaxies that would be considered dwarf ellipticals. Despite that NGC 1380 is more into the South direction of Fornax, it also has a substantial number of young CSSs in its vicinity. In general, the young and the intermediate-metallicity CSSs have an overall similar spatial distribution. Intermediate-age CSSs tend to be clustered around some of the brightest galaxies in Fornax, NGC 1399, NGC 1379 and NGC 1380, with few of them sparsely distributed at outer cluster radii. Old CSSs are not confined to any special places in the Fornax cluster. There are two main agglomerations of old CSS seen, one around NGC 1399 and in its South-West direction and the other one in the vicinity of the galaxy NGC 1374 with seems to have a group of dwarfs candidates orbiting it, but many of the old CSSs are located in between galaxies at larger distances from the cD galaxy.

The different distributions for the various metallicity and age CSS sub-groups give us a hint on how the assembly of the Fornax cluster might have occurred. The oldest and most metal-poor CSSs are more sparsely distributed. They may have formed in the initial epochs of the Fornax cluster and stayed on energetic orbits or were ejected out from the core regions when the cluster virialized and became more expanded as more structures were accreted. The young and intermediate-metallicity CSSs are distributed along the East-West region of the Fornax cluster. This spatial structure points to a picture in which the formation of new and more metal-enriched CSS sub-population occurred in a "disky" structure, likely due to galaxy mergers and interactions falling into Fornax along a filament. Spectroscopic follow-up shall provide invaluable access to the kinematics of these sub-groups in order to examine whether they show coherent phase-space signatures or whether they have just evolved as pressure supported systems. The intermediate-age and metal-rich CSSs seems to have a more centrally concentrated distribution towards the most inner core of Fornax, around NGC 1399, NGC 1404 and NGC 1387 with the exception of the lenticular galaxy, NGC 1380. These CSSs were likely formed within their parent galaxy halos where the most metal-enriched gas was available prior to their formation.

We point out that these spatial CSS configurations are reminiscent of the structures seen in the Chandra X-ray imaging of the Fornax core region, which shows the complexity of the temperature in the hot intracluster gas between NGC 1399, NGC 1404 and NGC 1387 (Scharf et al., 2005).

5.4.2 *Comparison with other CSSs*

The $(u'-i')_0$ vs. $(i'-K_s)_0$, or $u'i'K_s$ diagram and the $u'g'K_s$ diagram are illustrated in Figure 41 for CSS candidates. A reddening vector of $A_V = 0.5$ mag is shown in the upper-left part of each panel to point out how the intrinsic reddening of Fornax may affect our photometry, as we do not posses intrinsic extinction information. To understand the global trend of NGFS CSSs in color-color space, we fit a locally weighted scatterplot smoothing (LOWESS) to the data (e.g. Cleveland, 1981), shown as red curve. We compare our Fornax CSS sample with the CSS sample obtained from the closest galaxy cluster ($D_L = 16.5$ Mpc, Mei et al., 2007; Blakeslee et al., 2009) and observed by the *Next Generation Virgo Survey* and its near-infrared extension (NGVS and NGVS-IR; Ferrarese et al., 2012; Muñoz et al., 2014). For comparison, we plot the fiducial of the Virgo CSSs from Powalka et al. (2016b), shown as dark curve in Figure 41, who used aperture photometry with a broad SED distribution u^*, g, r, i, z, K_s to select the CSS in the core region of Virgo, with a total of 1846 candidates. They implemented strict selection criteria that remove all low-mass candidates ($\leqslant 10^{5.5}\,M_\odot$), which is driven mainly by the photometric uncertainties in the NGVS u^*-band. Their fiducial SEDs are estimated using maximum likelihood polynomial fits to the GC color-color distributions. Although NGVS and NGFS cover roughly the same spatial region in each galaxy cluster ($r \sim 300$ kpc and 350 kpc, respectively), we observe clear differences between the CSS color-color trends of both cluster core regions. Virgo CSSs have slightly steeper trends in the $u'i'K_s$ and $u'g'K_s$ diagrams in Figure 41 compared to Fornax CSSs with the largest offsets at the reddest CSS colors, while in the corresponding $g'i'K_s$ CMD, the complete Virgo fiducial seems to be shifted in $(i-K_s)$ by 0.1 or 0.15 mag towards redder colors. We will come back to this interesting difference between the two galaxy clusters in the discussion section.

5.5 SUMMARY

We have studied the compact stellar systems (CSSs) in the Fornax core region ($\leqslant r_{vir}/4$) using deep and homogeneous $u'g'i'JK_s$ photometry. A selection of 1666 CSS candidates was performed with support vector machine (SVM) machine-learning techniques using a training sample of confirmed stars and CSSs in the Fornax cluster, together with their broad photometric and compactness information. In the following we summarize our main results.

- Color-magnitude diagrams using various filter combinations show in all color-combinations that there is a larger fraction of blue CSSs compared to red ones. The clearest bimodality in color is seen in the g' and i' vs. $(g'-i')$ color-magnitude diagrams.

- Metallicities and ages were estimated for our CSS candidates using the $g'i'K_s$ information from BC03 models with the GRIDDATA interpolator. The CSSs span the entire range of metallicities in the model grid from $[\mathrm{Fe/H}] = -2.3$ to $+0.4$, with the majority having intermediate metallicities. The peak in the distribution is at $[\mathrm{Fe/H}] \simeq -0.7$ dex. The age distribution of Fornax CSSs shows a large fraction of CSSs with ages in the range 1-4 Gyr with the majority being younger than 8 Gyr.
- Stellar masses were computed for the CSS candidates using the GRIDDATA interpolator results for metallicity and age. The stellar mass distribution of our CSSs runs within the range of $\log(\mathcal{M}_\star/M_\odot) = 4.6$–$7.4$ with a mean uncertainty of $15 \pm 13\%$ and maximum mass uncertainty up to 50%.
- We divide the CSS into three subsamples according to their cluster-centric distances from NGC 1399, into inner and outer NGC 1399 CSSs and intra-cluster CSSs. The inner NGC 1399 CSSs shows a bimodal color distribution which is most noticeable in $(g' - i')$. Outside of cluster centric distances $r > 1 r_{\mathrm{eff}} \simeq 0.1$ deg, the number of red CSSs starts to decline, but a red CSS component is always present within the radii covered in this work, i.e. out to $r = 0.25\, r_{\mathrm{vir}} \simeq 350\mathrm{kpc}$.
- The mass distribution in the same three spatial sub-samples showed that the inner NGC 1399 CSSs are bimodal in mass with peaks at $\log(\mathcal{M}_\star/M_\odot) \simeq 5.5$ and 6.0. Away from the cD galaxy, the amount of low-mass CSSs grows and the number of massive CSSs declines. Few massive CSSs are found in the intra-cluster CSS sub-group.
- The mass distribution for the three metallicity sub-samples shows that the metal-poor CSS have a narrower distribution compared to the intermediate-metallicity and metal-rich CSSs which show an extended tail towards the most massive CSSs. The intermediate-metallicity CSSs show a dominant component of low-mass CSSs, with a peak around $\log(\mathcal{M}_\star/M_\odot) \simeq 5.4$. Metal-rich CSSs follow a broad Gaussian distribution with a peak at $\log(\mathcal{M}_\star/M_\odot) \simeq 5.7$.
- The mass distribution for the three age sub-samples shows that the most populated sub-group is the one of young CSSs with ages <4 Gyr, consistent with a bimodal mass distribution with peaks at $\log(\mathcal{M}_\star/M_\odot) \simeq 5.2$ and 5.7. The intermediate age CSSs also show evidence for a bimodal distribution with peaks at $\log(\mathcal{M}_\star/M_\odot) \simeq 5.6$ and 6.1. Old CSSs have a narrower distribution than the other two subgroups, with a predominant distribution around $\log(\mathcal{M}_\star/M_\odot) \simeq 6.0$.
- The spatial distribution of CSSs in the Fornax core region for the different age and metallicity sub-groups shows that the metal-poor and old CSSs are sparsely and widely distributed. The intermediate-metallicity and young CSSs are preferentially located along the East-West direction of Fornax centered on NGC 1399. The most metal-rich CSSs are concentrated in the vicinity of NGC 1399 and around the brightest Fornax galaxies. These different distributions for the metallicity and age sub-groups allow us to constrain the mass assembly history of the Fornax galaxy cluster.

The NGFS data presented here for the CSSs in the central regions of the Fornax galaxy cluster shows the powerful of broad SED coverage to study the stellar population properties of the CSS candidates. Not only in terms of selection method, but also to estimate important properties such as age, metallicity and mass. This is the first panchromatic catalog of CSSs in the Fornax cluster for a wide and homogeneously mapped area.

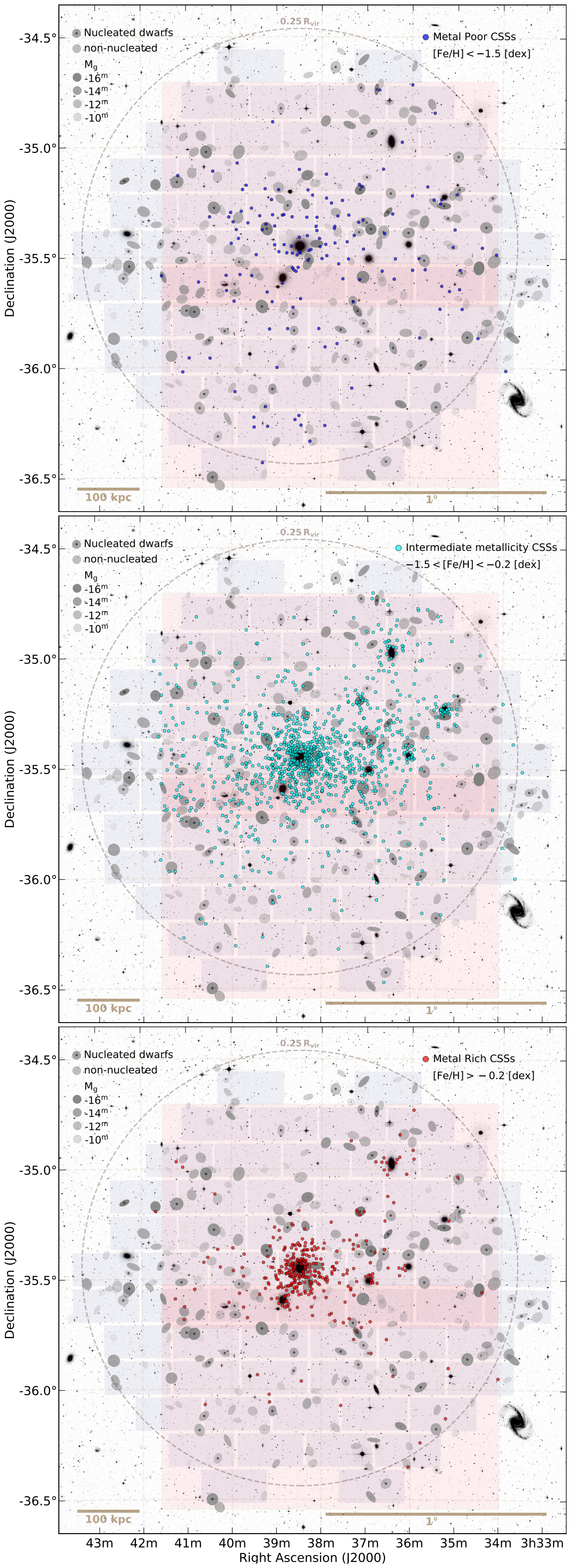

Figure 39: CSS spatial distribution in the central regions of the Fornax galaxy cluster for the three metallicity cuts. Metal-poor CSSs ($Z/Z_\odot \leqslant 0.004$) are shown as blue circles in the top panel, intermediate-metallicity CSSs ($0.004 < Z/Z_\odot \leqslant 0.5$) are shown as cyan circles in the middle panel and metal-rich CSSs ($Z/Z_\odot > 0.5$) are shown as red circles in the bottom panel. Each subplot shows the DECam footprint in shaded gray and two pointings of the VIRCam footprint in shaded red. Overplotted are the NGFS dwarfs in this region from Eigenthaler et al. (2018).

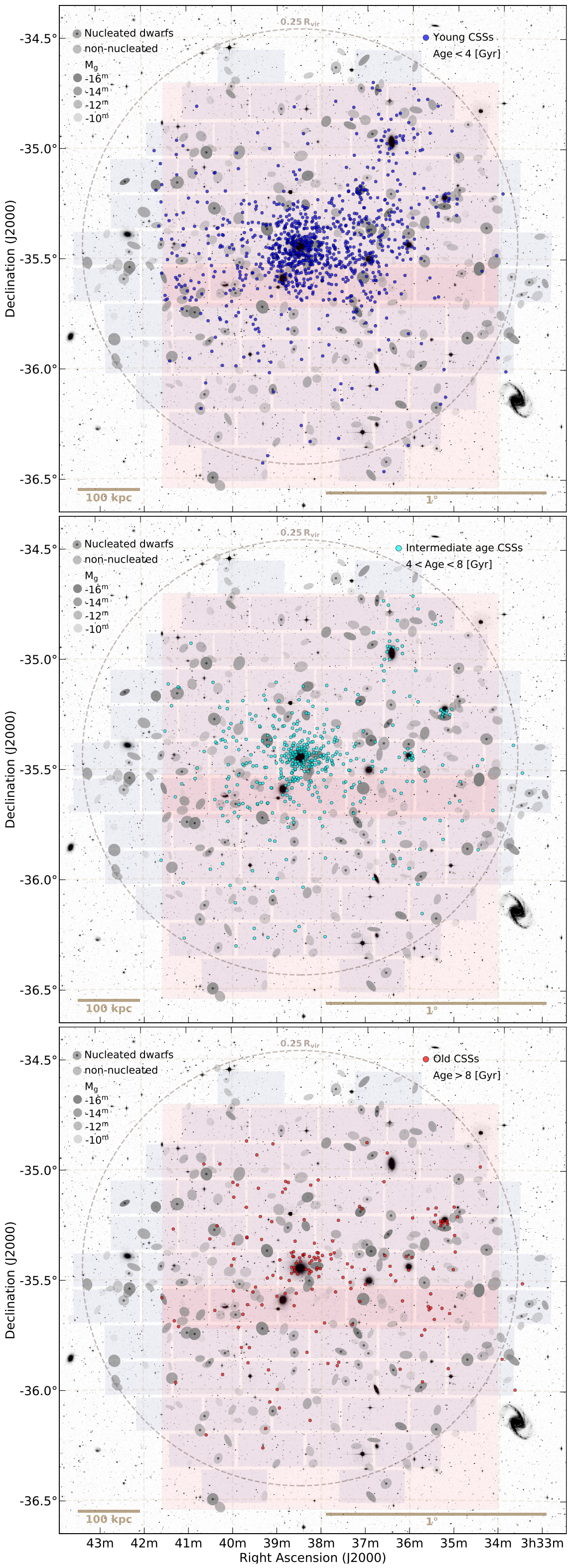

Figure 40: CSS spatial distribution of the three age sub-populations. Young CSSs (age $\leqslant$ 4 Gyr) are shown as blue circles in the top panel, intermediate-age CSSs ($4 <$ age $\leqslant 8$ Gyr) are shown as cyan circles in the middle panel and old CSSs (age > 8 Gyr) are shown as red circles in the bottom panel. Each subplot shows the DECam footprint in shaded grey and two pointings of the VIRCam footprint in shaded red. Overplotted are the NGFS dwarfs in this region from Eigenthaler et al. (2018).

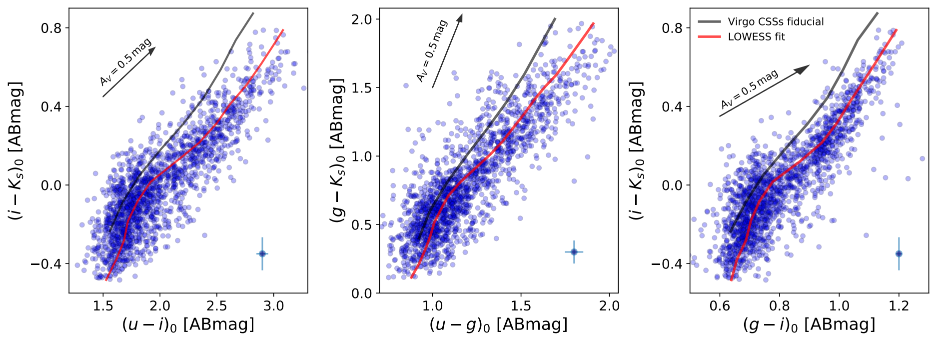

Figure 41: $u'i'K_s$ (left), $u'g'K_s$ (middle) and $g'i'K_s$ (right) color-color diagrams for the NGFS CSS candidates. Red curves show the LOWESS fits to the Fornax CSS color-color distributions. Black curves are the fiducial fits to the Virgo CSSs (Powalka et al., 2016b). Median color error bars are shown in the bottom-right side of each panel, together with a reddening vector of $A_V = 0.5\,\mathrm{mag}$ in the upper left corner of each panel.

6

DWARF GALAXIES IN A GROUP ENVIRONMENT: THE CASE OF HICKSON COMPACT GROUP 90

6.1 CONTEXT

In recent years, deep observations conducted with wide-field imaging cameras are reaching low-surface brightness (LSB) levels, comparable with the faint outer stellar halos of galaxies ($\mu_i \approx 28 - 30$ mag arcsec^{-2}). Many LSB dwarf and/or UDGs with $\langle\mu_i\rangle_{\mathrm{eff}} \geqslant 25$ mag arcsec^{-2} have been identified in a range of environments (see the introduction Sect.1.2) including the LG, nearby galaxies, loose galaxy groups, and in more massive and dense galaxy clusters. Such dense environments where galaxy-galaxy interactions are relatively common are interesting sites to study dwarfs due to their susceptibility to galaxy transformation processes.

The varied environments where faint dwarf galaxies have been detected so far make compact galaxy groups tempting places to look for LSB dwarfs and UDGs. In this work we report the discovery of five LSB dwarf galaxy candidates associated with HCG 90 based on deep U- and I-band imaging, and compare their properties with those of other LSB dwarf galaxies recently reported in the literature.

6.2 OBSERVATIONS AND DATA REDUCTION

We obtained deep near-ultraviolet (NUV) and optical imaging with the *Visible Multi-Object Spectrograph* (VIMOS) instrument in the U- and I-bands as part of the service-mode programme P94.B-0366 (PI: Taylor). VIMOS is mounted on UT3 (Melipal) of the *Very Large Telescope* (VLT), and is comprised of four CCDs each with a $7' \times 8'$field of view and a pixel size of 0.205"$\simeq$37.3 pc at a distance of 33.1 Mpc. The four VIMOS quadrants were placed to cover the four giant galaxies HCG 90a, b, c, and d, as well as several of the known group galaxies (see Fig. 42).

The NUV observations were broken up into five observing blocks (OBs) each consisting of 4×930 s exposures, conducted during the nights of October 24-25th, 2014. An additional OB with 3×930 s was observed on November 18th, 2014; however, we do not include these data in the present work due to the significantly poorer seeing ($\sim 1.8''$) compared to the previous observations ($0.7 - 1.2''$). The optical images were likewise taken under excellent seeing conditions ($0.6 - 1.0''$), and were broken up into two OBs each of 6×546 s exposures conducted on October 1st and 28th, 2014. All sub-integrations were dithered with steps of a few arcseconds. One quadrant of the VIMOS field of view was significantly vignetted by the guide probe and thus not used in the subsequent analysis (see dashed box in Fig. 42).

The raw images were processed by the VIMOS pipeline (v3.0.6) using the ESOREX (v3.12) framework to correct for bias, flat-fielding, bad pixels, and cosmic rays. The background (sky) subtraction and final image stacking were performed using custom PYTHON scripts. For the background subtraction, we mask objects in the field, and model the sky with a thin plate spline rather than using contiguous images to estimate the sky level. To register and stack the individ-

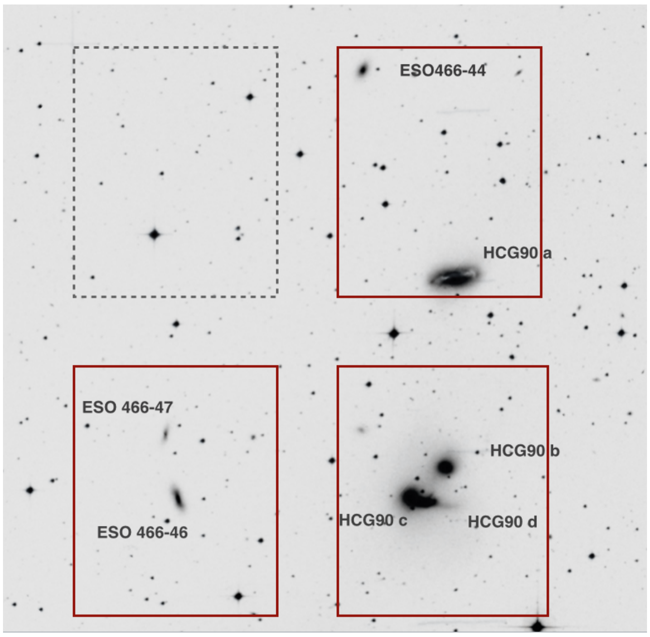

Figure 42: SDSS colored image of the central 21 ′ × 21′region in HCG 90, corresponding to 202 kpc × 202 kpc assuming a distance of 33.1 Mpc. Several prominent group members are indicated on the figure. The rectangles show the field of view of VLT/VIMOS. Note that due to severe guide-probe vignetting during the service-mode observations we were not able to use the upper left quadrant for our analysis (dashed rectangle).

ual exposures we use the ASTROMATIC[1] software SEXTRACTOR (v2.19.5; Bertin & Arnouts, 1996), SCAMP (v2.0.4; Bertin , 2006), and SWARP (v2.38.0; Bertin et al., 2002). For the astrometric calibration we use reference stars from the 2MASS Point Source Catalog (Skrutskie et al., 2006). Photometric zero points are calculated based on standard star fields from the Stetson catalog (Stetson, 2000) taken during the observations, which were processed in an identical way as the science frames.

6.3 ANALYSIS

The final U- and I-band stacks were visually inspected for diffuse sources characteristic of dwarf galaxies, revealing five potential candidates. The red boxes in Fig. 43 show the locations of the new dwarfs, while blue boxes show a dwarf galaxy previously discovered by Zabludoff & Mulchaey (1998) and tidal debris associated with HCG 90b. Four of the new dwarf candidates, HCG90-DW1, -DW2, -DW3 and -DW4 (see Fig. 43, panel *A*), are located between HCG 90a and ESO 466-44, while the fifth dwarf candidate, HCG90-DW5, is located to the SE of the three central HCG 90 galaxies (see panel *B*). Small postage-stamp panels show more detailed views of the new dwarf galaxies. From top-to-bottom in panel *A* we note a potentially nucleated dwarf candidate with a compact central component, a LSB candidate with a relatively undisturbed morphology, and lastly, a candidate with a very irregular shape. The latter object shows two

---

[1] http://www.astromatic.net

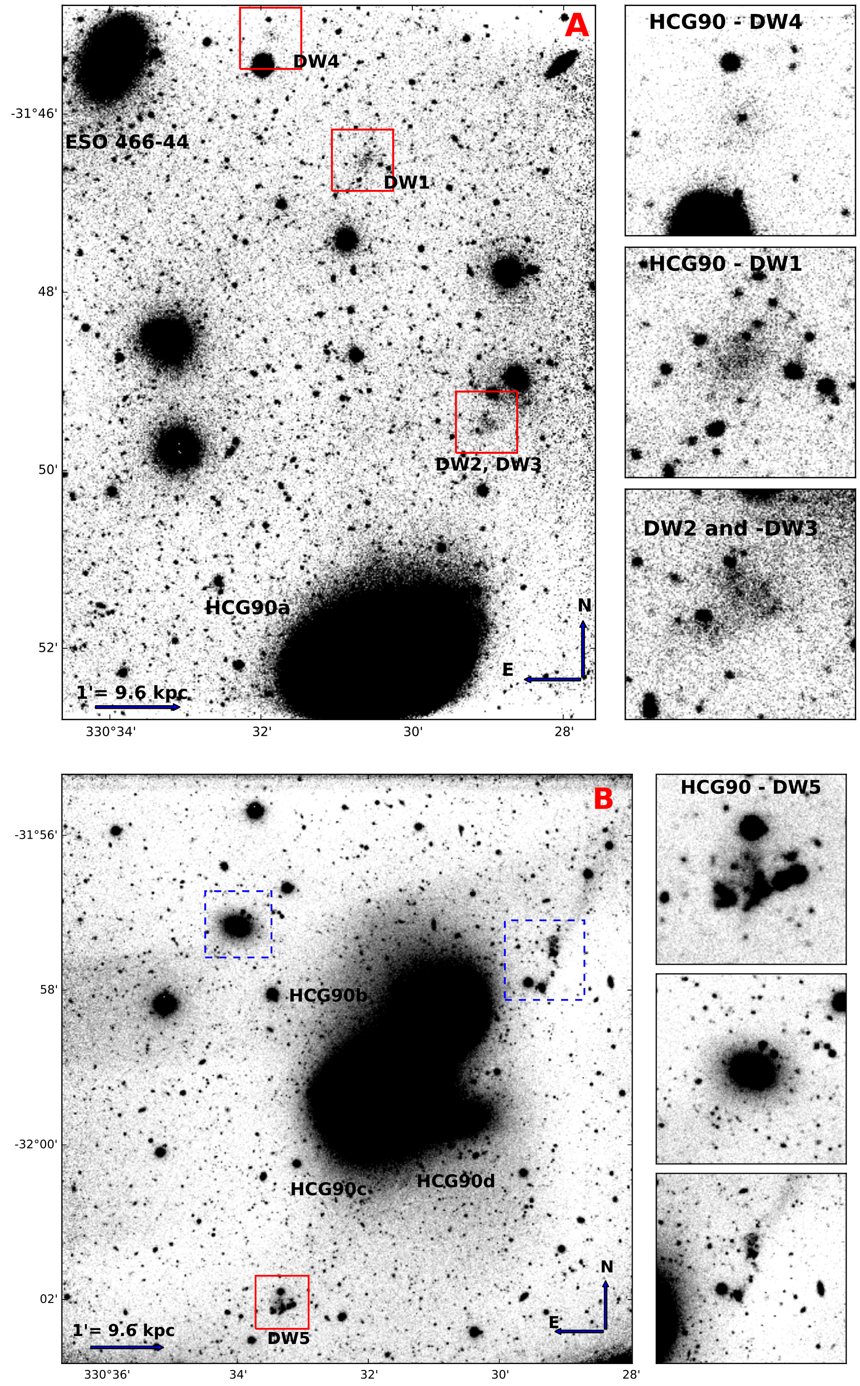

Figure 43: U-band VLT/VIMOS images of the new dwarf candidates, marked by red boxes. *Panel A:* The region around HCG90a and the galaxy ESO466-44 is shown alongside candidate postage-stamp cutouts of the individual dwarf candidates. *Panel B:* A similar view of the core region of HCG 90 is shown. A new dwarf galaxy candidate is indicated by the red box, while blue dashed boxes indicate a member previously catalogued by Zabludoff & Mulchaey (1998), as well as a candidate potentially caught in the process of being tidally disrupted by HCG 90b.

components that potentially represent a binary dwarf system similar to those identified in more diffuse galaxy groups (e.g. Crnojević et al., 2014).

The top postage stamp beside panel *B* shows the fifth dwarf candidate, which is unfortunately heavily contaminated by foreground stars that prevent accurate determination of its structural parameters. To the East of HCG 90b, we locate an object catalogued by Zabludoff & Mulchaey (1998) as a member of HCG 90 which is likely to be a dwarf galaxy; however, there are no further studies of this object in the literature. In the bottom postage-stamp panel, we show tidal features associated with the galaxy HCG 90b. This feature shows signs of an object caught in the act of disruption and/or tidal stripping. For the five new dwarf candidates, we derive structural parameters and investigate their morphological properties.

Table 3: HCG 90 LSB dwarf candidate photometry and structural parameters. The last row summarizes the corresponding information for the central object in HCG90-DW4 performed with Sérsic surface brightness model.

ID	RA(J2000) [hh:mm:ss.ss]	Dec(J2000) [dd:mm:ss.ss]	$M_{U,0}$ [mag]	n_U [a]	r_{eff_U} [arcsec]	r_{eff_U} [b] [kpc]	b/a	n_I [a]	r_{eff_I} [arcsec]	r_{eff_I} [b] [kpc]	$(U-I)_0$ [mag]
HCG90-DW1	22:02:02.47	−31:46:31.87	$-10.50^{+0.02}_{-0.09}$	0.51	$5.27^{+0.06}_{-0.08}$	$0.959^{+0.011}_{-0.014}$	0.67	0.42	$5.53^{+0.12}_{-0.01}$	$1.006^{+0.021}_{-0.001}$	2.21
HCG90-DW2	22:01:55.97	−31:49:29.46	$-10.83^{+0.08}_{-0.10}$	0.42	$6.06^{+0.40}_{-0.19}$	$1.103^{+0.072}_{-0.034}$	0.65	0.57	$8.34^{+0.60}_{-0.55}$	$1.520^{+0.108}_{-0.099}$	1.96
HCG90-DW3	22:01:56.58	−31:49:35.86	$-9.42^{+0.04}_{-0.03}$	0.35	$3.76^{+0.23}_{-0.32}$	$0.684^{+0.042}_{-0.058}$	0.55	0.48	$4.67^{+0.74}_{-0.32}$	$0.850^{+0.134}_{-0.058}$	1.16
HCG90-DW4	22:02:07.44	−31:45:07.32	$-10.02^{+0.1}_{-0.2}$	0.41	$4.11^{+0.11}_{-0.22}$	$0.747^{+0.021}_{-0.040}$	0.95	0.58	$4.43^{+0.42}_{-0.35}$	$0.805^{+0.076}_{-0.063}$	2.12
HCG90-DW5	22:02:13.41	−32:02:04.39	$-11.65^{+0.2}_{-0.2}$	0.35	$5.68^{+0.31}_{-0.30}$	$1.034^{+0.056}_{-0.054}$	0.65	0.31	$5.81^{+0.33}_{-0.30}$	$1.057^{+0.055}_{-0.060}$	1.14
HCG90-DW4n [c]	22:02:07.45	−31:45:07.12	$-7.42^{+0.1}_{-0.2}$	0.69	$0.35^{+0.06}_{-0.12}$	$0.063^{+0.010}_{-0.022}$	0.48	0.71	$0.25^{+0.11}_{-0.07}$	$0.046^{+0.020}_{-0.002}$	1.51

[a] Sérsic index (Sérsic , 1963; Caon et al., 1993);

[b] Assuming a distance of 33.1 Mpc (Blakeslee et al., 2001);

[c] HCG90-DW4 central object - Sérsic profile

The structural parameters for each dwarf candidate are determined using GALFIT (v.3.0.5.; Peng et al., 2010) following a multi-step procedure. We first create individual 41″×41″(7.4 × 7.4 kpc) cutout images centered on each candidate. Next we use the SExtractor segmentation maps to mask the neighboring sources to model only the dwarf light. In addition, an input PSF image is also used, which is created using PSFEx (v.3.16.1; Bertin, 2011). The surface brightness distributions are fit with a one-component Sérsic profile (Sérsic , 1963). As these dwarf candidates are LSB galaxies, GALFIT initially could not find stable fit solutions, except for HCG90-DW1, for which the solution easily converged. For the rest, we apply the same iterative technique developed for the recently discovered faint dwarf candidates in the Fornax cluster (Muñoz et al., 2015, see their § 3) to refine the fit. First, we estimate the total galaxy magnitude from SExtractor MAG_AUTO as an initial guess and keep it fixed while fitting the Sérsic model. The output parameters from this run are then fixed and the magnitude is recomputed. Finally, for the last run, we again estimate the parameters keeping the newly measured magnitude fixed. The resulting models and residuals are visually inspected for each dwarf candidate to confirm that the fits are robust, and we summarize the derived structural parameters in Table 3.

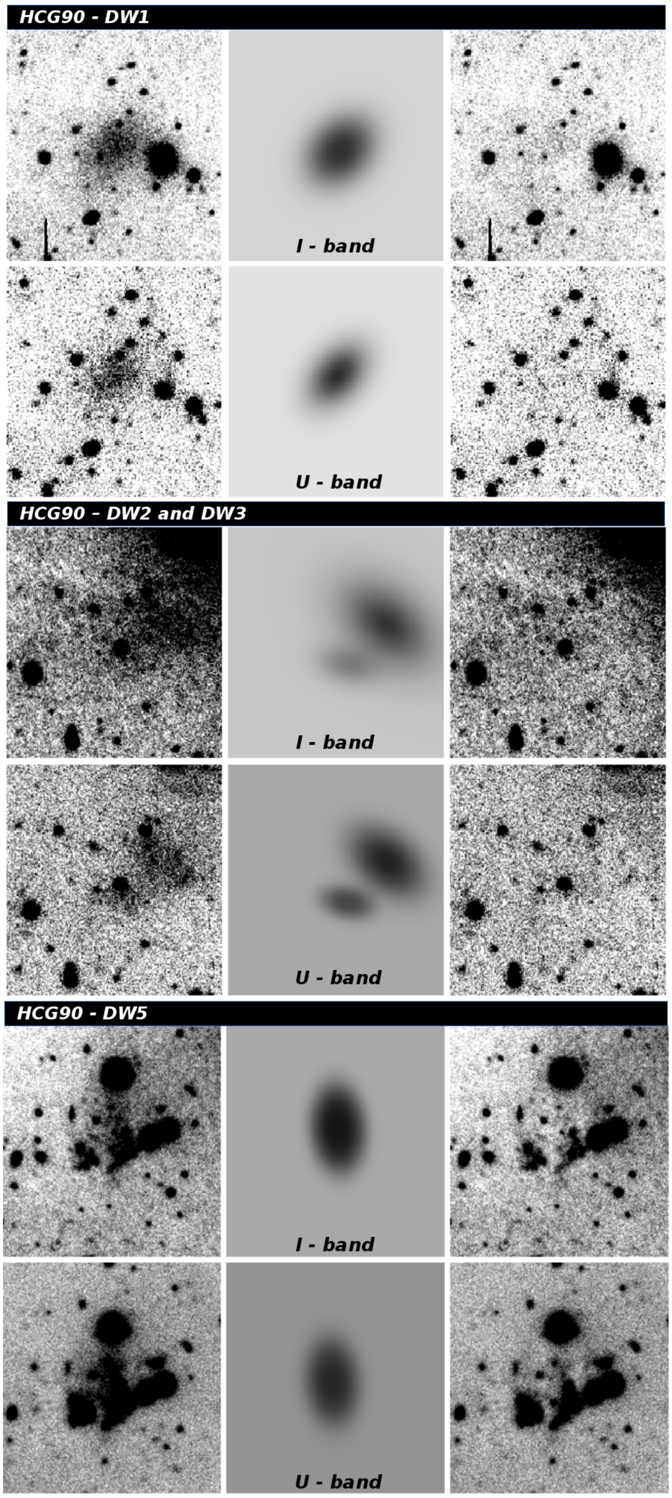

Figure 44: Illustrations of the surface brightness light profile fitting procedure, conducted in both I- and U-bands, shown in the top and bottom panel rows, respectively. For each of the three panels, the left-most postage stamps are the processed science frames in the corresponding filter, while the middle and right-most cutouts show our GALFIT models and residual images, respectively.

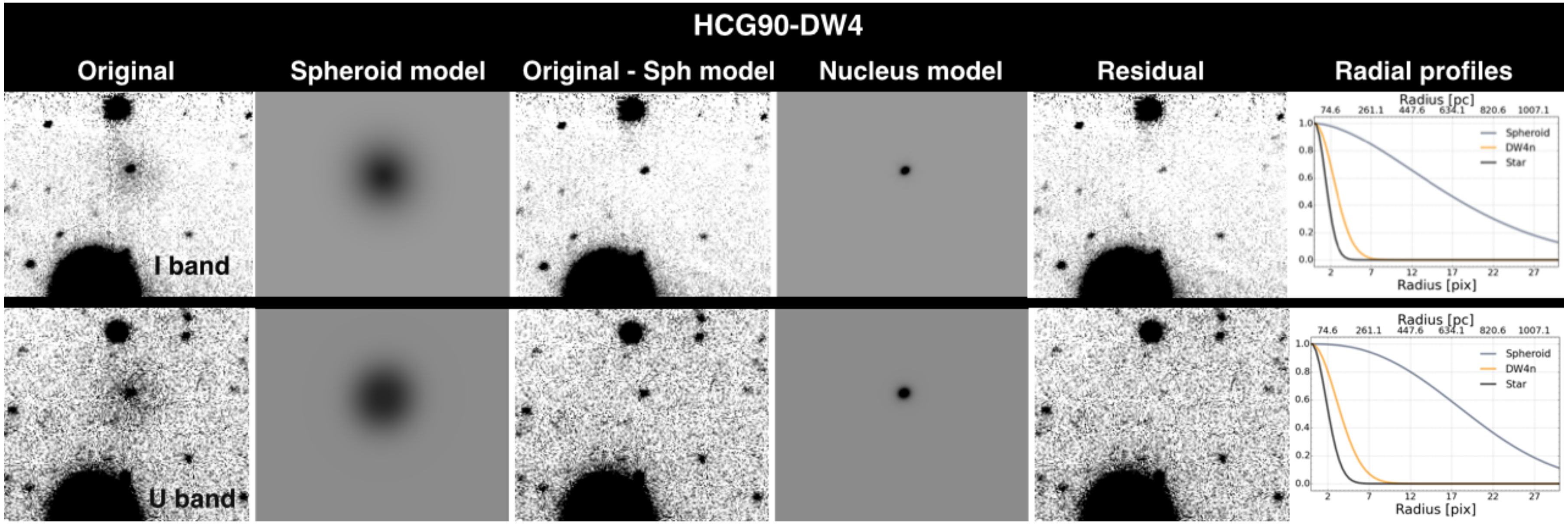

Figure 45: Illustrations of the surface brightness profile fitting for the spheroid and central object of HCG90-DW4 in I and U-band (top and bottom panel rows, respectively). The original image is shown in the left-most panel, then to the right follows the spheroid model with a spheroid-subtracted image. The following two panels show the nucleus model and the residual, where spheroid+nucleus model was subtracted. In the right-most panel we show the radial profiles of the spheroid Sérsic profile, the nucleus DW4n, and a stellar point spread function. Note that the nucleus, DW4n, is resolved and slightly more extended that the stellar profile. The image panels for each filter are shown with a greyscale stretch that is equal for each panel.

Fig. 44 shows the best fit models derived for four candidates in the U- and I-bands. For HCG90-DW4, the spheroid and the nuclear star cluster are treated separately (see Fig. 45 and § 6.5). We point out that the VIMOS PSF is fully accounted for in the surface brightness profile fit of every component, in particular the central object of HCG90-DW4. We correct the magnitudes for Galactic foreground extinction ($E_{B-V} = 0.024$ mag) using the latest Schlafly & Finkbeiner (2011) recalibration of the Schlegel et al. (1998) dust reddening maps. For HCG 90 the corresponding reddening values are $A_U = 0.115$ mag and $A_I = 0.04$ mag estimated with the Fitzpatrick (1999) reddening law ($R_V = 3.1$).

6.4 RESULTS

In general, the candidates are well characterized in the U-band with average effective surface brightness levels of $\langle\mu_U\rangle_e \simeq 26.7-28.1$ mag arcsec^{-2}, and spheroid effective radii of $r_{\rm eff} = 4-6''$corresponding to $0.68-1.10$ kpc.

For the dwarf pair HCG90-DW2 and HCG90-DW3, a single-component Sérsic profile did not result in a stable solution. However, we find that a two-component profile with different centers rapidly converges to a stable solution (see center panel in Fig. 44). We thus consider the two components separately. While both components of HCG90-DW2 and -DW3 are detected and fit in both filters, the saturation of a nearby star prohibits a robust estimation of their structural parameters in the I-band. Fortunately this is not the case for the U-band, so that the profile parameters from this filter can be used as first guess for the I-band surface brightness distribution fits. Despite finding a stable fitting solution, we point out that this requires considerable manual interaction with GALFIT. Our results imply that we are looking either at a dwarf pair (potentially in projection) or an extended dwarf irregular system. Given that we do not detect increased stochasticity in our U-band image that would indicate star-forming regions, with the current information we consider the dwarf pair scenario most likely.

Of the five new dwarf candidates, HCG90-DW4 represents the sole example of a nucleated dwarf galaxy (dE,N; see Fig. 45). Its spheroid component has $r_{\rm eff} \approx 750-800$ pc (see Table 3). Fitting the central object (DW4n) with a Sérsic profile yields an $n \simeq 0.6-0.7$ index, with $r_{\rm eff} \simeq 46-63$ pc and a magnitude of $M_{U,0} = -7.42$ mag. The corresponding nucleus to spheroid luminosity ratio is $\mathcal{L}_n/\mathcal{L}_g \simeq 0.091$, which is significantly above the 0.41 percent found by Turner et al. (2012) for bright Fornax early-type galaxies, but is in line with the results from the *Next Generation Fornax Survey* which found similarly elevated $\mathcal{L}_n/\mathcal{L}_g$ ratios for faint dwarf galaxies (Muñoz et al., 2015). We also find a moderate ellipticity of the central source, but as we are near the resolution limit of our data we cannot draw strong conclusions from this estimate. A faint residual is left near the centre of the nucleus, visible in the most right-panel of Fig. 45 for both bands. It is brighter in I than in the U-band, with a similar position angle, which might be a potential background source or a dust lane associated with the nucleus itself. Higher spatial resolution data is required to obtain further information about the morphology of this object. If DW4n is a nuclear star cluster (NSC), it appears to be larger and fainter than usual, falling well off the NSC and UCD size-luminosity relation (see Fig. 13 in Georgiev & Böker, 2014) while similarly comparing unfavourably with extremely extended Galactic globular clusters such as NGC 2419.

Finally, while contamination of HCG90-DW5 by foreground sources makes the structural parameter estimation of its spheroid component challenging, con-

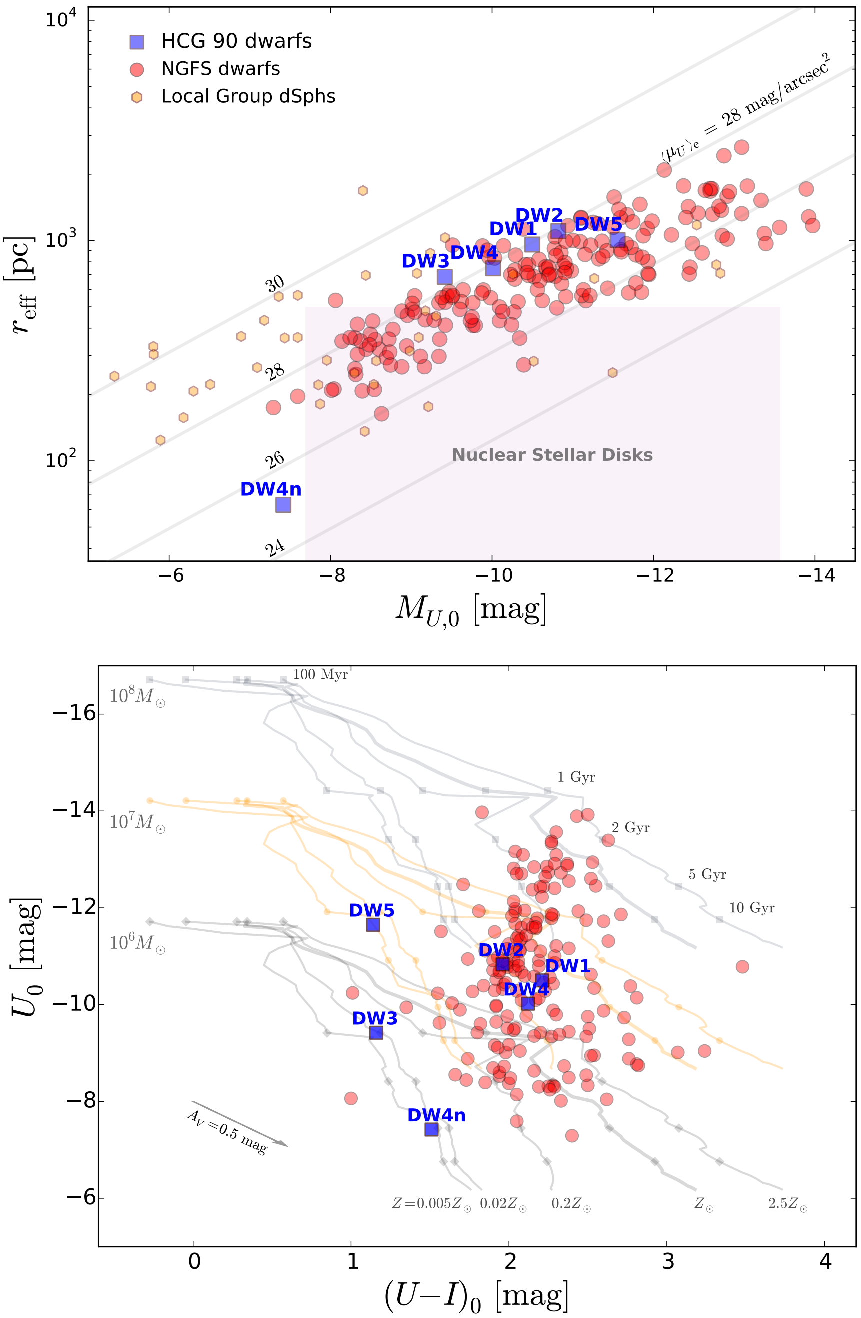

Figure 46: *Top panel:* The size-luminosity relation for dwarf galaxies. Effective radii vs. absolute U-band magnitude are shown for the LSB dwarf galaxy candidates in HCG 90 (blue squares). Lines of constant average effective surface brightness are shown for $\langle\mu_U\rangle_e$=30, 28, 26, 24 mag arcsec^{-2}. Red circles are the Fornax cluster dwarf candidates identified by Muñoz et al. (2015); Eigenthaler et al. (2018) and hexagons are the LG dSphs (McConnachie, 2012). The shaded area shows the parameter space of known nuclear stellar discs (Ledo et al., 2010). *Bottom panel:* Color-magnitude diagram, U_0 vs $(U-I)_0$ for the HCG 90 dwarf candidates (blue squares) and Fornax cluster dwarfs (red circles). SSP model predictions from Bruzual & Charlot (2003) are shown for three different total stellar masses (10^6, 10^7 and $10^8 M_\odot$) from top to bottom. Iso-metallicity tracks are shown for $Z = 0.05$, 0.02, 0.2, 1.0 (thicker line), and $2.5 Z_\odot$ and ages older than 100 Myr. The arrow in the upper left corner indicates a reddening vector corresponding to $A_V = 0.5$ mag.

structing a good mask for the surrounding objects allowed us to find a stable solution that is consistent across both filters (see Fig. 44).

6.5 DISCUSSION

We present the discovery of five new LSB dwarf galaxy candidates in HCG 90 based on VLT/VIMOS U− and I−band imaging. Assuming distances concurrent with HCG 90 ($D = 33.1$ Mpc), Table 3 lists their photometric and morphological properties. Three dwarfs show typical $r_{\rm eff} \approx 1$ kpc, while HCG90-DW3 and DW4 are smaller at $r_{\rm eff} \simeq 700-850$ pc. These $r_{\rm eff}$ are consistent with those found by van der Burg et al. (2016) for dwarfs in galaxy clusters in the sense that dwarfs at smaller cluster-centric radii are more compact with $r_{\rm eff} \leqslant 1$ kpc due to harassment and tidal limitation by the hostile intra-cluster gravitational field.

Fig. 46 (left panel) shows $r_{\rm eff}$ as a function of the absolute U-band magnitude for the new candidates, compared to Fornax cluster dwarfs (Muñoz et al., 2015; Eigenthaler et al., 2018) and the LG dwarf spheroidal (dSph) population, for which we estimate their U-band magnitudes based on the V-band luminosities and metallicities available in McConnachie (2012). With this information and assuming 12 Gyr old stellar populations, we use Bruzual & Charlot (2003) models (hereafter BC03) to obtain the corresponding $U-V$ colours to convert the tabulated V-band luminosities in McConnachie (2012) to the corresponding U-band fluxes. The new HCG 90 dwarf galaxy candidates have luminosities in the range of $-11.65 \leqslant M_{U_0} \leqslant -9.42$ and $-12.79 \leqslant M_{I_0} \leqslant -10.58$ mag, placing them in the magnitude regime of the average Fornax cluster dwarf, but with somewhat larger effective radii at a given luminosity. This combination places the HCG 90 dwarfs near the surface brightness limit of the Fornax dwarf sample.

The right panel of Fig. 46 shows the U_0 vs. $(U-I)_0$ colour-magnitude diagram (CMD) for the HCG90 and Fornax cluster dwarf galaxies. Population synthesis model predictions from BC03 are shown for three different total stellar masses: 10^6, 10^7 and 10^8 $M_\odot$. Despite the well-known age-metallicity-extinction degeneracy, with only two photometric bands our diagnostic capabilities are also degenerate with total stellar mass. However, as the reddening vector primarily points parallel to the model isochrones, our main limitation lies in the age-metallicity-mass (AMM) degeneracy. With this in mind, we estimate approximate ages and metallicities for the new dwarfs according to the model predictions.

DW1, DW2, and DW4 are likely to be older than 1 Gyr. Their CMD parameters are consistent with metallicities $\lesssim 0.02\, Z_\odot$ and ages $\gtrsim 10$ Gyr at $10^8\, M_\odot$ or super-solar metallicities for ages ~ 1 Gyr with SSP models scaled to $10^{6.5}\, M_\odot$. DW3 and DW5 have bluer $(U-I)_0$ colours and given all the AMM degeneracies, their colours and luminosities are consistent with ages $\lesssim 2$ Gyr, unless their stellar populations are metal-free, in which case they may be a few Gyr older. If DW3 is ~ 2 Gyr old its metallicity is $0.05\, Z_\odot$ with a total stellar mass of $10^{6.3}\, M_\odot$. If its metallicity is solar or higher, its age estimate lies at ~ 500 Myr with $10^{5.7}\, M_\odot$. Similar arguments apply to the 2.2 mag brighter DW5, for which a mass of $10^{7.2}\, M_\odot$ is consistent with an age of ~ 2 Gyr and a metallicity of $0.05\, Z_\odot$. If its metallicity is solar or above, it would have an age of ~ 500 Myr and a total stellar mass of $10^{6.3}\, M_\odot$. However, we caution that due to the severe contamination of the DW5 surface brightness model fits (see Fig. 44), we consider its stellar population characterization to be uncertain. In case of substantial internal reddening of the order $A_V = 0.5$ mag (see vector in the right panel of Fig. 46) ages would increase by a factor $\sim 2-5$, leaving the metallicity and stellar mass estimates

Table 4: Age, metallicity and mass (AMM) estimates for all of the HCG 90 LSB dwarf candidates. The two groups ($t_1, Z_1, M_{\star,1}$) and ($t_2, Z_2, M_{\star,2}$) show the stellar population parameter ranges, given the AMM degeneracy and measurement uncertainties (see text for details). The last row gives the corresponding information for the central object in HCG90-DW4.

ID	t_1	Z_1	$M_{\star,1}$	t_2	Z_2	$M_{\star,2}$
	[Gyr]	[$Z_\odot$]	[$M_\odot$]	[Gyr]	[$Z_\odot$]	[$M_\odot$]
HCG90-DW1	$\geqslant 10$	$\leqslant 0.02$	$10^{8.0}$	$\simeq 1$	2.5	$10^{6.5}$
HCG90-DW2	$\geqslant 10$	$\leqslant 0.02$	$10^{8.0}$	$\simeq 1$	2.5	$10^{6.5}$
HCG90-DW3	$\simeq 2$	$\leqslant 0.05$	$10^{6.3}$	$\simeq 0.5$	> 1	$10^{5.7}$
HCG90-DW4	$\geqslant 10$	$\leqslant 0.02$	$10^{8.0}$	$\simeq 1$	2.5	$10^{6.5}$
HCG90-DW5	$\simeq 2$	$\leqslant 0.05$	$10^{7.2}$	$\simeq 0.5$	> 1	$10^{6.3}$
HCG90-DW4n	$\geqslant 10$	$\leqslant 0.02$	$10^{6.5}$	0.7 - 1	>1	$10^{4.9}$

less affected. Clearly, supplemental near-infrared imaging and/or spectroscopic observations are needed to provide more robust stellar population parameter constraints.

Assuming ages and metallicities as predicted by the models from the CMD, we estimate their stellar masses, M_*, from the BC03 mass-to-light ratios adopting two metallicities: $0.02\,Z_\odot$ and $Z_\odot$. Our measured colours and luminosities for the spheroid components correspond to stellar mass ranges of $M_*|_{0.02 Z_\odot} \simeq 10^{6.3} - 10^{8}\,M_\odot$ and $M_*|_{Z_\odot} \simeq 10^{5.7} - 10^{6.5}\,M_\odot$, with DW3 and DW2 being the least and most massive dwarfs, respectively. For the nuclear object DW4n, we estimate $M_*|_{0.02 Z_\odot} \simeq 10^{6.5}$ and $M_*|_{Z_\odot} \simeq 10^{4.9}\,M_\odot$. A summary of the parameters can be found in Table 4.

All new LSB dwarf candidates are located within (projected) 70 kpc of the closest giant galaxy, although the limited VIMOS field-of-view makes it entirely possible that yet more dwarfs exist at larger radii. These properties, combined with their morphologies, resemble dSphs found in the LG (see Fig. 46) with closest LG dSph analogs being Fornax with $r_{\rm eff} = 710$ pc (though with higher surface brightness, $\mu_{V,\rm eff} = 24$ mag arcsec^{-2}), Cetus ($r_{\rm eff} = 710$ pc and $\mu_{V,\rm eff} = 26$ mag arcsec^{-2}), Andromeda I, II and XXIII with ($r_{\rm eff} = 672, 1176, 1029$ pc and $\mu_{V,\rm eff} = 25.8, 26.3, 27.8$ mag arcsec^{-2}, respectively; see McConnachie, 2012). Notably, the LG dSphs have similar stellar masses of a few $10^6 - 10^7\,M_\odot$ compared to the HCG 90 dwarf candidates in this work.

The case of HCG 90-DW2 and DW3 is interesting in that the light profile modelling solution strongly favours two distinct components seen closely in projection (see centre-panel of Fig. 44). While we cannot reject the possibility that DW2/3 is a single galaxy with an irregular shape, we may be observing a binary pair of LSB dwarfs with a projected separation of < 2 kpc. Dwarf binaries such as DW2/3 may not be unprecedented in the local universe. The most similar known systems are perhaps the LMC/SMC pair in the LG or the NGC 4681/4625 association reported by Pearson et al. (2016), both with much greater separations of 11 and (projected) 9.2 kpc, respectively. Intriguingly, DW2/3 are similar in both structural parameters and on-sky separation to those reported by Crnojević et al. (2014), which together lie ~90 kpc from their own giant host NGC 5128. In any case, if this pair is truly physically associated, then it implies that dwarf-dwarf interactions may not be uncommon in dense galactic environments.

The nearest dwarf to the core of the compact group is HCG90-DW5 with potentially interesting properties. It is the brightest candidate with the bluest $(U-I)_0 = 1.14$ mag colour index. Given its stellar population properties (see discussion above) and considering its close projected proximity to the three interacting giants, we suggest that this object may be a TDG arising from the tidal debris of the interacting giants. Noting the above, this interpretation is hampered by the contamination of DW5's light profile and will require careful follow-up observations to confirm.

The spheroid component of HCG90-DW4 appears to host a central compact object (DW4n) with $r_{\mathrm{eff}} \approx 46-63$ pc. However, its properties do not agree with those of a nuclear star cluster, which are generally about $5-10\times$ more compact and brighter than DW4n (e.g. Georgiev & Böker, 2014). Its size is marginally resolved by our data. This is illustrated by its radial profile in Fig. 45, which is slightly more extended than a stellar PSF. An alternative explanation is that DW4n could represent a so-called nuclear stellar disc (NSD). NSDs are typically located in the core regions of their host galaxies and have r_{eff} of 10s to 100s of pc (van den Bosch et al., 1994) and are regularly found in early-type galaxies, but rarely in spirals (Pizzella et al., 2002; Ledo et al., 2010). The shaded region of Fig.46 (left panel) shows the parameter space of a sample of nuclear discs studied by Ledo et al. (2010) where DW4n is slightly off from the faintest/smallest area of this range. DW4n's colour and luminosity are consistent with old ages >10 Gyr and metallicities $0.02\,Z_\odot$ at a stellar mass of $10^{6.5}\,M_\odot$ or younger ages $\sim 0.7-1$ Gyr and super-solar metallicities with a total stellar mass of $10^{4.9}\,M_\odot$ (see Table 4).

On the other hand, if DW4n is a background source, then at 100 Mpc distance (e.g. Coma cluster), it would have $r_{\mathrm{eff}} \simeq 170$ pc and $M_{U,0} \simeq -9.82$ mag, and at 750 Mpc (e.g. Abell 1689 cluster) this would increase further to $r_{\mathrm{eff}} \simeq 1.3$ kpc and $M_{U,0} \simeq -14.22$ mag. In these cases, HCG 90-DW4n falls on the faintest regions of the size-luminosity relation of early-type galaxies (see Fig. 46). Nonetheless, if it were an early-type galaxy we would expect a higher Sérsic index (e.g. $n \gtrsim 1$), consistent with massive ellipticals. With the current data we cannot confirm the nature of this object or its distance, and despite a lack of observational evidence for NSDs in dwarf galaxies, if DW4 is a member of HCG 90, then its structural parameters make it a good candidate for the first such object found inside a faint and relatively compact LSB host. Spectroscopic follow-up observations of DW4n should verify its HCG90 membership and, thereby, shed more light on its true nature.

6.6 SUMMARY

We have studied the compact group of galaxies HCG90 with deep U- and I-band images finding a very diverse set of five low-surface brightness (LSB) dwarf galaxy candidates. These are the first LSB dwarf galaxy candidates found in a compact group of galaxies. We measure spheroid half-light radii in the range $0.7 \lesssim r_{\mathrm{eff}}/\mathrm{kpc} \lesssim 1.5$ with luminosities of $-11.65 \lesssim M_U \lesssim -9.42$ and $-12.79 \lesssim M_I \lesssim -10.58$ mag, corresponding to a color range of $(U-I)_0 \simeq 1.1-2.2$ mag and surface brightness levels of $\mu_U \simeq 28.1$ mag/arcsec² and $\mu_I \simeq 27.4$ mag/arcsec². Their colours and luminosities are consistent with a diverse set of stellar population properties. Assuming solar and $0.02\,Z_\odot$ metallicities we obtain stellar masses in the range $M_*|_{Z_\odot} \simeq 10^{5.7-6.3}\,M_\odot$ and $M_*|_{0.02\,Z_\odot} \simeq 10^{6.3-8}\,M_\odot$. Three dwarfs are older than 1 Gyr, while the other two significantly bluer dwarfs are younger than ~2 Gyr at any mass/metallicity combination.

Altogether, the new LSB dwarf galaxy candidates share properties with dwarf galaxies found throughout the Local Volume and in nearby galaxy clusters such as Fornax. We find a pair of candidates with ~2 kpc projected separation, which may represent one of the closest dwarf galaxy pairs found. We also find a nucleated dwarf candidate, with a nucleus size of $r_{\rm eff} \simeq 46-63$ pc and magnitude $M_{U,0} = -7.42$ mag and $(U-I)_0 = 1.51$ mag, which is consistent with a nuclear stellar disc with a stellar mass in the range $10^{4.9-6.5}\,M_\odot$.

7

SUMMARY AND OUTLOOK

We have studied different stellar systems in the Fornax Galaxy Cluster: dwarf galaxies, the nucleus of dwarf galaxies and compact stellar systems. We have used the deepest and homogeneous data available for this galaxy cluster from the Next generation Fornax Survey.

In chapter 3 we presented the dwarf galaxy population studied in a radii of $0.25 < r/r_{\rm vir} \leqslant 0.5$. We identify 271 new dwarf galaxy candidates, of which 39 are nucleated. Taking into account the dwarfs from existing catalogs and the new NGFS dwarfs, the total Fornax dwarf galaxy population consists of 643 dwarfs, of which 462 are non-nucleated and 181 are nucleated. The dwarf candidates from the outer footprint have absolute i'-band magnitudes in the range $-18.80 \leqslant M_{i'} \leqslant -8.78$ with photometric errors <0.1 mag, effective radii between $1.8''$ to $22.8''$ ($r_{{\rm eff},i'} = 0.18-2.22$ kpc at the Fornax cluster distance of $D_L = 20.0$ Mpc). The projected dwarf galaxy surface number density profile shows a general concentration of dwarfs in the core regions of Fornax within $r \leqslant 350$ kpc. NGC 1399 itself can be seen to occupy an apparent saddle-point between two main dwarf galaxy over-densities towards the East and West. We find particularly strong evidence for dwarf clustering on sub-100 kpc scales for the overall and outer dwarf population. In particular, the outer dwarf galaxies appear more likely to be clustering on scales approaching ~ 50 kpc with a notable decrease on scales $\geqslant 100$ kpc.

In chapter 4 we characterized 61 nuclear star clusters in the Fornax cluster region ($\leqslant r_{\rm vir}/4$) with $u'g'i'JK_s$ photometry to obtain information on their luminosity and color distributions. The nucleus stellar mass distribution covers the range of $\log(\mathcal{M}_*/M_\odot) = 4.8-7.3$. We find that the nucleus mass distribution is bimodal, with peaks located at $\log(\mathcal{M}_*/M_\odot) \simeq 5.38$ and 6.25. The second peak is consistent with UCD masses. The combination of the $u'i'K_s$ diagram with SSP model predictions reveals a bimodality in the stellar population parameters of nuclei, which is congruent with the two groups in the mass distribution function of NGFS nuclei. Scaling relations such as the nucleus-to-galaxy mass relation ($\mathcal{M}_{\rm nuc}$ vs. $\mathcal{M}_{\rm gal}$) show a clear mass correlation between nuclei and their host galaxy over the entire mass range of our NGFS sample. This relation shows a break in the slope at $\log(\mathcal{M}_*/M_\odot) \simeq 9.7$ where we find a shallower slope for dwarf galaxies relative to their more massive counterparts. For the nuclei-to-galaxy mass ratio vs. galaxy mass relation ($\eta_n = \mathcal{M}_{\rm nucleus}/\mathcal{M}_{\rm galaxy}$ vs. $\mathcal{M}_{\rm galaxy}$) an interesting anti-correlation is found. The lower the galaxy mass the more prominent becomes the nucleus. These relatively strong trends for low-mass galaxies reach values up to $\eta_n \simeq 10\%$ for dwarf galaxies with a stellar mass of $10^7\,M_\odot$.The low-mass anti-correlation seems to be similar for ETGs and LTGs, suggesting that it is independent of galaxy type.

In chapter 5 we study the compact stellar systems in the core region of Fornax ($\leqslant r_{\rm vir}/4$) taking advantage of the broad SED coverage we estimate age, metallicity and mass for each CSS using the $g'i'K_s$ information from BC03 models. The CSSs cover the entire range of metallicity in the model grid from $[{\rm Fe/H}] = -2.3$ to 0.4, with a peak in the distribution at $[{\rm Fe/H}] \simeq -0.7$ dex. The age distribution goes from 1 to 14 Gyrs but most of them consistent with ages younger than 8 Gyr.The stellar mass distribution of our CSSs go from $\log(\mathcal{M}_\star/M_\odot) = 4.6-7.4$. Metal rich CSSs follow a broad gaussian distribution with peak at

$\log(\mathcal{M}_\star/M_\odot) \simeq 5.7$. The mass distribution for the inner NGC 1399 CSSs is bimodal with peaks at $\log(\mathcal{M}_\star/M_\odot) \simeq 5.5$ and 6.0. Outwards from the cD galaxy, the amount of low mass CSSs starts to rise and the most massive CSSs starts to decline. The young CSSs mass distribution is consistent with a bimodal distribution with peaks at $\log(\mathcal{M}_\star/M_\odot) \simeq 5.2$ and 5.7. The intermediate age CSSs also show evidence for a bimodal distribution with peaks at $\log(\mathcal{M}_\star/M_\odot) \simeq 5.6$ and 6.1. The spatial distribution for the different subgroups in age and metallicity are very intriguing, with the most metal poor and old CSSs sparsely distributed. The intermediate metallicity and young CSSs preferentially located along the East-West direction of Fornax, centered in NGC 1399. The most metal rich CSSs are concentrated in the vicinity of NGC 1399 and around the brightest galaxies. These different distributions shown in this work allow us to constrain the mass assembly history of the Fornax Cluster.

In chapter 6 we reported the discovery of five faint dwarf galaxies in the Hickson Compact Group 90. These are the first LSB dwarf galaxy candidates found in a compact group of galaxies. We measure spheroid half-light radii in the range $0.7 \lesssim r_{\rm eff}/\rm kpc \lesssim 1.5$ with luminosities of $-11.65 \lesssim M_U \lesssim -9.42$ and $-12.79 \lesssim M_I \lesssim -10.58$ mag. Comparing with stellar population models we find that three dwarfs are older than 1 Gyr, while the other two significantly bluer dwarfs are younger than ~2 Gyr at any mass/metallicity combination. Altogether, the new LSB dwarf galaxy candidates share properties with dwarf galaxies found throughout the Local Volume and in nearby galaxy clusters such as Fornax. We find a pair of candidates with ~ 2 kpc projected separation. We also find a nucleated dwarf candidate, with a nucleus size of $r_{\rm eff} \simeq 46{-}63$ pc and magnitude $M_{U,0} = -7.42$ mag.

7.1 OUTLOOK

An exaustive mapping of different environments, either galaxy groups, compact groups or galaxy clusters, covering a large fraction of its virial radius are ideal to understand the global picture of galaxy evolution and assembly over cosmic time. It is required to not only focus in the most massive member galaxies but the low mass regime as well, to probe deeper into the galaxy luminosity function and put more stringent constraints on the predictions of modern galaxy formation models (e.g. Mistani et al., 2016). Panchromatic view of the different stellar systems are also crucial to obtain information about their stellar population properties. One of the upcoming large surveys that will help to find answers for many astrophysical questions is the Large Synoptic Survey Telescope (LSST; LSST Science Collaboration et al., 2009) that has a large field of view and will take multiple images of the Southern sky in six bands, $ugrizy$. It will have around ~1000 visits for a single pointing in the sky over a 10-year period. The survey is expected to have its first light in 2020 and the regular image acquisition to start in 2022.

In the upcoming research about the Fornax cluster from the NGFS team: (1) For the CSSs we will extend their identification and characterization up to $\sim 0.5 r_{vir}$ but now reaching the faintest objects. With this complete sample we will be able to estimate accurate and deep GC luminosity function and mass function, specific frequencies. Study in detail the transition region between UCDs and GCs. (2) For nuclear star clusters, the extenstion to the outer region of Fornax and a study their GC population.(3) The dwarf galaxies have to be analysed in all photometric band including the NIR data. Study the galaxy luminosity function.

There is plenty of work to be done with the NGFS data. Spectra follow-up is necessary to confirm the candidates studied in this thesis and also to have chemical abundances for some of the brightest UCDs. We have already been awarded with observing time to study with high resolution spectra the chemical composition of UCDs.

Exciting times are coming with this era of deep and homogeneous data. We are preparing to handle this amount of information and extract the best results for a given question to be answered.

APPENDIX A

Table 5: Dwarf galaxies in the Fornax Cluster

ID	α_{2000}	δ_{2000}	m_i	M_i [a]	n [b]	r_{eff}	r_{eff} [a]	Type [c]	Reference
	hh:mm:ss.ss	*dd:mm:ss.s*	[mag]	[mag]		[arcsec]	[kpc]		
NGFS032601-364740	03:26:00.74	-36:47:39.8	19.90	-11.61	0.87	3.077	0.299	○	-
NGFS032601-364224	03:26:01.14	-36:42:23.5	20.88	-10.63	0.58	3.945	0.384	○	-
NGFS032607-350744	03:26:07.43	-35:07:43.9	16.22	-15.29	1.37	8.693	0.845	○	44
NGFS032611-345432	03:26:11.38	-34:54:31.5	21.57	-9.94	0.76	2.865	0.279	○	-
NGFS032614-343313	03:26:14.45	-34:33:12.9	18.90	-12.61	0.73	6.256	0.608	⊙	45
NGFS032622-343928	03:26:21.76	-34:39:27.6	17.63	-13.88	1.01	5.520	0.537	○	-
NGFS032629-350414	03:26:29.41	-35:04:14.4	20.38	-11.13	2.17	3.615	0.351	○	-
NGFS032633-350917	03:26:33.36	-35:09:15.7	19.85	-11.66	1.15	2.257	0.219	○	-
NGFS032635-342952	03:26:34.81	-34:29:52.1	18.81	-12.70	0.79	8.841	0.860	○	-
NGFS032636-363138	03:26:35.64	-36:31:38.3	19.78	-11.73	0.70	3.953	0.384	○	-
NGFS032638-364843	03:26:38.26	-36:48:42.9	21.71	-9.80	0.77	3.053	0.299	○	-
NGFS032640-351107	03:26:40.36	-35:11:06.6	20.42	-11.09	0.74	3.314	0.322	○	-
NGFS032643-343255	03:26:42.56	-34:32:54.8	15.84	-15.67	1.14	11.200	1.089	⊙	48
NGFS032651-343914	03:26:50.62	-34:39:14.0	20.95	-10.56	1.31	3.297	0.321	○	-
NGFS032653-364757	03:26:53.08	-36:47:56.7	17.79	-13.72	0.68	8.265	0.804	○	51
NGFS032654-353107	03:26:54.07	-35:31:06.7	15.85	-15.66	0.79	18.356	1.785	⊙	50
NGFS032708-350805	03:27:07.54	-35:08:04.5	20.65	-10.86	0.93	4.888	0.475	○	-
NGFS032708-342359	03:27:08.02	-34:23:59.4	17.40	-14.11	0.88	8.550	0.831	○	52
NGFS032712-370345	03:27:11.53	-37:03:45.3	19.56	-11.95	0.76	3.507	0.341	○	-
NGFS032721-342323	03:27:20.81	-34:23:22.6	19.42	-12.09	1.28	2.508	0.244	○	-

[a]: Assuming a distance modulus of $(m-M)_0 = 31.51$ mag or $D_L = 20.0$ Mpc (Blakeslee et al., 2009).

[b]: Sérsic index (Sérsic , 1963; Caon et al., 1993).

[c]: Morphological galaxy type classification: ⊙=nucleated, ○=non-nucleated dwarf galaxy.

ID	α_{2000} *hh:mm:ss.ss*	δ_{2000} *dd:mm:ss.s*	m_i [mag]	M_i [a] [mag]	n [b]	$r_{\rm eff}$ [arcsec]	$r_{\rm eff}$ [a] [kpc]	Type [c]	Reference
NGFS032727-364354	03:27:26.63	-36:43:53.8	20.35	-11.16	0.91	2.298	0.223	○	-
NGFS032728-364251	03:27:28.48	-36:42:51.4	20.75	-10.76	1.29	2.437	0.237	○	-
NGFS032729-345652	03:27:28.67	-34:56:51.5	18.05	-13.46	0.83	4.576	0.445	○	-
NGFS032733-351459	03:27:32.48	-35:14:58.8	19.24	-12.28	1.05	7.440	0.723	⊙	-
NGFS032743-354337	03:27:42.60	-35:43:36.5	19.51	-12.00	0.94	4.711	0.458	○	-
NGFS032748-345229	03:27:47.52	-34:52:28.8	21.42	-10.09	0.57	4.337	0.422	○	-
NGFS032753-345036	03:27:52.76	-34:50:36.3	21.28	-10.23	1.92	2.292	0.223	○	-
NGFS032753-350407	03:27:53.40	-35:04:06.6	21.09	-10.42	1.01	3.999	0.389	○	-
NGFS032754-354827	03:27:53.77	-35:48:27.0	18.27	-13.24	0.75	4.124	0.401	○	-
NGFS032800-350445	03:28:00.07	-35:04:44.8	20.18	-11.33	0.67	5.430	0.528	○	-
NGFS032801-364954	03:28:01.43	-36:49:54.1	21.69	-9.82	0.75	4.132	0.402	○	-
NGFS032807-351411	03:28:06.66	-35:14:11.5	16.19	-15.32	1.22	7.951	0.773	○	65
NGFS032810-343616	03:28:09.45	-34:36:16.3	20.09	-11.42	1.38	3.227	0.314	○	-
NGFS032816-353216	03:28:16.08	-35:32:16.0	19.22	-12.29	1.01	7.150	0.695	○	-
NGFS032824-354547	03:28:23.80	-35:45:46.5	20.54	-10.97	0.92	3.214	0.312	○	-
NGFS032824-353616	03:28:24.19	-35:36:15.7	20.67	-10.84	0.42	5.664	0.551	○	-
NGFS032835-372126	03:28:35.27	-37:21:25.7	18.78	-12.73	1.04	5.775	0.561	○	-
NGFS032841-352939	03:28:40.99	-35:29:39.4	21.24	-10.27	0.53	4.774	0.464	○	-
NGFS032843-351517	03:28:43.29	-35:15:17.3	21.70	-9.81	0.88	4.416	0.429	○	-
NGFS032847-363709	03:28:47.31	-36:37:09.1	20.80	-10.71	0.20	7.035	0.684	○	-
NGFS032854-335405	03:28:54.44	-33:54:05.2	19.71	-11.80	0.68	3.945	0.384	○	-
NGFS032857-362615	03:28:57.04	-36:26:15.3	19.01	-12.50	0.32	7.369	0.716	○	69

[a]: Assuming a distance modulus of $(m-M)_0 = 31.51$ mag or $D_L = 20.0$ Mpc (Blakeslee et al., 2009).

[b]: Sérsic index (Sérsic , 1963; Caon et al., 1993).

[c]: Morphological galaxy type classification: ⊙=nucleated, ○=non-nucleated dwarf galaxy.

ID	α_{2000} *hh:mm:ss.ss*	δ_{2000} *dd:mm:ss.s*	m_i [mag]	M_i [a] [mag]	n [b]	r_{eff} [arcsec]	r_{eff} [a] [kpc]	Type [c]	Reference
NGFS032858-370551	03:28:57.61	-37:05:50.7	21.96	-9.55	1.16	2.630	0.256	○	-
NGFS032902-372134	03:29:01.84	-37:21:38.7	17.29	-14.22	0.98	8.160	0.793	⊙	70
NGFS032904-372016	03:29:04.22	-37:20:15.5	20.70	-10.81	0.58	4.780	0.465	○	-
NGFS032907-360945	03:29:07.17	-36:09:44.8	19.08	-12.43	1.20	12.597	1.225	⊙	-
NGFS032912-361935	03:29:11.96	-36:19:35.4	19.46	-12.05	0.91	7.235	0.703	○	-
NGFS032921-370859	03:29:20.80	-37:08:58.8	21.23	-10.29	0.59	1.829	0.178	○	-
NGFS032922-342924	03:29:21.90	-34:29:24.0	20.79	-10.72	0.73	8.386	0.815	○	-
NGFS032926-353615	03:29:26.12	-35:36:15.3	19.43	-12.08	0.70	4.444	0.432	○	71
NGFS032931-342408	03:29:30.58	-34:24:08.3	20.80	-10.71	0.71	5.103	0.496	○	-
NGFS032932-365104	03:29:32.27	-36:51:03.5	21.56	-9.95	1.62	4.075	0.396	○	-
NGFS032933-355203	03:29:33.31	-35:52:03.2	18.29	-13.22	1.00	13.28	1.291	○	72
NGFS032934-364213	03:29:34.35	-36:42:12.5	18.60	-12.91	0.77	5.237	0.509	○	73
NGFS032938-352401	03:29:38.04	-35:24:00.8	19.13	-12.38	0.77	9.013	0.876	○	75
NGFS032942-362439	03:29:41.89	-36:24:39.2	18.27	-13.24	0.81	6.373	0.622	⊙	-
NGFS032942-361317	03:29:42.07	-36:13:17.4	17.28	-14.23	0.84	13.87	1.348	⊙	77
NGFS032945-360323	03:29:44.89	-36:03:23.0	17.64	-13.87	0.74	9.485	0.922	⊙	79
NGFS032945-352245	03:29:45.34	-35:22:44.6	18.02	-13.49	0.66	10.183	0.990	○	78
NGFS032951-362349	03:29:51.10	-36:23:49.4	20.19	-11.32	0.71	7.143	0.694	○	-
NGFS032958-342259	03:29:57.67	-34:22:59.1	21.42	-10.09	0.69	2.301	0.224	⊙	-
NGFS032959-350215	03:29:59.13	-35:02:15.0	21.17	-10.34	0.24	8.556	0.832	⊙	-
NGFS033010-344759	03:30:10.04	-34:47:59.0	20.80	-10.71	0.85	2.585	0.251	○	-
NGFS033010-344805	03:30:10.36	-34:48:04.5	20.35	-11.16	0.94	2.787	0.271	○	-

[a]: Assuming a distance modulus of $(m-M)_0 = 31.51$ mag or $D_L = 20.0$ Mpc (Blakeslee et al., 2009).

[b]: Sérsic index (Sérsic , 1963; Caon et al., 1993).

[c]: Morphological galaxy type classification: ⊙=nucleated, ○=non-nucleated dwarf galaxy.

ID	α_{2000} *hh:mm:ss.ss*	δ_{2000} *dd:mm:ss.s*	m_i [mag]	M_i [a] [mag]	n [b]	r_{eff} [arcsec]	r_{eff} [a] [kpc]	Type [c]	Reference
NGFS033011-352046	03:30:10.92	-35:20:46.0	20.48	-11.03	0.74	4.915	0.478	○	-
NGFS033018-350431	03:30:17.94	-35:04:31.4	19.81	-11.70	0.78	5.092	0.495	○	-
NGFS033023-361331	03:30:22.61	-36:13:31.2	21.94	-9.57	0.73	4.591	0.446	○	-
NGFS033028-340627	03:30:28.35	-34:06:27.0	19.14	-12.37	1.88	3.762	0.366	○	-
NGFS033030-341534	03:30:30.40	-34:15:34.4	15.09	-16.42	1.56	9.837	0.956	⊙	82
NGFS033034-350630	03:30:34.28	-35:06:30.3	20.86	-10.65	0.85	4.460	0.434	○	-
NGFS033037-350230	03:30:36.58	-35:02:30.1	17.80	-13.71	1.36	10.200	0.992	⊙	84
NGFS033039-351338	03:30:38.69	-35:13:38.0	19.31	-12.20	0.77	4.837	0.470	○	-
NGFS033039-362910	03:30:39.05	-36:29:09.7	19.23	-12.28	0.56	7.236	0.703	○	-
NGFS033046-353301	03:30:46.15	-35:33:00.9	14.69	-16.82	1.51	11.976	1.164	⊙	85
NGFS033047-352117	03:30:46.58	-35:21:17.0	16.54	-14.97	0.90	12.256	1.192	⊙	86
NGFS033053-353218	03:30:53.03	-35:32:17.6	21.84	-9.67	0.22	6.032	0.586	○	-
NGFS033057-354222	03:30:57.08	-35:42:21.9	21.92	-9.59	0.25	3.575	0.348	○	-
NGFS033059-344136	03:30:58.89	-34:41:36.0	20.87	-10.64	1.07	4.347	0.423	○	-
NGFS033101-353815	03:31:01.23	-35:38:14.9	20.05	-11.46	1.15	4.344	0.422	○	-
NGFS033105-340842	03:31:05.28	-34:08:41.5	20.49	-11.02	0.58	6.224	0.605	○	-
NGFS033117-345743	03:31:16.74	-34:57:42.5	19.27	-12.24	0.63	5.483	0.533	⊙	92
NGFS033119-350955	03:31:19.17	-35:09:55.1	20.46	-11.05	0.52	6.702	0.652	○	-
NGFS033121-354910	03:31:20.65	-35:49:10.1	19.24	-12.27	0.67	4.753	0.462	○	93
NGFS033123-345818	03:31:22.70	-34:58:18.3	18.42	-13.09	0.70	7.531	0.732	○	94
NGFS033125-351952	03:31:24.87	-35:19:52.2	12.71	-18.80	1.65	10.811	1.051	○	95
NGFS033127-360545	03:31:26.61	-36:05:44.8	21.77	-9.74	0.39	3.734	0.363	○	-

[a]: Assuming a distance modulus of $(m-M)_0 = 31.51$ mag or $D_L = 20.0$ Mpc (Blakeslee et al., 2009).

[b]: Sérsic index (Sérsic , 1963; Caon et al., 1993).

[c]: Morphological galaxy type classification: ⊙=nucleated, ○=non-nucleated dwarf galaxy.

ID	α_{2000}	δ_{2000}	m_i	M_i [a]	n [b]	r_{eff}	r_{eff} [a]	Type [c]	Reference
	hh:mm:ss.ss	*dd:mm:ss.s*	[mag]	[mag]		[arcsec]	[kpc]		
NGFS033127-352937	03:31:26.97	-35:29:36.7	18.25	-13.26	0.50	9.548	0.928	○	97
NGFS033139-361636	03:31:39.00	-36:16:35.8	17.46	-14.05	0.74	12.194	1.186	⊙	98
NGFS033145-342017	03:31:44.86	-34:20:17.3	15.85	-15.66	0.92	13.887	1.350	○	99
NGFS033146-361644	03:31:45.79	-36:16:44.2	21.52	-9.99	0.69	3.260	0.317	○	-
NGFS033147-354034	03:31:47.03	-35:40:33.8	16.46	-15.05	0.84	13.031	1.267	⊙	101
NGFS033148-350306	03:31:47.55	-35:03:06.0	14.00	-17.51	1.14	15.497	1.507	⊙	100
NGFS033149-353457	03:31:48.75	-35:34:57.4	19.13	-12.38	0.79	4.558	0.443	○	-
NGFS033151-345050	03:31:51.41	-34:50:49.5	20.60	-10.91	0.55	2.816	0.274	○	-
NGFS033155-361859	03:31:55.41	-36:18:59.2	19.94	-11.58	0.50	4.501	0.438	○	-
NGFS033158-353719	03:31:57.99	-35:37:19.3	20.41	-11.10	0.34	9.107	0.885	○	-
NGFS033202-362259	03:32:02.45	-36:22:58.9	21.65	-9.86	0.53	3.759	0.365	○	-
NGFS033205-352532	03:32:05.23	-35:25:32.1	18.12	-13.39	0.97	6.293	0.612	⊙	-
NGFS033205-354936	03:32:05.41	-35:49:35.8	20.67	-10.84	0.50	3.944	0.383	○	-
NGFS033211-361316	03:32:10.70	-36:13:16.3	15.47	-16.04	0.88	11.691	1.137	○	102
NGFS033222-352422	03:32:22.00	-35:24:21.5	19.25	-12.26	0.48	7.722	0.751	⊙	-
NGFS033227-354631	03:32:27.28	-35:46:31.2	18.50	-13.01	0.85	8.925	0.868	○	103
NGFS033228-350645	03:32:28.27	-35:06:45.0	21.54	-9.97	0.30	3.269	0.318	○	-
NGFS033230-360519	03:32:29.76	-36:05:19.3	16.56	-14.95	0.66	14.22	1.383	⊙	105
NGFS033230-342055	03:32:30.36	-34:20:54.5	18.29	-13.22	0.70	6.766	0.658	○	104
NGFS033232-364758	03:32:31.78	-36:47:58.1	21.08	-10.43	0.83	2.237	0.216	○	-
NGFS033239-373918	03:32:38.69	-37:39:18.2	19.35	-12.16	0.98	5.117	0.497	⊙	-
NGFS033239-332028	03:32:39.20	-33:20:28.4	19.36	-12.15	1.00	4.048	0.394	○	-

[a]: Assuming a distance modulus of $(m-M)_0 = 31.51$ mag or $D_L = 20.0$ Mpc (Blakeslee et al., 2009).

[b]: Sérsic index (Sérsic , 1963; Caon et al., 1993).

[c]: Morphological galaxy type classification: ⊙=nucleated, ○=non-nucleated dwarf galaxy.

ID	α_{2000}	δ_{2000}	m_i	M_i [a]	n [b]	$r_{\rm eff}$	$r_{\rm eff}$ [a]	Type [c]	Reference
	hh:mm:ss.ss	*dd:mm:ss.s*	[mag]	[mag]		[arcsec]	[kpc]		
NGFS033247-373832	03:32:46.89	-37:38:31.6	17.71	-13.80	0.83	7.139	0.694	○	109
NGFS033248-341420	03:32:47.68	-34:14:19.7	12.98	-18.53	1.61	8.439	0.821	○	106
NGFS033248-355647	03:32:48.46	-35:56:47.2	18.40	-13.11	0.77	7.138	0.694	○	-
NGFS033249-360913	03:32:48.57	-36:09:13.2	18.54	-12.97	0.66	6.083	0.591	⊙	108
NGFS033257-354415	03:32:57.31	-35:44:15.4	15.86	-15.65	1.04	15.67	1.523	○	110
NGFS033260-341909	03:32:59.92	-34:19:08.8	20.07	-11.44	1.32	5.115	0.497	○	-
NGFS033303-362635	03:33:03.28	-36:26:34.6	16.27	-15.24	1.14	13.151	1.279	⊙	112
NGFS033304-334329	03:33:03.61	-33:43:29.2	15.78	-15.73	1.21	12.868	1.251	⊙	111
NGFS033309-354308	03:33:09.28	-35:43:07.8	15.42	-16.09	0.85	18.617	1.810	○	115
NGFS033312-350208	03:33:11.89	-35:02:07.9	19.83	-11.68	0.98	12.386	1.204	○	-
NGFS033313-360103	03:33:12.75	-36:01:02.7	14.98	-16.53	1.25	14.096	1.371	⊙	116
NGFS033314-350139	03:33:14.33	-35:01:39.0	20.71	-10.80	1.02	4.603	0.447	○	-
NGFS033316-360541	03:33:16.47	-36:05:41.1	20.61	-10.90	1.10	2.726	0.265	○	-
NGFS033319-351548	03:33:18.70	-35:15:47.6	18.77	-12.74	0.91	10.59	1.030	○	-
NGFS033323-364059	03:33:22.69	-36:40:58.6	19.31	-12.20	0.99	4.554	0.443	○	-
NGFS033324-355915	03:33:24.05	-35:59:14.5	20.13	-11.38	0.58	6.667	0.648	○	-
NGFS033328-355756	03:33:27.64	-35:57:53.5	20.56	-10.95	0.67	3.323	0.323	○	-
NGFS033329-350736	03:33:28.63	-35:07:35.7	20.39	-11.12	0.62	6.236	0.606	○	-
NGFS033331-351621	03:33:30.96	-35:16:21.3	21.58	-9.93	0.81	2.422	0.235	○	-
NGFS033331-342721	03:33:31.21	-34:27:20.9	16.54	-14.97	0.82	9.010	0.876	⊙	118
NGFS033333-354218	03:33:32.91	-35:42:18.3	19.64	-11.87	0.96	4.383	0.426	○	-
NGFS033334-363620	03:33:34.14	-36:36:20.4	15.58	-15.93	0.80	18.29	1.778	○	120

[a]: Assuming a distance modulus of $(m-M)_0 = 31.51$ mag or $D_L = 20.0$ Mpc (Blakeslee et al., 2009).

[b]: Sérsic index (Sérsic , 1963; Caon et al., 1993).

[c]: Morphological galaxy type classification: ⊙=nucleated, ○=non-nucleated dwarf galaxy.

ID	α_{2000} *hh:mm:ss.ss*	δ_{2000} *dd:mm:ss.s*	m_i [mag]	M_i [a] [mag]	n [b]	$r_{\rm eff}$ [arcsec]	$r_{\rm eff}$ [a] [kpc]	Type [c]	Reference
NGFS033335-342760	03:33:34.85	-34:27:59.9	21.30	-10.21	0.49	4.792	0.466	○	-
NGFS033338-372432	03:33:38.05	-37:24:31.9	20.98	-10.53	0.79	3.510	0.341	○	-
NGFS033344-331404	03:33:43.78	-33:14:04.4	20.75	-10.76	0.70	2.689	0.261	○	-
NGFS033344-332242	03:33:44.45	-33:22:41.9	19.04	-12.47	1.10	3.625	0.352	○	-
NGFS033349-372027	03:33:48.62	-37:20:26.6	20.16	-11.35	1.37	2.175	0.211	○	-
NGFS033349-341012	03:33:48.95	-34:10:11.7	17.27	-14.24	0.78	10.209	0.993	⊙	124
NGFS033354-342559	03:33:53.97	-34:25:58.6	21.20	-10.31	1.17	3.151	0.306	○	-
NGFS033355-342049	03:33:55.41	-34:20:48.6	19.00	-12.51	0.77	5.336	0.519	○	126
NGFS033357-362257	03:33:56.73	-36:22:56.6	20.44	-11.07	0.74	3.839	0.373	○	-
NGFS033358-361127	03:33:58.18	-36:11:27.0	21.01	-10.50	0.63	6.359	0.618	○	-
NGFS033358-363548	03:33:58.21	-36:35:48.0	20.93	-10.58	0.51	3.719	0.362	○	-
NGFS033402-371055	03:34:02.08	-37:10:55.0	20.89	-10.62	0.83	3.288	0.320	○	-
NGFS033407-362758	03:34:07.02	-36:27:58.2	15.87	-15.64	0.92	8.734	0.849	○	128
NGFS033408-360415	03:34:07.70	-36:04:14.5	18.73	-12.78	0.67	8.611	0.837	⊙	129
NGFS033411-364501	03:34:11.21	-36:45:00.7	21.62	-9.89	0.74	3.314	0.322	○	-
NGFS033412-361717	03:34:11.81	-36:17:16.9	19.79	-11.72	0.75	6.075	0.591	○	-
NGFS033416-335603	03:34:15.81	-33:56:03.4	18.57	-12.94	0.66	4.870	0.474	○	-
NGFS033416-331736	03:34:16.10	-33:17:35.5	20.15	-11.36	0.67	4.940	0.480	○	-
NGFS033416-363524	03:34:16.43	-36:35:23.6	20.79	-10.72	0.69	1.948	0.189	○	-
NGFS033420-332542	03:34:20.41	-33:25:41.5	17.45	-14.06	0.87	5.298	0.515	○	-
NGFS033422-343533	03:34:21.70	-34:35:33.2	16.80	-14.71	0.75	6.284	0.611	○	134
NGFS033431-325308	03:34:30.70	-32:53:08.4	20.02	-11.49	0.82	6.014	0.585	○	-

[a]: Assuming a distance modulus of $(m-M)_0 = 31.51$ mag or $D_L = 20.0$ Mpc (Blakeslee et al., 2009).

[b]: Sérsic index (Sérsic , 1963; Caon et al., 1993).

[c]: Morphological galaxy type classification: ⊙=nucleated, ○=non-nucleated dwarf galaxy.

ID	α_{2000}	δ_{2000}	m_i	M_i [a]	n [b]	$r_{\rm eff}$	$r_{\rm eff}$ [a]	Type [c]	Reference
	hh:mm:ss.ss	*dd:mm:ss.s*	[mag]	[mag]		[arcsec]	[kpc]		
NGFS033431-341752	03:34:30.87	-34:17:51.8	14.37	-17.14	1.39	14.546	1.414	⊙	135
NGFS033433-325003	03:34:33.07	-32:50:02.9	17.05	-14.46	0.74	10.244	0.996	⊙	-
NGFS033438-364801	03:34:38.22	-36:48:00.7	20.71	-10.80	1.13	2.073	0.202	○	-
NGFS033441-342117	03:34:40.50	-34:21:16.8	21.17	-10.34	0.11	8.109	0.788	○	-
NGFS033442-344760	03:34:42.29	-34:47:59.5	19.84	-11.67	0.51	4.104	0.399	○	-
NGFS033451-362747	03:34:51.11	-36:27:46.6	18.97	-12.54	0.51	8.833	0.859	○	-
NGFS033451-361926	03:34:51.44	-36:19:26.1	17.85	-13.66	0.81	5.840	0.568	○	138
NGFS033454-342140	03:34:53.65	-34:21:39.7	19.89	-11.62	0.64	6.137	0.597	○	-
NGFS033455-331233	03:34:55.11	-33:12:32.6	21.49	-10.02	0.37	5.477	0.532	○	-
NGFS033459-361150	03:34:58.73	-36:11:49.7	21.19	-10.32	0.76	4.379	0.426	○	-
NGFS033501-343209	03:35:00.67	-34:32:08.5	16.70	-14.81	1.21	12.824	1.247	⊙	-
NGFS033512-363433	03:35:12.26	-36:34:32.8	19.56	-11.95	0.74	7.127	0.693	○	-
NGFS033513-343235	03:35:12.45	-34:32:34.8	19.17	-12.34	0.44	6.644	0.646	○	-
NGFS033514-362321	03:35:13.87	-36:23:21.1	19.80	-11.71	0.47	3.846	0.374	⊙	-
NGFS033524-373706	03:35:23.60	-37:37:05.8	20.06	-11.45	0.68	3.428	0.333	○	-
NGFS033538-341717	03:35:37.80	-34:17:16.7	19.44	-12.07	0.41	13.490	1.313	○	-
NGFS033605-373655	03:36:04.77	-37:36:55.1	19.99	-11.53	0.82	4.554	0.443	○	-
NGFS033606-333333	03:36:05.69	-33:33:32.9	21.64	-9.87	0.88	5.134	0.499	○	-
NGFS033608-372618	03:36:08.21	-37:26:18.3	21.07	-10.44	1.79	3.786	0.368	○	-
NGFS033610-340453	03:36:10.42	-34:04:53.3	21.52	-9.99	0.39	3.716	0.361	○	-
NGFS033612-325233	03:36:11.89	-32:52:33.4	20.77	-10.74	0.24	6.002	0.584	○	-
NGFS033623-342043	03:36:22.92	-34:20:43.3	20.59	-10.92	0.24	13.25	1.288	○	-

[a]: Assuming a distance modulus of $(m-M)_0 = 31.51$ mag or $D_L = 20.0$ Mpc (Blakeslee et al., 2009).

[b]: Sérsic index (Sérsic , 1963; Caon et al., 1993).

[c]: Morphological galaxy type classification: ⊙=nucleated, ○=non-nucleated dwarf galaxy.

ID	α_{2000}	δ_{2000}	m_i	M_i ^{a}	n ^{b}	$r_{\rm eff}$	$r_{\rm eff}$ ^{a}	Type ^{c}	Reference
	hh:mm:ss.ss	*dd:mm:ss.s*	[mag]	[mag]		[arcsec]	[kpc]		
NGFS033624-370950	03:36:23.96	-37:09:50.1	17.22	-14.29	0.78	9.333	0.907	⊙	166
NGFS033625-370731	03:36:25.14	-37:07:30.8	18.69	-12.82	0.74	3.426	0.333	⊙	-
NGFS033633-374046	03:36:32.55	-37:40:45.6	20.80	-10.71	0.85	4.734	0.460	○	-
NGFS033637-372155	03:36:36.79	-37:21:55.1	18.93	-12.58	0.90	6.243	0.607	○	172
NGFS033643-340933	03:36:43.02	-34:09:32.8	17.12	-14.39	0.77	8.054	0.783	⊙	173
NGFS033645-330051	03:36:45.42	-33:00:50.6	15.41	-16.10	1.18	7.396	0.719	⊙	174
NGFS033649-341649	03:36:48.62	-34:16:48.5	16.20	-15.31	1.17	10.908	1.061	⊙	178
NGFS033650-332739	03:36:49.71	-33:27:38.9	15.52	-15.99	1.19	11.218	1.091	○	-
NGFS033657-374916	03:36:56.85	-37:49:16.0	19.06	-12.45	0.37	8.398	0.816	○	-
NGFS033658-380754	03:36:58.40	-38:07:53.9	17.61	-13.90	0.69	10.575	1.028	○	186
NGFS033659-330943	03:36:58.45	-33:09:42.7	21.04	-10.47	0.82	2.991	0.291	○	-
NGFS033716-365031	03:37:15.45	-36:50:30.6	20.64	-10.87	0.89	2.795	0.272	○	-
NGFS033723-341715	03:37:22.62	-34:17:14.6	18.78	-12.73	0.66	5.451	0.530	○	-
NGFS033727-331719	03:37:26.57	-33:17:19.0	18.86	-12.65	0.73	6.902	0.671	○	-
NGFS033730-341329	03:37:29.86	-34:13:28.5	19.77	-11.74	0.82	3.313	0.322	⊙	-
NGFS033731-340545	03:37:30.86	-34:05:45.2	20.64	-10.87	0.36	3.658	0.356	⊙	-
NGFS033731-364640	03:37:31.10	-36:46:40.4	21.81	-9.70	0.83	2.282	0.222	○	-
NGFS033732-363241	03:37:32.42	-36:32:40.7	18.66	-12.86	0.84	4.368	0.425	○	-
NGFS033743-371231	03:37:42.65	-37:12:30.8	17.12	-14.39	0.81	8.913	0.867	○	198
NGFS033744-364337	03:37:43.64	-36:43:36.7	18.43	-13.08	0.56	7.033	0.684	○	199
NGFS033754-371648	03:37:53.66	-37:16:47.9	15.88	-15.63	0.75	11.361	1.105	⊙	201
NGFS033756-375122	03:37:55.47	-37:51:21.7	17.34	-14.17	0.99	9.450	0.919	○	-

^{a}: Assuming a distance modulus of $(m-M)_0 = 31.51$ mag or $D_L = 20.0$ Mpc (Blakeslee et al., 2009).

^{b}: Sérsic index (Sérsic , 1963; Caon et al., 1993).

^{c}: Morphological galaxy type classification: ⊙=nucleated, ○=non-nucleated dwarf galaxy.

ID	α_{2000} *hh:mm:ss.ss*	δ_{2000} *dd:mm:ss.s*	m_i [mag]	M_i [a] [mag]	n [b]	r_{eff} [arcsec]	r_{eff} [a] [kpc]	Type [c]	Reference
NGFS033757-331620	03:37:56.50	-33:16:20.0	19.17	-12.34	0.76	5.538	0.538	○	-
NGFS033757-334953	03:37:57.00	-33:49:53.1	19.79	-11.72	0.51	10.226	0.994	○	-
NGFS033758-370709	03:37:58.02	-37:07:09.1	20.81	-10.70	0.18	10.647	1.035	○	-
NGFS033759-343148	03:37:59.06	-34:31:48.3	19.69	-11.82	0.89	6.445	0.627	○	-
NGFS033803-330514	03:38:02.99	-33:05:14.2	19.04	-12.47	0.67	6.319	0.614	○	-
NGFS033803-364431	03:38:03.21	-36:44:30.5	21.93	-9.58	0.38	3.201	0.311	○	-
NGFS033807-380534	03:38:07.42	-38:05:33.5	16.63	-14.88	0.62	11.463	1.115	⊙	205
NGFS033808-335847	03:38:08.00	-33:58:46.5	18.51	-13.00	0.95	6.493	0.631	⊙	-
NGFS033808-330133	03:38:08.33	-33:01:32.8	20.42	-11.09	1.05	2.047	0.199	○	-
NGFS033809-343108	03:38:09.08	-34:31:08.3	14.32	-17.19	1.28	15.758	1.532	⊙	203
NGFS033811-331204	03:38:11.12	-33:12:04.3	20.53	-10.98	0.83	4.936	0.480	○	-
NGFS033814-371724	03:38:13.48	-37:17:23.7	14.97	-16.54	0.97	16.781	1.632	○	206
NGFS033814-330738	03:38:13.55	-33:07:38.4	13.64	-17.87	1.12	18.460	1.795	⊙	204
NGFS033814-341343	03:38:13.63	-34:13:42.5	20.06	-11.45	0.80	8.911	0.866	○	-
NGFS033821-362449	03:38:21.08	-36:24:48.5	17.09	-14.42	0.59	15.460	1.503	⊙	212
NGFS033822-340144	03:38:21.59	-34:01:43.9	19.73	-11.78	0.32	3.509	0.341	○	-
NGFS033823-333938	03:38:22.50	-33:39:38.4	18.11	-13.40	0.62	7.292	0.709	⊙	209
NGFS033823-363304	03:38:23.27	-36:33:03.7	20.38	-11.13	0.89	5.515	0.536	⊙	-
NGFS033827-364424	03:38:27.37	-36:44:24.0	20.44	-11.07	0.71	9.889	0.961	○	-
NGFS033833-333948	03:38:33.10	-33:39:47.8	20.73	-10.78	0.51	3.570	0.347	○	-
NGFS033839-363331	03:38:39.33	-36:33:31.1	18.61	-12.90	0.55	6.493	0.631	○	216
NGFS033842-364339	03:38:41.66	-36:43:38.8	18.69	-12.82	1.14	5.586	0.543	⊙	217

[a]: Assuming a distance modulus of $(m-M)_0 = 31.51$ mag or $D_L = 20.0$ Mpc (Blakeslee et al., 2009).

[b]: Sérsic index (Sérsic , 1963; Caon et al., 1993).

[c]: Morphological galaxy type classification: ⊙=nucleated, ○=non-nucleated dwarf galaxy.

ID	α_{2000}	δ_{2000}	m_i	M_i [a]	n [b]	$r_{\rm eff}$	$r_{\rm eff}$ [a]	Type [c]	Reference
	hh:mm:ss.ss	*dd:mm:ss.s*	[mag]	[mag]		[arcsec]	[kpc]		
NGFS033854-363652	03:38:53.47	-36:36:52.0	20.23	-11.28	0.47	4.632	0.450	○	-
NGFS033904-363333	03:39:03.68	-36:33:32.9	21.27	-10.24	1.52	4.229	0.411	○	-
NGFS033907-341550	03:39:06.46	-34:15:49.7	18.53	-12.98	0.81	3.651	0.355	○	-
NGFS033907-342246	03:39:06.88	-34:22:46.1	20.75	-10.76	0.77	3.661	0.356	○	-
NGFS033909-330219	03:39:08.92	-33:02:18.6	17.40	-14.11	1.16	7.063	0.687	⊙	-
NGFS033915-342325	03:39:14.48	-34:23:25.3	20.99	-10.52	0.77	2.465	0.240	○	-
NGFS033915-341113	03:39:15.21	-34:11:12.9	21.68	-9.83	0.67	3.412	0.333	○	-
NGFS033921-340503	03:39:20.87	-34:05:02.7	22.07	-9.44	0.77	2.414	0.235	○	-
NGFS033921-380411	03:39:21.11	-38:04:10.6	21.15	-10.36	0.67	4.016	0.390	○	-
NGFS033925-363720	03:39:25.07	-36:37:20.0	20.64	-10.87	0.38	5.997	0.583	○	-
NGFS033932-333634	03:39:32.10	-33:36:34.0	20.81	-10.70	0.73	8.468	0.823	○	-
NGFS033938-363313	03:39:37.90	-36:33:13.2	18.92	-12.59	0.91	7.717	0.750	○	225
NGFS033948-330319	03:39:47.64	-33:03:18.5	18.02	-13.50	2.42	3.591	0.349	○	-
NGFS033955-364402	03:39:54.98	-36:44:01.9	21.31	-10.20	0.46	4.212	0.410	⊙	-
NGFS034005-341005	03:40:04.67	-34:10:04.7	17.69	-13.82	0.76	8.533	0.830	⊙	231
NGFS034005-374545	03:40:04.67	-37:45:44.8	21.46	-10.05	0.46	5.523	0.537	○	-
NGFS034007-363336	03:40:06.97	-36:33:35.8	18.08	-13.43	0.69	8.670	0.843	⊙	-
NGFS034010-342650	03:40:09.77	-34:26:50.0	16.34	-15.17	0.90	14.885	1.447	⊙	234
NGFS034015-363648	03:40:14.54	-36:36:47.6	21.35	-10.16	0.50	2.968	0.289	○	-
NGFS034019-372958	03:40:18.61	-37:29:57.7	17.66	-13.85	0.99	8.678	0.844	○	239
NGFS034019-332517	03:40:18.88	-33:25:16.9	16.73	-14.78	1.08	9.829	0.956	⊙	237
NGFS034021-373839	03:40:20.52	-37:38:39.2	16.93	-14.58	0.80	13.759	1.338	⊙	242

[a]: Assuming a distance modulus of $(m-M)_0 = 31.51$ mag or $D_L = 20.0$ Mpc (Blakeslee et al., 2009).

[b]: Sérsic index (Sérsic , 1963; Caon et al., 1993).

[c]: Morphological galaxy type classification: ⊙=nucleated, ○=non-nucleated dwarf galaxy.

ID	α_{2000}	δ_{2000}	m_i	M_i [a]	n [b]	r_{eff}	r_{eff} [a]	Type [c]	Reference
	hh:mm:ss.ss	*dd:mm:ss.s*	[mag]	[mag]		[arcsec]	[kpc]		
NGFS034030-332042	03:40:30.24	-33:20:42.2	19.60	-11.91	0.74	4.322	0.420	○	-
NGFS034033-363448	03:40:32.95	-36:34:48.2	21.22	-10.29	0.50	5.042	0.490	○	-
NGFS034033-363317	03:40:33.24	-36:33:17.2	21.78	-9.73	0.23	4.861	0.473	○	-
NGFS034036-364759	03:40:35.68	-36:47:59.3	21.75	-9.76	0.70	3.945	0.384	○	-
NGFS034044-372430	03:40:44.33	-37:24:29.5	16.14	-15.37	0.82	8.735	0.849	⊙	250
NGFS034055-373060	03:40:54.46	-37:30:59.7	19.17	-12.35	0.63	6.344	0.617	⊙	-
NGFS034055-375016	03:40:55.22	-37:50:16.0	15.38	-16.14	1.23	10.989	1.068	⊙	253
NGFS034058-375321	03:40:57.94	-37:53:20.9	18.76	-12.75	0.75	5.880	0.572	○	-
NGFS034101-334858	03:41:01.39	-33:48:58.1	17.78	-13.73	0.79	5.421	0.527	○	-
NGFS034103-344144	03:41:03.26	-34:41:43.5	20.79	-10.72	0.36	6.213	0.604	○	-
NGFS034107-370125	03:41:06.58	-37:01:25.3	20.12	-11.39	0.73	6.329	0.615	⊙	-
NGFS034109-331717	03:41:09.16	-33:17:16.7	20.65	-10.86	0.55	6.276	0.610	○	-
NGFS034113-375821	03:41:12.63	-37:58:20.6	20.58	-10.93	0.83	2.365	0.231	○	-
NGFS034118-344444	03:41:17.73	-34:44:43.9	20.96	-10.55	0.41	5.786	0.563	○	-
NGFS034121-334612	03:41:21.38	-33:46:11.6	14.91	-16.60	1.12	15.414	1.499	⊙	261
NGFS034126-341516	03:41:25.88	-34:15:15.6	19.36	-12.15	0.99	9.592	0.933	○	-
NGFS034131-365523	03:41:31.19	-36:55:22.9	19.25	-12.26	0.48	7.890	0.767	○	-
NGFS034136-372237	03:41:36.30	-37:22:36.6	21.81	-9.70	0.62	1.955	0.190	○	-
NGFS034139-345002	03:41:39.05	-34:50:01.7	20.70	-10.81	0.70	6.204	0.603	○	-
NGFS034140-362147	03:41:39.69	-36:21:46.8	19.01	-12.51	0.74	6.425	0.625	○	-
NGFS034146-372859	03:41:45.89	-37:28:59.2	19.82	-11.69	0.79	4.838	0.470	○	-
NGFS034147-361330	03:41:47.32	-36:13:29.5	21.95	-9.56	1.30	3.039	0.295	⊙	-

[a]: Assuming a distance modulus of $(m-M)_0 = 31.51$ mag or $D_L = 20.0$ Mpc (Blakeslee et al., 2009).

[b]: Sérsic index (Sérsic , 1963; Caon et al., 1993).

[c]: Morphological galaxy type classification: ⊙=nucleated, ○=non-nucleated dwarf galaxy.

ID	α_{2000}	δ_{2000}	m_i	M_i [a]	n [b]	r_{eff}	r_{eff} [a]	Type [c]	Reference
	hh:mm:ss.ss	*dd:mm:ss.s*	[mag]	[mag]		[arcsec]	[kpc]		
NGFS034150-363750	03:41:49.78	-36:37:49.8	17.59	-13.92	0.74	7.223	0.702	⊙	268
NGFS034158-362823	03:41:57.92	-36:28:23.2	22.73	-8.78	0.66	2.635	0.256	○	-
NGFS034160-370018	03:41:59.51	-37:00:17.7	18.58	-12.93	0.57	13.481	1.311	○	-
NGFS034160-373802	03:41:59.78	-37:38:02.4	18.90	-12.62	0.60	6.154	0.598	⊙	270
NGFS034201-345530	03:42:01.20	-34:55:30.1	21.46	-10.05	1.13	2.750	0.267	○	-
NGFS034206-345101	03:42:06.20	-34:51:01.3	18.09	-13.42	0.78	6.813	0.662	⊙	271
NGFS034207-361349	03:42:07.27	-36:13:49.4	20.98	-10.53	0.50	3.691	0.359	○	-
NGFS034210-334146	03:42:09.55	-33:41:45.9	19.49	-12.02	0.68	8.532	0.829	○	-
NGFS034213-343223	03:42:13.17	-34:32:23.3	21.76	-9.75	0.45	2.726	0.265	⊙	-
NGFS034215-360745	03:42:15.09	-36:07:45.0	21.46	-10.05	0.86	2.409	0.234	○	-
NGFS034216-342721	03:42:15.80	-34:27:20.6	18.19	-13.32	0.80	5.800	0.564	⊙	273
NGFS034219-370424	03:42:19.00	-37:04:23.8	19.60	-11.91	0.67	7.857	0.764	⊙	-
NGFS034226-344744	03:42:26.12	-34:47:44.4	19.03	-12.48	0.59	10.608	1.031	⊙	-
NGFS034226-364113	03:42:26.29	-36:41:12.7	15.99	-15.53	0.88	12.586	1.224	⊙	279
NGFS034227-335215	03:42:27.18	-33:52:14.6	15.85	-15.67	1.30	7.545	0.734	○	278
NGFS034231-350129	03:42:31.42	-35:01:29.2	21.12	-10.39	0.59	3.103	0.302	○	-
NGFS034236-341427	03:42:35.87	-34:14:27.2	20.98	-10.53	1.23	3.639	0.354	○	-
NGFS034239-343953	03:42:39.06	-34:39:52.8	21.03	-10.48	0.20	6.494	0.631	⊙	-
NGFS034241-344543	03:42:40.80	-34:45:43.0	19.51	-12.00	0.59	5.373	0.522	○	-
NGFS034242-370401	03:42:42.08	-37:04:00.5	22.48	-9.03	0.71	2.785	0.271	○	-
NGFS034246-335513	03:42:45.48	-33:55:13.2	13.39	-18.13	0.86	12.287	1.195	○	282
NGFS034255-352037	03:42:55.17	-35:20:37.3	18.60	-12.91	0.76	8.578	0.834	○	284

[a]: Assuming a distance modulus of $(m-M)_0 = 31.51$ mag or $D_L = 20.0$ Mpc (Blakeslee et al., 2009).

[b]: Sérsic index (Sérsic , 1963; Caon et al., 1993).

[c]: Morphological galaxy type classification: ⊙=nucleated, ○=non-nucleated dwarf galaxy.

ID	α_{2000}	δ_{2000}	m_i	M_i [a]	n [b]	r_{eff}	r_{eff} [a]	Type [c]	Reference
	hh:mm:ss.ss	*dd:mm:ss.s*	[mag]	[mag]		[arcsec]	[kpc]		
NGFS034301-364453	03:43:01.07	-36:44:52.5	20.84	-10.67	0.38	5.434	0.528	○	-
NGFS034302-351503	03:43:01.51	-35:15:03.1	21.18	-10.33	0.72	5.975	0.581	○	-
NGFS034302-351940	03:43:01.98	-35:19:39.7	20.56	-10.95	0.52	5.181	0.504	○	-
NGFS034313-343835	03:43:12.70	-34:38:35.0	17.09	-14.42	0.80	5.966	0.580	⊙	286
NGFS034320-371344	03:43:19.90	-37:13:44.4	20.78	-10.73	0.48	3.879	0.377	○	-
NGFS034323-335621	03:43:22.63	-33:56:20.7	14.08	-17.43	1.01	15.136	1.472	⊙	288
NGFS034323-344144	03:43:23.12	-34:41:43.8	17.87	-13.64	0.91	7.459	0.725	○	289
NGFS034325-370632	03:43:24.51	-37:06:31.9	19.50	-12.01	0.52	6.995	0.680	○	-
NGFS034326-351344	03:43:25.75	-35:13:44.1	21.30	-10.21	0.71	3.247	0.316	○	-
NGFS034326-363427	03:43:26.19	-36:34:26.6	21.17	-10.34	0.78	2.221	0.216	○	-
NGFS034327-341441	03:43:26.70	-34:14:41.2	19.48	-12.03	0.68	4.727	0.460	○	-
NGFS034333-340457	03:43:31.27	-34:04:56.5	20.86	-10.65	0.51	2.835	0.276	○	-
NGFS034333-360023	03:43:32.98	-36:00:22.5	19.23	-12.28	0.79	7.486	0.728	○	-
NGFS034338-344636	03:43:37.53	-34:46:36.3	20.64	-10.87	0.48	5.405	0.525	⊙	-
NGFS034339-352513	03:43:38.62	-35:25:13.4	21.89	-9.62	0.59	4.216	0.410	○	-
NGFS034340-351259	03:43:39.71	-35:12:58.7	18.53	-12.99	0.89	8.916	0.867	○	291
NGFS034343-364144	03:43:42.75	-36:41:43.9	21.41	-10.11	0.55	2.860	0.278	○	-
NGFS034349-353733	03:43:48.80	-35:37:32.6	18.11	-13.40	0.87	13.146	1.278	○	-
NGFS034352-364928	03:43:51.89	-36:49:28.2	20.74	-10.77	1.24	2.730	0.265	○	-
NGFS034356-354948	03:43:56.43	-35:49:48.4	20.67	-10.84	0.92	3.534	0.344	○	-
NGFS034405-374533	03:44:04.54	-37:45:32.5	20.03	-11.48	0.65	2.823	0.274	○	-
NGFS034408-353258	03:44:08.22	-35:32:58.0	17.58	-13.93	0.91	6.312	0.614	⊙	-

[a]: Assuming a distance modulus of $(m-M)_0 = 31.51$ mag or $D_L = 20.0$ Mpc (Blakeslee et al., 2009).

[b]: Sérsic index (Sérsic , 1963; Caon et al., 1993).

[c]: Morphological galaxy type classification: ⊙=nucleated, ○=non-nucleated dwarf galaxy.

ID	α_{2000} *hh:mm:ss.ss*	δ_{2000} *dd:mm:ss.s*	m_i [mag]	M_i [a] [mag]	n [b]	r_{eff} [arcsec]	r_{eff} [a] [kpc]	Type [c]	Reference
NGFS034410-361043	03:44:10.25	-36:10:43.0	19.22	-12.29	1.19	5.332	0.518	⊙	-
NGFS034412-363139	03:44:12.39	-36:31:39.3	20.35	-11.16	0.40	8.006	0.778	○	-
NGFS034423-343722	03:44:22.86	-34:37:21.9	21.57	-9.94	1.43	2.927	0.285	○	-
NGFS034425-355124	03:44:25.10	-35:51:24.3	16.83	-14.68	0.80	10.867	1.056	⊙	293
NGFS034427-353956	03:44:27.15	-35:39:56.1	16.64	-14.87	0.93	13.832	1.345	⊙	294
NGFS034429-360209	03:44:29.15	-36:02:08.9	18.58	-12.93	0.74	10.714	1.042	⊙	-
NGFS034430-351043	03:44:30.08	-35:10:43.3	18.03	-13.48	0.99	7.603	0.739	○	295
NGFS034433-351145	03:44:32.80	-35:11:45.2	15.22	-16.29	1.56	10.574	1.028	⊙	296
NGFS034439-355859	03:44:39.24	-35:58:58.8	17.34	-14.17	0.63	11.074	1.077	○	297
NGFS034444-354102	03:44:44.43	-35:41:01.6	15.47	-16.04	1.34	7.514	0.731	⊙	298
NGFS034445-351612	03:44:45.01	-35:16:11.5	20.23	-11.28	0.45	7.997	0.777	○	-
NGFS034450-353208	03:44:49.80	-35:32:08.0	20.64	-10.87	0.70	3.245	0.315	○	-
NGFS034451-354718	03:44:50.86	-35:47:17.6	21.78	-9.73	0.63	2.911	0.283	○	-
NGFS034453-351609	03:44:53.27	-35:16:08.5	21.74	-9.77	0.48	2.220	0.216	○	-
NGFS034455-335242	03:44:54.63	-33:52:41.5	20.61	-10.90	0.80	2.733	0.266	○	-
NGFS034455-362950	03:44:54.75	-36:29:49.9	19.44	-12.07	0.84	6.190	0.602	○	-
NGFS034460-361911	03:44:59.84	-36:19:10.9	14.74	-16.77	1.08	19.889	1.934	⊙	300
NGFS034501-344437	03:45:00.49	-34:44:36.6	21.28	-10.23	0.94	2.177	0.212	⊙	-
NGFS034501-333940	03:45:00.55	-33:39:40.1	20.14	-11.37	1.05	2.927	0.285	○	-
NGFS034501-343506	03:45:01.03	-34:35:06.0	19.25	-12.26	0.79	4.627	0.450	○	-
NGFS034504-333732	03:45:03.98	-33:37:32.3	22.21	-9.30	0.58	3.043	0.296	○	-
NGFS034509-363855	03:45:08.64	-36:38:55.1	19.07	-12.44	0.59	7.941	0.772	⊙	-

[a]: Assuming a distance modulus of $(m-M)_0 = 31.51$ mag or $D_L = 20.0$ Mpc (Blakeslee et al., 2009).

[b]: Sérsic index (Sérsic , 1963; Caon et al., 1993).

[c]: Morphological galaxy type classification: ⊙=nucleated, ○=non-nucleated dwarf galaxy.

ID	α_{2000} *hh:mm:ss.ss*	δ_{2000} *dd:mm:ss.s*	m_i [mag]	M_i [a] [mag]	n [b]	r_{eff} [arcsec]	r_{eff} [a] [kpc]	Type [c]	Reference
NGFS034514-365612	03:45:14.03	-36:56:12.4	14.07	-17.44	1.25	14.148	1.376	⊙	303
NGFS034517-365827	03:45:17.09	-36:58:26.9	18.63	-12.89	1.03	8.067	0.784	○	-
NGFS034522-353619	03:45:21.88	-35:36:11.8	21.69	-9.82	0.80	2.300	0.224	○	-
NGFS034531-343020	03:45:30.79	-34:30:20.1	18.17	-13.34	0.56	10.556	1.026	⊙	304
NGFS034533-345906	03:45:32.98	-34:59:05.6	19.88	-11.63	0.46	6.420	0.624	⊙	-
NGFS034534-370459	03:45:33.67	-37:04:58.7	14.46	-17.06	1.32	18.708	1.819	⊙	305
NGFS034534-354119	03:45:34.41	-35:41:18.6	19.25	-12.26	0.66	5.485	0.533	⊙	-
NGFS034538-365235	03:45:38.29	-36:52:34.7	20.75	-10.76	0.64	4.013	0.390	○	-
NGFS034541-345002	03:45:40.94	-34:50:01.9	22.64	-8.87	0.60	2.671	0.260	○	-
NGFS034548-350337	03:45:47.96	-35:03:36.9	17.07	-14.44	0.59	19.985	1.943	⊙	307
NGFS034549-345255	03:45:48.96	-34:52:55.3	21.66	-9.85	0.43	4.069	0.396	○	-
NGFS034550-355825	03:45:50.11	-35:58:25.3	19.99	-11.53	0.54	8.180	0.795	⊙	-
NGFS034552-335031	03:45:52.13	-33:50:30.6	21.40	-10.11	0.76	2.959	0.288	○	-
NGFS034553-345608	03:45:53.27	-34:56:08.4	20.25	-11.26	0.59	4.222	0.410	○	-
NGFS034557-353626	03:45:56.79	-35:36:25.6	19.95	-11.56	0.34	6.657	0.647	○	-
NGFS034601-351560	03:46:01.31	-35:15:59.7	19.36	-12.15	0.80	5.720	0.556	○	-
NGFS034608-364921	03:46:07.98	-36:49:21.2	16.92	-14.59	0.71	16.083	1.564	⊙	309
NGFS034615-344531	03:46:15.00	-34:45:31.3	21.87	-9.64	0.92	4.126	0.401	⊙	-
NGFS034618-364713	03:46:18.15	-36:47:13.3	21.72	-9.79	0.54	3.655	0.355	○	-
NGFS034618-334550	03:46:18.20	-33:45:48.6	15.71	-15.80	0.83	16.769	1.630	⊙	311
NGFS034620-343112	03:46:19.67	-34:31:12.3	20.62	-10.89	0.96	2.293	0.223	○	-
NGFS034634-344110	03:46:33.50	-34:41:10.1	16.40	-15.11	1.04	15.088	1.467	⊙	313

[a]: Assuming a distance modulus of $(m-M)_0 = 31.51$ mag or $D_L = 20.0$ Mpc (Blakeslee et al., 2009).

[b]: Sérsic index (Sérsic , 1963; Caon et al., 1993).

[c]: Morphological galaxy type classification: ⊙=nucleated, ○=non-nucleated dwarf galaxy.

ID	α_{2000} *hh:mm:ss.ss*	δ_{2000} *dd:mm:ss.s*	m_i [mag]	M_i [a] [mag]	n [b]	r_{eff} [arcsec]	r_{eff} [a] [kpc]	Type [c]	Reference
NGFS034634-352022	03:46:33.76	-35:20:21.8	20.93	-10.58	0.92	2.367	0.230	○	-
NGFS034637-364149	03:46:37.31	-36:41:49.4	20.43	-11.08	1.59	3.000	0.292	○	-
NGFS034647-350016	03:46:47.12	-35:00:16.4	21.24	-10.28	0.61	3.634	0.353	○	-
NGFS034658-350352	03:46:57.55	-35:03:51.6	21.11	-10.40	0.72	3.873	0.377	○	-
NGFS034701-350051	03:47:00.88	-35:00:50.8	19.50	-12.01	0.61	4.362	0.424	⊙	-
NGFS034701-362615	03:47:01.35	-36:26:15.3	15.30	-16.21	1.24	15.045	1.464	⊙	316
NGFS034708-361937	03:47:08.14	-36:19:37.4	14.99	-16.52	0.99	16.035	1.559	⊙	318
NGFS034717-343759	03:47:16.99	-34:37:59.2	18.60	-12.91	0.63	10.712	1.042	○	-
NGFS034724-344646	03:47:23.87	-34:46:45.7	17.06	-14.45	0.95	6.896	0.670	○	-
NGFS034724-355319	03:47:24.31	-35:53:18.9	21.18	-10.33	0.84	2.435	0.237	○	-
NGFS034737-362149	03:47:37.41	-36:21:49.4	16.93	-14.58	0.71	9.306	0.905	○	323
NGFS034744-350259	03:47:44.40	-35:02:59.3	19.76	-11.75	0.98	4.627	0.450	⊙	-
NGFS034746-360923	03:47:46.07	-36:09:23.0	20.84	-10.67	0.97	2.770	0.269	○	-
NGFS034747-365728	03:47:46.68	-36:57:28.1	19.05	-12.46	0.77	4.191	0.407	○	-
NGFS034747-353935	03:47:46.91	-35:39:35.3	19.23	-12.28	0.70	5.754	0.559	⊙	-
NGFS034753-362818	03:47:52.68	-36:28:18.1	14.14	-17.38	1.13	22.81	2.218	⊙	324
NGFS034754-350218	03:47:54.29	-35:02:17.6	19.72	-11.79	0.54	4.895	0.476	○	-
NGFS034802-350136	03:48:02.18	-35:01:35.9	17.26	-14.25	0.88	11.218	1.091	○	325
NGFS034803-364127	03:48:03.01	-36:41:27.4	19.92	-11.59	0.61	6.707	0.652	○	-
NGFS034804-364446	03:48:04.26	-36:44:45.9	17.63	-13.88	0.62	8.815	0.857	⊙	326
NGFS034819-354617	03:48:18.70	-35:46:17.2	21.40	-10.11	0.30	4.223	0.411	○	-
NGFS034821-362047	03:48:20.47	-36:20:46.9	21.10	-10.41	0.50	4.647	0.452	⊙	-

[a]: Assuming a distance modulus of $(m-M)_0 = 31.51$ mag or $D_L = 20.0$ Mpc (Blakeslee et al., 2009).

[b]: Sérsic index (Sérsic , 1963; Caon et al., 1993).

[c]: Morphological galaxy type classification: ⊙=nucleated, ○=non-nucleated dwarf galaxy.

ID	α_{2000} *hh:mm:ss.ss*	δ_{2000} *dd:mm:ss.s*	m_i [mag]	M_i [a] [mag]	n [b]	r_{eff} [arcsec]	r_{eff} [a] [kpc]	Type [c]	Reference
NGFS034822-360622	03:48:21.72	-36:06:22.2	17.77	-13.74	0.73	11.698	1.137	⊙	328
NGFS034844-352112	03:48:44.26	-35:21:12.1	19.87	-11.64	0.61	4.320	0.420	○	-
NGFS034853-335708	03:48:53.39	-33:57:08.4	21.41	-10.10	0.36	2.328	0.226	○	-
NGFS034855-355710	03:48:55.44	-35:57:10.3	17.02	-14.49	1.13	5.998	0.583	○	329
NGFS034906-343156	03:49:06.02	-34:31:56.0	21.24	-10.27	0.77	2.537	0.247	○	-
NGFS034913-365827	03:49:12.49	-36:58:26.6	16.48	-15.03	0.74	14.808	1.440	○	331
NGFS034914-355537	03:49:13.77	-35:55:37.1	18.50	-13.01	0.85	5.151	0.501	○	330
NGFS034917-365307	03:49:17.41	-36:53:06.8	22.10	-9.41	1.08	6.270	0.610	○	-
NGFS034918-335748	03:49:18.28	-33:57:47.8	20.83	-10.68	1.07	2.993	0.291	○	-
NGFS035009-362439	03:50:09.28	-36:24:39.2	19.67	-11.84	0.69	8.374	0.814	○	-
NGFS035022-353945	03:50:21.66	-35:39:45.1	20.47	-11.04	1.16	5.260	0.511	○	-
NGFS035101-364102	03:51:01.28	-36:41:01.5	17.19	-14.32	0.75	11.474	1.116	⊙	337

[a]: Assuming a distance modulus of $(m-M)_0 = 31.51$ mag or $D_L = 20.0$ Mpc (Blakeslee et al., 2009).

[b]: Sérsic index (Sérsic , 1963; Caon et al., 1993).

[c]: Morphological galaxy type classification: ⊙=nucleated, ○=non-nucleated dwarf galaxy.

Table 6: Nuclear star clusters parameters

Nucleus	RA (J2000)	Dec(J2000)	u'	g'	i'	J	K_s	$\log(\mathcal{M}_{*,\mathrm{nucleus}})$
	hh:mm:ss.ss	*dd:mm:ss.s*	[AB mag]	[AB mag]	[AB mag]	[AB mag]	[AB mag]	[$M_\odot$]
NGFS033322-353620n	03:33:22.19	−35:36:20.2	-	24.078±0.023	23.368±0.023	-	-	$5.370^{+0.009}_{-0.008}$
NGFS033332-353942n	03:33:32.16	−35:39:42.3	-	24.543±0.033	24.072±0.044	-	-	$5.184^{+0.013}_{-0.013}$
NGFS033346-353455n	03:33:46.05	−35:34:56.0	-	25.335±0.084	-	-	-	-
NGFS033412-351343n	03:34:12.18	−35:13:42.6	-	25.046±0.052	23.735±0.036	23.222±0.101	-	$5.490^{+0.137}_{-0.041}$
NGFS033420-352145n	03:34:20.17	−35:21:44.7	-	21.712±0.004	21.050±0.004	20.740±0.010	-	$6.310^{+0.227}_{-0.249}$
NGFS033444-355141n	03:34:44.17	−35:51:41.4	23.173±0.034	22.169±0.008	21.490±0.006	21.289±0.014	21.895±0.053	$6.087^{+0.284}_{-0.269}$
NGFS033446-345334n	03:34:46.13	−34:53:34.2	-	25.351±0.087	24.025±0.062	-	-	$5.395^{+0.059}_{-0.066}$
NGFS033453-353411n	03:34:52.74	−35:34:10.7	-	25.883±0.116	24.942±0.096	-	-	$4.804^{+0.106}_{-0.087}$
NGFS033456-351127n	03:34:56.49	−35:11:27.0	24.360±0.085	23.195±0.015	22.494±0.014	22.415±0.041	22.520±0.096	$5.658^{+0.215}_{-0.261}$
NGFS033458-350235n	03:34:58.21	−35:02:33.9	-	22.424±0.007	21.736±0.007	21.533±0.024	-	$6.010^{+0.240}_{-0.253}$
NGFS033512-351923n	03:35:11.50	−35:19:22.6	25.020±0.162	23.638±0.018	22.997±0.018	22.775±0.052	22.724±0.101	$5.460^{+0.354}_{-0.267}$
NGFS033524-362150n	03:35:24.08	−36:21:50.7	-	-	19.645±0.004	19.555±0.008	19.632±0.013	$6.562^{+0.118}_{-0.230}$
NGFS033525-361044n	03:35:25.20	−36:10:44.2	24.796±0.113	23.662±0.020	22.911±0.019	22.390±0.049	18.202±0.003	$5.655^{+0.229}_{-0.281}$
NGFS033543-353051n	03:35:42.79	−35:30:50.7	24.258±0.066	23.245±0.019	22.587±0.013	22.362±0.033	22.849±0.108	$5.636^{+0.273}_{-0.262}$
NGFS033546-355921n	03:35:46.30	−35:59:21.4	22.322±0.013	21.393±0.003	20.679±0.003	20.410±0.008	20.973±0.024	$6.405^{+0.290}_{-0.268}$
NGFS033604-352320n	03:36:04.05	−35:23:19.7	23.968±0.060	22.917±0.011	22.191±0.013	-	21.973±0.054	$5.759^{+0.370}_{-0.252}$
NGFS033624-355442n	03:36:23.64	−35:54:40.8	24.483±0.086	23.405±0.013	22.664±0.012	22.421±0.048	23.081±0.164	$5.627^{+0.254}_{-0.276}$
NGFS033628-351239n	03:36:27.96	−35:12:38.4	-	24.569±0.044	23.847±0.042	23.251±0.090	-	$5.340^{+0.433}_{-0.297}$
NGFS033632-362537n	03:36:32.21	−36:25:37.3	-	22.419±0.007	21.653±0.006	21.423±0.057	-	$6.087^{+0.161}_{-0.159}$
NGFS033637-352309n	03:36:37.27	−35:23:09.1	22.412±0.015	21.366±0.005	20.699±0.0032	20.320±0.006	20.909±0.020	$6.438^{+0.254}_{-0.277}$
NGFS033653-345619n	03:36:53.26	−34:56:18.1	23.056±0.021	21.836±0.005	21.093±0.0038	20.806±0.012	-	$6.202^{+0.346}_{-0.255}$
NGFS033657-355011n	03:36:57.12	−35:50:11.4	-	25.144±0.060	24.266±0.0491	-	-	$5.035^{+0.065}_{-0.045}$

Nucleus	RA (J2000)	Dec(J2000)	u'	g'	i'	J	K_s	$\log(\mathcal{M}_{*,\text{nucleus}})$
	hh:mm:ss.ss	*dd:mm:ss.s*	[AB mag]	[AB mag]	[AB mag]	[AB mag]	[AB mag]	$[M_\odot]$
NGFS033700-350816n	03:36:59.85	−35:08:15.4	-	25.062±0.051	24.563±0.0676	23.917±0.182	-	$5.050^{+0.099}_{-0.303}$
NGFS033700-352035n	03:36:59.83	−35:20:36.0	23.493±0.029	22.538±0.007	21.914±0.0065	21.519±0.017	21.984±0.053	$5.918^{+0.318}_{-0.263}$
NGFS033703-354802n	03:37:03.42	−35:48:02.1	-	24.784±0.041	23.696±0.0295	22.995±0.073	-	$5.461^{+0.139}_{-0.270}$
NGFS033708-344353n	03:37:08.16	−34:43:52.4	24.208±0.067	22.791±0.010	22.121±0.0117	21.655±0.038	21.697±0.091	$5.857^{+0.273}_{-0.274}$
NGFS033710-352312n	03:37:10.04	−35:23:11.8	-	24.537±0.090	23.664±0.0386	22.914±0.059	-	$5.539^{+0.233}_{-0.282}$
NGFS033710-355317n	03:37:10.35	−35:53:16.9	-	25.336±0.072	24.608±0.0793	-	-	$4.867^{+0.031}_{-0.028}$
NGFS033718-354157n	03:37:17.93	−35:41:57.3	23.708±0.049	22.711±0.010	21.929±0.0082	21.439±0.018	21.835±0.047	$5.972^{+0.336}_{-0.290}$
NGFS033727-355747n	03:37:27.49	−35:57:46.8	-	24.945±0.046	25.017±0.0928	-	-	$5.023^{+0.018}_{-0.020}$
NGFS033734-354945n	03:37:34.04	−35:49:44.9	24.632±0.095	23.451±0.015	22.754±0.0142	22.449±0.048	22.879±0.133	$5.565^{+0.315}_{-0.263}$
NGFS033742-343816n	03:37:41.97	−34:38:15.7	-	21.601±0.004	20.961±0.0031	20.670±0.028	-	$6.203^{+0.120}_{-0.204}$
NGFS033817-353028n	03:38:16.64	−35:30:27.5	24.332±0.089	23.276±0.017	22.637±0.0145	22.458±0.043	22.588±0.094	$5.586^{+0.274}_{-0.260}$
NGFS033837-355002n	03:38:36.63	−35:50:02.1	-	25.875±0.105	24.899±0.0889	22.174±0.034	-	$5.671^{+0.349}_{-0.270}$
NGFS033837-355502n	03:38:37.23	−35:55:01.5	-	26.191±0.153	25.057±0.1063	22.630±0.057	-	$5.440^{+0.370}_{-0.272}$
NGFS033838-354527n	03:38:37.66	−35:45:27.6	23.502±0.031	22.544±0.007	21.866±0.0057	21.346±0.015	22.084±0.058	$5.997^{+0.208}_{-0.287}$
NGFS033845-351600n	03:38:45.40	−35:15:59.6	24.432±0.074	23.578±0.015	22.883±0.0141	22.341±0.038	23.053±0.156	$5.611^{+0.176}_{-0.295}$
NGFS033854-344932n	03:38:54.26	−34:49:32.4	-	24.096±0.021	23.307±0.0243	-	-	$5.377^{+0.016}_{-0.009}$
NGFS033906-360557n	03:39:05.77	−36:05:56.2	22.584±0.018	21.526±0.004	20.786±0.003	20.440±0.008	21.080±0.030	$6.368^{+0.278}_{-0.270}$
NGFS033913-352217n	03:39:13.32	−35:22:16.8	22.080±0.014	21.274±0.005	20.526±0.0037	20.229±0.006	20.775±0.018	$6.486^{+0.269}_{-0.275}$
NGFS033920-354329n	03:39:19.69	−35:43:28.6	22.946±0.024	22.073±0.006	21.356±0.0055	21.036±0.011	21.840±0.045	$6.156^{+0.266}_{-0.275}$
NGFS033950-353122n	03:39:50.08	−35:31:22.1	24.062±0.074	23.256±0.014	22.706±0.015	22.249±0.032	22.985±0.126	$5.640^{+0.289}_{-0.307}$
NGFS033955-353943n	03:39:55.44	−35:39:42.9	-	25.251±0.063	24.227±0.0465	-	-	$5.127^{+0.064}_{-0.049}$
NGFS033956-353721n	03:39:56.45	−35:37:20.7	24.124±0.055	23.166±0.011	22.419±0.01	22.106±0.033	22.604±0.090	$5.699^{+0.299}_{-0.266}$
NGFS034001-344323n	03:40:00.56	−34:43:23.3	23.817±0.057	23.103±0.013	22.244±0.011	22.302±0.067	22.264±0.169	$5.798^{+0.214}_{-0.259}$
NGFS034010-355011n	03:40:09.77	−35:50:10.1	-	24.234±0.029	23.735±0.03	23.271±0.128	-	$5.214^{+0.226}_{-0.247}$

Nucleus	RA (J2000)	Dec(J2000)	u'	g'	i'	J	K_s	$\log(\mathcal{M}_{*,\text{nucleus}})$
	hh:mm:ss.ss	*dd:mm:ss.s*	[AB mag]	[AB mag]	[AB mag]	[AB mag]	[AB mag]	$[M_\odot]$
NGFS034019-361850n	03:40:19.35	−36:18:49.9	-	24.579±0.033	23.819±0.0315	-	-	$5.127^{+0.064}_{-0.049}$
NGFS034023-351636n	03:40:23.52	−35:16:35.7	22.556±0.016	21.593±0.004	20.832±0.0028	20.676±0.008	21.187±0.029	$6.380^{+0.215}_{-0.284}$
NGFS034027-362957n	03:40:26.99	−36:29:55.8	-	21.709±0.006	20.978±0.0048	-	-	$6.318^{+0.002}_{-0.002}$
NGFS034031-355241n	03:40:30.65	−35:52:40.7	-	-	23.878±0.0505	22.741±0.068	-	$5.735^{+0.091}_{-0.272}$
NGFS034034-350122n	03:40:33.83	−35:01:22.3	22.702±0.038	21.597±0.006	20.768±0.0041	20.656±0.011	21.121±0.036	$6.421^{+0.181}_{-0.271}$
NGFS034038-360716n	03:40:37.76	−36:07:16.4	-	24.655±0.038	23.903±0.0386	-	-	$5.127^{+0.064}_{-0.049}$
NGFS034044-361108n	03:40:43.85	−36:11:07.7	-	24.081±0.025	23.509±0.0293	23.049±0.191	-	$5.235^{+0.153}_{-0.222}$
NGFS034050-354454n	03:40:50.40	−35:44:54.4	20.788±0.005	19.603±0.002	18.718±0.0011	18.389±0.002	18.771±0.003	$7.255^{+0.289}_{-0.261}$
NGFS034101-354434n	03:41:00.78	−35:44:33.2	21.995±0.010	20.959±0.003	20.272±0.0019	19.993±0.007	20.546±0.018	$6.558^{+0.305}_{-0.264}$
NGFS034107-353052n	03:41:07.23	−35:30:51.9	-	24.355±0.035	23.706±0.0335	23.204±0.115	-	$5.310^{+0.143}_{-0.289}$
NGFS034113-350932n	03:41:12.87	−35:09:31.3	21.879±0.010	20.890±0.003	20.223±0.0024	20.212±0.010	20.674±0.029	$6.490^{+0.081}_{-0.015}$
NGFS034135-352625n	03:41:35.06	−35:26:24.3	-	23.736±0.018	22.882±0.0143	-	-	$6.318^{+0.002}_{-0.002}$
NGFS034217-353227n	03:42:17.25	−35:32:26.6	-	20.562±0.003	19.801±0.0018	-	-	$6.780^{+0.001}_{-0.001}$
NGFS034218-352819n	03:42:17.83	−35:28:18.7	-	25.447±0.082	24.545±0.0717	-	-	$4.938^{+0.076}_{-0.069}$
NGFS034225-353541n	03:42:25.22	−35:35:41.5	-	24.208±0.024	23.421±0.0212	-	-	$5.127^{+0.064}_{-0.049}$

BIBLIOGRAPHY

Abell, G. O. 1958, The Astrophysical Journal Supplement Series, 3, 211.

Abell, G. O., Corwin, H. G., & Olowin, R. P. 1989, The Astrophysical Journal Supplement Series, 70, 1.

Ahn, C. P., Seth, A. C., den Brok, M., et al. 2017, ApJ, 839, 72.

Amorisco, N. C. 2018, MNRAS, 475, L116

Annibali, F., Nipoti, C., Ciotti, L., et al. 2016, ApJ, 826, L27

Antonini, F. 2013, ApJ, 763, 62

Antonini, F., Barausse, E., & Silk, J. 2015, ApJ, 812, 72

Armandroff, T. E., & Zinn, R. 1988, AJ, 96, 92.

Astropy Collaboration, Robitaille, T. P., Tollerud, E. J., et al. 2013,A&A, 558, A33

Babul92, A., & Rees, M. J. 1992, MNRAS, 255, 346

Baldry, I. K., Glazebrook, K., Brinkmann, J., et al.\2004, ApJ, 600, 681.

Balogh, M. L., Morris, S. L., Yee, H. K. C., et al. 1997, ApJ, 488, L75.

Balogh, M. L., Schade, D., Morris, S. L., et al. 1998, ApJ, 504, L75.

Balogh, M. L., Baldry, I. K., Nichol, R., et al. 2004, ApJ, 615, L101.

Barmby, P., Huchra, J. P., Brodie, J. P., et al. 2000, AJ, 119, 727.

Bassino, L. P., Muzzio, J. C., & Rabolli, M. 1994, ApJ, 431, 634

Bassino, L. P., Richtler, T., & Dirsch, B. 2006, MNRAS, 367, 156.

Bastian, N., & Lardo, C. 2017, ArXiv e-prints , arXiv:1712.01286.

Baum, W. A. 1959, Publications of the Astronomical Society of the Pacific, 71, 106.

Beasley, M. A., Romanowsky, A. J., Pota, V., et al. 2016, ApJ, 819, L20

Bechtol, K., Drlica-Wagner, A., Balbinot, E., et al.\2015, ApJ, 807, 50.

Becker, M. R., McKay, T. A., Koester, B., et al. 2007, ApJ, 669, 905.

Beers, T. C., & Geller, M. J. 1983, ApJ, 274, 491.

Bekki K., 1998, ApJ, 502, L133

Bekki, K., Couch, W. J., & Drinkwater, M. J. 2001a, ApJ, 552, L105

Bekki, K., Couch, W. J., Drinkwater, M. J., et al. 2001b, ApJ, 557, L39.

Bekki, K., Couch, W. J., Drinkwater, M. J., & Shioya, Y. 2003, MNRAS, 344, 399

Bekki, K. 2007, PASA, 24, 77

Bekki, K., & Graham, A. W. 2010, ApJ, 714, L313.

Bell, E. F., McIntosh, D. H., Katz, N., & Weinberg, M. D. 2003, ApJS, 149, 289

Bellazzini, M., Ibata, R. A., Chapman, S. C., et al. 2008, AJ, 136, 1147

Belokurov, V., Zucker, D. B., Evans, N. W., et al.\2006, ApJ, 647, L111.

Bergond, G., Athanassoula, E., Leon, S., et al. 2007, A&A, 464, L21.

Bernardeau, F., Colombi, S., Gaztañaga, E., & Scoccimarro, R. 2002, Phys. Rep., 367, 1

Bertin, E., & Arnouts, S. 1996, A&AS, 117, 393

Bertin, E., Mellier, Y., Radovich, M., et al. 2002, in Astronomical Society of the Pacific Conference Series, Vol. 281, Astronomical Data Analysis Software and Systems XI, ed. D. A. Bohlender, D. Durand, & T. H. Handley, 228

Bertin, E. 2006, in Astronomical Society of the Pacific Conference Series, Vol. 351, Astronomical Data Analysis Software and Systems XV, ed. C. Gabriel, C. Arviset, D. Ponz, & S. Enrique, 112

Bertin, E. 2011, Astronomical Data Analysis Software and Systems XX, 442, 435

Binggeli, B., Sandage, A., & Tammann, G. A. 1985, AJ, 90, 1681

Binggeli, B., & Cameron, L. M. 1991, A&A, 252, 27.

Blakeslee, J. P., Lucey, J. R., Barris, B. J. et al. 2001, MNRAS, 327, 1004

Blakeslee, J. P., Franx, M., Postman, M., et al. 2003, ApJ, 596, L143.

Blakeslee, J. P., Jordán, A., Mei, S., et al. 2009, The Astrophysical Journal, 694, 556.

Blanton, M. R., & Roweis, S. 2007, The Astronomical Journal, 133, 734.

Blumenthal, G. R., Faber, S. M., Primack, J. R., et al. 1984, Nature, 311, 517.

Boch, T., & Fernique, P. 2014, in Astronomical Society of the Pacific Conference Series, Vol. 485, Astronomical Data Analysis Software and Systems XXIII, ed. N. Manset & P. Forshay, 277

Böker, T., Sarzi, M., McLaughlin, D. E., et al. 2004, AJ, 127, 105

Bonnarel, F., Fernique, P., Bienaymé, O., et al. 2000, A&AS, 143, 33

Bosler, T. L., Smecker-Hane, T. A., & Stetson, P. B. 2007, MNRAS, 378, 318.

Bovill, M. S., Puzia, T. H., Ricotti, M., & Taylor, M. A. 2016, ApJ, 832, 88

Bower, R. G., Lucey, J. R., & Ellis, R. S.\1992, MNRAS, 254, 601

Boylan-Kolchin, M., Bullock, J. S., & Kaplinghat, M. 2011, MNRAS, 415, L40.

Brodie, J. P., & Strader, J. 2006, Annual Review of Astronomy and Astrophysics, 44, 193.

Bruzual, G., & Charlot, S. 2003, MNRAS, 344, 1000.

Bullock, J. S., & Boylan-Kolchin, M. 2017, Annual Review of Astronomy and Astrophysics, 55, 343.

Butcher, H., & Oemler, A.\1978, ApJ, 219, 18.

Butcher, H., & Oemler, A.\1984, ApJ, 285, 426.

Campos, P. E., Mendes de Oliveira, C., & Bolte, M. 2004, IAU Colloq. 195: Outskirts of Galaxy Clusters: Intense Life in the Suburbs, 441

Caon, N., Capaccioli, M., & D'Onofrio, M. 1993, MNRAS, 265, 1013

Caon, N., Capaccioli, M., & D'Onofrio, M. 1994, A&AS, 106, 199

Capaccioli, M., Corwin, H. G., & Bottinelli, L. 1989, World of Galaxies (le Monde Des Galaxies), 208.

Carretta, E., Gratton, R. G., Clementini, G., et al. 2000, ApJ, 533, 215.

Carretta, E., Bragaglia, A., Gratton, R. G., et al. 2009, A&A, 505, 117.

Carrasco, E. R., Mendes de Oliveira, C., & Infante, L. 2006, AJ, 132, 1796

Carollo, C. M., Stiavelli, M., & Mack, J. 1998, AJ, 116, 68.

Cerviño, M., & Luridiana, V. 2004, A&A, 413, 145

Cerviño, M., Valls-Gabaud, D., Luridiana, V., & Mas-Hesse, J. M. 2002, A&A, 381, 51

Chatzopoulos, S., Fritz, T. K., Gerhard, O., et al. 2015, MNRAS, 447, 948.

Chiboucas, K., Jacobs, B. A., Tully, R. B., et al.\2013, AJ, 146, 126.

Chilingarian, I., Cayatte, V., Chemin, L., et al. 2007, A&A, 466, L21.

Chilingarian, I. V. 2009, MNRAS, 394, 1229.

Chilingarian, I., & Zolotukhin, I. 2015, Science, 348, 418.

Chincarini, G. L., Giovanelli, R., & Haynes, M. P. 1983, ApJ, 269, 13.

Cleveland, W. 1981, The American Statistician,, 35, 54

Cohen, J. G., Blakeslee, J. P., & Ryzhov, A. 1998, ApJ, 496, 808.

Colless, M., Dalton, G., Maddox, S., et al. 2001, MNRAS, 328, 1039.

Cooray, A., & Sheth, R. 2002, Phys. Rep., 372, 1

Connolly, A. J., Scranton, R., Johnston, D., et al. 2002, ApJ, 579, 42

Conselice, C. J., Gallagher, J. S., III, & Wyse, R. F. G. 2003, AJ, 125, 66

Côté, P. 1999, AJ, 118, 406.

Côté, P., Piatek, S., Ferrarese, L., et al. 2006, ApJS, 165, 57

Couture, J., Harris, W. E., & Allwright, J. W. B. 1991, ApJ, 372, 97.

Crnojević, D., Sand, D. J., Caldwell, N., et al. 2014, ApJ, 795, L35

Crnojević, D., Sand, D. J., Spekkens, K., et al. 2015, arXiv:1512.05366

Curir, A., Mazzei, P., & Murante, G. 2008, A&A, 481, 651

Curir, A., de Romeri, V., & Murante, G. 2010, Ap&SS, 327, 259

Dabringhausen, J., Hilker, M., & Kroupa, P. 2008, MNRAS, 386, 864.

Davies, R. D., & Lewis, B. M. 1973, MNRAS, 165, 231.

Da Rocha, C., Mieske, S., Georgiev, I. Y., et al. 2011, A&A, 525, A86

de Boer, T. J. L., Tolstoy, E., Hill, V., et al. 2012a, A&A, 539, A103.

de Boer, T. J. L., Tolstoy, E., Hill, V., et al. 2012b, A&A, 544, A73.

de Boer, T. J. L., Belokurov, V., & Koposov, S. 2015, MNRAS, 451, 3489

de Carvalho, R. R., Ribeiro, A. L. B., & Zepf, S. E. 1994, ApJS, 93, 47

Dekel, A., & Silk, J. 1986, ApJ, 303, 39.

den Brok, M., Peletier, R. F., Valentijn, E. A., et al. 2011, MNRAS, 414, 3052

den Brok, M., Peletier, R. F., Seth, A., et al. 2014, MNRAS, 445, 2385

De Propris, R., Colless, M., Peacock, J. A., et al.\2004, MNRAS, 351, 125.

Desjardins, T. D., Gallagher, S. C., Tzanavaris, P., et al. 2013, ApJ, 763, 121

de Vaucouleurs, G.\1948, Annales d'Astrophysique, 11, 247.

de Vaucouleurs, G. 1961, The Astrophysical Journal Supplement Series, 5, 233.

de Vaucouleurs, G., de Vaucouleurs, A., Corwin, H. G., Jr., et al. 1991, Third Reference Catalogue of Bright Galaxies. Volume I: Explanations and references. Volume II: Data for galaxies between 0^h and 12^h. Volume III: Data for galaxies between 12^h and 24^h., by de Vaucouleurs, G.; de Vaucouleurs, A.; Corwin, H. G., Jr.; Buta, R. J.; Paturel, G.; Fouqué, P.. Springer, New York, NY (USA), 1991, 2091 p.

Dirsch, B., Richtler, T., Geisler, D., et al. 2004, AJ, 127, 2114.

Djorgovski, S., & Davis, M. 1987, ApJ, 313, 59.

Dolney, D., Jain, B., & Takada, M. 2006, MNRAS, 366, 884

Domínguez, M. J., Zandivarez, A. A., Martínez, H. J., et al. 2002, MNRAS, 335, 825.

Dotter, A., Sarajedini, A., Anderson, J., et al. 2010, ApJ, 708, 698.

Dotter, A., Sarajedini, A., & Anderson, J. 2011, ApJ, 738, 74

Dressler, A. 980, ApJ, 236, 351.

Dressler, A., & Gunn, J. E. 1982, ApJ, 263, 533.

Dressler, A., & Gunn, J. E. 1992, The Astrophysical Journal Supplement Series, 78, 1.

Dressler, A. 1984, Annual Review of Astronomy and Astrophysics, 22, 185.

Dressler, A., Thompson, I. B., & Shectman, S. A. 1985, ApJ, 288, 481.

Drinkwater, M. J., Jones, J. B., Gregg, M. D., et al. 2000, Publications of the Astronomical Society of Australia, 17, 227.

Drinkwater, M. J., Gregg, M. D., & Colless, M. 2001, ApJ, 548, L139

Drinkwater, M. J., Gregg, M. D., Hilker, M., et al. 2003, Nature, 423, 519.

Eigenthaler, P., Puzia, T. H., Taylor, M. A., et al. 2018, ApJ, 855, 142.

Einasto, J. 1965, Trudy Astrofizicheskogo Instituta Alma-Ata, 5, 87

Einasto, J., & Haud, U. 1989, A&A, 223, 89

Ellis, R. S., Smail, I., Dressler, A., et al. 1997, ApJ, 483, 582.

Ellingson, E., Lin, H., Yee, H. K. C., et al.\2001, ApJ, 547, 609.

Evstigneeva, E. A., Gregg, M. D., Drinkwater, M. J., & Hilker, M. 2007, AJ, 133, 1722

Evstigneeva, E. A., Drinkwater, M. J., Peng, C. Y., et al. 2008, AJ, 136, 46

Faber, S. M. 1973, ApJ, 179, 423.

Faber, S. M., & Jackson, R. E. 1976, ApJ, 204, 668.

Faber, S. M., Dressler, A., Davies, R. L., et al. 1987, Nearly Normal Galaxies. From the Planck Time to the Present, 175.

Fall, S. M., & Rees, M. J. 1985, ApJ, 298, 18.

Fattahi, A., Navarro, J. F., Frenk, C. S., et al. 2018, MNRAS, 476, 3816.

Fellhauer, M., & Kroupa, P. 2002, MNRAS, 330, 642.

Fellhauer, M., & Kroupa, P. 2005, MNRAS, 359, 223.

Ferguson, H. C., & Sandage, A. 1988, AJ, 96, 1520.

Ferguson, H. C. 1989, AJ, 98, 367

Ferguson, H. C., & Binggeli, B.\1994, Astronomy and Astrophysics Review, 6, 67.

Ferrarese, L., & Merritt, D. 2000, ApJ, 539, L9.

Ferrarese, L., Côté, P., Jordán, A., et al. 2006a, ApJS, 164, 334

Ferrarese, L., Côté, P., Dalla Bontà, E., et al. 2006b, ApJ, 644, L21

Ferrarese, L., Côté, P., Cuillandre, J.-C., et al. 2012, ApJS, 200, 4

Ferrarese, L., Côté, P., Sánchez-Janssen, R., et al. 2016, ApJ, 824, 10

Fitzpatrick, E. L. 1999, PASP, 111, 63

Flaugher, B., Diehl, H. T., Honscheid, K., et al. 2015, AJ, 150, 150

Flores, R. A., & Primack, J. R. 1994, ApJ, 427, L1.

Forbes, D. A., & Bridges, T. 2010, MNRAS, 404, 1203

Forbes, D. A., Bastian, N., Gieles, M., et al. 2018, Proceedings of the Royal Society of London Series A, 474, 20170616.

Fouesneau, M., & Lançon, A. 2010, A&A, 521, A22

Foyle, K., Rix, H.-W., & Zibetti, S. 2010, MNRAS, 407, 163

Francis, K. J., Drinkwater, M. J., Chilingarian, I. V., Bolt, A. M., & Firth, P. 2012, MNRAS, 425, 325

Frank, M. J., Hilker, M., Mieske, S., et al. 2011, MNRAS, 414, L70.

Gaia Collaboration, Brown, A. G. A., Vallenari, A., et al. 2018, A&A, 616, A1.

Galleti, S., Federici, L., Bellazzini, M., et al. 2006, A&A, 456, 985.

Gebhardt, K., & Kissler-Patig, M. 1999, AJ, 118, 1526.

Gallagher, S. C., Durrell, P. R., Elmegreen, D. M., et al. 2010, AJ, 139, 545

Gebhardt, K., Lauer, T. R., Kormendy, J., et al. 2001, AJ, 122, 2469.

Geha, M., Guhathakurta, P., & van der Marel, R. P. 2003, AJ, 126, 1794.

Geisler, D., Smith, V. V., Wallerstein, G., et al. 2005, AJ, 129, 1428.

Genzel, R., Eisenhauer, F., & Gillessen, S. 2010, Reviews of Modern Physics, 82, 3121.

Georgiev, I. Y., Hilker, M., Puzia, T. H., Goudfrooij, P., & Baumgardt, H. 2009, MNRAS, 396, 1075

Georgiev, I. Y., Puzia, T. H., Goudfrooij, P., et al. 2010, MNRAS, 406, 1967.

Georgiev, I. Y., & Böker, T. 2014, MNRAS, 441, 3570

Georgiev, I. Y., Böker, T., Leigh, N., Lützgendorf, N., & Neumayer, N. 2016, MNRAS, 457, 2122

Gisler, G. R.\1978, MNRAS, 183, 633.

Girardi, M., Biviano, A., Giuricin, G., Mardirossian, F., & Mezzetti, M. 1993, ApJ, 404, 38

Giovanelli, R., & Haynes, M. P. 1983, AJ, 88, 881.

Goerdt, T., Moore, B., Kazantzidis, S., et al. 2008, MNRAS, 385, 2136

Gómez, P. L., Nichol, R. C., Miller, C. J., et al.\2003, ApJ, 584, 210.

González-Lópezlira, R. A., Lomelí-Núñez, L., Álamo-Martínez, K., et al. 2017, ApJ, 835, 184.

Goudfrooij, P., Strader, J., Brenneman, L., et al. 2003, MNRAS, 343, 665.

Goto, T., Yamauchi, C., Fujita, Y., et al. 2003, MNRAS, 346, 601.

Goz, D., Monaco, P., Murante, G., & Curir, A. 2015, MNRAS, 447, 1774

Graham, A. W. 2002, ApJ, 568, L13.

Graham, A. W., & Guzmán, R. 2003, AJ, 125, 2936.

Graham, A. W., & Driver, S. P. 2007, ApJ, 655, 77.

Graham, A. W., & Spitler, L. R. 2009, MNRAS, 397, 214

Grebel, E. K. 2001, Astrophysics and Space Science Supplement, 277, 231.

Grebel, E. K., Gallagher, J. S., III, & Harbeck, D. 2003, AJ, 125, 1926

Gregg, M. D., Drinkwater, M. J., Evstigneeva, E., et al. 2009, AJ, 137, 498.

Guérou, A., Emsellem, E., McDermid, R. M., et al. 2015, ApJ, 804, 70.

Gunn, J. E., & Gott, J. R. 1972, ApJ, 176, 1.

Haines, C. P., Smith, G. P., Egami, E., et al. 2009, ApJ, 704, 126.

Hanes, D. A. 1977, MNRAS, 180, 309.

Hansson, K. S. A., Lisker, T., & Grebel, E. K. 2012, MNRAS, 427, 2376

Harrington, R. G., & Wilson, A. G. 1950, Publications of the Astronomical Society of the Pacific, 62, 118.

Harris, W. E., & van den Bergh, S. 1981, AJ, 86, 1627.

Harris, W. E., Burbidge, G., Layzer, D., et al. 1991, Annual Review of Astronomy and Astrophysics, 29, 543.

Harris, W. E. 1996, AJ, 112, 1487.

Harris, W. E., Labhardt, L., & Binggeli, B. 2001, Saas-fee Advanced Course 28: Star Clusters, 223.

Harris, W. E. 2009, ApJ, 699, 254.

Haşegan, M., Jordán, A., Côté, P., et al. 2005, ApJ, 627, 203.

Hempel, M., Hilker, M., Kissler-Patig, M., et al. 2003, A&A, 405, 487.

Herschel, W. 1786, Philosophical Transactions of the Royal Society of London Series I, 76, 457.

Herschel, W. 1789, Philosophical Transactions of the Royal Society of London Series I, 79, 212.

Hickson, P., Mendes de Oliveira, C., Huchra, J. P., & Palumbo, G. G. 1992, ApJ, 399, 353

Hickson, P. 1982, ApJ, 255, 382.

Hickson, P. 1997, ARA&A, 35, 357

Hilker, M., Infante, L., Vieira, G., et al. 1999, Astronomy and Astrophysics Supplement Series, 134, 75.

Hilker, M. 2006, A&A, 448, 171.

Hilker, M. 2009, Reviews in Modern Astronomy, 21, 199.

Ho, L. C., Li, Z.-Y., Barth, A. J., Seigar, M. S., & Peng, C. Y. 2011, ApJS, 197, 21

Hodge, P. W. 1959, Publications of the Astronomical Society of the Pacific, 71, 28.

Hodge, P. W., Pyper, D. M., & Webb, C. J.\1965, AJ, 70, 559.

Hodge, P. W.\1971, Annual Review of Astronomy and Astrophysics, 9, 35.

Hodge, P. W. 1978, The Astrophysical Journal Supplement Series, 37, 429.

Holmberg, E. 1958, Meddelanden fran Lunds Astronomiska Observatorium Serie II, 136, 1.

Holtzman, J. A., Faber, S. M., Shaya, E. J., et al. 1992, AJ, 103, 691.

Horellou, C., Casoli, F., & Dupraz, C. 1995, A&A, 303, 361.

Hubble, E. P. 1926, ApJ, 64, 321.

Hubble, E. 1929, Proceedings of the National Academy of Science, 15, 168.

Hubble, E. P. 1936, Realm of the Nebulae.

Hunter, J. D. 2007, Computing In Science & Engineering, 9, 90

Huxor, A. P., Phillipps, S., & Price, J. 2013, MNRAS, 430, 1956.

Impey, C., Bothun, G., & Malin, D.\1988, ApJ, 330, 634.

Ibata, R. A., Lewis, G. F., Conn, A. R., et al. 2013, Nature, 493, 62

Ideta, M., & Makino, J. 2004, ApJ, 616, L107.

Iodice, E., Capaccioli, M., Grado, A., et al. 2016, ApJ, 820, 42.

Ivezić, Ž., Connolly, A., Vanderplas, J., & Gray, A. 2014, Statistics, Data Mining and Machine Learning in Astronomy (Princeton University Press)

James, P. A., & Percival, S. M. 2018, MNRAS, 474, 3101

Janssens, S., Abraham, R., Brodie, J., et al. 2017, ApJ, 839, L17

Janz, J., Laurikainen, E. and Lisker, T. et al. 2012, ApJ, 745, 24

Janz, J., Norris, M. A., Forbes, D. A., et al. 2016, MNRAS, 456, 617.

Javanmardi, B., Martinez-Delgado, D., Kroupa, P., et al. 2016, A&A, 588, A89

Jedrzejewski, R. I. 1987, MNRAS, 226, 747.

Johnson, T. L., Rigby, J. R., Sharon, K., et al. 2017, ApJ, 843, L21.

Jones, J. E., & Jones, B. J. T. 1980, MNRAS, 191, 685.

Jones, E., Oliphant, T., Peterson, P., et al. 2001–, SciPy: Open source scientific tools for Python.

Jones, J. B., Drinkwater, M. J., Jurek, R., et al. 2006, AJ, 131, 312.

Jordi, K., Grebel, E. K., & Ammon, K. 2006, A&A, 460, 339

Jordán, A., Côté, P., West, M. J., et al. 2004, AJ, 127, 24.

Jordán, A., Côté, P., Blakeslee, J. P., et al. 2005, ApJ, 634, 1002.

Jordán, A., McLaughlin, D. E., Côté, P., et al. 2007a, The Astrophysical Journal Supplement Series, 171, 101.

Jordán, A., Blakeslee, J. P., Côté, P., et al. 2007b, The Astrophysical Journal Supplement Series, 169, 213.

Jorgensen, I., Franx, M., & Kjaergaard, P. 1996, MNRAS, 280, 167.

Karachentseva, V. E., Karachentsev, I. D., & Boerngen, F. 1985, Astronomy and Astrophysics Supplement Series, 60, 213.

Kennicutt, R. C. 1983, AJ, 88, 483.

Kawakatu, N., & Umemura, M. 2002, MNRAS, 329, 572

Kewley, L. J., & Ellison, S. L. 2008, ApJ, 681, 1183

Kim, D.-W., & Fabbiano, G. 2003, ApJ, 586, 826.

Kim, H.-S., Yoon, S.-J., Sohn, S. T., et al. 2013, ApJ, 763, 40

King, I. 1962, AJ, 67, 471.

Kirby, E. N., Rizzi, L., Held, E. V., et al. 2017, ApJ, 834, 9.

Kissler-Patig, M., Brodie, J. P., Schroder, L. L., et al. 1998, AJ, 115, 105

Kissler-Patig, M., Brodie, J. P., & Minniti, D. 2002, A&A, 391, 441.

Klypin, A., Kravtsov, A. V., Valenzuela, O., et al. 1999, ApJ, 522, 82.

Koch, A., Grebel, E. K., Gilmore, G. F., et al. 2008a, AJ, 135, 1580.

Koch, A., McWilliam, A., Grebel, E. K., et al. 2008b, ApJ, 688, L13.

Koda, J., Yagi, M., Yamanoi, H., & Komiyama, Y. 2015, ApJ, 807, L2

Kodama, T., & Arimoto, N. 1997, A&A, 320, 41

Koleva, M., de Rijcke, S., Prugniel, P., et al. 2009, MNRAS, 396, 2133.

Konstantopoulos, I. S., Maybhate, A., Charlton, J. C., et al. 2013, ApJ, 770, 114

Koposov, S. E., Belokurov, V. et al. 2015, ApJ, 805, 130

Kormendy, J. 1977, ApJ, 217, 406.

Kormendy, J. 1979, ApJ, 227, 714.

Kormendy, J. 1985, ApJ, 295, 73.

Kormendy, J., Fisher, D. B., Cornell, M. E., et al. 2009, The Astrophysical Journal Supplement Series, 182, 216.

Kormendy, J., & Ho, L. C. 2013, ARA&A, 51, 511

Kron, G. E., & Mayall, N. U. 1960, AJ, 65, 581.

Kroupa, P. 2001, MNRAS, 322, 231

Kroupa, P., Theis, C., & Boily, C. M. 2005, A&A, 431, 517

Kroupa, P., Famaey, B., de Boer, K. S., et al. 2010, A&A, 523, A32

Kruijssen, J. M. D. 2015, MNRAS, 454, 1658.

Krusch, E., Rosenbaum, D., Dettmar, R.-J., et al. 2006, A&A, 459, 759

Kundu, A., & Whitmore, B. C. 2001, AJ, 121, 2950.

Laevens, B. P. M., Martin, N. F., Bernard, E. J., et al.\2015, ApJ, 813, 44.

Lauberts, A., & Valentijn, E. A. 1989, Garching: European Southern Observatory, |c1989,

Landy, S. D., & Szalay, A. S. 1993, ApJ, 412, 64

Larsen, S. S., Brodie, J. P., Huchra, J. P., et al. 2001, AJ, 121, 2974.

Launhardt, R., Zylka, R., & Mezger, P. G. 2002, A&A, 384, 112.

Leaman, R., VandenBerg, D. A., & Mendel, J. T. 2013, MNRAS, 436, 122

Ledo, H. R., Sarzi, M., Dotti, M., Khochfar, S., & Morelli, L. 2010, MNRAS, 407, 969

Lee, M. G., Kang, J., Lee, J. H., & Jang, I. S. 2017, ApJ, 844, 157

Lewis, I., Balogh, M., De Propris, R., et al.\2002, MNRAS, 334, 673.

Li, H., Gnedin, O. Y., Gnedin, N. Y., et al. 2017, ApJ, 834, 69.

Lin, D. N. C., & Faber, S. M. 1983, ApJ, 266, L21

Lisker, T., Grebel, E. K., & Binggeli, B. 2006a, AJ, 132, 497

Lisker, T., Glatt, K., Westera, P., & Grebel, E. K. 2006b, AJ, 132, 2432

Lisker, T., Grebel, E. K., Binggeli, B., & Glatt, K. 2007, ApJ, 660, 1186

Lisker, T. 2009, Astronomische Nachrichten, 330, 1043

Liu, C., Peng, E. W., Côté, P., et al. 2015, ApJ, 812, 34.

Longeard, N., Martin, N., Starkenburg, E., et al. 2018, MNRAS, 1901.

Lotz, J. M., Telford, R., Ferguson, H. C., et al. 2001, ApJ, 552, 572

Lotz, J. M., Miller, B. W., & Ferguson, H. C. 2004, ApJ, 613, 262

LSST Science Collaboration, Abell, P. A., Allison, J., et al. 2009, ArXiv e-prints , arXiv:0912.0201.

Ma, J., van den Bergh, S., Wu, H., et al. 2006, ApJ, 636, L93

Madau, P., & Dickinson, M. 2014, Annual Review of Astronomy and Astrophysics, 52, 415.

Madrid, J. P., Graham, A. W., Harris, W. E., et al. 2010, ApJ, 722, 1707.

Magorrian, J., Tremaine, S., Richstone, D., et al. 1998, AJ, 115, 2285.

Mamon, G. A. 1992, ApJ, 401, L3

Mapelli, M., Rampazzo, R., & Marino, A. 2015, A&A, 575, A16.

Maraston, C., Bastian, N., Saglia, R. P., et al. 2004, A&A, 416, 467.

Martin, D. C., Wyder, T. K., Schiminovich, D., et al. 2007, The Astrophysical Journal Supplement Series, 173, 342.

Marín-Franch, A., Aparicio, A., Piotto, G., et al. 2009, ApJ, 694, 1498

Martínez-Delgado, D., Romanowsky, A. J., Gabany, R. J., et al. 2012, ApJ, 748, L24

Matteucci, F., & Greggio, L. 1986, A&A, 154, 279

Matteucci, F., & Recchi, S. 2001, ApJ, 558, 351

Matthews, T. A., Morgan, W. W., & Schmidt, M. 1964, ApJ, 140, 35.

Matthews, L. D., & Gallagher, J. S. 1997, AJ, 114, 1899.

McConnachie, A. W. 2012, AJ, 144, 4

McConnell, N. J., & Ma, C.-P. 2013, ApJ, 764, 184

Mei, S., Holden, B. P., Blakeslee, J. P., et al. 2006, ApJ, 644, 759.

Mei, S., Blakeslee, J. P., Côté, P., et al. 2007, ApJ, 655, 144.

Mei, S., Holden, B. P., Blakeslee, J. P., et al. 2009, ApJ, 690, 42.

Mendes de Oliveira, C., & Hickson, P. 1994, ApJ, 427, 684

Merritt, A., van Dokkum, P., & Abraham, R.\2014, ApJ, 787, L37.

Messier, C. 1764, Philosophical Transactions of the Royal Society of London Series I, 54, 68.

Messier, C. 1798, in Connaissance des Temps, 1801, 461

Michielsen, D., Boselli, A., Conselice, C. J., et al. 2008, MNRAS, 385, 1374.

Mieske, S., Hilker, M., & Infante, L. 2004, A&A, 418, 445.

Mieske, S., Infante, L., Hilker, M., et al. 2005, A&A, 430, L25.

Mieske, S., Hilker, M., Infante, L., & Mendes de Oliveira, C. 2007, A&A, 463, 503

Mieske, S., Hilker, M., Jordán, A., et al. 2008, A&A, 487, 921.

Mieske, S., Hilker, M., Misgeld, I., et al. 2009, A&A, 498, 705.

Mieske, S., Hilker, M., & Misgeld, I. 2012, A&A, 537, A3.

Mieske, S., Frank, M. J., Baumgardt, H., et al. 2013, A&A, 558, A14

Mihos, J. C., & Hernquist, L. 1994, ApJ, 437, L47

Mihos, J. C., Mulchaey, J. S., Dressler, A., et al. 2004, Clusters of Galaxies: Probes of Cosmological Structure and Galaxy Evolution, 277.

Mihos, J. C., Harding, P., Feldmeier, J., & Morrison, H. 2005, ApJ, 631, L41

Mihos, J. C., Durrell, P. R., Ferrarese, L., et al. 2015, ApJ, 809, 21

Mihos, J. C., Harding, P., Feldmeier, J. J., et al. 2017, ApJ, 834, 16

Miller, B. P., Gallo, E., Greene, J. E., et al. 2015, ApJ, 799, 98.

Milone, A. P., Piotto, G., Bedin, L. R., et al. 2012, ApJ, 744, 58.

Minniti, D. 1995, AJ, 109, 1663.

Misgeld, I., Mieske, S., & Hilker, M. 2008, A&A, 486, 697

Misgeld, I., & Hilker, M. 2011, MNRAS, 414, 3699

Mistani, P. A., Sales, L. V., Pillepich, A., et al. 2016, MNRAS, 455, 2323.

Moore, B. 1994, Nature, 370, 629.

Moore, B., Lake, G., & Katz, N. 1998, ApJ, 495, 139.

Moore, B., Ghigna, S., Governato, F., et al. 1999, ApJ, 524, L19.

Morgan, W. W., & Lesh, J. R. 1965, ApJ, 142, 1364.

Müller, O., Jerjen, H., & Binggeli, B. 2017, A&A, 597, A7

Muñoz, R. P., Puzia, T. H., Lançon, A., et al. 2014, ApJS, 210, 4

Muñoz, R. P., Eigenthaler, P., Puzia, T. H., et al. 2015, ApJ, 813, L15

Mucciarelli, A., Bellazzini, M., Ibata, R., et al. 2017, A&A, 605, A46

Mutlu-Pakdil, B., Sand, D. J., Carlin, J. L., et al. 2018, ApJ, 863, 25.

Naab, T., & Burkert, A. 2003, ApJ, 597, 893.

Neumayer, N., & Walcher, C. J. 2012, Advances in Astronomy, 2012, 709038

Nguyen, D. D., Seth, A. C., den Brok, M., et al. 2017, ApJ, 836, 237

Nguyen, D. D., Seth, A. C., Neumayer, N., et al. 2018, ApJ, 858, 118.

Nieto, J.-L., & Prugniel, P. 1987, A&A, 186, 30.

Norris, M. A., & Kannappan, S. J. 2011, MNRAS, 414, 739.

Norris, M. A., Kannappan, S. J., Forbes, D. A., et al. 2014, MNRAS, 443, 1151.

Norris, M. A., Escudero, C. G., Faifer, F. R., et al. 2015, MNRAS, 451, 3615.

Ordenes-Briceño, Y., Taylor, M. A., Puzia, T. H., et al. 2016, MNRAS, 463, 1284

Ordenes-Briceño, Y., Eigenthaler, P., Taylor, M. A., et al. 2018a, ApJ, 859, 52.

Ordenes-Briceño, Y., Puzia, T. H., Eigenthaler, P., et al. 2018b, ApJ, 860, 4.

Osterbrock, D. E.\1960, ApJ, 132, 325.

Pancino, E., Carrera, R., Rossetti, E., et al. 2010, A&A, 511, A56.

Paolillo, M., Fabbiano, G., Peres, G., et al. 2002, ApJ, 565, 883.

Paudel, S., Lisker, T. & Janz, J. 2010, ApJ, 724, L64

Paudel, S., Lisker, T., & Kuntschner, H. 2011, MNRAS, 413, 1764

Paudel, S., Lisker, T., Hansson, K. S. A., et al. 2014, MNRAS, 443, 446.

Pawlowski, M. S., Pflamm-Altenburg, J., & Kroupa, P. 2012, MNRAS, 423, 1109

Pawlowski, M. S., Famaey, B., Jerjen, H., et al. 2014, MNRAS, 442, 2362

Pearson, S., Besla, G. et al. 2016, MNRAS, tmp, 538

Pedregosa, F., Varoquaux, G., Gramfort, A., et al. 2012, JMLR, 12, 2825

Peebles, P. J. E., & Dicke, R. H. 1968, ApJ, 154, 891.

Peebles, P. J. E. 1982, ApJ, 263, L1.

Peletier, R. F., & Balcells, M. 1996, AJ, 111, 2238.

Peng, C. Y., Ho, L. C., Impey, C. D., & Rix, H.-W. 2002, AJ, 124, 266

Peng, E. W., Jordán, A., Côté, P., et al. 2006, ApJ, 639, 95.

Peng, E. W., Jordán, A., Côté, P., et al. 2008, ApJ, 681, 197.

Peng, C. Y., Ho, L. C., Impey, C. D. and Rix, H.-W. 2010, AJ, 139, 2097

Penzias, A. A., & Wilson, R. W. 1965, ApJ, 142, 419.

Peterson, C. J., & King, I. R. 1975, AJ, 80, 427.

Pfeffer, J., & Baumgardt, H. 2013, MNRAS, 433, 1997

Pfeffer, J., Kruijssen, J. M. D., Crain, R. A., et al. 2018, MNRAS, 475, 4309.

Piotto, G., Bedin, L. R., Anderson, J., et al. 2007, ApJ, 661, L53.

Piotto, G., Milone, A. P., Anderson, J., et al. 2012, ApJ, 760, 39.

Pizzella, A., Corsini, E. M. et al. 2002, ApJ, 573, 131

Plana, H.,Mendes de Oliveira, C. et al. 1998, AJ, 116, 2123

Planck Collaboration, Aghanim, N., Akrami, Y., et al. 2018, ArXiv e-prints , arXiv:1807.06209.

Ponman et al. 1996, MNRAS, 283, 690

Postman, M., & Geller, M. J. 1984, ApJ, 281, 95.

Powalka, M., Lançon, A., Puzia, T. H., et al. 2016a,ApJS, 227, 12

Powalka, M., Puzia, T. H., Lançon, A., et al. 2016b, ApJ, 829, L5

Powalka, M., Lançon, A., Puzia, T. H., et al. 2017, ApJ, 844, 104

Price, J., Phillipps, S., Huxor, A., et al. 2009, MNRAS, 397, 1816.

Pryor, C., Meylan, G., Djorgovski, S. G., et al. 1993, Structure and Dynamics of Globular Clusters, 357.

Proctor, R. N., Forbes, D. A., Hau, G. K. T., Beasley, M. A. et al. 2004, MNRAS, 349, 1381

Puzia, T. H., Kissler-Patig, M., Brodie, J. P., et al. 1999, AJ, 118, 2734.

Puzia, T. H., Zepf, S. E., Kissler-Patig, M., et al. 2002, A&A, 391, 453.

Puzia, T. H., Kissler-Patig, M., Thomas, D., et al. 2005, A&A, 439, 997

Puzia, T. H., Paolillo, M., Goudfrooij, P., et al. 2014, ApJ, 786, 78

Quintana, H., & Lawrie, D. G. 1982, AJ, 87, 1.

Rejkuba, M. 2012, Ap&SS, 341, 195

Renaud, F., Agertz, O., & Gieles, M. 2017, MNRAS, 465, 3622.

Renzini, A.\2006, Annual Review of Astronomy and Astrophysics, 44, 141.

Rhode, K. L., & Zepf, S. E. 2004, AJ, 127, 302.

Rhode, K. L., Zepf, S. E., & Santos, M. R. 2005, ApJ, 630, L21.

Ribeiro, A. L. B., de Carvalho, R. R., & Zepf, S. E. 1994, MNRAS, 267, L13

Richtler, T., Grebel, E. K., Domgoergen, H., et al. 1992, A&A, 264, 25.

Roediger, J. C., Ferrarese, L., Côté, P., et al. 2017, ApJ, 836, 120

Rong, Y., Guo, Q., Gao, L., et al. 2017, MNRAS, 470, 4231

Rood, H. J., & Sastry, G. N. 1971, Publications of the Astronomical Society of the Pacific, 83, 313.

Rossa, J., van der Marel, R. P., Böker, T., et al. 2006, AJ, 132,1074

Rubin et al. 1991, ApJS, 76, 153

Ryś, A., van de Ven, G., & Falcón-Barroso, J. 2014, MNRAS, 439, 284

Ryś, A., Koleva, M., Falcón-Barroso, J., et al. 2015, MNRAS, 452, 1888

Saito, R. K., Hempel, M., Minniti, D., et al. 2012, A&A, 537, A107.

Salpeter, E. E. 1955, ApJ, 121, 161.

Sánchez-Blázquez, P., Peletier, R. F., Jiménez-Vicente, J., et al. 2006, MNRAS, 371, 703

Sandage, A., & Visvanathan, N. 1978, ApJ, 223, 707.

Sandage, A., & Tammann, G. A. 1981, Washington: Carnegie Institution.

Sandage, A., & Binggeli, B. 1984, AJ, 89, 919

Sarajedini, A., Bedin, L. R., Chaboyer, B., et al. 2007, AJ, 133, 1658.

Sato, M., Hamana, T., Takahashi, R., et al. 2009, ApJ, 701, 945

Scharf, C. A., Zurek, D. R., & Bureau, M. 2005, ApJ, 633, 154.

Schlafly, E. F., & Finkbeiner, D. P. 2011, ApJ, 737, 103

Schlegel, D. J., Finkbeiner, D. P., & Davis, M. 1998, ApJ, 500, 525

Schneider, P. 2015, Extragalactic Astronomy and Cosmology: An Introduction.

Schödel, R., Merritt, D., & Eckart, A. 2009, A&A, 502, 91.

Schödel, R., Feldmeier, A., Kunneriath, D., et al. 2014, A&A, 566, A47

Schombert, J. M. 1986, The Astrophysical Journal Supplement Series, 60, 603.

Schombert, J. M., Pildis, R. A., Eder, J. A., et al. 1995, AJ, 110, 2067.

Schuberth, Y., Richtler, T., Hilker, M., et al. 2010, A&A, 513, A52.

Schweizer, F. 1980, ApJ, 237, 303.

Seth, A. C., van den Bosch, R., Mieske, S., et al. 2014, Nature, 513, 398.

Seth, A., Agüeros, M., Lee, D., et al. 2008, ApJ, 678, 116.

Sérsic, J. L. 1963, Boletin de la Asociacion Argentina de Astronomia La Plata Argentina, 6, 41

Shapley, H. 1938, Nature, 142, 715.

Shapley, H. 1939, Proceedings of the National Academy of Science, 25, 565.

Skrutskie, M. F., Cutri, R. M., Stiening, R., et al. 2006, AJ, 131, 1163

Smith Castelli, A. V., Cellone, S. A., Faifer, F. R., et al. 2012, MNRAS, 419, 2472.

Smith, R., Sánchez-Janssen, R., Fellhauer, M., et al. 2013, MNRAS, 429, 1066

Smith, R., Sánchez-Janssen, R., Beasley, M. A., et al. 2015, MNRAS, 454, 2502

Sparke, L. S., & Gallagher, J. S. 2007, Galaxies in the Universe: An Introduction. Second Edition. By Linda S. Sparke and John S. Gallagher.

Springel, V., Di Matteo, T., & Hernquist, L. 2005, MNRAS, 361, 776.

Spengler, C., Côté, P., Roediger, J., et al. 2017, ApJ, 849, 55

Stanford, S. A., Eisenhardt, P. R., & Dickinson, M. 1998, ApJ, 492, 461.

Stetson, P. B. 2000, PASP, 112, 925

Stierwalt, S., Liss, S. E., Johnson, K. E., et al. 2017, Nature Astronomy, 1, 0025

Strateva, I., Ivezić, Ž., Knapp, G. R., et al.\2001, AJ, 122, 1861.

Sutherland, W., Emerson, J., Dalton, G., et al. 2015, A&A, 575, A25

Taylor, M. A., Puzia, T. H., Harris, G. L., et al. 2010,ApJ, 712, 1191

Taylor, M. A., Puzia, T. H., Gomez, M., et al. 2015, ApJ, 805, 65.

Taylor, E. N., Hopkins, A. M., Baldry, I. K., et al. 2015, MNRAS, 446, 2144.

Tegmark, M., Dodelson, S., Eisenstein, D. J., et al. 2002, ApJ, 571, 191

Tegmark, M., Blanton, M. R., Strauss, M. A., et al. 2004, ApJ, 606, 702

Thilker, D. A., Bianchi, L., Schiminovich, D., et al. 2010, ApJ, 714, L171.

Thomas, D., Maraston, C., Bender, R., & Mendes de Oliveira, C. 2005,ApJ, 621, 673

Tody, D. 1986, Instrumentation in Astronomy VI, 733.

Toloba, E., Guhathakurta, P., Boselli, A., et al. 2015, ApJ, 799, 172.

Tolstoy, E., Hill, V., & Tosi, M. 2009, Annual Review of Astronomy and Astrophysics, 47, 371.

Toomre, A., & Toomre, J. 1972, ApJ, 178, 623.

Torrey, P., Vogelsberger, M., Marinacci, F., et al. 2017, ArXiv e-prints, arXiv:1711.05261

Tremaine, S. D., Ostriker, J. P., & Spitzer, Jr., L. 1975, ApJ, 196, 407

Tremonti, C. A., Heckman, T. M., Kauffmann, G., et al. 2004, The Astrophysical Journal, 613, 898.

Tsujimoto, T., Nomoto, K., Yoshii, Y., et al. 1995, MNRAS, 277, 945

Tully, R. B., Libeskind, N. I., Karachentsev, I. D., et al. 2015, ApJ, 802, L25

Turner, M. L., Côté, P., Ferrarese, L., et al. 2012, ApJS, 203, 5

Valdes, F., Gruendl, R., & DES Project 2014, Astronomical Data Analysis Software and Systems XXIII, 485, 379

Valluri, M., Ferrarese, L., Merritt, D., et al. 2005, ApJ, 628, 137.

van den Bergh, S. 1986, AJ, 91, 271

van den Bergh, S., Morbey, C., & Pazder, J. 1991, ApJ, 375, 594.

Vandenberg, D. A., Bolte, M., & Stetson, P. B. 1990, AJ, 100, 445.

VandenBerg, D. A., Brogaard, K., Leaman, R., & Casagrande, L. 2013, ApJ, 775, 134

van den Bosch, F. C., Ferrarese, L., Jaffe, W. et al. 1994, AJ, 108, 1579

van der Burg, R. F. J., Muzzin, A., & Hoekstra, H. 2016, A&A, 590, A20

van der Burg, R. F. J., Hoekstra, H., Muzzin, A., et al. 2017, A&A, 607, A79

VanderPlas, J., Connolly, A. J., Ivezic, Z., & Gray, A. 2012, Proceedings of Conference on Intelligent Data Understanding (CIDU), pp. 47-54, 2012., 47

Van Der Walt, S., Colbert, S. C. and Varoquaux, G. 2011, Comp. in Sci. and Eng., 13, 22

van Dokkum, P. G., Abraham, R., Merritt, A., et al. 2015, ApJ, 798, L45

van Dokkum, P., Abraham, R., Brodie, J., et al. 2016, ApJ, 828, L6

Vanzella, E., Calura, F., Meneghetti, M., et al. 2017, MNRAS, 467, 4304.

Venhola, A., Peletier, R., Laurikainen, E., et al. 2017, A&A, 608, A142

Verde, L., Heavens, A. F., Percival, W. J., et al. 2002b, ArXiv e-prints , astroâph/0212311.

Verde, L., Heavens, A. F., Percival, W. J., et al. 2002a, MNRAS, 335, 432.

Villegas, D., Jordán, A., Peng, E. W., et al. 2010, ApJ, 717, 603.

Visvanathan, N., & Sandage, A.\1977, ApJ, 216, 214.

Wade, C. M. 1963, National Radio Astronomy Observatory Publications, 1, 99.

Walcher, C. J., Böker, T., Charlot, S., et al. 2006, ApJ, 649, 692

Welch, G. A., Chincarini, G., & Rood, H. J. 1975, AJ, 80, 77.

Wenger, M., Ochsenbein, F., Egret, D., et al. 2000, A&AS, 143, 9

Wetzel, A. R., Deason, A. J., & Garrison-Kimmel, S. 2015, ApJ, 807, 49

Wheeler, C., Oñorbe, J., Bullock, J. S., et al. 2015, MNRAS, 453, 1305

White, P. M., Bothun, G., Guerrero, M. A. et al. 2003, ApJ, 585, 739

White, S. D. M., & Rees, M. J. 1978, MNRAS, 183, 341.

Whitmore, B. C., Chandar, R., Schweizer, F., et al. 2010, AJ, 140, 75.

Willman, B., & Strader, J. 2012, AJ, 144, 76

Wilson, A. G. 1955, Publications of the Astronomical Society of the Pacific, 67, 27.

Wirth, A., & Gallagher, J. S. 1984, ApJ, 282, 85.

Wittmann, C., Lisker, T., Pasquali, A., Hilker, M., & Grebel, E. K. 2016, Monthly Notices of the Royal Astronomical Society, 459, 4450.

Wittmann, C., Lisker, T., Ambachew Tilahun, L., et al. 2017, MNRAS, 470, 1512

Worthey, G. 1994, The Astrophysical Journal Supplement Series, 95, 107.

Wyder, T. K., Martin, D. C., Schiminovich, D., et al. 2007, The Astrophysical Journal Supplement Series, 173, 293.

Yi, S. K. 2003, ApJ, 582, 202.

York, D. G., Adelman, J., Anderson, J. E., et al. 2000, AJ, 120, 1579.

Zabludoff, A. I. and Mulchaey, J. S. 1998, ApJ, 496, 39

Zandivarez, A., Díaz-Giménez, E., Mendes de Oliveira, C., & Gubolin, H. 2014, A&A, 572, A68

Zepf, S. E., & Ashman, K. M. 1993, MNRAS, 264, 611.

Zepf, S. E., Ashman, K. M., English, J., et al. 1999, AJ, 118, 752.

Zhang, Q., & Fall, S. M. 1999, ApJ, 527, L81.

Zhang, H.-X., Puzia, T. H., & Weisz, D. R. 2017, ApJS, 233, 13

Zinn, R. 1985, ApJ, 293, 424.

Zinnecker, H., Keable, C. J., Dunlop, J. S., Cannon, R. D., & Griffiths, W. K. 1988, in IAU Symposium, Vol. 126, The Harlow-Shapley Symposium on Globular Cluster Systems in Galaxies, ed. J. E. Grindlay & A. G. D. Philip, 603

Zwicky, F., Herzog, E., Wild, P., et al. 1961, Pasadena: California Institute of Technology (CIT.